The University of Sheffield

Investigation of Interior Permanent Magnet Machines and Variable Reluctance Resolvers Accounting for Manufacturing Issues

Xiao Ge

A thesis submitted for the degree of Doctor of Philosophy (PhD)

Department of Electronic and Electrical Engineering

University of Sheffield

United Kingdom

March 2016

ABSTRACT

This thesis investigates the electromagnetic performance of interior permanent magnet (IPM) machines for electric power steering application and variable reluctance (VR) resolvers for electric/hybrid electric vehicles, with particular reference to the manufacturing issues. It aims to reduce the cogging torque in IPM machines, to improve the position detection accuracy of VR resolvers, and to identify the influence of manufacturing tolerances.

For IPM machines, optimal step-skewing methods are firstly proposed to reduce the residual cogging torque component caused by the axial flux interaction between rotor steps, followed by corrections accounting for the machine materials and the tolerance of axial assembling gaps. Further, the influence of manufacturing tolerances is investigated, i.e. PM diversity, rotor eccentricities, stator out-of-roundness and skewing angle errors, resulting in lower orders of additional cogging torque components which cannot be effectively reduced by skewing. Amongst random distributions of different manufacturing tolerances, the most sensitive cases are identified respectively for predicting the ultimate values of potential cogging torques. Moreover, the influence is also investigated and compared amongst different IPM machine designs (i.e. different rotor contours and different slot/pole combinations, etc.), as a reference for selecting proper designs for applications with strict requirements on cogging torque and torque ripple. In addition, the field spatial harmonics are analyzed with and without manufacturing tolerances considered, in order to illustrate the origins of additional cogging torque components.

For VR resolvers, the basic operating principle and the winding configurations are firstly analyzed, based on which optimal stator slot (Z) and rotor saliency (p) number combinations are obtained. Further, a novel VR resolver topology with non-overlapping tooth-coil windings (NTWVRR) is proposed to simplify the manufacturing process of conventional VR resolvers, while the identical stator (and windings) of the proposed design can be employed in three different poles of resolvers. With actual application conditions considered, the proposed VR resolver proves to be a strong candidate of position sensor for hybrid electric/electric vehicle (HEV/EV) systems. Moreover, a novel design of rotor contour by injecting auxiliary air-gap permeance harmonics (AAPH rotor) is further proposed to eliminate the output voltage harmonics, which effectively improves the detection accuracy of the proposed and the conventional (Z=4p) VR resolver topologies. In addition, the influence of typical manufacturing tolerances (i.e. asymmetric coil locations and assembling eccentricities) on the detection accuracy is investigated and compared for different resolver designs.

As verification of the foregoing analyses, several IPM machine and VR resolver prototypes are fabricated and tested on the cogging torque and the position detection accuracy respectively.

ACKNOWLEDGEMENTS

Foremost, I would like to express my sincere gratitude to my supervisor, Professor Zi-Qiang Zhu, for his continuous encouragement and support throughout my PhD study, and for his invaluable advice and guidance to my career. Being his student is my good fortune and great honour!

I would also like to thank Mr. Peilin Xu, Dr. Yuan Ren, Dr. Wenqiang Chu, and all my fellows of Electrical Machines and Drives Group at The University of Sheffield for their help and inspired discussions. The experience of studying in the group will be my forever memory!

I would also like to thank Welling Motor Manufacturing Co., Ltd, China, for the sponsorship and the opportunity to boost my career. Special thanks also go to Dr. Jintao Chen for his kind recommendation and valuable help.

Finally, I would like to thank my wife, Yani Qu, my daughter, Benyi Ge, my parents and all my family members, for their love, understanding and encouragement to conquer all difficulties in my life.

CONTENTS

LIST OF SYMBOLS

Symbol	Description	Unit
A	Eccentric distance in the air-gap function of eccentric rotor contour	m
a	Length factor in the air-gap function of sinusoidal rotor contour	
B_r	PM remanence	T
B_{rk}	The kth order of radial air-gap flux density component	T
B_{tk}	The kth order of circumferential air-gap flux density component	T
b	Shape factor in the air-gap function of sinusoidal rotor contour	
E_{sk}	Voltage induced in SINE output coil on the kth stator tooth	V
E_m	Exciting electromotive force magnitude	V
E_s	Synthetic voltage of SINE output winding	V
E_c	Synthetic voltage of COSINE output winding	V
E_{sm}	Magnitude of motional electromotive force	V
E_{st}	Magnitude of transformer electromotive force	V
f	Frequency of exciting current	Hz
I_m	Exciting current	A
K	Fundamental wave factor in sinusoidal air-gap length function	
k	Auxiliary harmonic factor in AAPH rotor	
L_{ef}	Effective axial length of stator/rotor core	m
N_{e0}	Turns of exciting coil on each stator tooth	
N_{s0}	Maximum turns of SINE output coils	
N_{sk}	Turns of SINE output coil on the kth stator tooth	
n	Number of rotor steps for step-skewing rotor	
P_0	Constant component of air-gap permeance	H
P_e	Equivalent air-gap permeance under exciting teeth	H
P_k	Air-gap permeance facing to the kth stator tooth	H
P_{m1}	Sinusoidal component of air-gap permeance	H
P_{sc}	Equivalent air-gap permeance under output teeth	H

p	Number of rotor pole pairs of IPM machines or rotor saliencies of resolvers	
p_w	Number of output winding polarity pairs	
q	Selection factor of stator slot and rotor pole combinations	
$R_r(\theta)$	Outer radius of rotor pole shoe at different rotor positions	m
R_s	Inner radius of stator	m
r	Radius of eccentric pole shoe arcs for eccentric rotor contour	m
r_δ	Air-gap radius	m
T_c	Synthetic cogging torque	Nm
T_{ck}	The k^th^ cogging torque produced by the k^th^ flux density component	Nm
U_{in}	Exciting voltage	V
U_m	Magnitude of exciting voltage	V
X_{in}	Input reactance	Ω
Z	Number of stator teeth	
α_k	Electrical angle difference between the first and the k^th^ stator teeth	rad
α_{rk}	Angle of the k^th^ radial air-gap flux density component	rad
α_{tk}	Angle of the k^th^ circumferential air-gap flux density component	rad
δ	Air-gap length between the stator and the rotor	m
δ_{min}	Minimum air-gap length between the stator and the rotor	m
δ_{max}	Maximum air-gap length between the stator and the rotor	m
ε	Transformation ratio	
θ	Rotational angle (Mechanical)	rad
θ_{sk}	Theoretical step-skewing angle for cogging torque reduction	rad
μ_0	Vacuum permeability	H/m
Ψ_{sk}	Flux-linkage of SINE output coil on the k^th^ stator tooth	Wb
ω	Electric angular frequency of exciting signal	rad/s
ω_m	Mechanical angular frequency	rad/s

LIST OF ABBREVIATIONS

AAPH	Auxiliary air-gap permeance harmonics
AFVR	Axial flux variable reluctance
EMF	Electromotive force
EPS	Electric power steering
EV	Electric vehicle
FE	Finite element
FSCW	Fractional-slot-concentrated-winding
Hall-RM	Hall sensor combined with auxiliary inner-and outer ring magnet
HEV	Hybrid electric vehicle
HF	High frequency
IPM	Interior permanent magnet
ISG	Integrated-starter-generator
LCM	Lowest common multiple
MMF	Magnetomotive force
WF	Wound field
NTWVRR	Variable reluctance resolver with non-overlapping tooth-coil windings
PCB	Printed circuit board
PM	Permanent magnet
SPM	Surface-mounted permanent magnet
THD	Total harmonic distortion
VR	Variable reluctance

CHAPTER 1 GENERAL INTRODUCTION

1.1 Introduction

In the past decades, permanent magnet (PM) machines have attracted increasing research interest due to advantages in several aspects [CAR98], [ZHU07], [PER09], [TEN14]. First, without the need of an exciting current, the magnetic field in the air-gap is excited by the PMs, which avoids the additional excitation loss and consequently improves the machine efficiency. Second, strong PM materials, e.g. the sintered NdFeB magnet, can be employed to establish a high-intensity of magnetic field and the power/torque density can be enhanced. Therefore, the conflict between the power/torque output capability and the available space envelop can be solved, which is a common issue for the machines used in hybrid electric/electric vehicles (HEVs/EVs) [WAN08], [RED12], [PEL12], [MIR13], e.g. the traction machine, the integrated-starter-generator (ISG) machine, the electric power steering (EPS) motor etc. In addition, PM machines with fractional-slot concentrated windings (FSCW) can reduce the end winding length and the copper loss, through which the power/torque density and the efficiency can be further improved. With the increasing global environmental awareness and energy conservation demand considered, PM machines prove to be strong candidates for industrial and domestic applications.

However, as an inherent issue of PM machines, cogging torque is introduced by the interaction between the stator slot openings and the magnetic field produced by the PMs, which deteriorates the torque smoothness and also proves to be a potential source of noise and vibration [ISL10], [HWA01a]. Therefore, strict requirements on cogging torque are usually emphasized, and special design considerations should be made on the machine configurations.

Moreover, the position sensor is another important component of the electrical machine drive system. Different position sensors can be employed to perform the detection task, i.e. the Hall sensor, the encoders, and the resolvers, etc. Selecting proper sensors usually requires an overall evaluation of the cost, the reliability, the detection accuracy and the installation space.

Exemplified by the EPS application, the development on the employed PM machines and position sensors in recent years is illustrated [GE12], as shown in Table 1.1. It can also be seen that the manufacturing process is increasingly emphasized, directly relating to the performance of the electrical machine drive systems and the overall cost of products. Nowadays, the designs with simplified manufacturing process and decreased sensitivity to tolerances are more popular with the manufacturers, which usually exhibit great competitiveness.

TABLE 1.1

Development of EPS Motors and Position Sensors [GE12]

Manufacturer	Stator	Rotor	Position sensor
NIDEC 00’ 12-slot/8-pole		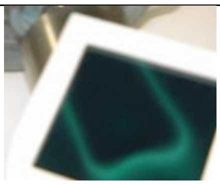	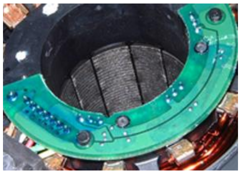
DELPHI 05’ 27-slot/6-pole			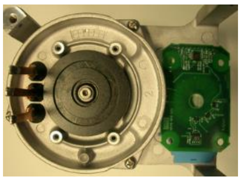
MITSUBSHI08’ 12-slot/8-pole		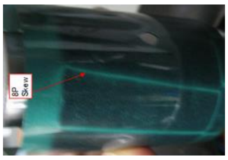	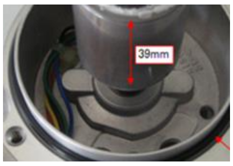
ASMOL 08’ 12-slot/14-pole			
HITACHI 08’ 12-slot/10-pole			
NIDEC 09’ 12-slot/8-pole		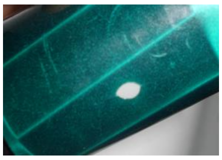	
ASMOL10’ 12-slot/10-pole	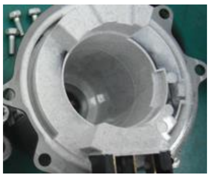		
BROSE (New product) 12-slot/10-pole			-
TRW (New product) 12-slot/8-pole			-

1.2 PM Machine Designs for Cogging Torque Reduction

As shown in Table 1.1, in order to reduce the cogging torque and provide a pleasant driving experience, many different design considerations on the EPS motors have been made by the worldwide leading manufacturers, e.g. the stator slot/rotor pole combinations [ZHU00], [HWA01b], the tooth shapes [ZHU00], [BIA02], [FEI11], [LI88], the auxiliary teeth [ZHU00], [BIA02], the PM magnetization styles [ZHU05], the step-skewing methods [HAN97], [FEI13], and the rotor shaping approaches [HWA01b], [CHE10], [DUB02], etc.

In order to select a competitive design configuration, conventional methods for cogging torque reduction are illustrated in Fig. 1.1. Due to the inherent feature of low cogging torque and the simplified winding fabrication [ZHU00], [ZHU12], [REF10a], fractional-slot PM machines are more popular with these applications. Amongst these specific methods, more practical and representative designs are further discussed and compared in this section considering the manufacturing process and the potential manufacturing tolerances.

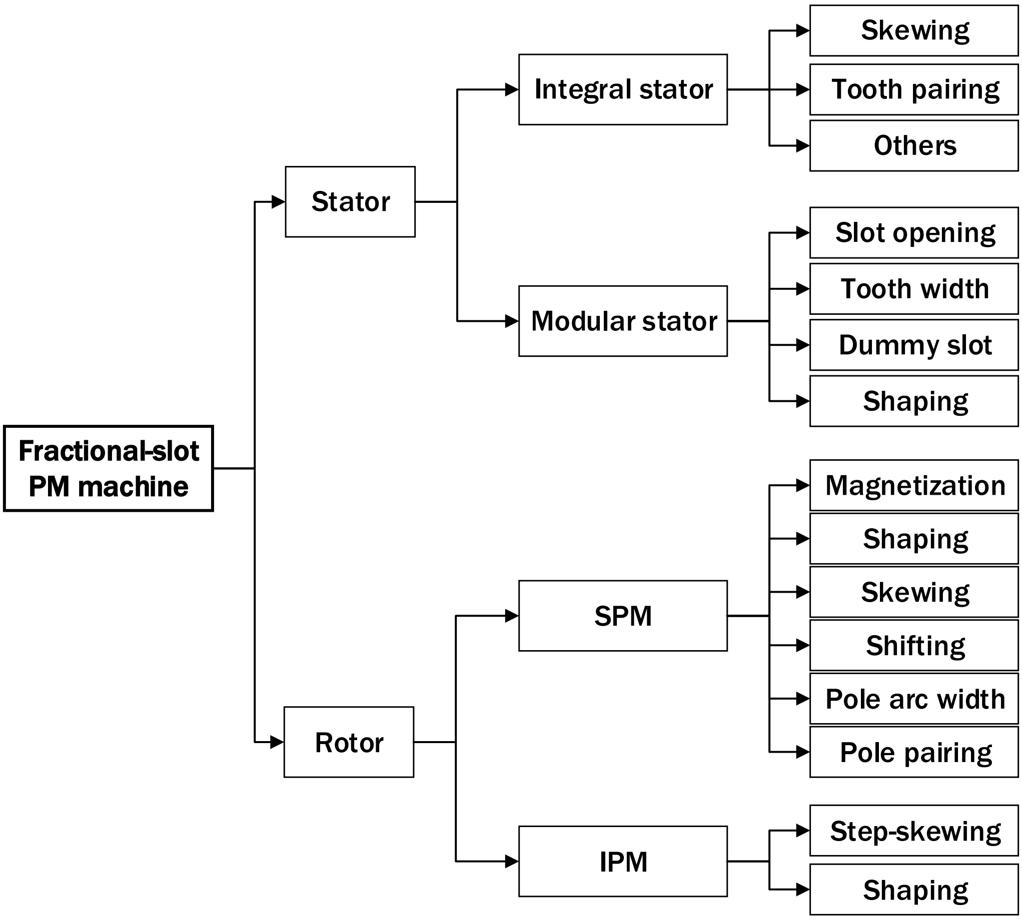

Fig. 1.1 Conventional methods for cogging torque reduction.

1.2.1 Stator Slot and Rotor Pole Combinations

It has been proven that low cogging torque performance can be achieved in fractional-slot PM machines [ZHU00], [BIA02], which can also be seen from the existing topologies in Table 1.1. Two representative topologies ever employed are illustrated, i.e. the 27-slot/6-pole and the 12-slot/8-pole designs, as shown in Fig. 1.2. It can be seen that two significantly different winding configurations are employed – the over-lapping distributed and the non-overlapping concentrated windings respectively, both of which can realize the automatic winding fabrication. Despite this, the distributed windings usually require shaping operation on the over-hang coils, which poses a potential threat to the wire insulation. Moreover, the length of over-hang coils and the packing factor still prove to be two insurmountable issues, which limit the torque density and the efficiency of such machine topologies. Instead, the non-overlapping concentrated windings can be employed in the 12-slot/8-pole machines, and the much shorter over-hang coils avoid the aforementioned issues. Therefore, the fractional-slot PM machines with concentrated windings (FSCW PM machines) become more popular with the applications.

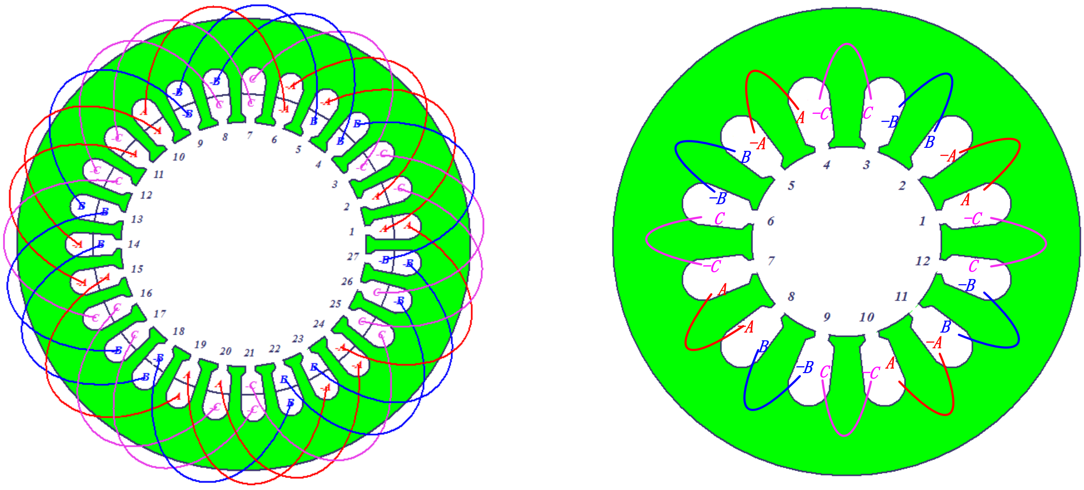

(a) Overlapping distributed (27-slot/6-pole)

(b) Non-overlapping concentrated (12-slot/8-pole)

Fig. 1.2 Fractional-slot PM machine topologies (rotor not shown).

In order to further ease the winding fabrication, the modular stator techniques are more frequently employed in FSCW PM machines, two representatives of which are illustrated in Fig. 1.3, i.e. modular stators by individual tooth/back-iron and separated tooth/back-iron [ZHU12], [REF10a]. High packing factor can be achieved by both of the two techniques, which consequently facilitates the improvement on machine efficiency.

However, additional gaps during the assembling of separated components usually exist, and it has been proven that the non-uniform stator gaps would significantly increase the magnitudes and the periodicity of cogging torque [ZHU12]. Moreover, the stator out-of-roundness may also deteriorate due to the potential tooth-bulges during the assembling, the influence of which on cogging torque should also be further investigated.

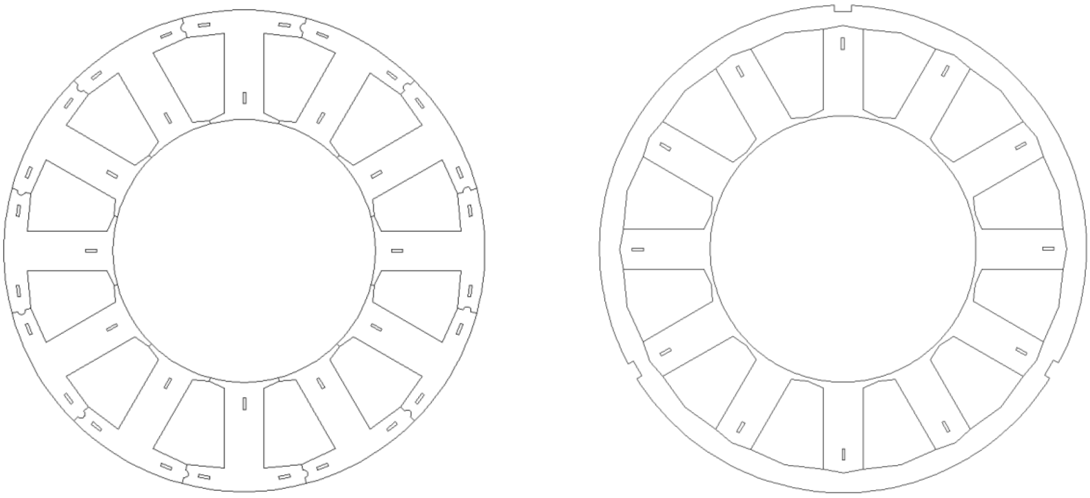

(a) Individual stator tooth/back-iron

(b) Separated tooth and back-iron

Fig. 1.3 Modular stator techniques in FSCW PM machines [ZHU12].

In addition, it can be seen from Table 1.1 that the 12-slot/8-pole and the 12-slot/10-pole are the most popular combinations amongst the existing products. For comparison, the cogging torque performance should also be further investigated and compared between the different slot/pole combinations, especially when the manufacturing tolerances are considered.

1.2.2 Magnetization Methods

Before the selection of rotor configurations, it is necessary to evaluate the available PM magnetization process, which is an important procedure and the quality is closely related to the machine performance. In recent years, the influence of magnetization directions has been investigated, including the parallel and the radial styles [WAN05], [KIM13a]. Moreover, the Halbach distribution of PM segments has been proposed [ZHU01], [JAN01], through which more sinusoidal air-gap flux density and minimum cogging torque can be achieved. However, the assembling of magnetized PMs complicates the rotor fabrication whilst the technology of post-assembly magnetization for such designs is more difficult.

As a key technology of SPM machines, the ring magnet by NdFeB material has been produced by a leading manufacturer [ESA06], and even the skewing magnetization can be realized, as shown in Fig. 1.4. It can be deduced that more simplified rotor manufacturing process and more efficient use of PM materials can be achieved with the ring magnet employed. However, the high price of the ring magnet still hinders further application of this technology, especially when the cost is emphasized.

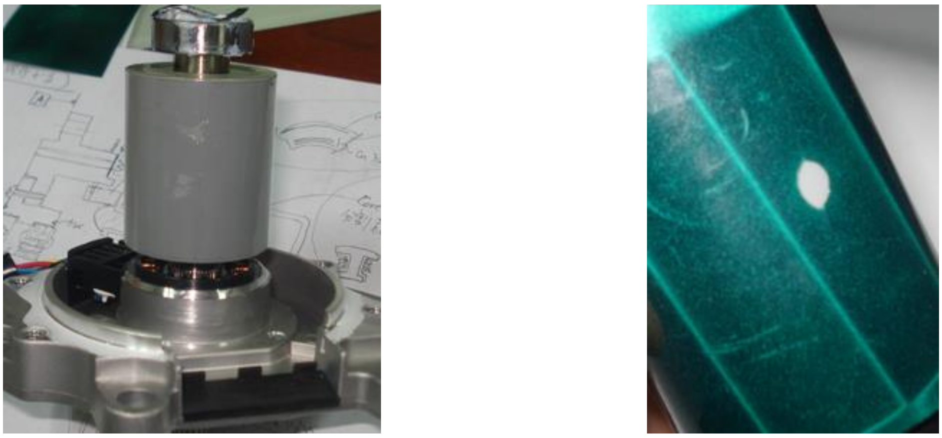

(a) Rotor with ring magnet (b) Magnetization

Fig. 1.4 Ring magnet with skewing magnetization technology (NdFeB).

Nowadays, in order to ease the assembling of PMs and reduce the PM diversity by unstable magnetizing conditions, the post-assembly magnetization technology by an integral magnetizer has been widely employed during the fabrication of conventional PM machine topologies, e.g. SPM machines, radial-type IPM machines, etc. Despite this, the PM magnetic property (e.g. the PM remanence) usually exhibits inevitable tolerances due to the PM material divergence, and it is still necessary to investigate the potential influence of PM diversity on cogging torque performance.

1.2.3 Shaping Methods

Another frequently employed approach is the rotor shaping [HWA01b], [DUB02], [CHE10a], [CHE14], i.e. the magnet shaping in SPM machines and the rotor contour shaping in IPM machines, as shown in Figs. 1.5(a) and (b) respectively. With the field harmonics decreased, the cogging torque of PM machines can be effectively reduced.

Compared with the magnet shaping in SPM machines, the IPM rotor contour shaping can be more conveniently performed during the punching process of silicon-steel laminations [EVA10], with the shape of rectangular PMs unchanged. Therefore, more efficient use of the PM materials is realized, which consequently reduces the overall cost.

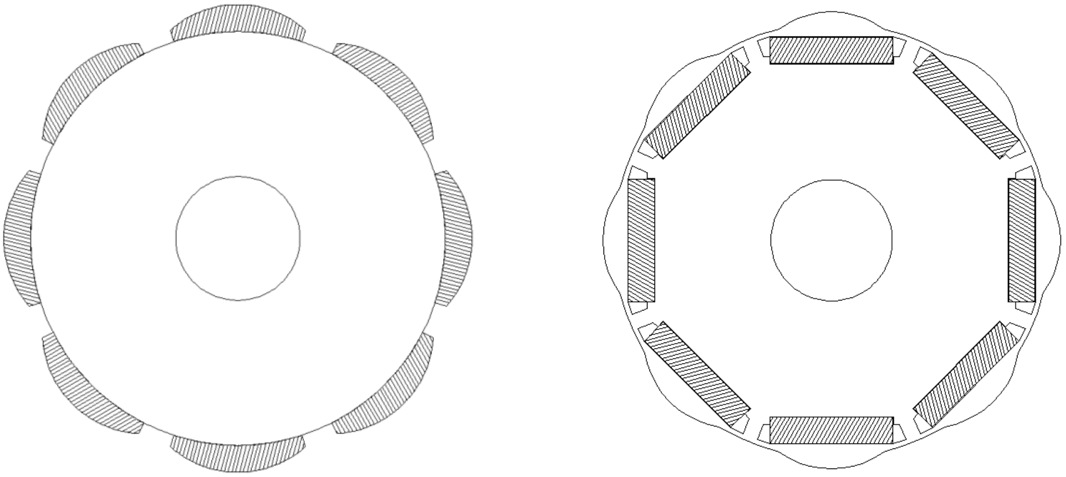

(a) SPM rotor magnet [CHE14]　　(b) IPM rotor contour [EVA10]

Fig. 1.5 Shaping methods in SPM and IPM rotors.

More specifically, different shaping methods of rotor contour have been investigated, e.g. the eccentric and the sinusoidal designs, as shown in Fig. 1.6. For the eccentric rotor contour, the pole shoes are formed by eccentric arcs (the arc centers deviate from the rotor center by an eccentric distance), which are joined by concentric arcs at inter-polar locations. According to Fig. 1.6 (a), the outer radius of the rotor pole shoes can be described by:

$$R_r(\theta) = A\cos(\theta) + \sqrt{r^2 - (Asin(\theta))^2} \tag{1. 1}$$

where θ is the mechanical angle, A and r represent the eccentric distance and the radius of these eccentric arcs respectively. Different from that of the eccentric rotor contour, each pole shoe of the sinusoidal design is formed by an inverse cosine function, as shown in Fig. 1.6 (b). According to the minimum air-gap length, the outer radius of the rotor pole shoes can be expressed by:

$$R_r(\theta) = R_s - \frac{\delta_{min}}{\cos(p\theta)} \quad (-\frac{\pi}{2p} < \theta < \frac{\pi}{2p}) \tag{1. 2}$$

where R_s and δ_{min} represent the stator inner radius and the minimum air-gap length respectively, p is the number of pole pairs.

Therefore, it can be deduced that the sinusoidal design of rotor pole shoe is only defined by the minimum (δ_{min}) and maximum (corresponds to the maximum θ) air-gap lengths whilst the eccentric design is still subject to the eccentric distance (r).

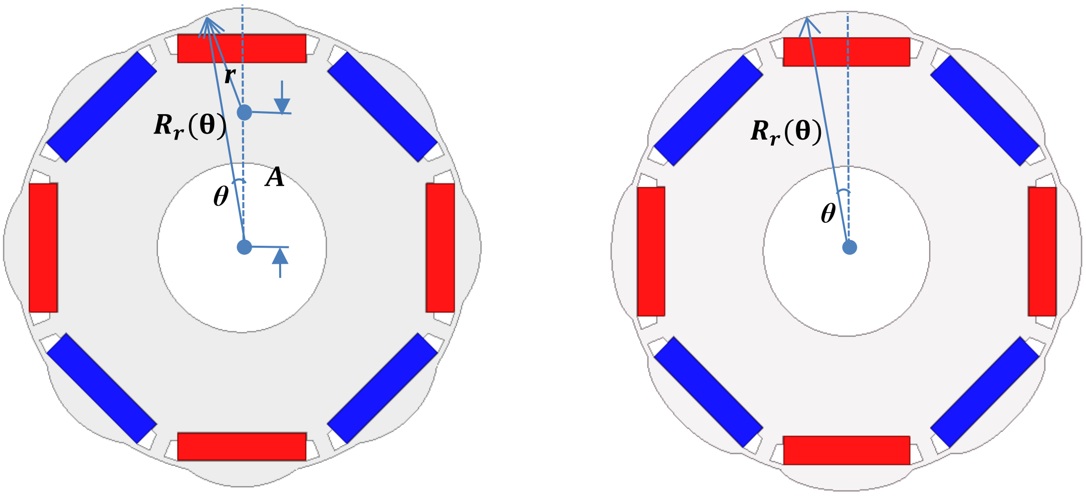

(a) Eccentric design (b) Sinusoidal design

Fig. 1.6 IPM rotor contours by different shaping methods [EVA10].

Under ideal conditions, both of the two designs can be employed to reduce the cogging torque of IPM machines. However, manufacturing tolerances are usually inevitable, and it is still necessary to investigate the specific influence on cogging torque and compare the sensitivities between the two designs, as a reference for selecting proper designs and parameters.

1.2.4 Skewing Methods

In order to further reduce the cogging torque, skewing methods can be employed, either on the stator or the rotor side. When the stator or rotor is skewed by a proper angle, the cogging torque can be theoretically eliminated under ideal conditions [HAN97], [ZHU00]. However, with the winding fabrication considered, skewing methods on the rotor are more convenient than on the stator, e.g. magnet skewing for SPM machines, including the step-skewing and the continuous skewing styles, as shown in Fig. 1.7.

Compared with SPM machines, the rotor continuous skewing for IPM machines is much more difficult to perform, due to the irregular PM shape and the complicated magnetization. Instead, the step-skewing rotor proves to be more practical to realize and the similar skewing effect can be achieved [BIA02], [JAN97], [FEI13], [ISL09], [CHU13], [ZHU12], [FEI10], [FEI12], [KIM14], [CHE10], and [EAS97], as shown in Fig. 1.8. Considering the unchanged rectangular PM shapes, IPM machines by step-skewing rotor exhibit obvious competitiveness on the production cost of PMs compared with SPM machines.

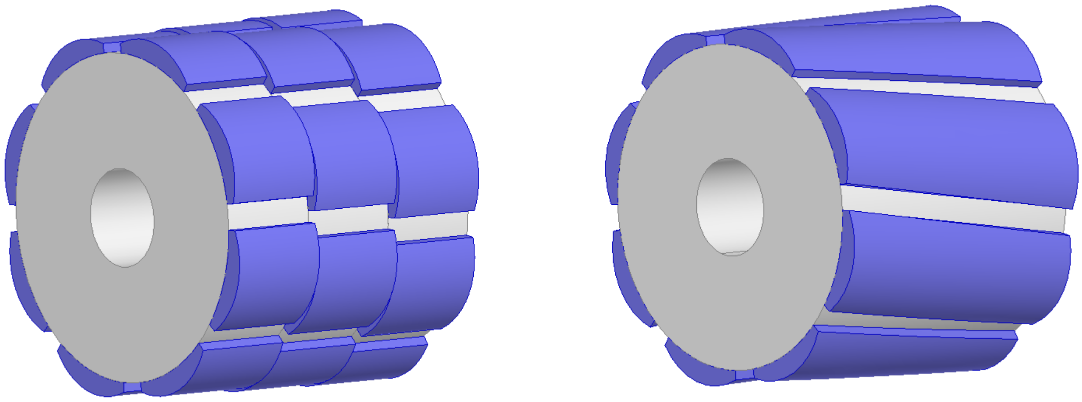

(a) Step-skewing (b) Continuous-skewing

Fig. 1.7 Skewing methods in SPM machines [BIA02].

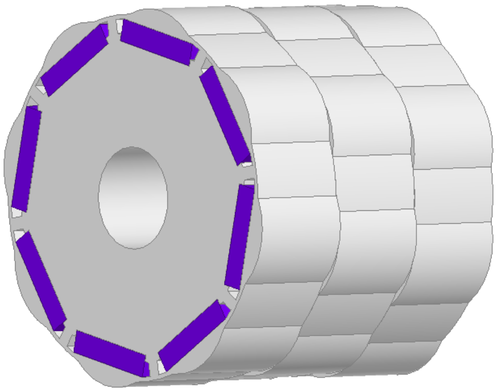

Fig. 1.8 Step-skewing method in IPM machines [ZHU12].

However, during the manufacturing process of IPM machines by step-skewing rotors, tolerances of the skewing angles may be introduced, resulting in residual cogging torque components. Therefore, it is necessary to investigate the potential influence. Moreover, the axial flux interaction between adjacent rotor steps and the end effect of side rotor steps always exist, of which the influence on cogging torque performance has not been investigated in previous research. In addition, the axial assembling gaps between the adjacent steps are also difficult to avoid, which should also be further considered in the design of step-skewing rotors.

1.2.5 Comparison amongst Different PM Machine Designs

In order to reduce the cogging torque, conventional approaches employed in PM machines have been presented. With the manufacturing process and the competitiveness of products considered, the fundamental principle of selecting PM machine configurations and cogging torque reduction methods can be generalized.

First, the stator slot and rotor pole combinations should be evaluated. With the winding fabrication and the assembling space considered, the FSCW PM machines prove to be an ideal selection, which also exhibit lower cogging torque. In order to further increase the packing factor and machine efficiency, modular stator techniques can be employed.

Second, proper rotor configurations should be chosen. The employed design should be capable of post-assembly magnetization, in order to avoid the assembling of magnetized PMs and reduce the potential PM diversity by unstable magnetizing conditions.

Third, the PM assembling process and the material consumption should be considered in order to reduce the overall cost. Compared with SPM machines, more simplified manufacturing process and higher reliability can both be achieved by the IPM designs, in which the PMs are conveniently embedded in the rotor core without the need of additional bonding. Moreover, the higher reliability can also be reflected by improved demagnetization withstand capacity under overload conditions, since the PMs do not directly face the armature field. Furthermore, the rectangular shape of PMs facilitates more efficient use of PM materials, which also reduces the overall cost of products.

In addition, skewing methods can be employed when the cogging torque requires further reduction. It proves to be more convenient to perform the task on the rotor side. For IPM machines, the step-skewing methods can significantly simplify the manufacturing process, in which the number of rotor steps should also account for the specific cogging torque components.

For the applications such as EPS motors, it can be seen that the FSCW PM machines using the modular stator techniques usually exhibit obvious advantages by employing a step-skewing IPM rotors with particular design of rotor contours, e.g. simplified winding fabrication and rotor assembling, decreased assembling space, improved reliability, and more competitive overall cost, etc. Therefore, the analyses in this thesis will be carried out mainly based on this configuration.

1.3 Position Sensors for Electric Machines

In order to guarantee favourable dynamic performance of the machine, it is well known that accurate rotor position signals should be provided to the machine driver, and this task is usually performed through a position sensor. As can be seen from Table 1.1, different types of position sensors have been employed in the EPS motors during the past few years. In addition, worldwide investigation has been carried out on sensorless control and several methods have been proposed by researchers in this field. In order to select the proper position detection methods for the EPS motor, it is necessary to review the existing solutions.

1.3.1 Hall Sensor

As a common approach, position signals by Hall sensors can be used for the commutation of brushless DC motors [PHC00], with the fundamental operating principle shown in Fig. 1.9. The Hall Effect is a phenomenon which shows that if a magnetic field is perpendicular to a thin strip of conductive material and an electric current flows lengthwise through the strip, the mobile charges that carry the current will drift to one edge as they move along the strip, as shown in Fig. 1.9 (a). Many types of sensors use the Hall Effect to detect the presence of magnetic fields and Fig. 1.9 (b) illustrates a conceptual drawing of this kind of sensor. A constant current runs through a conductive Hall strip inside the sensor. When the magnet rotates, the alternating field will cause an alternating Hall Effect voltage to be generated across the strip, which is fed into circuitry that shapes the waveform. The output of the circuitry is a digital signal that is either +5VDC or 0. It should be noted that the sensor requires power connections for its internal circuitry (+5VDC and Ground). In addition, although the actual Hall Effect voltage generated inside the sensor is an analog signal, the output is a digital signal, either ON or OFF. As shown in Fig. 1.9 (c), a typical application of the Hall sensors in brushless DC motors are illustrated.

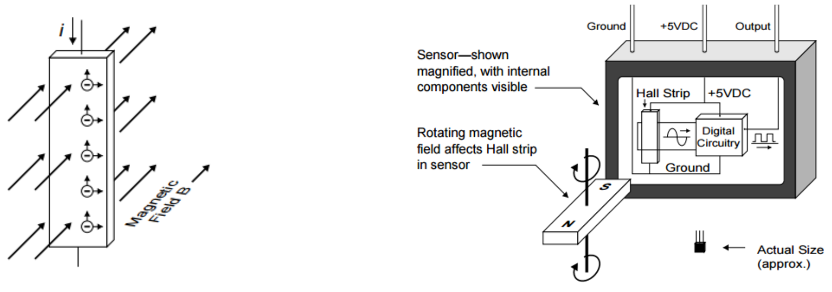

(a) Hall Effect (b) Hall Effect sensor

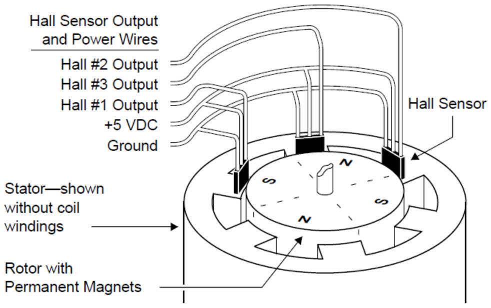

(c) Hall sensor application

Fig. 1.9 Hall sensor [PHC00].

Several advantages can be achieved by employing Hall sensors, of which the most significant one is very low price. In addition, they can be conveniently integrated into a motor due to small size, e.g. embedded in the stator bobbin. However, continuous position signals should be provided for high-performance machine systems, which cannot be performed by Hall sensors.

1.3.2 Hall Sensors Combined with Auxiliary Inner-and-Outer Ring Magnet (Hall-RM)

In order to improve the detection accuracy, Hall sensors combined with auxiliary inner-and-outer ring magnet (Hall-RM) is proposed, as shown in Fig. 1.10. It can be found that three Hall sensors are integrated to the PCB board facing to the 6 inner magnet poles of the auxiliary ring magnet (corresponding to the 6-pole machine), and another two Hall sensors are placed over the 72 outer magnet poles. In addition, two phases of micro windings are also integrated into the PCB board, which provide two orthogonal (SINE and COSINE) signals reflecting the 6-pole variation. Therefore, the first three Hall sensors provide the U/V/W signals and the second two produce the A/B signals whilst the counting error can be corrected by the SINE and COSINE coil voltages. The PCB board, the ring magnet and the three types of position signals are illustrated, as shown in Fig. 1.10.

It can be deduced that the position detection accuracy is obviously improved by the Hall-RM sensor. However, it requires complicated fabrication process and multiple components, e.g. 5 Hall sensors, auxiliary inner-and-outer ring magnet, micro windings inside the PCB, which obviously increase the production cost. In addition, the installation of Hall-RM sensor usually occupies more axial space. Due to these issues, this kind of sensor has not been widely employed in industrial applications.

(a) Installation

(b) Inner-and-outer ring magnet

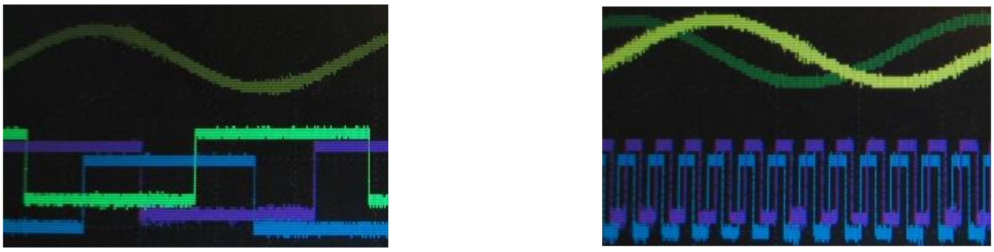

(c) Three-inner-Hall signals

(d) Dual-outer-Hall signals and coil signals

Fig. 1.10 Hall sensors combined with auxiliary inner-and-outer ring magnet [JIN10].

1.3.3 Optical and Magnetic Encoders

A. Optical Encoder

Due to the advantages of the semi-conductor technology incorporated, optical encoders are the preferred solution in many industrial applications [EPC06], with the basic construction and operating mechanism shown in Fig. 1.11. As can be seen, a beam of light emitted from an LED passes through a transparent disk patterned with opaque lines, which is picked by a photodiode array. The photodiode array (also called a photo sensor) responds by producing a sinusoidal waveform which is transformed into a square wave, or pulse train.

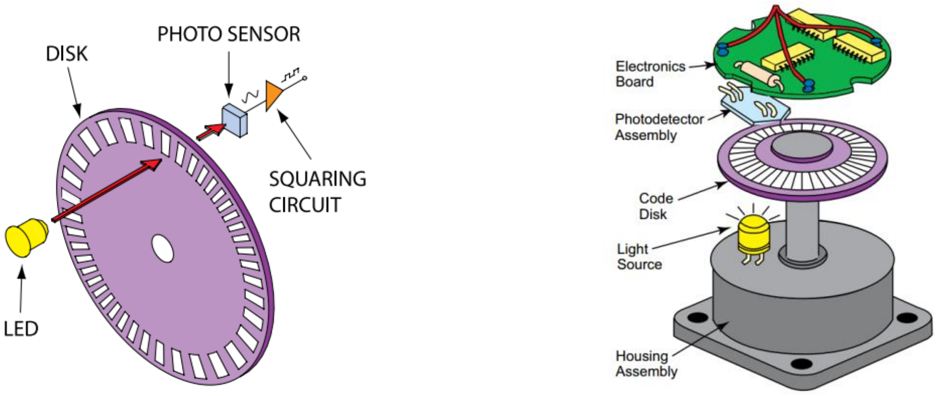

(a) Basic operating mechanism

(b) Basic construction

Fig. 1.11 Optical encoder [EPC06].

As a frequently employed branch, the incremental optical encoders are available in two basic channel types: single channel and quadrature. A single channel encoder is normally used in systems that rotate in one direction only and require simple position and velocity information. Quadrature encoders have dual channels, phased 90 electric degrees apart. These two output signals also determine the direction of rotation by detecting the leading or lagging signal in their phase relationship. Very high speed bi-directional information can be achieved by quadrature encoders for complex motion control applications. Moreover, incremental encoders provide a once-per-revolution pulse (often called marker, index, or reference) that occurs at the same mechanical point of encoder shaft revolution. This pulse is on a separate output channel (Z-channel) from the signal channel or quadrature outputs. The index pulse is often used to position motion control applications to a known mechanical reference. In addition, resolution is a term used to describe the cycles per revolution for incremental encoders. Each encoder has a defined number of cycles that are generated for each full 360 degree shaft revolution. These cycles are monitored by a counter or motion controller and converted to counts for position and speed control.

Nowadays, very high detection accuracy can be achieved by optical encoders, and this kind of sensor turns out to be a good option for precise position control systems. However, some typical problems still hinder further application of optical encoders, e.g. the high cost due to the complicated structure, the relatively low reliability, the application life of the light source and the sensor, etc.

B. Magnetic Encoder

In addition to the optical encoder, another kind of encoders has been proposed and utilized in recent years, designated as magnetic encoder [AUS10], as shown in Fig. 1.12. This kind of sensor is composed of two fundamental components: a chip (an integrated circuit with built-in Hall elements) and a permanent magnet. With a proper arrangement of multiple Hall elements and digital signal processing, the chip can precisely detect the rotating angle of the magnet which is installed facing to the chip.

As can be seen from Fig. 1.12, a group of four (or eight) Hall sensors are arranged in a circular array and embedded in the silicon chip. Opposite Hall sensors are combined by differential amplification and the SINE/COSINE signals are digitized by two parallel ADCs with a subsequent digital filter reducing the noise. Then, the SINE and COSINE signals are converted into angle and magnitude signals.

Compared with optical encoder, it can be seen that the magnetic encoder has decreased number of components (a magnet and a minimum number of external components), which results in higher reliability and much lower cost. Due to the circular array of Hall sensors, a much higher detection accuracy can be achieved by employing the magnetic encoder, when compared with that of Hall sensor. Therefore, when the detection accuracy cannot be satisfied by Hall sensor, this magnetic encoder become a better choice.

(a) Magnet and signal processing chip (b) Integration into electric machine

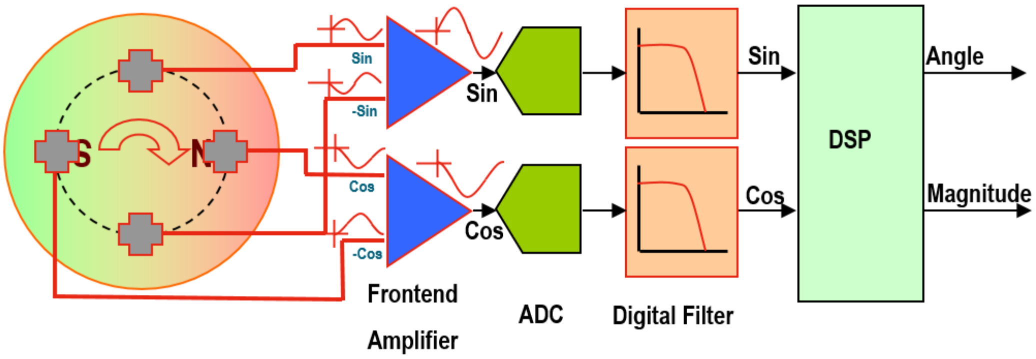

(c) Basic operating mechanism

Fig. 1.12 Magnetic encoder [AUS10].

However, the application of magnetic encoder also has some problems. First, in order to integrate it into a machine, it is necessary to arrange axial space for this sensor during the stage of structural design, which increases the overall axial length. Second, a non-magnetic stainless steel shaft or auxiliary materials should be employed to install the permanent magnet which provides the necessary axial magnetic field for the chip. Therefore, the manufacturing process is complicated and the overall cost is increased. In addition, the detection accuracy of this sensor is still limited, which is based on Hall elements. These existing problems hinder further application of the magnetic encoder.

1.3.4 Resolvers

Besides the Hall sensors and the encoders, resolvers are another kind of position sensors for electric machines. According to the operating principle, resolvers can be divided into two main categories: the wound field (WF) type [FIG11], [BEN13], [HOS07] and the variable reluctance (VR) type [SUN04], [SUN08], [CUI12], [KIM13b], whilst the VR type can be further divided into the axial flux VR and the radial flux VR topologies.

Before the introduction of different resolver topologies, a fundamental theory for this kind of position sensors is firstly presented. As shown in Fig. 1.13, typical input and output signals in resolvers are illustrated. It can be seen that a high-frequency exciting current is input to the exciting coil and two orthogonal signals are induced in the sine and cosine output coils. Through an arc tangent operation of the output signals, the rotor position can be obtained.

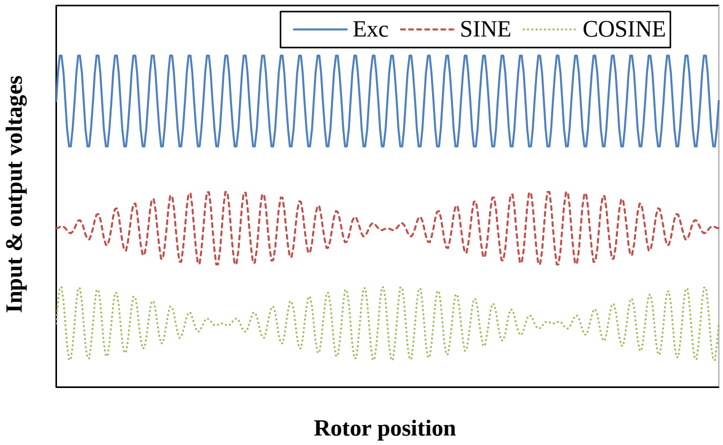

Fig. 1.13 Typical input and output signals in resolvers.

In order to better describe the operating principle, signal processing methods for resolvers are also illustrated in this part, and this task is always performed by commercial decoding chips, e.g. AU6802, AD2S80 and related subseries [TAM02], [ANA08]. Usually, the input and output voltages can be described by:

$$U_{in} = U_m \sin(\omega t) \tag{1. 3}$$

$$E_s = \varepsilon\, U_m \sin(p\theta)\sin(\omega t) \tag{1. 4}$$

$$E_c = \varepsilon\, U_m \cos(p\theta)\sin(\omega t) \tag{1. 5}$$

where U_m and ω represent the magnitude and the angular frequency of exciting voltage. The symbol of p and ε are the number of rotor saliencies and the transformation ratio respectively. By demodulation and an arc tangent calculation of (1.4) and (1.5), the rotor positions can be obtained. As an example, the signal processing by the decoding chip AU6802n1 is introduced, as shown in Fig. 1.14. It can be seen that when the output of the voltage comparator is equal to zero, the angle of θ_r will be the actual rotor rotation angle.

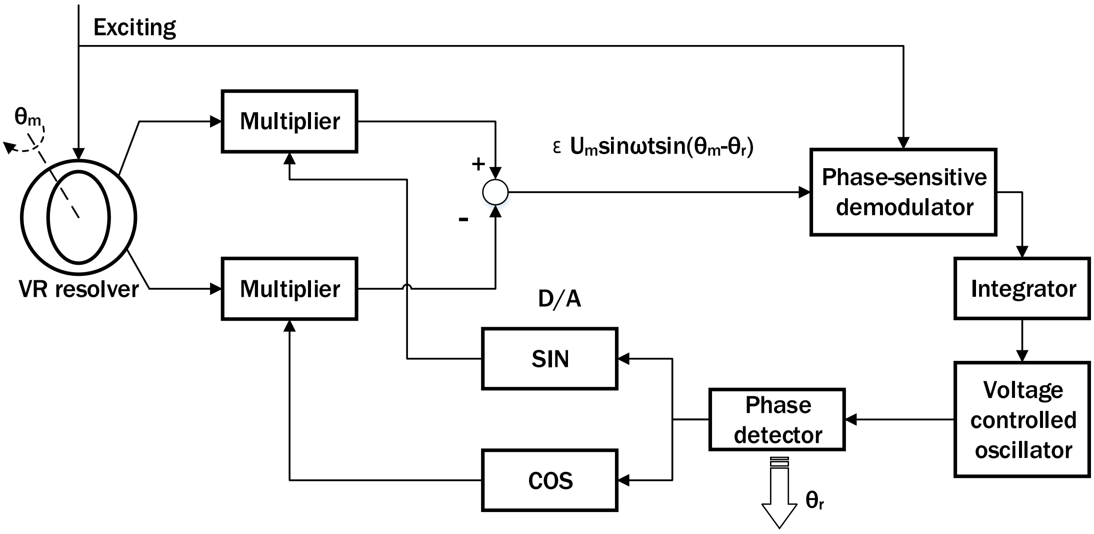

Fig. 1.14 TAMAGAWA AU6802 schematic diagram [TAM02].

A. Wound-Field (WF) Type of Resolver (TAMAGAWA)

The WF type of resolver is an important branch, as shown in Fig. 1.15, in which the output windings and the exciting winding are located on the stator and the rotor respectively. As can be seen, a ring transformer is employed to realize the brushless design, through which the high frequency exciting signal is transmitted from the primary to the secondary winding of transformer, as an input for the exciting winding of resolver. With the sinusoidally distributed winding employed, approximately sinusoidal air-gap flux density can be established. Two phases of orthogonal output signals can be obtained in the two phases of output windings on the stator, corresponding to the rotor position. By demodulation and arc tangent calculation of the signal, the rotor positions can be obtained.

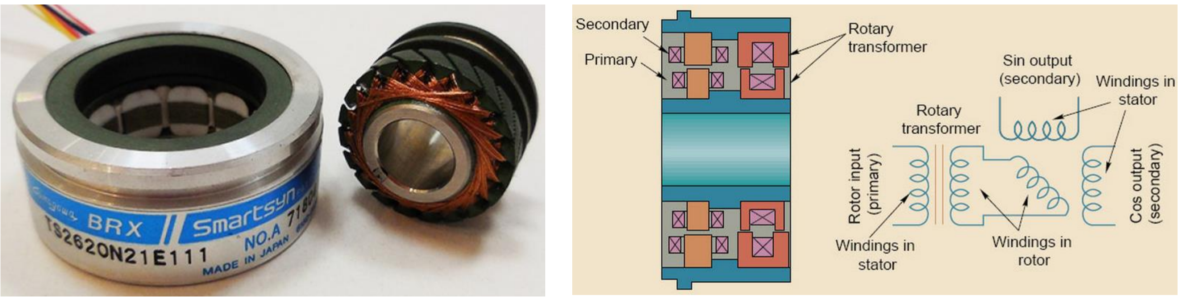

(a) Typical product (b) Winding arrangement

Fig. 1.15 WF resolver [TAM04].

As the output voltage quality is closely related to the detection accuracy, sinusoidally distributed output windings and exciting windings are usually employed to eliminate the voltage harmonics. In addition, a skewed rotor is always required to further reduce the tooth harmonics which cannot be reduced by the two windings. Therefore, a high detection accuracy can be achieved by this kind of sensor. Moreover, high reliability can also be realized due to the employment of only copper wires and silicon steel laminations. With these advantages considered, WF resolvers are frequently used in industrial applications.

Despite these advantages, some problems still exist in the manufacturing and application of WF resolvers. First, the manufacturing process is complicated, e.g. the sinusoidally distributed windings, the skewed rotor, the additional ring transformer, which may increase the overall cost of product. In addition, the axial length is significantly increased with the ring transformer employed. Due to these existing problems, WF resolvers are seldom used in vehicle applications.

B. Axial Flux Variable-Reluctance (AFVR) Resolver (Admotec)

Based on the principle of variable reluctance, AFVR type of resolver was firstly invented in 1970s, through which absolute rotor position signals can be obtained [SHA12], as shown in Fig. 1.16. Different from the WF type of resolver, the two phases of output windings and the exciting winding are all located on the stator which are composed of three steps, thus brushless design can be easily realized without the need of the ring transformer. More importantly, sinusoidal air-gap permeance is obtained by changing the electro-magnetic coupling area between the stator and rotor core in AFVR resolvers, rather than through a sinusoidally distributed magnetomotive force (MMF) by exciting winding in WF resolvers. Therefore, a particular design is required for the rotor core, which is composed of two parts: magnetic material for flux circulation and non-magnetic material for upholding the foregoing part. By employing an appropriate shape of inclined ring of rotor, sinusoidal air-gap permeance can be obtained, as well as the expected output voltages.

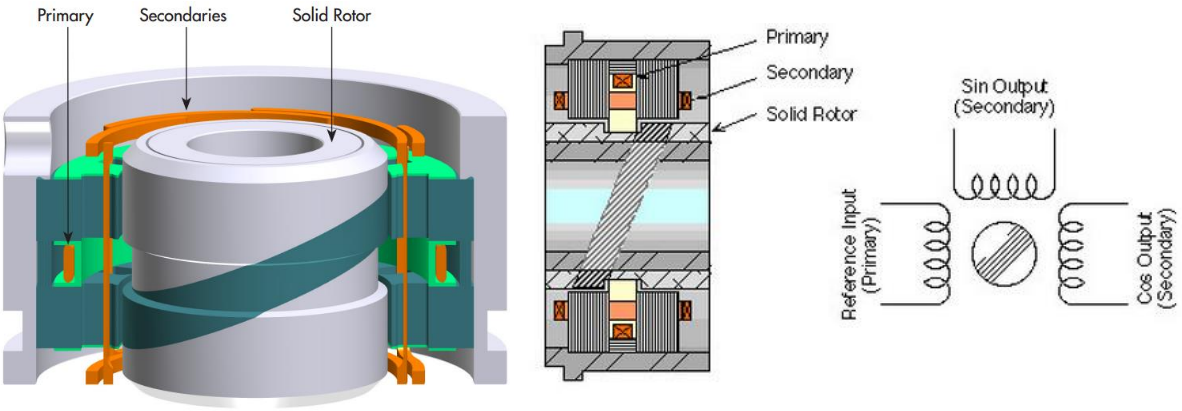

(a) Fundamental structure (b) Winding arrangement

Fig. 1.16 AFVR resolver [ADM08].

However, this kind of resolver also has some disadvantages. For example, the stator and rotor cores are composed of three axial steps to provide the necessary flux circulating paths, which consequently increase the total axial length although no ring transformer is needed. Moreover, the rotor fabrication proves to be a difficult task and the production quality directly influences the detection accuracy. In addition, the winding fabrication is complicated due to the fact that the exciting winding and the two phases of output windings are vertical to each other. Therefore, the manufacturing process proves to be very complicated for AFVR resolver and the product quality is difficult to guarantee.

C. Conventional Variable-Reluctance Resolver (TAMAGAWA, Minebea)

In addition to the AFVR resolver, another type of VR resolver becomes a hotspot in recent years [SUN04], [SUN08], [KIM09], [KIM10], [KIM13b], [CUI12], as shown in Fig. 1.17. Fig. 1.17 (a) shows a typical structure of early VR resolver. With multiple teeth on the rotor and sub-teeth on the stator, sinusoidally modulated signals can be obtained through the varying reluctance in the air-gap. However, the detection accuracy is always restricted to the number of rotor teeth and it fails to provide absolute position signals for most of industrial applications. In order to solve the problem, a modern VR resolver topology is proposed, as shown in Fig. 1.17 (b). Sinusoidal air-gap permeance is easily obtained through a particular design of the rotor contour, with a proper air-gap length function employed. Compared with WF resolver, brushless design can be easily realized without the need of a ring transformer and much smaller axial length is achieved, which also significantly decreases the overall cost. Different from AFVR resolver, sinusoidal air-gap permeance is obtained through variation of the air-gap length function by the modern resolver topology, rather than through changing the electro-magnetic coupling area between the stator and rotor core. It can be deduced that the manufacturing process is obviously simplified by this VR resolver topology, through which the fabrication cost and the total axial length of products can be effectively reduced. With these advantages considered, the modern VR resolvers are increasingly employed in industrial applications, especially in HEV/EV systems.

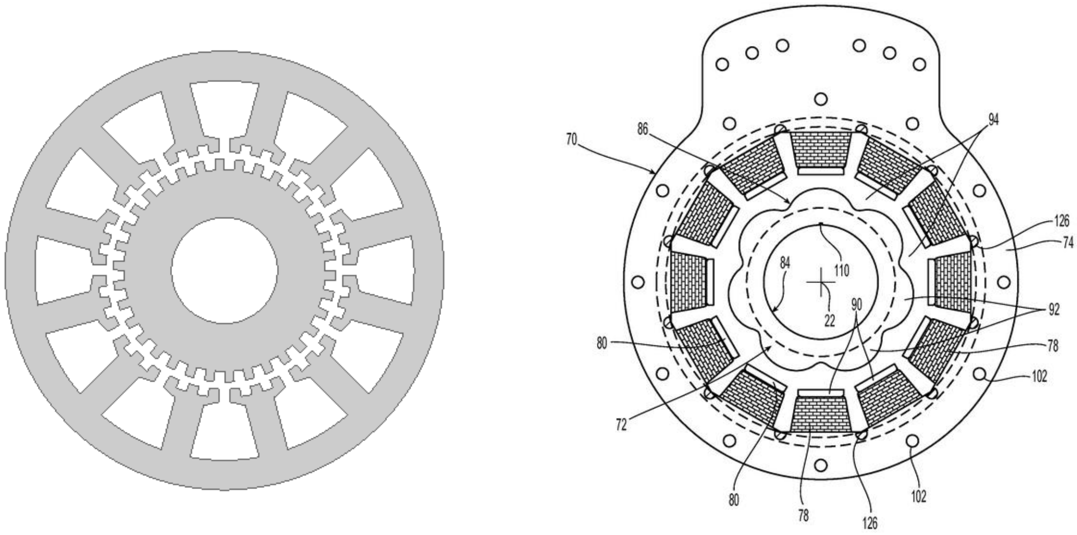

(a) Early topology (lamination)
[KRO57], [HAN89]

(b) Conventional topology (lamination)
[GAL14]

Fig. 1.17 Conventional VR resolvers.

1.3.5 Sensorless Control Methods

In recent years, sensorless techniques have been widely investigated to simplify the machine systems and reduce the overall cost. Without the need of a physical position sensor, different methods of on-line rotor position estimation have been proposed, which can be classified into two groups, i.e. fundamental model based and saliency based methods, as shown in Fig. 1.18.

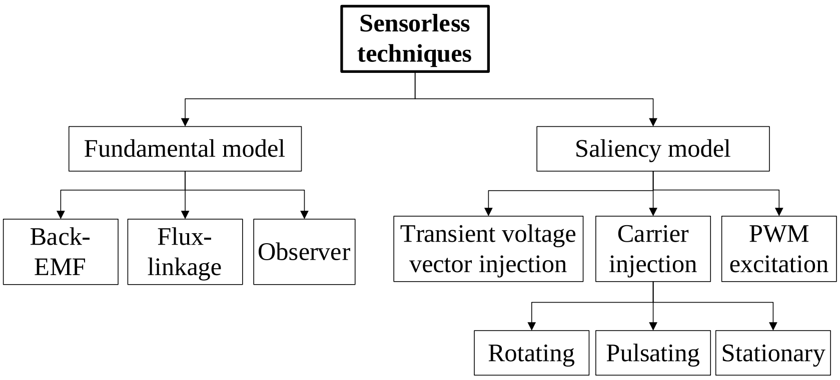

Fig. 1.18 Sensorless control techniques for PM machines.

The first groups of techniques have presented excellent position estimation performance in the middle- and high-speed region, [LI07], [CHI09]. Generally, the sliding mode observer, extended Kalman filter, adaptive observer etc., have been utilised for phase back-EMF estimation. As an example, the block diagram for the sliding mode observer based position estimation is shown in Fig. 1.19, through which the system robustness, immunity to parameter variations and disturbance rejection can be improved [CHI09].

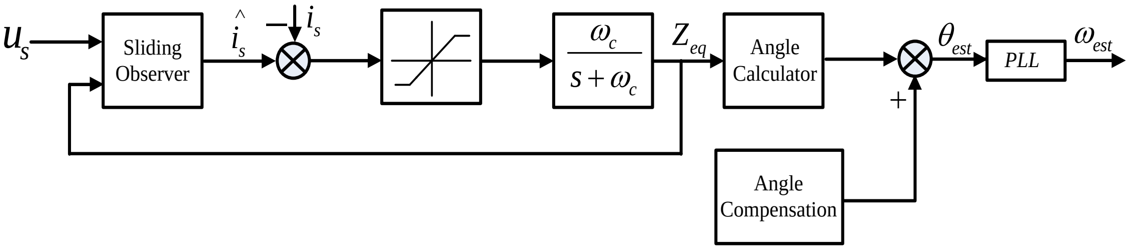

Fig. 1.19 Position estimation using sliding-mode observer [CHI09].

However, the amplitude of back-EMF is proportional to the rotor speed, and the performance in the low-speed region cannot be guaranteed due to the weak back-EMF signals. To solve this problem, sensorless methods exploiting machine saliencies are employed due to the effectiveness at standstill and low speed region, e.g. transient voltage vector injection pulses, PWM excitation or continuous high frequency (HF) carrier signal injection, etc.

Discrete voltage pulses, e.g. using additional impulse voltage vectors [SCH94], are superimposed during zero vector dwelling for standard PWM, as shown in Fig. 1.20. Moreover, the current derivative measured is synchronized to the test voltage vectors. However, the major problem for the standard 'INFORM' method is the introduced current disturbance due to the additional transient voltage vectors [SCH94]. On the other hand, with additional transient voltage vectors applied to the salient machine, the resultant zero sequence voltage for star-connection and zero sequence current derivatives for delta-connection also contain saliency position information [HOL98], [STA06].

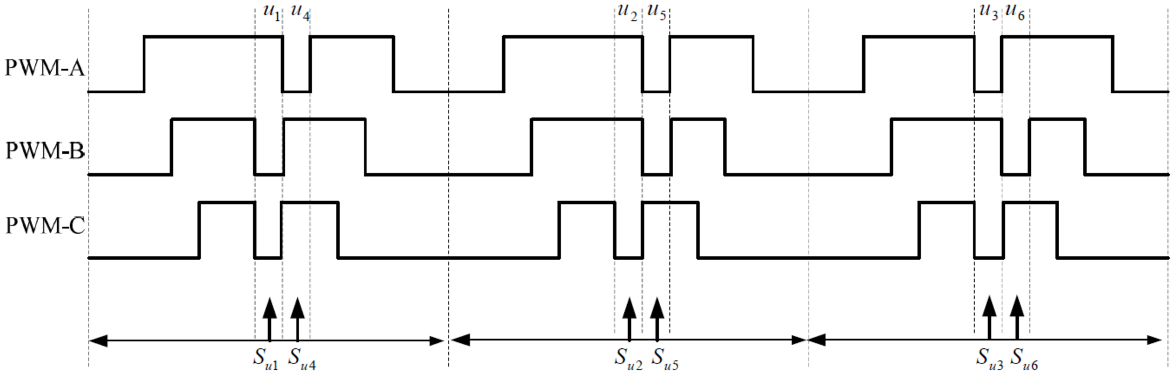

Fig. 1.20 'INFORM' method for rotor position estimation [SCH94].

Similar to the discrete voltage techniques, the basic idea of PWM excitation is also based on the saliency position modulated reactance, which can be reflected in the phase current derivatives, [HOL05], [GAO07], [HUA11], [BOL11], [LEI11]. Without additional signal injection, the inherent PWM excitation based sensorless methods are suitable for wide speed range operation. Moreover, faster dynamic performance can also be achieved due to the high frequency PWM. However, the requirement of current derivative synchronous measurement is an obstacle for practical applications, besides the frailty to measurement noise and parameter variation [YOO09]. By contrast, continuous carrier signal injection methods have been widely employed with the advantages of simple implementation and low-cost measurement, etc. These injection methods can be mainly classified into the rotating signal injection [JAN95], [DEG98], [BRI04], [BIA07], [ZHU11b], etc., and the pulsating signal injection [BIA07], [ZHU11b], [JAN03], [LI09], [YOO09], etc., in the stationary reference frame and the estimated synchronous reference frame, respectively.

In summary, the presented sensorless techniques simplify the machine systems to some extent. However, the aforementioned inherent problems with these methods still prove to be obstacles for wide applications.

1.3.6 Comparison amongst Different Positions Sensors

Different types of position sensors have been presented, together with the typical sensorless control methods. For comparison, the merits and demerits of these sensors are illustrated, as shown in Table 1.2. With the reliability, the detection accuracy and the installing space considered, the VR resolvers prove to be an ideal selection for vehicle applications.

TABLE 1.2

COMPARISON AMONGST DIFFERENT POSITION SENSORS

Position sensors		**Merits**	**Demerits**
Hall sensor		√ Low price √ Easy installation	× Discrete position signal
Hall-RM		√ Moderate detection accuracy √ Moderate price	× Complicated components × Axial installation space
Encoders	Optical	√ Very high detection accuracy	× Sensitive to interference × Axial installation space × High price
	Magnetic	√ Moderate detection accuracy √ Moderate price	× Axial installation space × Non-magnetic material
Resolvers	WF	√ High detection accuracy √ High reliability	× Auxiliary ring transformer × Axial length
	AFVR	√ High detection accuracy √ High reliability	× Axial installation space × Rotor fabrication × Winding configuration
	VR	√ High detection accuracy √ High reliability √ Easy installation	× Winding fabrication × Permeance harmonics
Sensorless methods*	BEMF	√ Middle and high speed √ Easy utilization	× Signal lost at low speeds
	Saliency	√ Standstill and low speed	× Injection signal interference × Poor robustness

* Sensorless methods are listed for reference.

1.4 Existing Manufacturing Issues

In HEV/EV systems, VR resolvers are usually integrated into IPM machines to provide the rotor position signals for precise control. As can be seen, common manufacturing issues in IPM machines and VR resolvers are to simplify the manufacturing process and to reduce the sensitivity to manufacturing tolerances. Moreover, similar design considerations should be carried out for both of the two devices, e.g. selecting proper slot/pole number combinations and optimal rotor contours, etc. Therefore, this thesis investigates the two devices respectively in order to enhance the competitiveness of IPM machine products with VR resolvers inside.

1.4.1 IPM Machines

As an inherent issue, the cogging torque of IPM machines can be theoretically eliminated by employing the step-skewing methods [FEI13], [CHE10b]. However, the end leakage flux and the axial flux interaction between rotor steps have not been investigated for I-shaped IPM machines in previous literature and a residual cogging torque component may exist, even though the machine is ideally fabricated.

Meanwhile, the cogging torque is still subject to tolerances during the manufacturing process, and some types of tolerances have been investigated in literature [KIM04], [ISL04], [GAS09], [NAK15], [COE12], [ZHU14], [QIA14], [ZHU12]. In [KIM04], the axial displacement of a skewed SPM rotor was analysed and a tolerance analysis procedure combining the FE method and the magnetic circuit network was proposed. In [ISL04], the cogging torque related issues in mass production had been presented, e.g. the magnet, the slot opening, the lamination anisotropies, the eccentricity, etc. Among these issues, the tolerance of PM irregularities was the most common case ever discussed, e.g. the dimensional variation in [GAS09], the PM shape and location in [NAK15], and the magnetization faults in [COE12], which consequently introduced additional cogging torque harmonics in PM machines. Moreover, analytical methods had also been employed to investigate the influence of eccentricities [ZHU14], [QIA14], from which the operating principle of additional cogging torque harmonics could be well understood. In addition, the influence of additional gaps between modular stators was investigated with the modern modular stator techniques considered [ZHU12], and it was proven that the non-uniform stator gaps would significantly increase the magnitudes and the periodicity of the cogging torque. In addition to the foregoing issues, other types of tolerances from the stator side (e.g. stator-out-of-roundness) have not been investigated.

In addition, different IPM machine designs may exhibit different sensitivities to the manufacturing tolerances. As a reference for selecting proper designs for applications with strict requirements on cogging torque, it is also necessary to investigate and compare the different influences amongst different IPM machines, e.g. different rotor contours, different stator slot/rotor pole combinations, etc.

Therefore, with the manufacturing process and tolerances considered, the existing problems with cogging torque reduction in IPM machines, as illustrated in Fig. 1.21, include:

(a) Residual cogging torque component caused by the end leakage flux and axial flux interaction between rotor steps of the step-skewing rotor.

(b) Additional cogging torque components caused by different manufacturing tolerances, and the most sensitive cases of different tolerances which should be avoided during the mass production.

(c) Differences of the most sensitive cases amongst different IPM designs, and the different sensitivities of cogging torque to manufacturing tolerances.

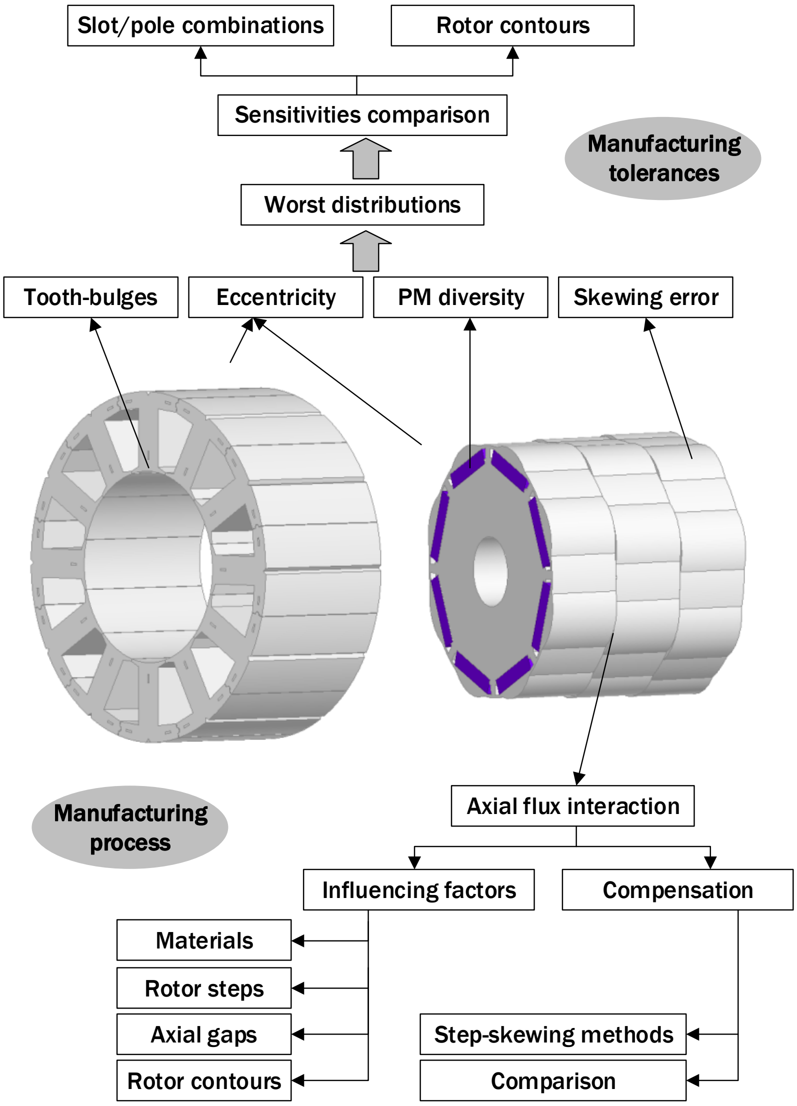

Fig. 1.21 Existing manufacturing issues of IPM machines.

1.4.2 VR Resolvers

Despite the aforementioned advantages, several problems still exist in conventional VR resolvers, especially the complicated manufacturing process and the potential deterioration to the detection accuracy.

A. Stator and Windings

As can be seen from the fundamental structure of conventional VR resolvers, two phases of output coils and one exciting coil are wound on each stator tooth, and multiple winding operations on each stator tooth will make the resolver quality difficult to guarantee. Common problems such as asymmetric coil locations, damage to wire insulation will deteriorate the position detection accuracy, or even cause the product to fail [XIN09], [KIM10]. Furthermore, output windings are usually sinusoidally distributed and the number coil turns is different from one another [MAS96], [XIO13], [SUN08], which makes the winding fabrication even more complicated. Besides the problems associated with fabrication described above, the application of resolvers also involves some burdens. As it is well known, different poles of PM machine designs have been employed in industrial and domestic applications, but there are not so many options of the present resolver products. By way of example, due to outstanding performance such as low cogging torque and torque ripple, PM machines with the 12-slot/10-pole design are widely used [ISH06], [XIA10], [ZHU12a]. However, leading manufacturers have not developed the resolver products for these machines. It is often suggested that the manufacturers should exploit a resolver product (a component of resolver product, e.g. the stator and windings) for multi-purpose applications. In brief, there is an urgent need of solving these existing problems. However, previously published papers mostly focus on the signal processing [HAN91], [WAN01], [MUR02], whilst very few are on solving the foregoing problems with the VR resolver itself.

B. Rotor Contour

In addition to the stator and windings, the rotor is another key component of a VR resolver, in which a sinusoidal design of rotor contour is usually employed to eliminate field harmonics [CUI12], [PAR14]. However, the exciting magnetic flux in the air-gap is not along straight lines towards the rotor centre, especially in regions with large air-gap lengths [LI08], [SUN08]. Consequently, a series of air-gap permeance harmonics may be introduced, which bring in additional voltage harmonics and degrade the position detection accuracy. Moreover, in order to reduce the output coil turns for cost reduction, higher sinusoidal component of air-gap permeance is usually employed to maintain the output voltages, whilst the detection accuracy may deteriorate due to higher harmonic components of air-gap permeance by larger maximum air-gap lengths. Therefore, a conflict exists during the design of VR resolvers. However, no efficient or effective solutions have been proposed in literature.

In brief, these existing problems with the VR resolvers shown in Fig. 1.22 are highlighted:

(a) The three sets of windings, i.e. the exciting winding, the SINE and the COSINE windings, are overlapping on each stator tooth.

(b) The two phases of output windings are sinusoidally distributed, the coil turns of which are different from tooth to tooth.

(c) Resolver products capable of multi-purpose applications, e.g. different poles of machines, are expected to be developed.

(d) A series of air-gap permeance harmonics may be introduced since the exciting magnetic flux in the air-gap is not along straight lines towards the rotor centre, which bring in additional voltage harmonics and degrade the position detection accuracy.

(e) The influence of manufacturing tolerances on the position detection accuracy should be further investigated and compared between different VR resolver topologies.

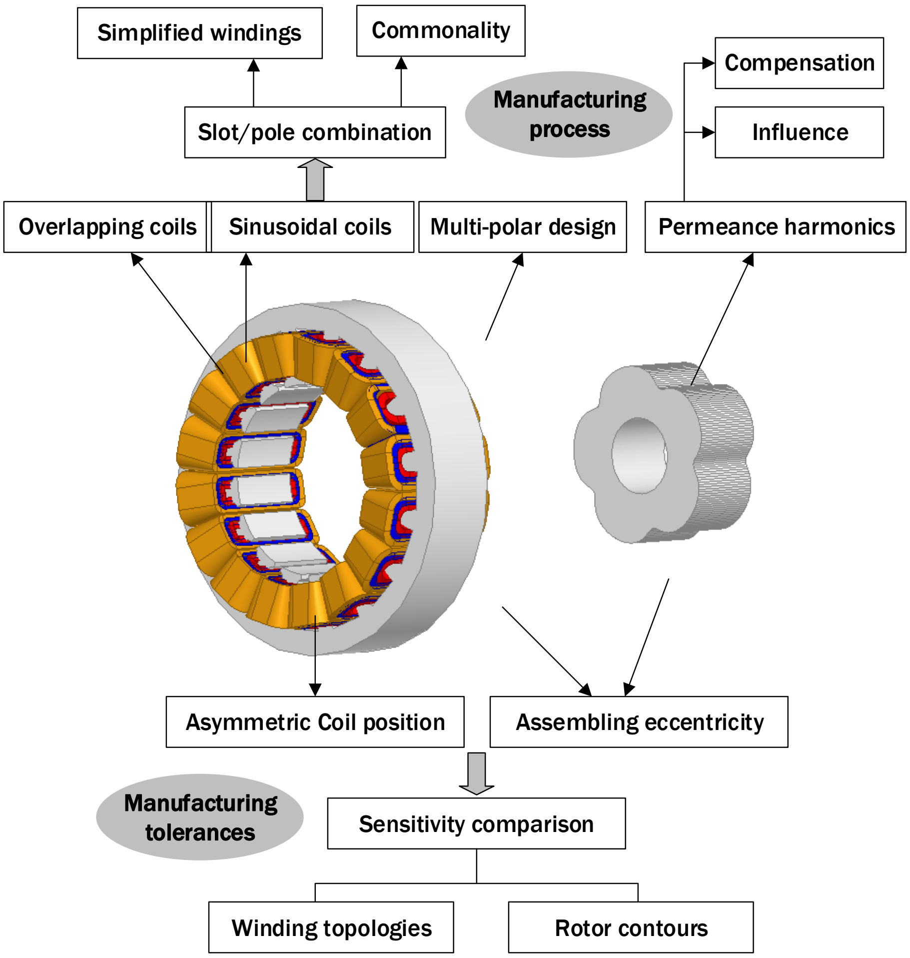

Fig. 1.22 Existing manufacturing issues of VR resolvers.

1.5 Outline and Contributions of the Thesis

This thesis mainly focuses on typical issues during the manufacturing of IPM machines and VR resolvers, which aims to reduce the cogging torque in IPM machines and to improve the position detection accuracy of VR resolvers respectively with simplified manufacturing process, and to identify the influence of manufacturing tolerances. As shown in Fig. 1.23, a schematic diagram of the research structure is illustrated, including the key points at each stage.

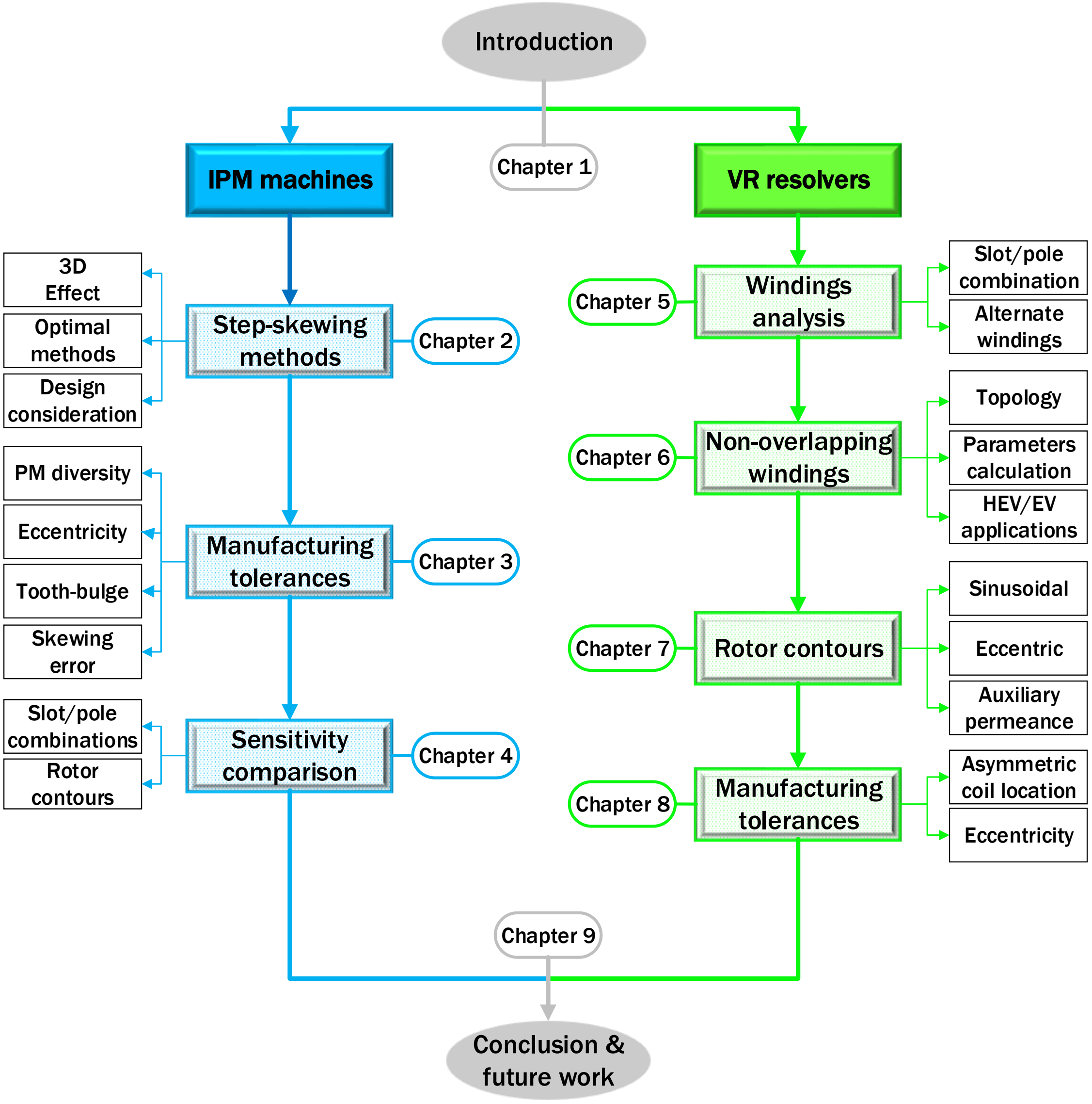

Fig. 1.23 Schematic diagram of thesis research structure.

The specific topologies of analyzed IPM machines and VR resolvers are illustrated in Fig. 1.24 and Fig. 1.25 respectively.

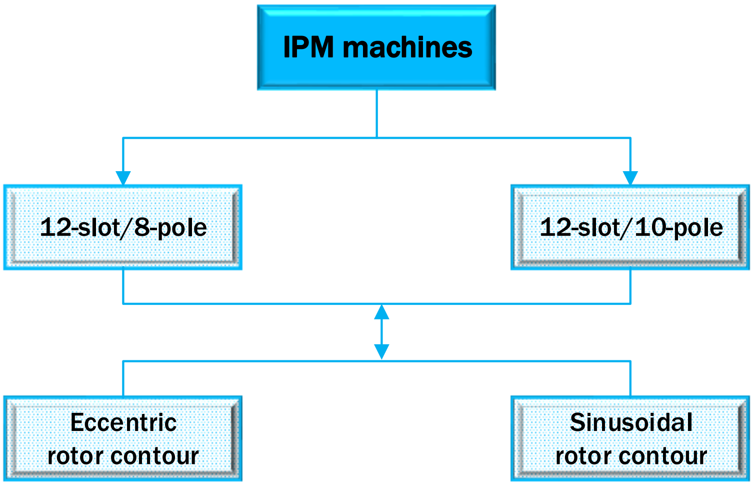

(a) Diagram of analysed IPM machine topologies

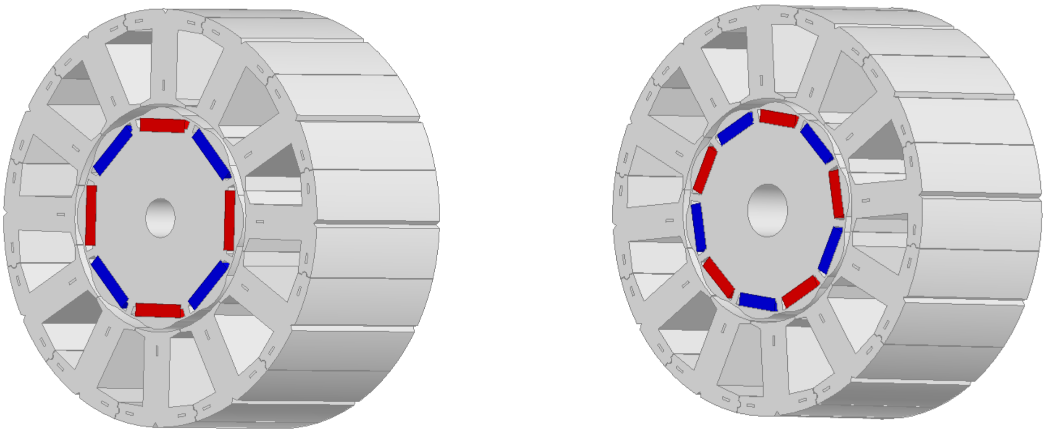

(b) 12-slot/8-pole design

(c) 12-slot/10-pole design

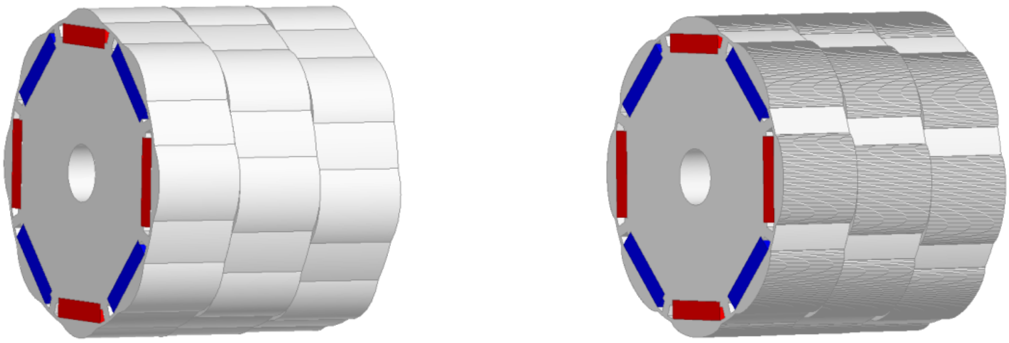

(d) Eccentric rotor contour design

(e) Sinusoidal rotor contour design

Fig. 1.24 Analysed IPM machine topologies.

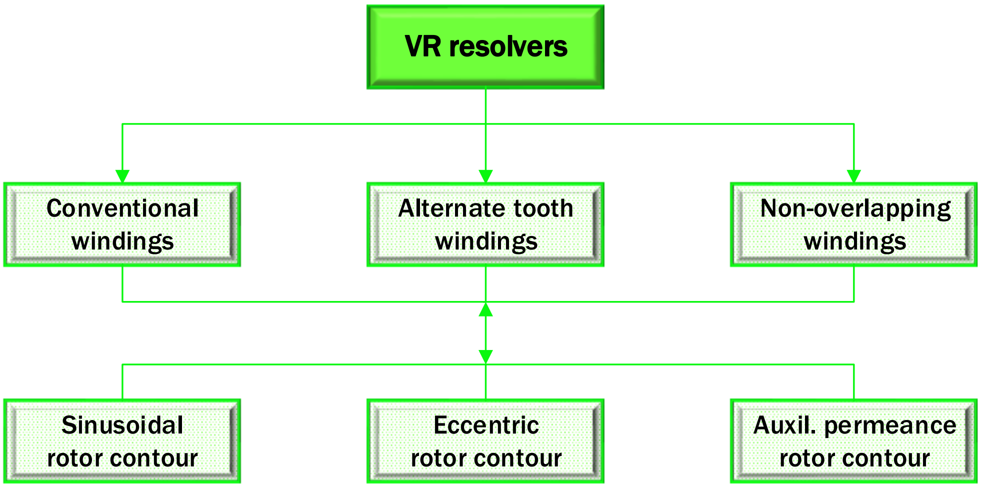

(a) Diagram of analysed VR resolver topologies

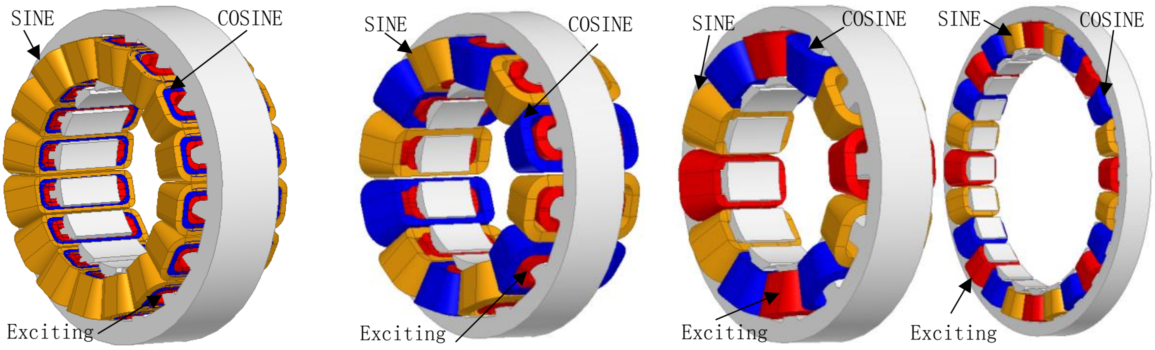

(b) Conventional windings (c) Alternate tooth windings (d) Non-overlapping windings

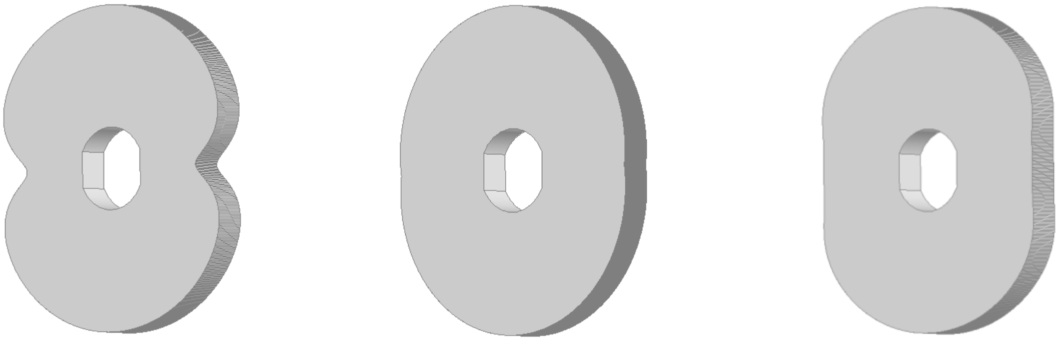

(e) Sinusoidal rotor (f) Eccentric rotor (g) Auxiliary permenace rotor

Fig. 1.25 Analysed VR resolver topologies.

The thesis is organized as follows:

Chapter 1 reviews the previous research work, presents the main objectives and generalizes the contributions of the thesis.

Chapter 2 proposes optimal step-skewing methods for IPM machines accounting for the end leakage flux and the axial flux interaction between rotor steps, in order to effectively reduce the residual cogging torque components. With the machine materials and the tolerance of axial assembling gaps considered, consequent corrections are further proposed.

Chapter 3 investigates the influence of manufacturing tolerances on cogging torque based on the 12-slot/8-pole IPM machine, i.e. PM diversity, assembling eccentricities, stator out-of-roundness and skewing angle errors, resulting in lower orders of additional cogging torque components which cannot be effectively reduced by skewing. Amongst random distributions of different manufacturing tolerances, the most sensitive cases are identified respectively for predicting the ultimate values of potential cogging torques.

Chapter 4 extends the analyses of manufacturing tolerances to different IPM machine designs, i.e. different rotor contours, different slot/pole combinations, based on the most sensitive cases generalized for different designs. In order to further verify the different sensitivities, the spatial field harmonics with and without considering the manufacturing tolerances are analysed and compared amongst different IPM designs, which can also illustrate the origins and the differences of the additional cogging torque components.

Chapter 5 analyses the winding theory of conventional VR resolvers, through which the operating principle is verified and the relationship between stator slot and rotor pole combination is analytically derived. Also, a simple factor is defined for selecting optimal stator slot/rotor pole combinations, and several designs of VR resolvers with alternate tooth windings are proposed to simplify the fabrication of output windings.

Chapter 6 proposes a novel VR resolver topology with non-overlapping tooth-coil windings, which proves to be a strong candidate for HEV/EV applications. The specific research work includes the operating principle verification, parameters calculation, design optimization, as well as the influences of actual application conditions. In addition, the feasibility of identical stator and windings for different poles of resolvers is investigated.

Chapter 7 proposes a novel design of rotor contour for VR resolvers by injecting auxiliary air-gap permeance harmonics to solve the conflict between output voltage magnitudes and voltage harmonics, which can also be employed in a conventional VR resolver topology.

Chapter 8 investigates the influence of manufacturing tolerances on the detection accuracy of the conventional and the proposed VR resolver topologies with different rotor contours, including the asymmetric coil locations and the assembling eccentricities.

Chapter 9 makes conclusions for the whole thesis and presents a discussion for future research work.

Major contributions of the research work in this thesis:

(a) Optimal step-skewing methods have been proposed to eliminate the residual cogging torque components caused by the axial flux interaction and the end leakage flux in IPM machines. Moreover, corrections are further proposed accounting for the influence of machine materials and the tolerance of axial assembling gaps.

(b) The influence of manufacturing tolerances on cogging torque in IPM machines has been investigated and the most sensitive cases of different tolerances are identified amongst numerous random distributions, based on which the ultimate additional cogging torques can be predicted and requirements on manufacturing process can be deduced.

(c) It has been proven that different IPM machine designs (e.g. different rotor contours and different slot/pole combinations) exhibit different sensitivities to the manufacturing tolerances, which can be a reference for selecting proper machine designs for applications with strict requirements on cogging torque.

(d) The basic operating principle of VR resolvers has been analytically derived, based on which a simple index is defined to select optimal stator slot/rotor pole combinations. In addition, several designs with alternate tooth windings are presented to simplify the fabrication of output windings in VR resolvers.

(e) A novel VR resolver topology with non-overlapping tooth-coil windings is proposed and analysed, which significantly simplifies the manufacturing process of VR resolvers. Moreover, it has been proven that the identical stator and windings of the proposed design can be employed in three different poles of resolvers.

(f) A novel design of rotor contour by injecting auxiliary air-gap permeance harmonics is proposed to eliminate the output voltage harmonics and improve the detection accuracy of the proposed VR resolver, which can also be employed in a conventional VR resolver topology to reduce the tooth harmonics.

CHAPTER 2 ANALYSIS OF STEP-SKEWING METHOD IN INTERIOR PERMANENT MAGNET MACHINES ACCOUNTING FOR 3-DIEMENSIONAL EFFECT

2.1 Introduction

Compared with SPM machines, IPM designs exhibit obvious superiorities in several aspects [RED12], [DUT08]. First, the magnets can be easily embedded in rotor slots without the need of additional bindings, which eases the manufacturing process and improves the reliability as well. Second, considerable reluctance torque can be achieved in IPM machines due to saliency effect, especially for integral-slot designs [CHA09]. Third, a lower risk of demagnetization can be realized since the magnets are not directly facing the armature field. Moreover, due to the higher d-axis inductance, IPM machines illustrate obvious better flux weakening capability. In addition, more efficient use of permanent magnet (PM) materials can be achieved by the rectangular shape of magnets. Due to these advantages, IPM machines are widely used in industrial applications. However, the cogging torque index is usually emphasized in many applications [SIM12], [DAN14], e.g. the servo motors and the electric power steering (EPS) motors, which require special design considerations.

Over the last few decades, techniques of cogging torque reduction in PM machines have been extensively investigated, and many effective approaches have been proposed. Selecting proper stator slot and rotor pole combinations can globally guarantee lower level of cogging torque [ZHU00], [GUE11], [ACK92], [HWA01b], [HWA98], and favorable results can be often achieved by fractional-slot designs. Then, a variety of methods can be employed in the design and optimization of stator and rotor respectively. From the stator side, conventional optimization can be carried out on tooth width [ACK92], [JIA09], slot-opening width [AZA12], stator dummy slot [ZHU00], [BIA02], tooth shifting [WAN12] and skewing [ZHU00], [HWA01b], [HAN97], [XIA15], etc. Similarly, optimization of the rotor parameters also proves to be effective in cogging torque reduction, e.g. pole arc width [ZHU00], [BIA02], [FEI11], [LI88], pole shaping [HWA01b], [CHE10], [DUB02], pole shifting [WAN10], [TUD12], magnetization mode [ZHU05], rotor skewing [ZHU00], [HWA01b], [HAN97], etc. As can be seen, the skewing method can be employed in either the stator or the rotor side. However, skewed stator teeth usually complicate the automatic winding fabrication, whilst skew magnets are difficult to produce and magnetize as well.

For IPM machines, a more practical approach is to employ step-skewing rotors [BIA02], [JAN97], [FEI13], [ISL09], [CHU13], [ZHU12], [FEI10], [FEI12], [LAT06], [KIM14], [CHE10], [EAS97], instead of continuous stator or rotor skewing. The operating mechanism and the theoretical step-skewing angles have been investigated [BIA02], and novel herringbone skewing techniques have been proposed to eliminate potential axial unbalance magnetic force [JAN97], [FEI13]. Moreover, torque ripple performance has also been investigated for machines with step-skewing designs, and sensitive parameters, e.g. the magnet shape, have been highlighted [ISL09], [CHU13]. In addition, further investigation has been carried out on the influence of manufacturing tolerances from the stator side [ZHU12], e.g. additional air-gaps between stator segments, which proves to be very important for mass production of machines. It can be found that very in-depth research work has been done on the step-skewing techniques. However, the end leakage flux and the axial flux interaction between rotor steps have not been investigated for I-shaped IPM machines in previous literature, and the influence of manufacturing tolerances from the skewing-rotor side has not been considered either.

In order to investigate the influence of axial leakage flux on the step-skewing approach, a 12-slot/8-pole IPM machine model is established according to the basic parameters shown in Table 2.1, with the stator and rotor shown in Figs. 2.1 (a) and (b) respectively. As a popular design, the eccentric rotor contour is employed [EVA10] (back-EMF harmonics are usually produced by conventional cylindrical rotors, and a series of cogging torque harmonics may be introduced). For this design, the rotor pole shoes are formed by eccentric arcs (the arc centers deviate from the rotor center by an eccentric distance), which are joined by concentric arcs at inter-polar locations, as shown in Fig. 2.1 (b). Therefore, the outer radius of the rotor pole shoe can be described by:

$$R_r(\theta) = A\cos(\theta) + \sqrt{r^2 - (Asin(\theta))^2} \tag{2. 1}$$

where θ is the mechanical angle, *A* and *r* represent the eccentric distance and the radius of these eccentric arcs respectively.

TABLE 2.1

BASIC PARAMETERS OF IPM MACHINE DESIGN

Parameters	Values
Stator slot and rotor pole number	12/8
Stator outer diameter (mm)	85
Stator inner diameter (mm)	46.4
Stator tooth width (mm)	7.0
Slot opening width (mm)	3.0
Min. and Max. air-gap lengths (mm)	0.6/1.65
Iron bridge width (mm)	0.5
PM size (mm/mm/mm)	12.5/12.1/2.6
PM remanence (T, 20° C)	1.32
Core axial length (mm)	37.5
Number of turns per coil	27
Parallel branches	2
Peak current (A)	95

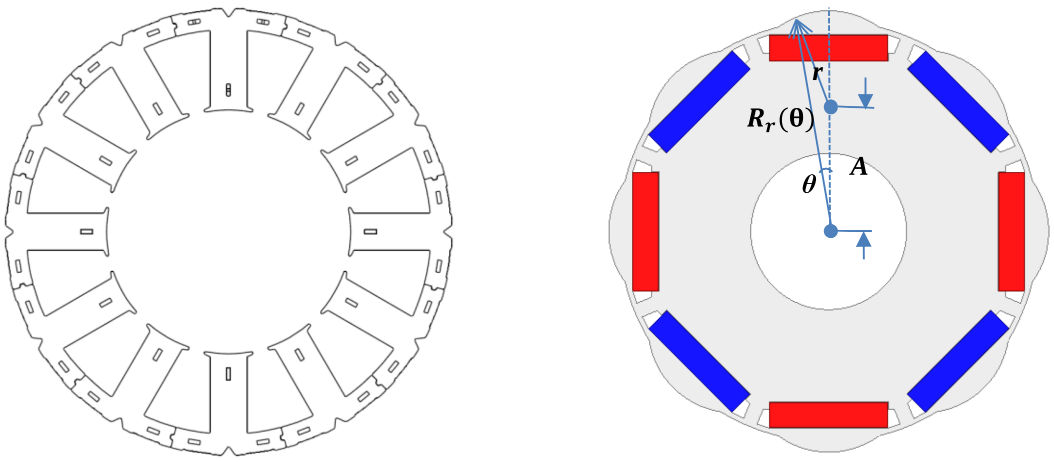

(a) Stator (b) Rotor

Fig. 2.1 12-slot/8-pole IPM machine by eccentric design of rotor contour.

It can be found from (2.1) that the rotor pole shoe shape directly depends on the eccentric distance when the minimum and the maximum air-gap lengths are defined. Therefore, it is necessary to investigate the influence of this parameter on the machine performance. As shown in Fig. 2.2, the cogging torque and the rated torque are calculated by 2-dimensional (2D) finite element (FE) method respectively, with different values of eccentric distance employed. It can be seen that the cogging torque increases from 87mNm to 221mNm when the eccentric distance changes from 12mm (lower eccentric distances are not investigated to guarantee the minimum effective width of iron bridges) to 15mm. In addition, the average output torque almost remains stable whilst the torque ripple significantly increases from 7.6% to 13.7%. However, both of the cogging torque and the torque ripple can be reduced to very low extent when the step-skewing approach is employed, e.g. a three-step-skewing rotor by skewing -5 °, 0 °and 5 °.

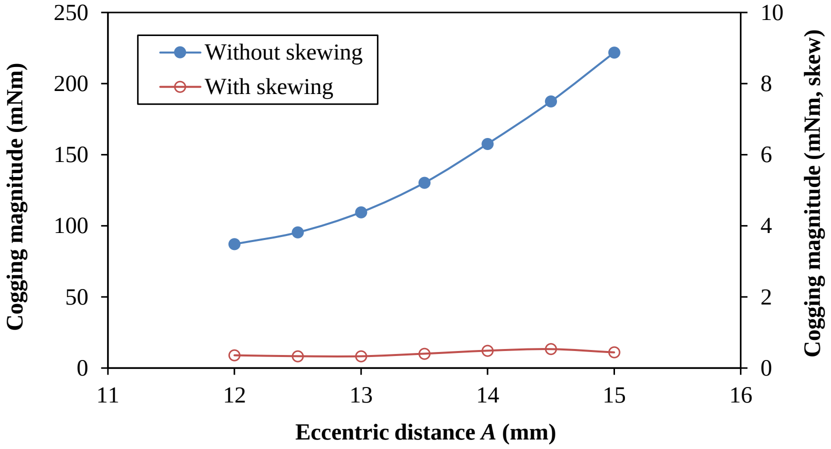

(a) Cogging torque

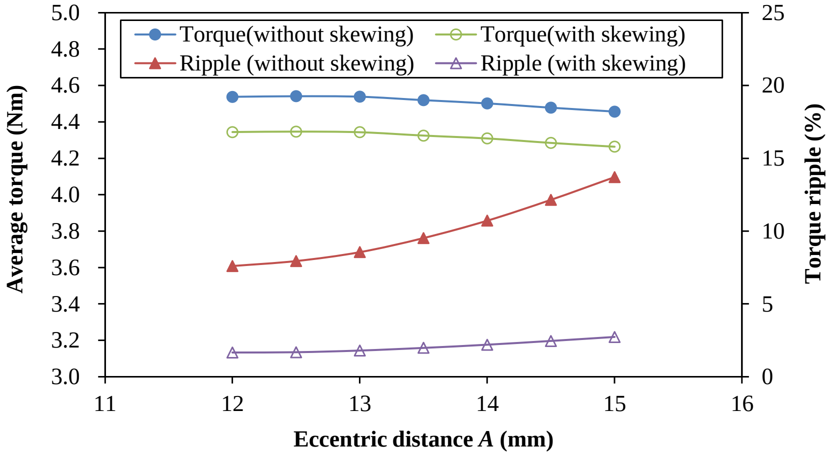

(b) Rated torque (95A, I_d=0)

Fig. 2.2 Influence of eccentric distance (*A*) on IPM machine by eccentric rotor contour.

According to the analyses shown in Fig. 2.2, the cogging torque and the torque ripple can be reduced to very low extent with the step-skewing rotor employed, when the eccentric distance changes from 12mm to 15mm. In this thesis, an eccentric rotor contour is established by employing 13.8mm for this parameter, with the cogging torque, back EMF and on-load torque shown in Fig. 2.3. The influence of eccentric distance will also be further investigated.

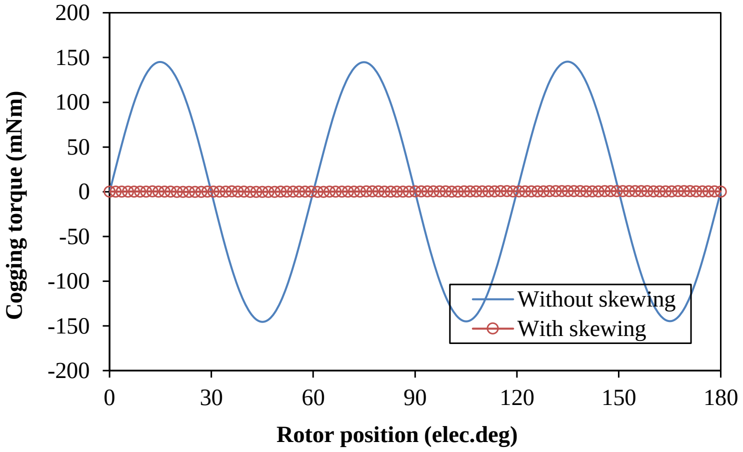

(a) Cogging torque

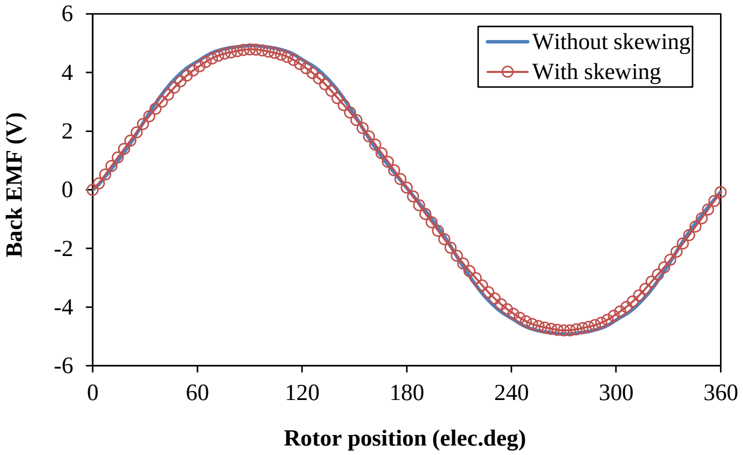

(b) Back EMF (1500rpm)

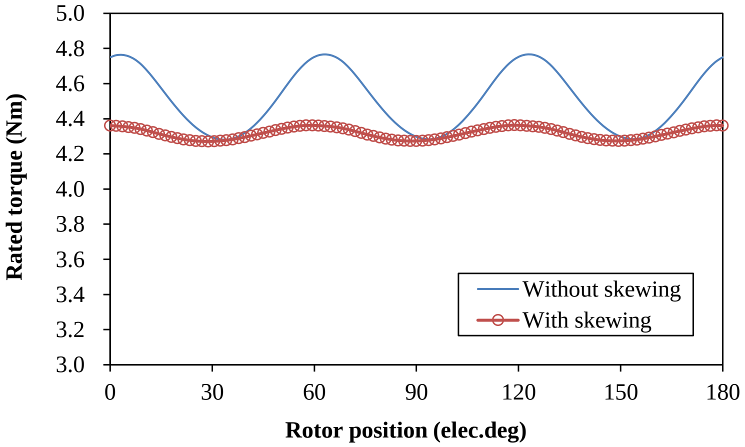

(c) Rated torque (95A, I_d=0)

Fig. 2.3 Cogging torque and rated torque of IPM machine by eccentric rotor contour (A=13.8mm).

2.2 Analysis of Step-Skewing Method Used in IPM Machines

2.2.1 Conventional Step-Skewing Method and 2D FE Verification

For an IPM machine with step-skewing rotor, the theoretical step-skewing angles have been derived, which can be described by [BIA02], [FEI13]:

$$\theta_{sk} = \frac{2k\pi}{nLCM(Z,2p)} \qquad k = 1,2,3\ldots \tag{2. 1}$$

where n is the number of rotor steps and LCM (Z, $2p$) represents the lowest common multiple between the numbers of stator slots (Z) and rotor poles ($2p$). For the aforementioned 12-slot/8-pole model, it can be deduced that the skewing angles of the three rotor steps should be +5 °, 0 ° and -5 ° respectively (designated as skewing ±5.0 °) – equivalent to 15 ° total skewing angle, through which the 24th order of cogging torque (fundamental cogging torque) can be eliminated.

As it is well known, different numbers of rotor skewing steps can be employed, e.g. 2 steps, 3 steps and 4 steps, as shown in Fig. 2.4. In order to illustrate the operating mechanism, the vector diagram method is employed, as shown in Fig. 2.5. With the decreasing magnitudes considered, only the fundamental order, the double order, the triple order and the quadruple order of cogging components are illustrated. It can be seen that only the cogging harmonics with the orders being multiples of number of rotor steps cannot be reduced [BIA02], [FEI13]. Despite this, the cogging torque can be still effectively reduced due to the elimination of other orders of cogging harmonics.

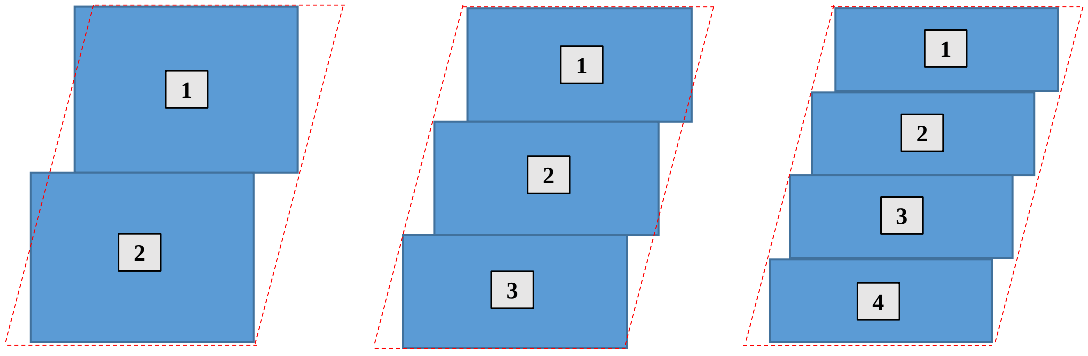

(a) 2-step (b) 3-step (c) 4-step

Fig. 2.4 Schematic drawing of conventional step-skewing rotors in IPM machines.

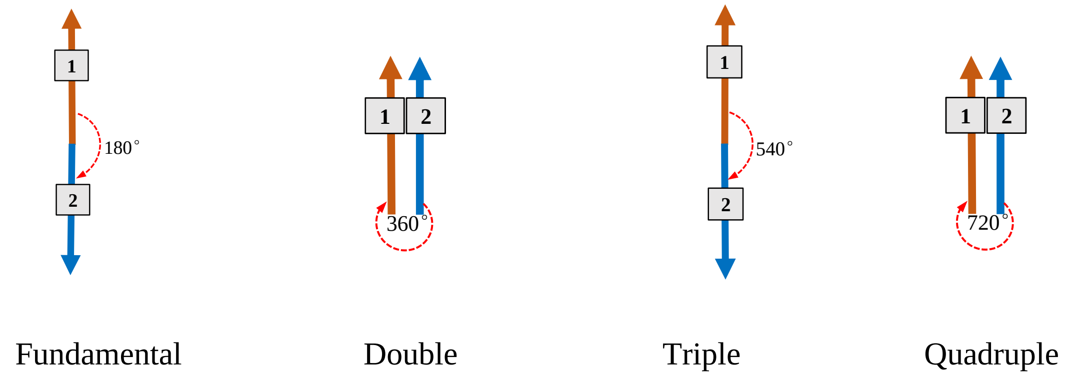

(a) 2-step

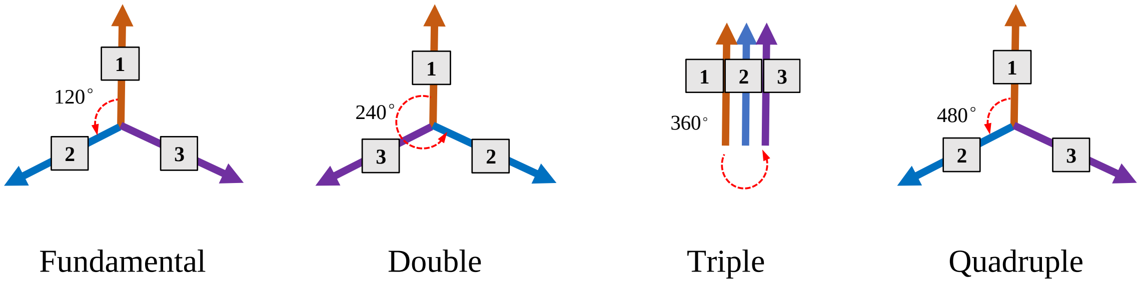

(b) 3-step

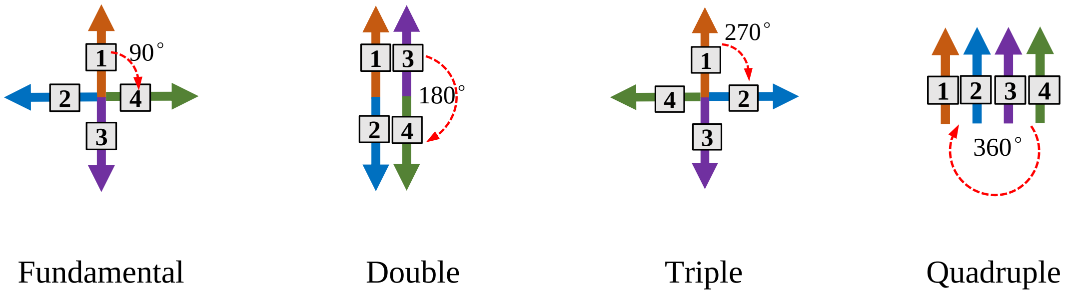

(c) 4-step

Fig. 2.5 Cogging torque reduction mechanism by step-skewing rotor.

As a verification of the analyses, a 2D FE model is established according to parameters of the aforementioned 12-slot/8-pole machine shown in Table 2.1. The synthetic cogging torque with the skewing rotor can be obtained by cogging superposition of each rotor step, as shown in Fig. 2.6, including the waveforms and the harmonics. As can be seen, the cogging torque is significantly reduced from ±144mNm to very low extent, with only higher orders of cogging components left (corresponding to the number of rotor steps).

Since the synthetic cogging torque by the step-skewing rotor is obtained by superposition of each rotor step, which is based on the 2D FE results, the end effect of rotor steps is not considered. However, the 3-dimensional (3D) effect is usually more obvious and cannot be ignored in IPM machines, especially for flat shape of designs. Therefore, it is necessary to further investigate the specific influence on cogging torque by the 3D FE method.

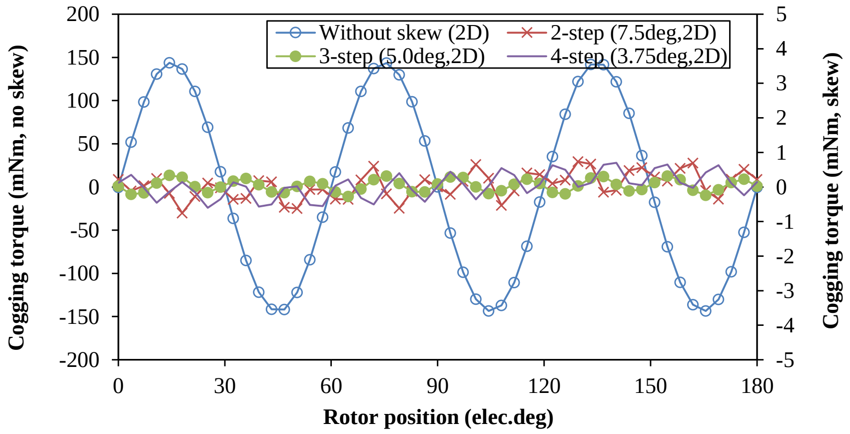

(a) Waveforms (1/8 revolution)

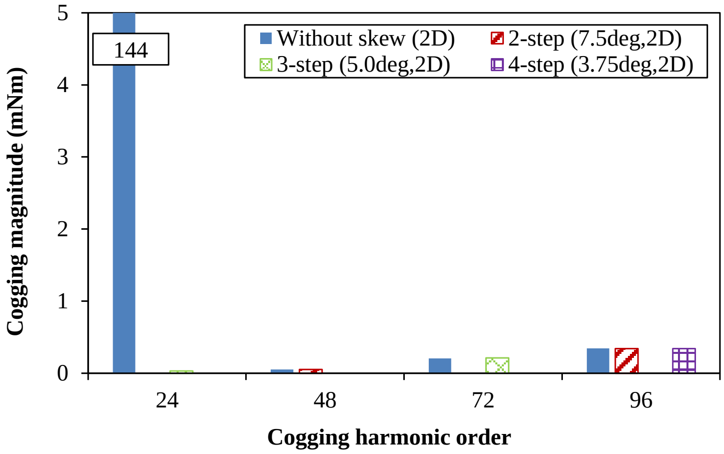

(b) Harmonics

Fig. 2.6 Cogging torque of IPM machine with and without rotor step skewed (2D FE).

2.2.2 Influence of 3D Effect on Cogging Torque

In this section, the 3D FE method (by using the JMag software) is employed to further investigate the cogging torque performance of the 12-slot/8-pole motor with step-skewing rotor. First, a 3-step-skewing rotor (skew ±5.0°) is analyzed as an example. In order to simplify the time-consuming analyses, a 3D FE module model (1/4) is established with the symmetric property considered, as shown in Fig. 2.7. When the rotor rotates from 0 to 180 electric degrees (1/8 revolution), the cogging torque is calculated and compared with the 2D FE results, as shown in Fig. 2.8.

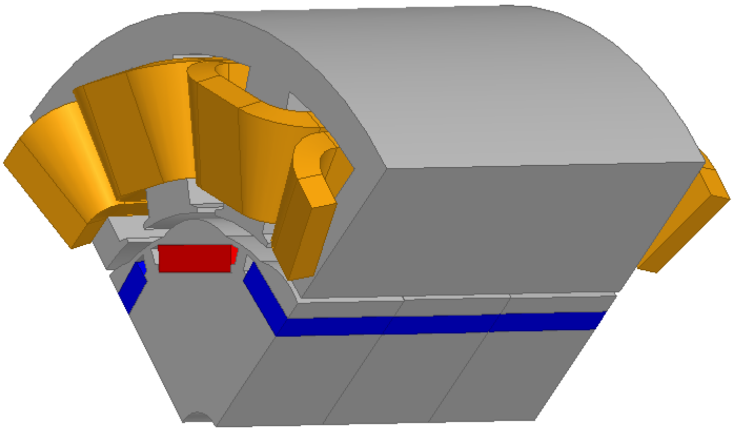

Fig. 2.7 3D FE module model of 12-stator/8-pole IPM motor with 3-step-skewing rotor.

As can be seen, significant difference exists between the 2D and the 3D FE results, and the 24th order of cogging torque with a much higher magnitude 17.8mNm is introduced. Therefore, the conventional 3-step-skewing rotor with theoretical skewing angles (±5.0°) proves to be not so effective in cogging reduction for the 12-slot/8-pole motor, with the 3D effect considered.

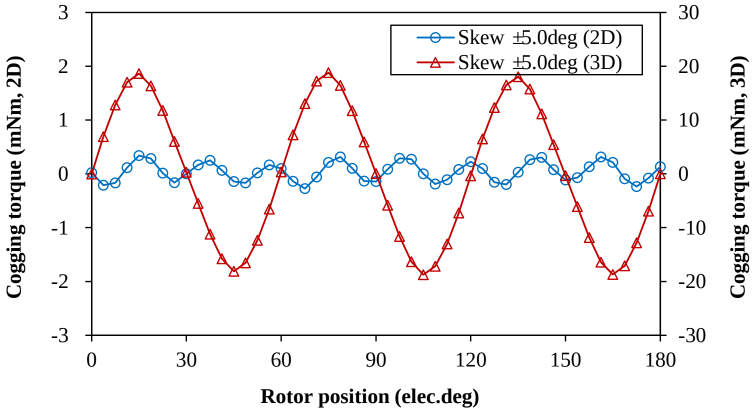

Fig. 2.8 Comparison of cogging torque performance between 2D and 3D FE results (3-step-skewing rotor, 1/8 revolution).

In order to reduce the residual cogging torque, it is necessary to firstly investigate the origins of the increased 24th cogging harmonic. As a representative property, the flux densities in the 3-step-skewing rotor and in the air-gap are obtained by 3D FE method, as shown in Fig. 2.9 (the label of ‘rotor position’ represents different angular positions). Two typical features can be found from the flux distribution. The first one is the end leakage flux known as the conventional end effect in IPM machines, and the second is the axial flux interaction between adjacent rotor steps, neither of which can be considered by 2D FE method.

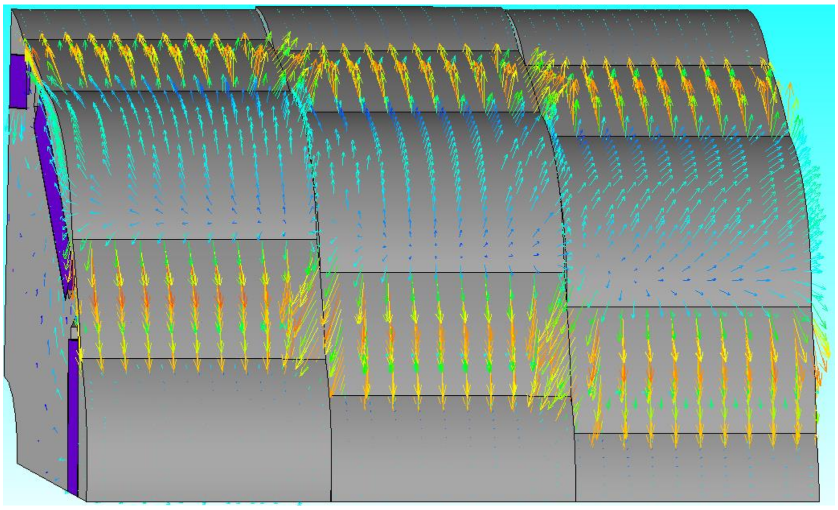

(a) Flux density vector in the 3-step-skewing rotor

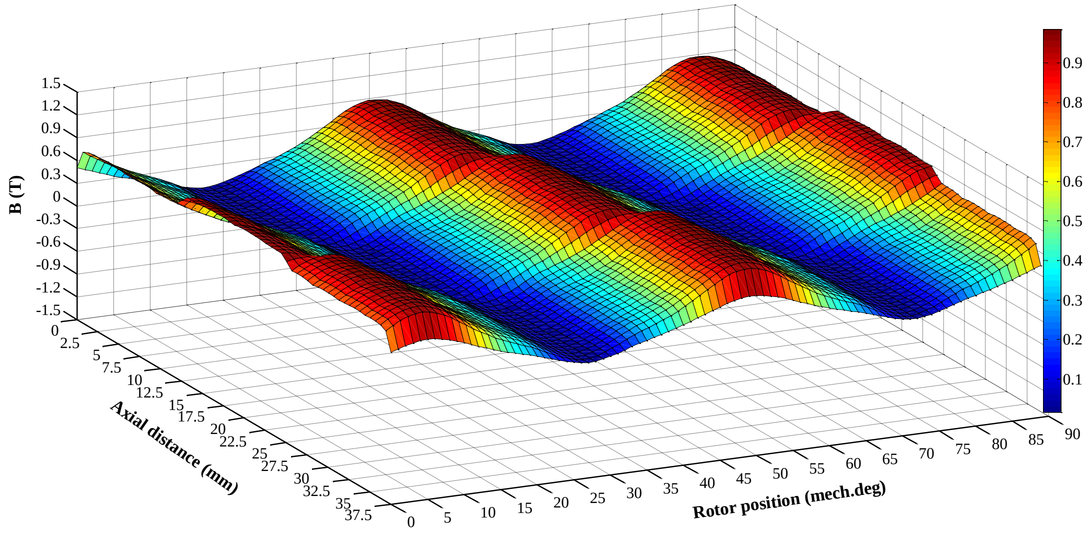

(b) Flux density in the air-gap

Fig. 2.9 Open-circuit flux density.

Due to the close relationship between cogging torque and air-gap magnetic field, the air-gap flux density (one pair of poles) at different axial locations is further investigated in order to clearly describe the influence of end effect and axial interaction between different rotor steps, as shown in Fig. 2.10. It should be noted that Figs. 2.10 (a), (b) and (c) represent the air-gap flux densities above the three different rotor steps respectively, whilst each figure illustrates the air-gap flux densities at three different axial locations of one rotor step, i.e. the left end, the central line and the right end.

Compared with the middle step (step 2), the side rotor steps, i.e. step 1 and step 3, are skewed by $+5.0^{o}$ and -5.0^{o} respectively, which can be reflected on the axes of air-gap flux density (red lines without marks) at the central line of each rotor step, i.e. 50^{o}, 45^{o} and 40^{o}. However, the air-gap flux densities at the left and right ends exhibit different variations. For step 1, it can be seen from Fig. 2.10 (a) that the air-gap flux density at the left end (blue line with triangle marks) is obviously reduced due to end leakage flux, although the axis remains at 50^{o}. Moreover, the air-gap flux density at the right end (black line with circle marks) has a shift on the axis (between 45^{o} and 50^{o}) due to the flux interaction with step 2, although the magnitude almost keeps stable. Similarly, such phenomenon can also be found in the air-gap flux density above step 3, as shown in Fig. 2.10 (c).

By re-examination of the vector diagram shown in Fig. 2.5, it can be found that the 24th cogging component of the 12-slot/8-pole motor cannot be eliminated by the rotor with conventional skewing angles, due to the decreased magnitude and phase angle of side steps. Therefore, origins of the residual 24th cogging torque have been verified, which are mainly due to two aspects: the end leakage flux and the axial flux interaction between adjacent rotor steps.

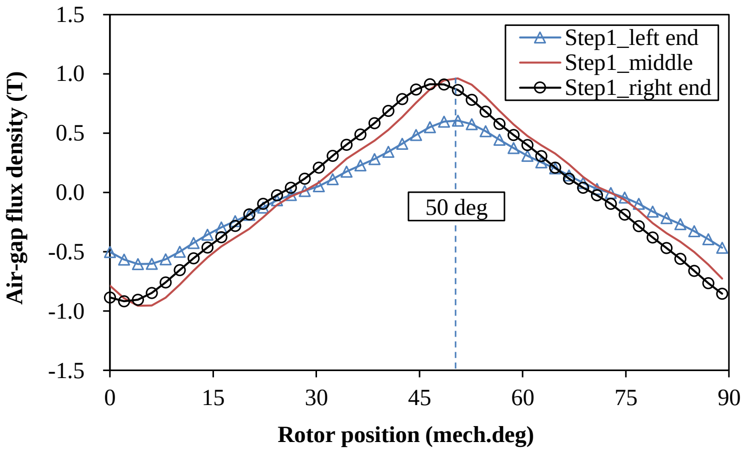

(a) Two ends of step 1

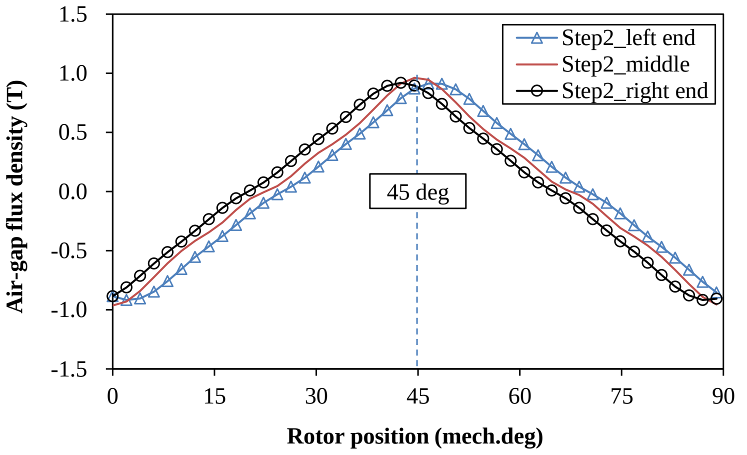

(b) Two ends of step 2

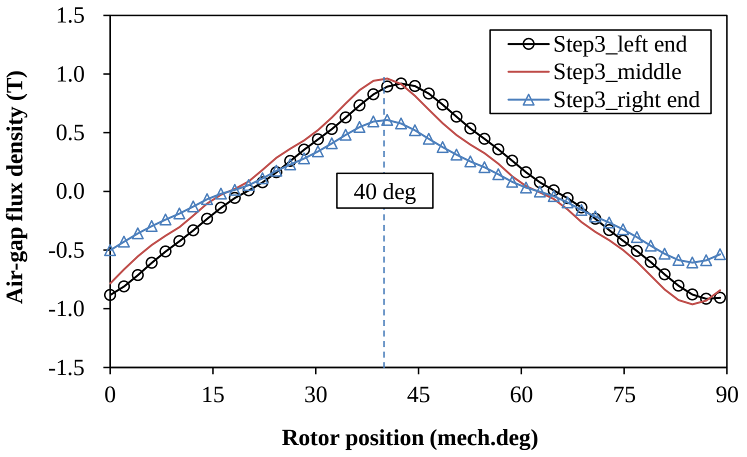

(c) Two ends of step 3

Fig. 2.10 Air-gap flux densities above the 3 rotor steps at different axial locations (3D FE analyses, slot openings not considered).

2.2.3 Influence of 3D Effect on Other Electromagnetic Performance

In addition to the cogging torque, the influence of 3D effect on other electromagnetic performance is also investigated, i.e. the back EMF and the on-load torque, as shown in Fig. 2.11 and Fig. 2.12 respectively. According to the comparison between the 2D and 3D FE results shown in Fig. 2.11, it can be seen that very little influence is introduced in the back EMF by the 3D effect – the magnitude only decreases from 4.83V to 4.8V and the 5th harmonic increases from 0.03V to 0.1V. Moreover, it can be seen from Fig. 2.12 that the average torque is reduced from 4.32Nm to 4.26Nm whilst the 6th order of torque harmonic only increases from 0.045Nm to 0.075Nm, which is mainly caused by the 5th back-EMF harmonic and the 24th residual cogging torque.

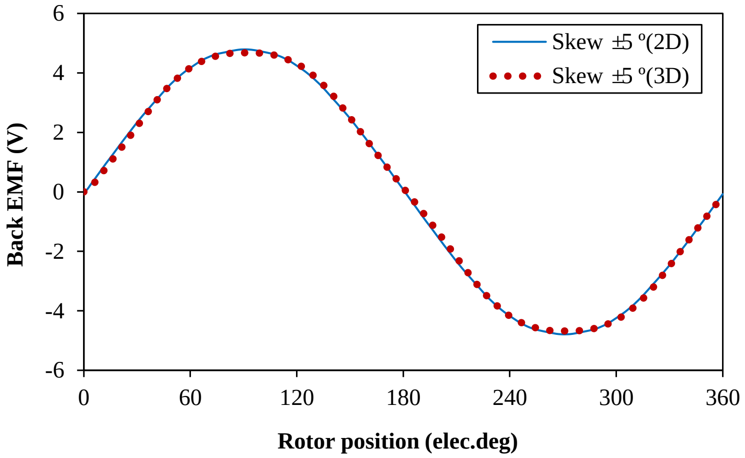

(a) Waveforms (1/4 revolution)

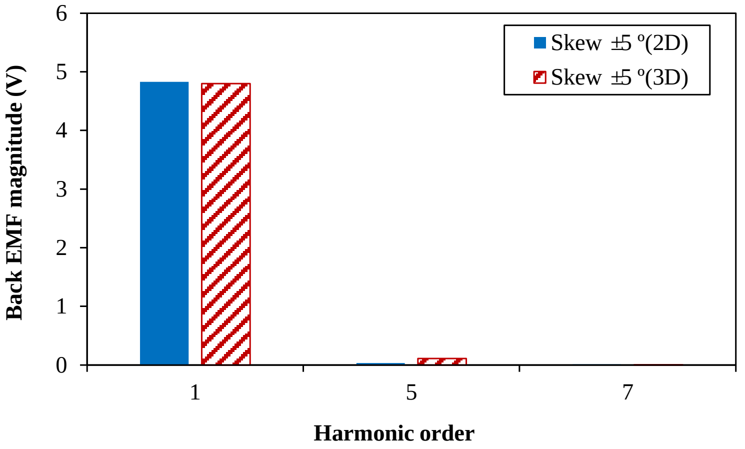

(b) Harmonics

Fig. 2.11 Comparison of back EMF between 2D and 3D FE results

(3-step-skewing rotor, 1500rpm).

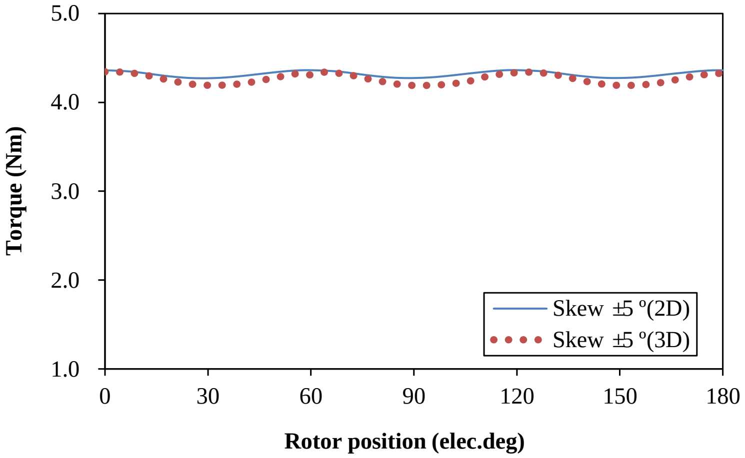

(a) Waveforms (1/8 revolution)

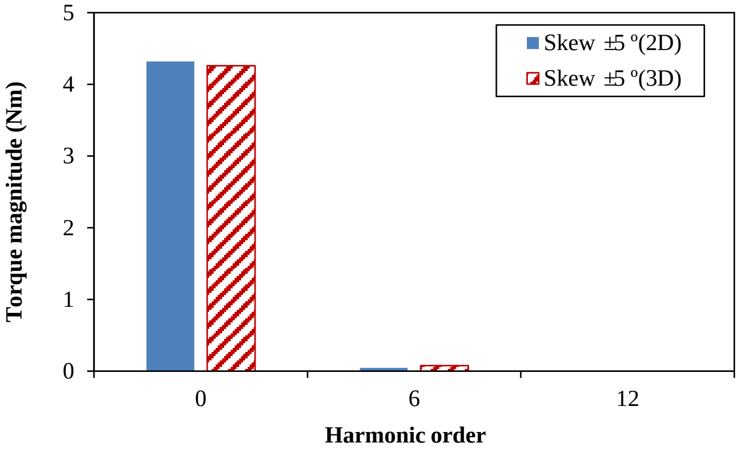

(b) Harmonics

Fig. 2.12 Comparison of on-load torque between 2D and 3D FE results

(3-step-skewing rotor, 95A, I_d=0).

Compared with the residual cogging torque, it can be seen that the influence of 3D effect on the back EMF and the on-load torque is negligible. Therefore, the following analyses in this chapter will focus on the cogging torque performance.

2.2.4 Comparison amongst Different Designs of Step-Skewing Rotors

A. Designs with different numbers of rotor steps

In addition to the 3-step-skewing rotor, the 2-step and 4-step rotors are also investigated, as shown in Fig. 2.13. By 3D FE method, the cogging torque performance is obtained, as shown in Fig. 2.14. It can be seen that residual cogging torque components of the 24th order always exist in the three cases. Compared with the 3-step and the 4-step cases, the 2-step design presents a little higher value of the 24th cogging torque (19.7mNm). Moreover, due to the distortion of air-gap flux density caused by axial flux interaction, the 48th order of cogging torque component is generated, whilst it cannot be eliminated by the 2-step design and thus obviously increases to 3.53mNm. Therefore, the 2-step design exhibits more residual cogging torque, including the 24th and the 48th orders. In addition, very similar cogging torque performance can be obtained by the 3-step and the 4-step designs. With the manufacturing cost considered, the 3-step-skewing design proves to be a better selection.

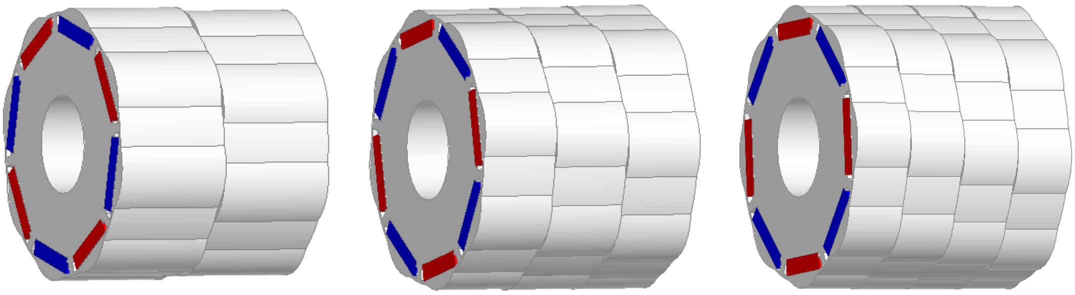
(a) 2-step (skew 7.5°) (b) 3-step (skew 5.0°) (c) 4-step (skew 3.75°)

Fig. 2.13 3D FE models of IPM rotor with different skewing steps.

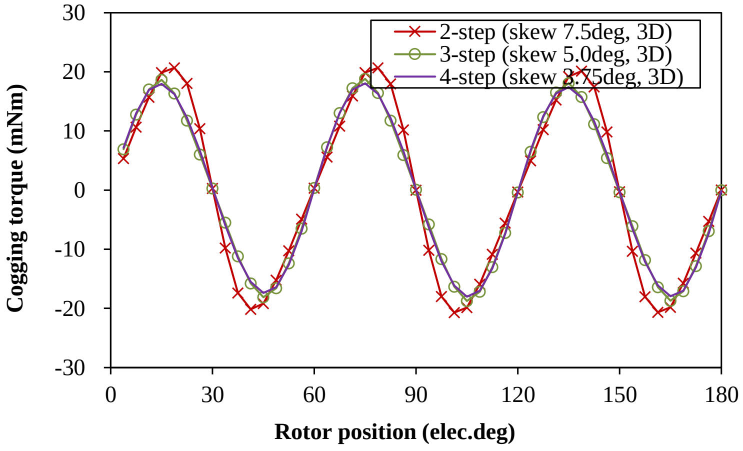

(a) Waveforms (1/8 revolution)

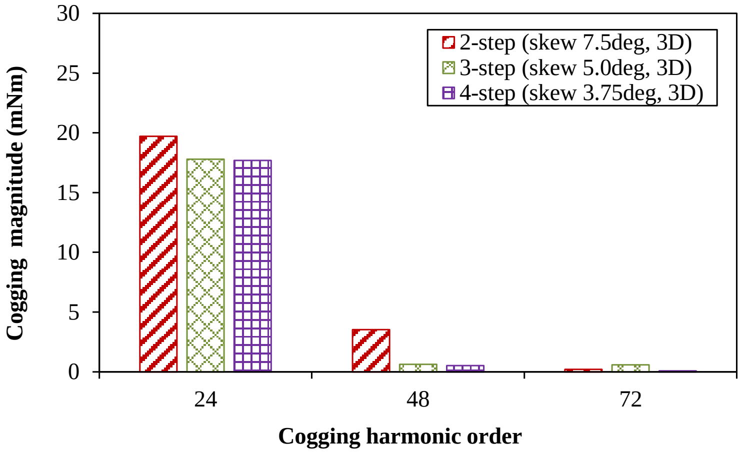

(b) Harmonics

Fig. 2.14 Cogging torques of IPM motor with different numbers of rotor steps (3D FE).

B. Designs with different rotor contours (different eccentric distances)

When the minimum and maximum air-gap lengths remain unchanged, the pole shoe shape of the eccentric rotor design can be adjusted by employing different eccentric distances, as shown in Fig. 2.15. With the foregoing 3-step-skewing method employed, the influence of eccentric distance on the cogging torque performance is investigated by the 3D FE method, as shown in Fig. 2.16. It can be seen that the 24th residual cogging torque increases from 11.3mNm to 20.5mNm when the eccentric distance changes from 12mm to 15mm, which is mainly due to the increasing saturation level in rotor laminations.

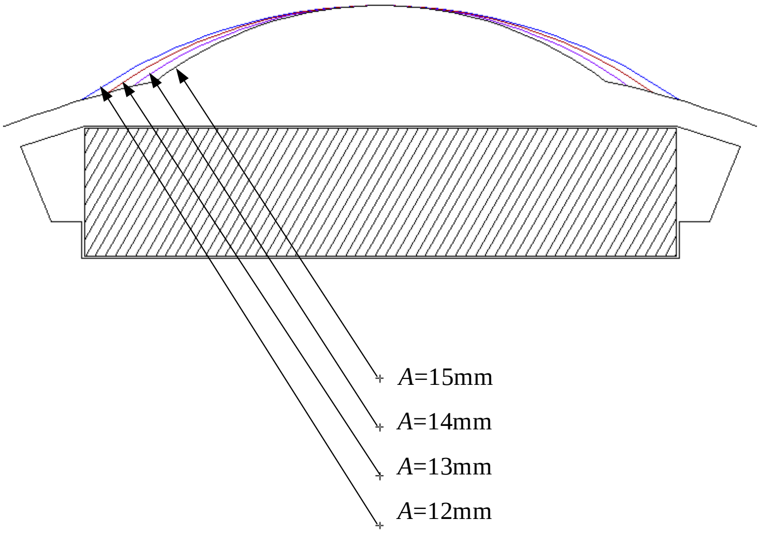

Fig. 2.15 Eccentric designs of rotor contour by different eccentric distances *A*.

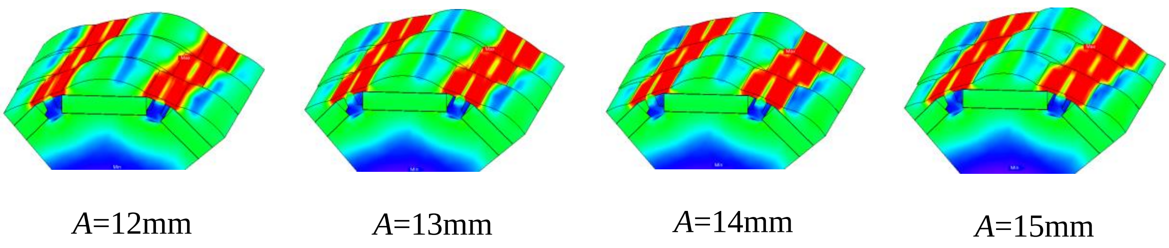

(a) Flux density in rotor

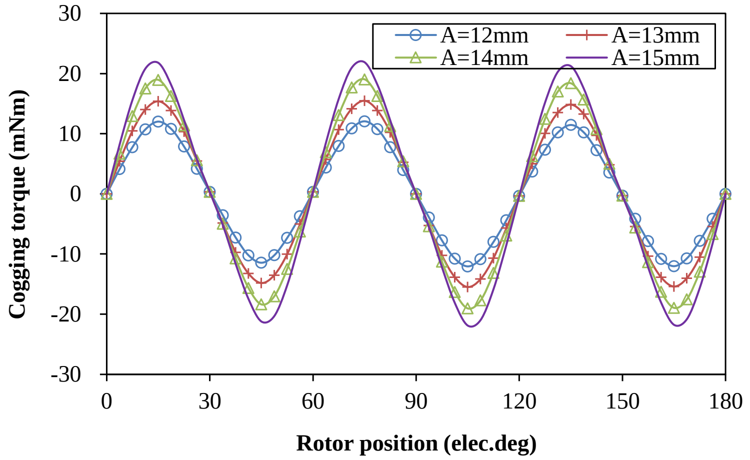

(b) Waveforms

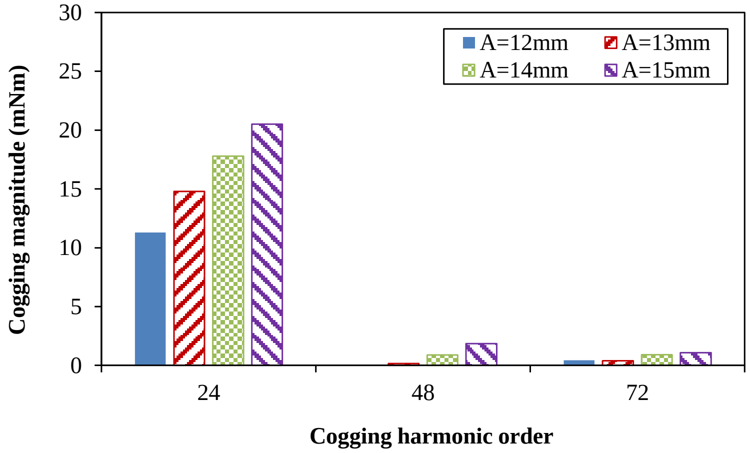

(c) Harmonics

Fig. 2.16 Cogging torques of eccentric designs with different eccentric distances *A* (3D FE).

In addition to the eccentric design, the sinusoidal rotor contour can also be employed for the IPM machine. Due to the much lower original cogging torque, the residual cogging torque component in the sinusoidal design can be ignored. In the following chapters, more specific analyses and comparison will be carried out for the two different rotor contour designs.

2.3 Optimal Step-Skewing Methods for Cogging Torque Reduction Accounting for 3D Effect

With the end leakage flux and axial interaction between the side and middle rotor steps considered, the 24th cogging torque component of the 12-slot/8-pole motor cannot be eliminated by the conventional step-skewing rotor. In this section, two optimal step-skewing solutions are proposed to improve the cogging torque performance.

2.3.1 Step-Skewing Rotor with Optimal Skewing Angles

According to the foregoing analyses, the equivalent skewing angle of each side rotor step proves to be lower than the theoretical value due to the axial flux interaction between rotor steps. Therefore, it is necessary to investigate the specific influence of step-skewing angles on cogging torque reduction. By 3D FE model of the 3-step-skewing design, the cogging torque performance under different step-skewing angles is investigated, as shown in Fig. 2.17. It can be seen that the 24th cogging torque is reduced from 17.8mNm to very low extent when the skewing angle increases from 5.0° to 5.6°, and then the cogging torque starts to rise again. Therefore, ±5.6° proves to be the optimal skewing angles for the aforementioned motor. For comparison, the cogging torque waveforms by designs with the theoretical (±5.0°) and optimal skewing angles (±5.6°) are illustrated in Fig. 2.17 (b). It can be also seen that the residual 24th cogging torque is eliminated, replaced by higher order of harmonics with much lower magnitudes.

Therefore, it can be deduced that the optimal skewing angles for the step-skewing rotor are different from the theoretical values, and the 3D end effect can be compensated by selecting an optimal skewing angle.

Similarly, investigation on the 2-step and the 4-step designs is also carried out with the proposed approach employed, as shown in Fig. 2.18. For comparison, the equivalent skewing angle (step-skewing angle multiplied by the number of rotor steps) is illustrated. As can be seen, the residual 24th cogging torque components of the three designs can be significantly reduced by selecting optimal skewing angles respectively, which verifies the effectiveness of the proposed skewing method. However, amongst the three designs, the optimal equivalent skewing angles gradually increase, i.e. 16.6° (2-step case), 16.8° (3-step case) and 17.0° (4-step case) respectively.

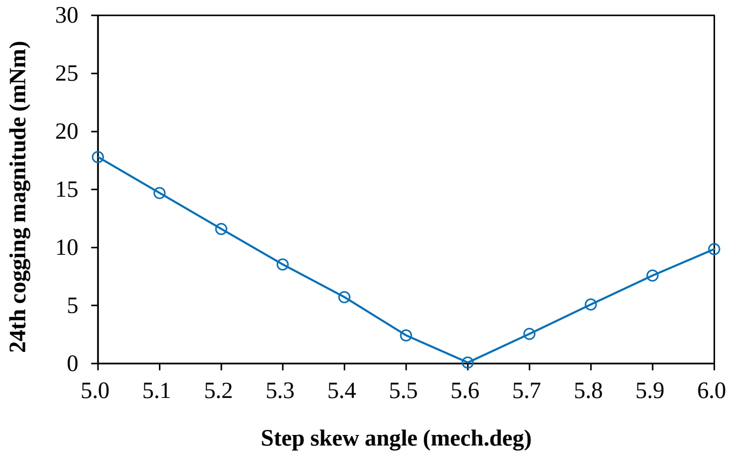

(a) Magnitudes under different skewing angles

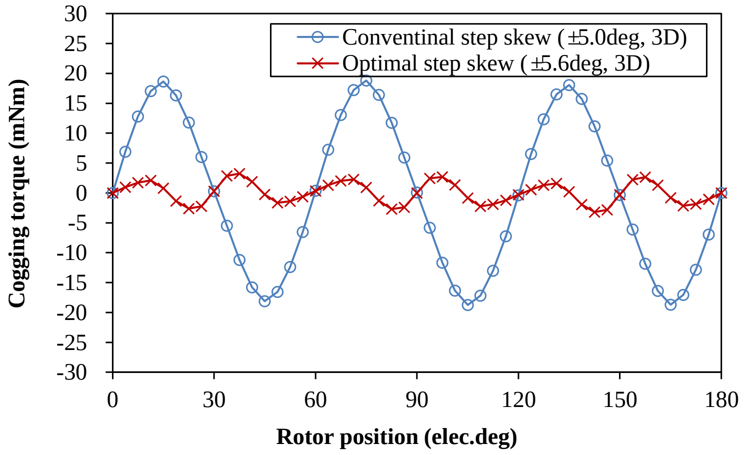

(b) Waveforms by conventional and optimal step-skewing angles

Fig. 2.17 Influence of step-skewing angles on cogging torque (3D FE).

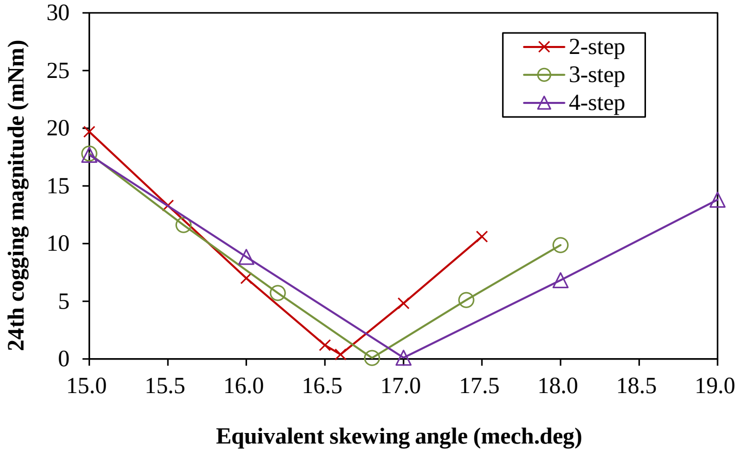

Fig. 2.18 Optimal skewing angles for designs with different numbers of rotor steps (3D FE).

2.3.2 Step-Skewing Rotor with Optimal Lengths of Rotor Steps

Without adjustment on the skewing angles (±5.0°), another approach is proposed by employing different axial lengths of rotor steps (the total axial length remains stable at 37.5mm for this model), i.e. longer side steps and shorter middle step, as shown in Fig. 2.19.

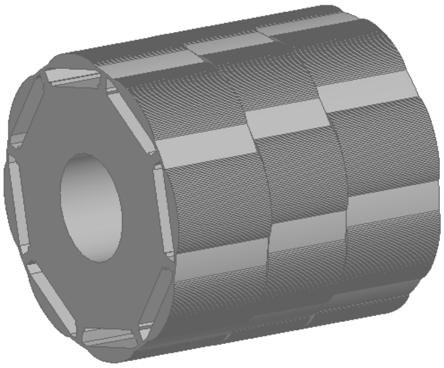

Fig. 2.19 Step-skewing rotor with different step lengths.

Based on the existing 3D FE model of 3-step-skewing design, the influence of middle step length on the 24th cogging torque is analyzed, as shown in Fig. 2.20. It can be seen that the 24th cogging torque is significantly reduced from 17.8mNm to a minimum value when the middle step length decreases from 12.5mm to 9.0mm (the side step length increases from 12.5mm to 14.25mm to guarantee the uniform total length), followed by a rising trend. The cogging torque waveforms for designs with equal and optimal step lengths are also illustrated, as shown in Fig. 2.20 (b). It can be seen that the step-skewing rotor with optimal step lengths can also be employed to eliminate the residual 24th cogging torque caused by the end leakage and axial flux interaction.

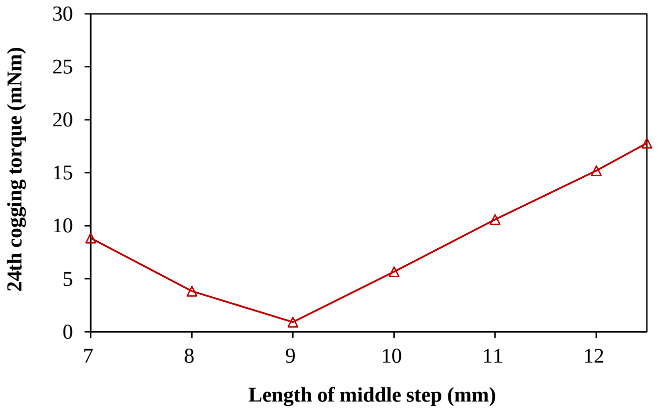

(a) Magnitudes under different middle step lengths

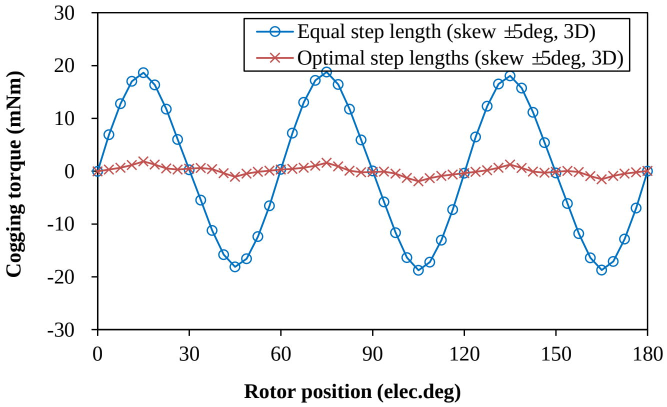

(b) Comparison between designs with equal and optimal step lengths

Fig. 2.20 Influence of rotor step lengths on cogging torque (skew ±5.0°, 3D FE).

2.3.3 Comparison between the Two Proposed Methods

In order to improve the residual cogging torque caused by 3D effect, two kinds of step-skewing methods have been proposed, i.e. rotors with optimal step-skewing angles and optimal step lengths. A comparison is carried out between the two proposed methods to evaluate their specific performance, including the cogging torque, the rated torque, and the axial unbalance magnetic force.

With identical stator (and windings) employed, the motor performance is calculated by 3D FE method, as shown in Fig. 2.21. For comparison, the design with conventional step-skewing rotor (skewing angle ±5.0°, equal length of rotor steps) is also illustrated. As can be seen, the cogging torque can be significantly improved by the two proposed designs, both decreasing from ±17.8mNm to very low extent. Moreover, the torque quality is also investigated and compared, as shown in Fig. 2.21 (b). It can be seen that the average torque is slightly decreased from 4.26Nm to 4.21Nm (design by optimal skewing angles) and 4.24Nm (design by optimal step lengths), respectively. However, the rated torque ripple is effectively improved, decreasing from 3.6% to 2.3% - a similar value between the two designs, which is mainly due to the elimination of the residual 24th cogging torque. In addition, it can be seen from Fig. 2.21 (c) that the axial unbalance magnetic force slightly increases with the second proposal employed, which is mainly due to the increase of side step length. However, it is also worth noting that in terms of manufacturing, optimal PM step skew is better than the optimal PM axial length since the later needs two magnets of different axial lengths.

Actually, the foregoing 3D FE analyses are all based on ideal conditions, whilst the influence of manufacturing tolerances is not considered. Moreover, due to the axial flux interaction is very sensitive to the core saturation, it is also necessary to investigate the influence of machine materials during the manufacturing.

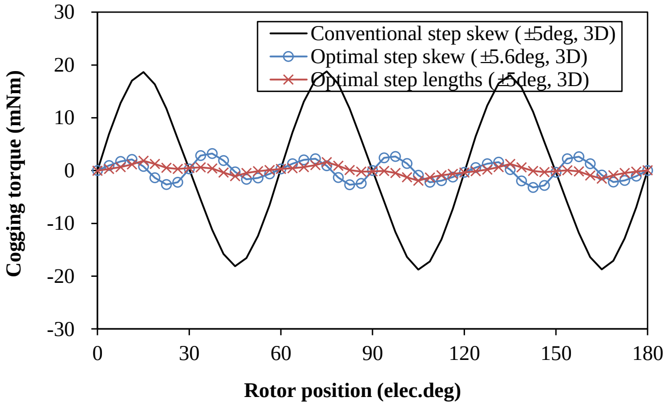

(a) Cogging torque

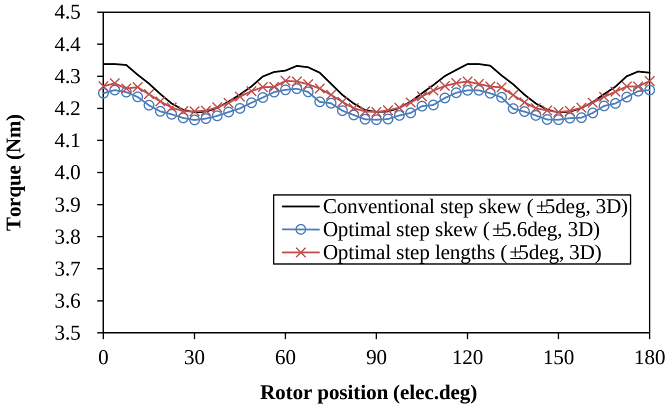

(b) On-load torque

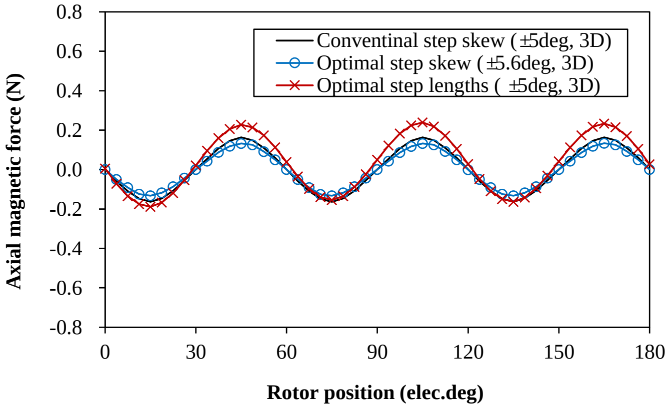

(c) No-load axial unbalance magnetic force

Fig. 2.21 Performance comparison between designs with the conventional and the proposed step-skewing methods (3D FE, 1/8 revolution).

2.4 Design Considerations Accounting for Manufacturing Issues of Step-Skewing Rotor

Based on certain machine materials, the foregoing analyses are carried out under ideal conditions, in which the influence of machine materials and manufacturing tolerances are not considered. However, different materials may be employed in different applications, including the silicon-steel laminations and the PM materials. In addition, manufacturing tolerances are usually inevitable. Therefore, the corresponding influence will be investigated in this section.

2.4.1 Influence of Machine Materials

A. Silicon-steel lamination materials

Usually, the machine performance is closely related to the lamination materials, and two typical silicon-steel laminations materials are selected to evaluate the corresponding influence, with the B-H curves shown in Fig. 2.22. As can be seen, the saturation flux density of DW310-35 is obviously lower than that of the material used in previous FE models (CS1000-50).

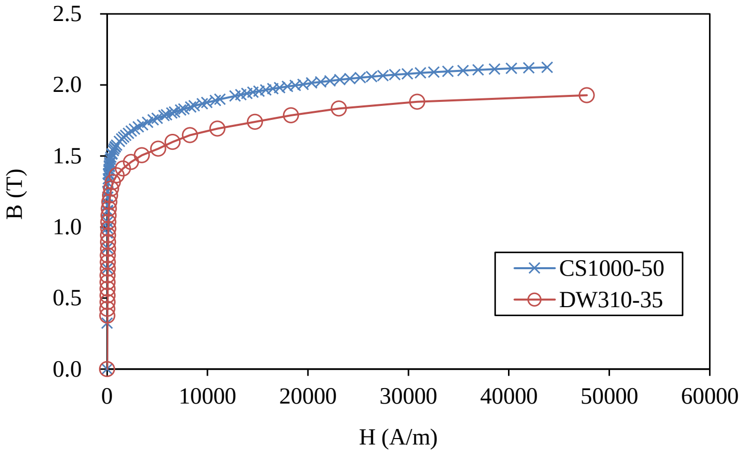

Fig. 2.22 B-H curves of two typical materials of silicon-steel laminations.

Based on the identical machine model, the cogging torque is obtained respectively with the 3D FE method employed, as shown in Fig. 2.23. It can be seen from Fig. 2.23 (a) that the residual cogging torque increases from ±17.8mNm to ±23.6mNm with DW310-35 material employed. Actually, more axial flux interaction is introduced due to the increased saturation level, which results in the higher residual cogging torque. Further, the optimal step-skewing angles for designs with the two materials are obtained respectively, as shown in Fig. 2.23 (b). It can be seen that the optimal skewing angle increases from 5.6 °to 5.8 °in order to compensate the more severe axial flux interaction between adjacent rotor steps.

Therefore, it can be deduced that the design by lower saturation flux density of silicon-steel material would result in higher residual cogging torque, which requires a higher optimal step-skewing angle as a consequence.

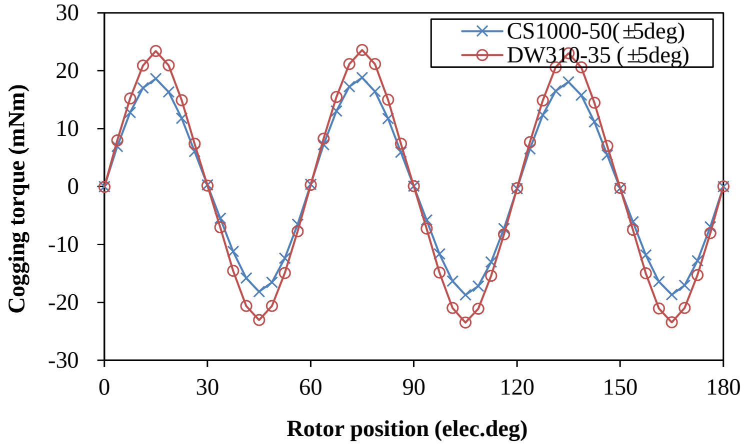

(a) Cogging torque (skewing ±5°)

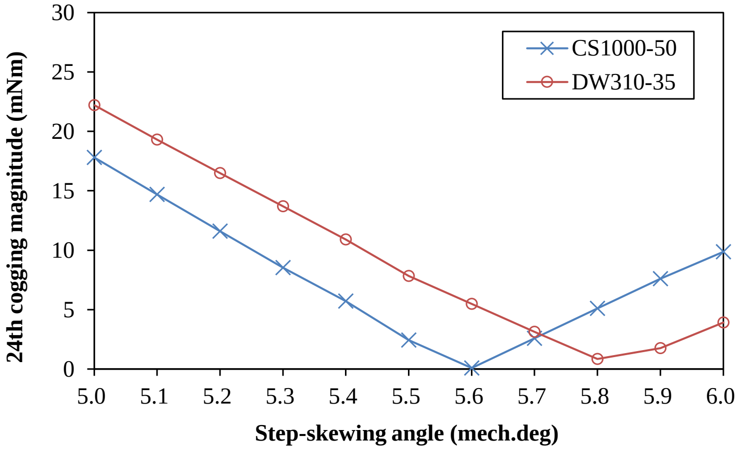

(b) Optimal step-skewing angles

Fig. 2.23 Comparison of residual cogging torque and optimal step-skewing angles for different silicon-steel materials (3-step, 3D FE).

B. PM Materials

In addition to the silicon steel lamination, the PM is another important component, which directly relates to the cogging torque and the core saturation level. Two PM materials are selected for comparison, i.e. N42SH and N35SH, with the magnetic properties shown in Table 2.2 respectively.

Similarly, the cogging torque performance is investigated by 3D FE method with the two PM materials employed respectively, as shown in Fig. 2.24. It can be seen that the residual cogging torque decreases from ±17.8mNm to ±12.6mNm, which is mainly due to the decrease of air-gap flux density and core saturation level. Consequent influence is also reflected on the optimal step-skewing angles, as shown in Fig. 2.24 (b). It can be seen that this angle is reduced from 5.6 ° to 5.5 ° for this IPM machine design.

TABLE 2.2

MAGNETIC PROPERTIES OF TWO PM MATERIALS

PM material	PM remanence (T, 20 ℃)	PM coercive force (A/m)
N42SH	1.32	972614
N35SH	1.20	884193

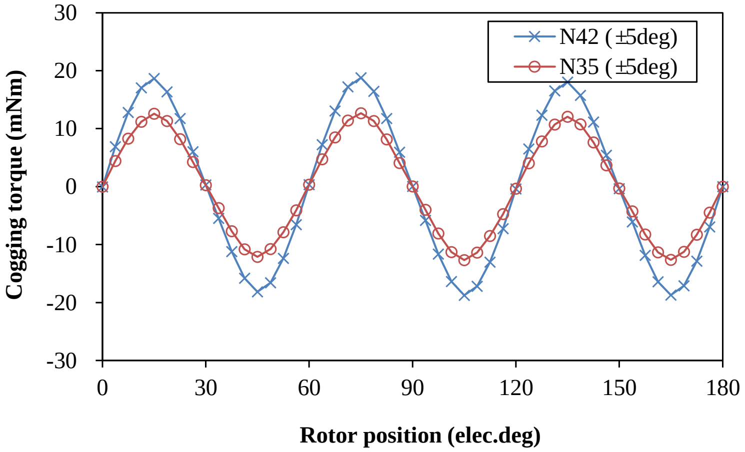

(a) Waveforms

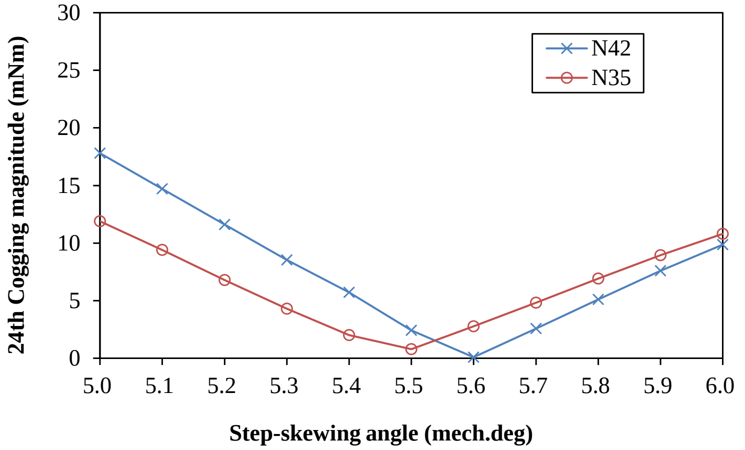

(b) Optimal step-skewing angles

Fig. 2.24 Comparison of residual cogging torque and optimal step-skewing angles for different PM materials (3-step, 3D FE).

2.4.2 Influence of Axial Assembling Air-Gaps between Rotor Steps

Two improved step-skewing methods have been proposed to compensate the influence of end leakage flux and axial flux interaction, through which much lower values of cogging torque can be obtained. Also, the influence of machine materials have been investigated, which indicates that the core saturation level directly relates to the residual cogging torque and the optimal skewing angle. However, the aforementioned analyses are carried out under ideal conditions whilst the influence of actual manufacturing tolerances is not considered, e.g. the axial assembling gaps between different rotor steps, as shown in Fig. 2.25. Usually, such kind of tolerances are very difficult to avoid during the manufacturing process, and the magnets of same polarity repel each other as well. In this section, the 3D FE method is employed to investigate the corresponding influence with the axial assembling gaps considered (In the areas with small air-gaps, the JMag software can automatically create much smaller sizes of mesh, according to the gap lengths).

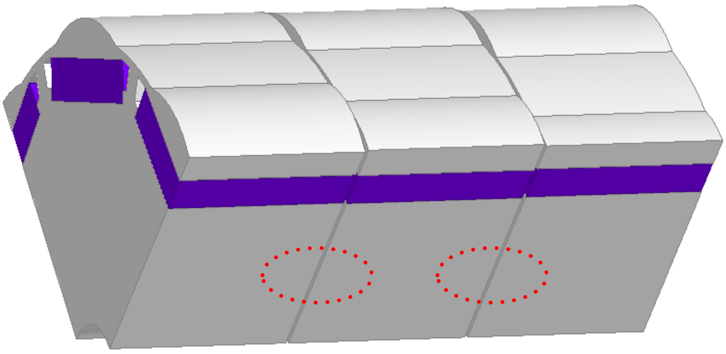

Fig. 2.25 Axial assembling gaps between rotor steps.

For the aforementioned machine with a conventional step-skewing rotor (skewing ±5.0^{o}), the influence on cogging torque by axial assembling gaps is firstly investigated, as shown in Fig. 2.26. It can be seen that the 24th cogging torque is reduced from 17.8mNm to 12mNm with 0.05mm axial gaps considered, which is mainly due to the decrease of axial flux interaction between side and middle rotor steps. Then the cogging torque decreases gradually to 8.45mNm when 0.20mm axial gaps are involved, as shown in Fig. 2.26 (b).

Due to the significant decrease of the residual cogging torque, it can be deduced that there will be corresponding influence on the optimal skewing angles and step lengths. Take the first proposed approach for example, the influence of axial gaps (e.g. 0.10mm) on the optimal step-skewing angle is further investigated, as shown in Fig. 2.27. It can be seen that the residual cogging torque is effectively reduced from 10mNm to very low extent when the skewing angle increases from 5.0 ° to 5.3 °, and then it starts to rise again. Therefore, a minimum cogging torque can be obtained with a ±5.3° step-skewing rotor employed, which is different from the previous optimal skewing angles (±5.6°) obtained under ideal conditions. Similarly, it can be deduced that corrections should also be made on the optimal step lengths obtained under ideal conditions, which will not be duplicated here.

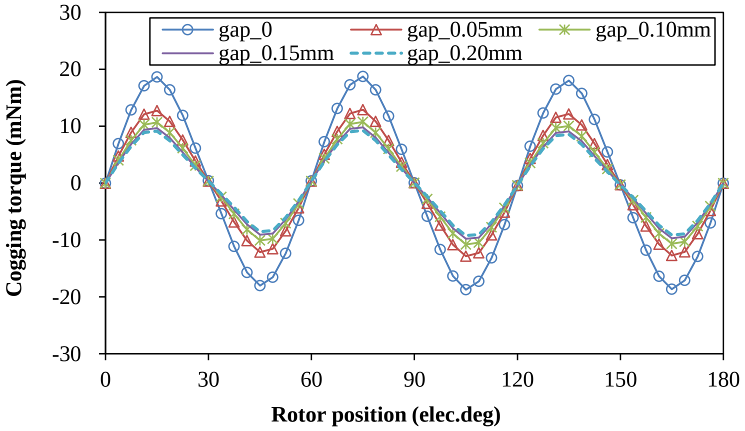

(a) Waveforms

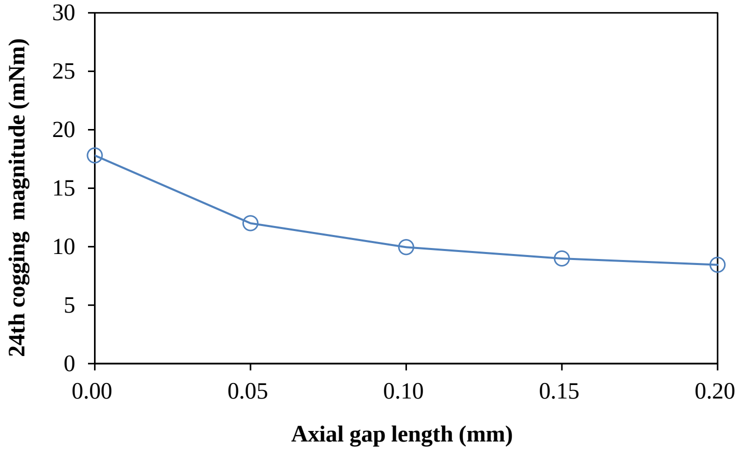

(b) 24th cogging torque magnitudes

Fig. 2.26 Influence of axial gaps on cogging torque (3D FE, skewing ±5.0 °).

Therefore, obvious influence on the cogging torque will be introduced by manufacturing tolerances, which requires approximate corrections of the proposed methods according to actual manufacturing conditions.

Based on the foregoing analyses, it can be seen that the machine materials and the manufacturing process significantly influence the residual cogging torque. With the manufacturing process considered, further corrections on the optimal step-skewing angles or step lengths should be made by 3D FE method.

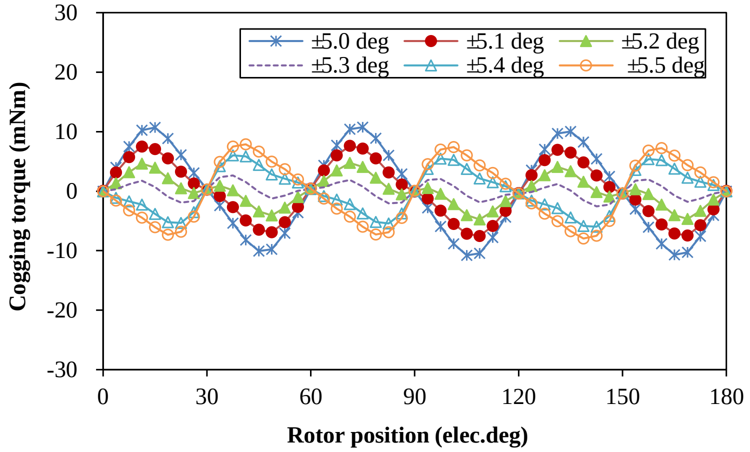

(a) Waveforms (1/8 revolution)

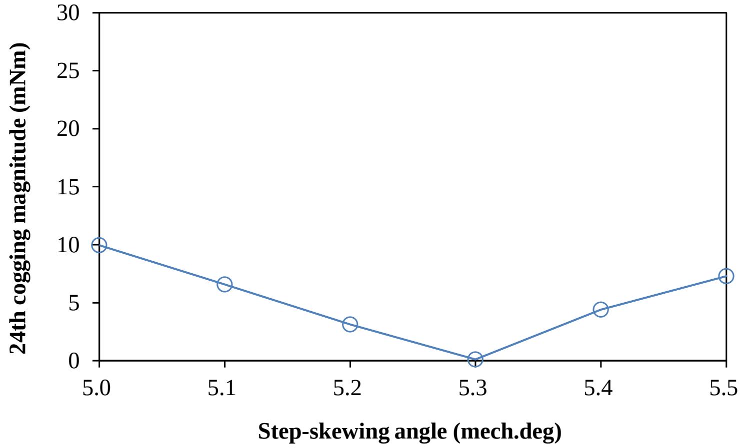

(b) 24th cogging torque magnitudes

Fig. 2.27 Cogging torque under different step-skewing angles with 0.10mm axial gaps between rotor steps considered (3D FE).

2.4.3 Other Step-Skewing Scheme by Axial Auxiliary Gaps between Rotor Steps

The influence of axial assembling gaps on the cogging torque has been investigated in the foregoing analyses, which shows that the axial flux interaction closely relates to the gaps between rotor steps. Based on the relation, an alternative step-skewing scheme is proposed, as shown in Fig. 2.28 (a), in which an additional gap is placed between the 2 rotor steps. With the 3D FE method employed, the cogging torque performance is compared between the designs with and without axial gaps, as shown in Fig. 2.28 (b). It can be seen that the residual cogging torque is significantly improved, reducing from ±20.7mNm to ±5.6mNm with a 1.0mm gap employed. Similarly, it can be also seen from Fig. 2.28 (c) that the 24th cogging torque harmonic is reduced from ±19.7mNm to ±3.86mNm, together with a slight decrease of the 48th cogging torque. Therefore, it can be seen that the residual 24th cogging torque can be effectively reduced by this design, which is mainly due to the decrease of axial flux interaction between adjacent rotor steps.

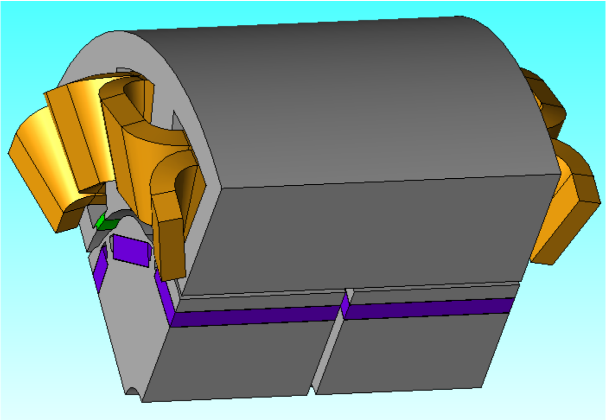

(a) Modular 3D FE model

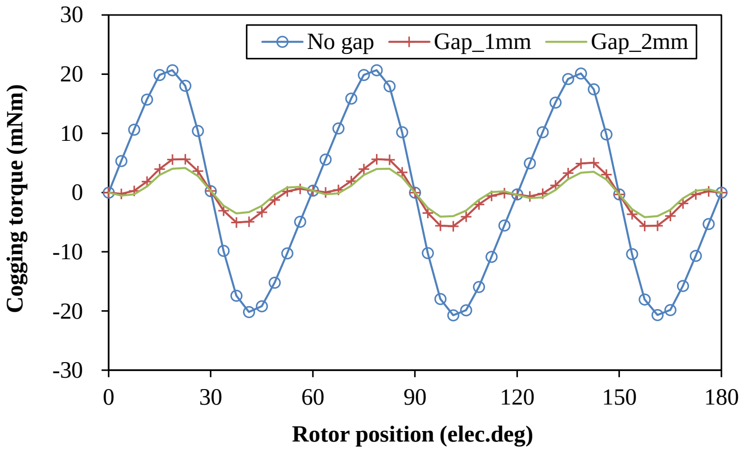

(b) Waveforms (1/8 revolution)

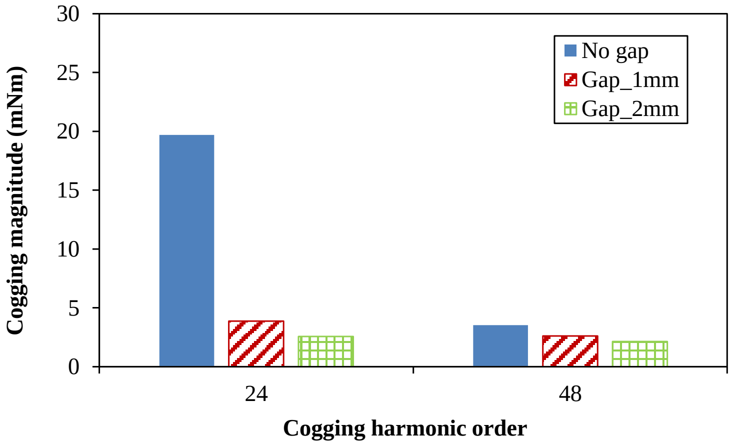

(c) Harmonics

Fig. 2.28 Comparison of cogging torque between designs with and without axial auxiliary gaps (3D FE).

However, it can be found that the 24th cogging torque only decreases from ±3.86mNm to ±2.56mNm when a larger gap (2mm) is employed. Considering the limit of machine total axial length, the step-skewing angles can also be optimized in order to further reduce the residual cogging torque, as shown in Fig. 2.29 (a). It can be seen that the optimal step-skewing angle is significantly reduced from 8.3° to 7.65°, which is mainly due to the decreased residual cogging torque. In addition, the torque quality is also compared between the designs with and without axial gaps, as shown in Fig. 2.29 (b). It can be seen that the average torque is slightly increased from 4.25Nm to 4.32Nm by the design with axial gaps, whilst the torque ripple remains similar.

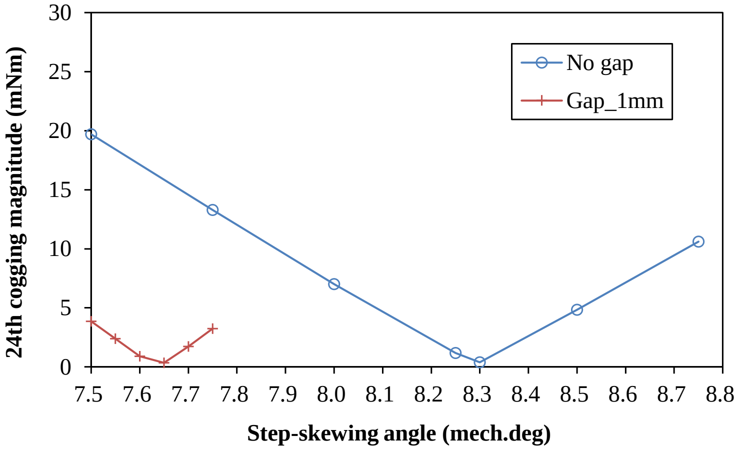

(a) Optimal step-skewing angles

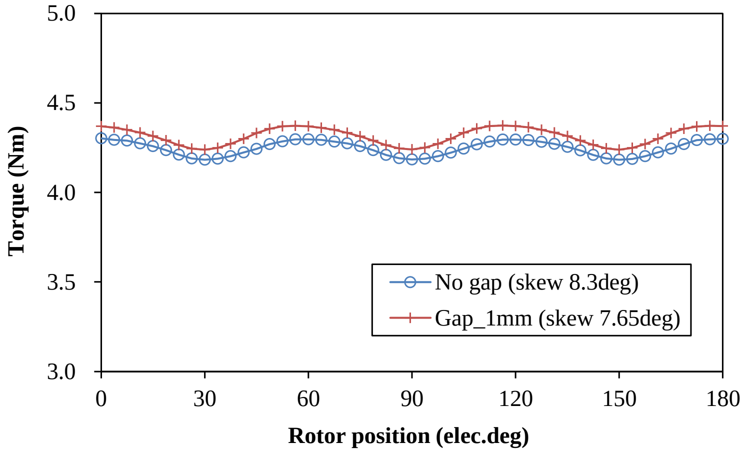

(b) Torque quality (equal active rotor length: 37.5mm)

Fig. 2.29 Comparison of optimal step-skewing angles and torque quality between designs with and without axial gaps (3D FE).

2.5 Prototype and Test

In order to verify the effectiveness of the proposed step-skewing methods, prototypes are fabricated based on the parameters shown in Table 2.1. For comparison, two step-skewing rotors with conventional and optimal skewing angles are fabricated respectively, in addition to a stator for common use, as shown in Fig. 2.30.

Moreover, a test platform is established on basis of a lathe, as shown in Fig. 2.31, which is frequently used for the measurement of cogging torque and static torque in electric machines [ZHU09a]. As can be seen, the frame of the prototype is fixed by the chuck of lathe and the shaft is equipped with a balanced beam, one end of which is connected to a digital scale. When the lathe rotates, the cogging torque at every rotor position can be reflected through the weight shown on the scale.

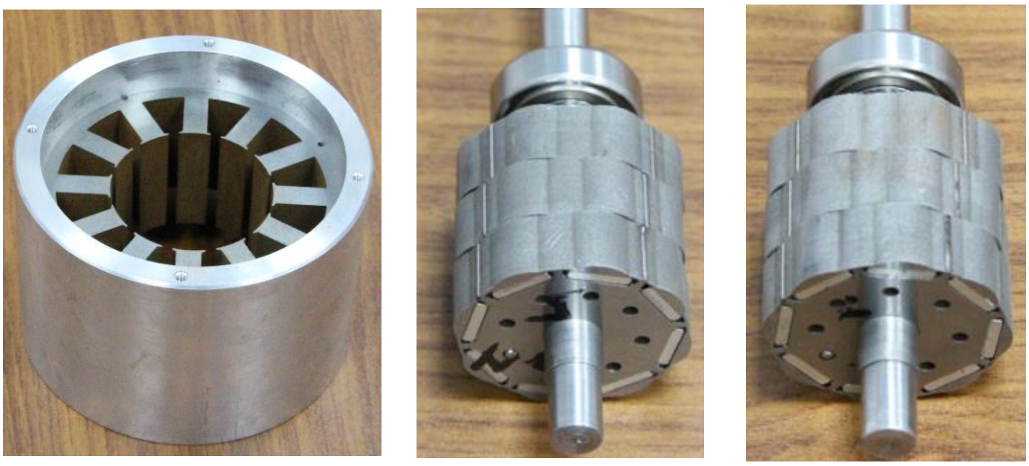

(a) Stator

(b) Conventional rotor (step-skew ±5.0°)

(c) Proposed rotor (step-skew ±5.3°)

Fig. 2.30 Prototypes.

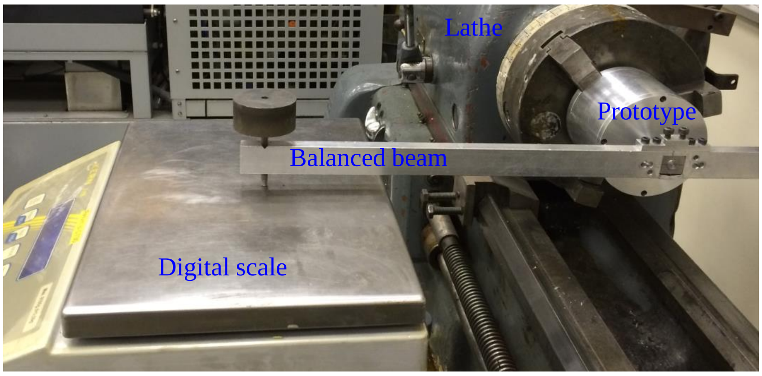

Fig. 2.31 Cogging torque test platform.

Since the axial assembling gaps are usually difficult to avoid, the step-skewing angle of the proposed rotor is 5.3 °, and the cogging torque waveforms by the 3D FE method are shown in Fig. 2.32 (a). On basis of the platform, the two prototypes are measured respectively, with the cogging torque waveforms shown in Fig. 2.32 (b). As can be seen, the cogging torque magnitude is obviously reduced from ±16.5mNm to ±8mNm with the proposed step-skewing rotor employed. In addition, the cogging torque harmonics are also analysed and compared, as shown in Fig. 2.32 (c). Clearly, it can be seen than the 24th order of cogging torque component is significantly reduced from 9.5mNm to 3mNm by the proposed rotor.

It should also be noted that the 8th order of cogging torque harmonics are introduced in the two prototypes, which are mainly caused by imperfection of stator components (which will be further investigated in Chapter 3). However, the effectiveness of the proposed design can still be verified by the test and the significant reduction of the cogging torque.

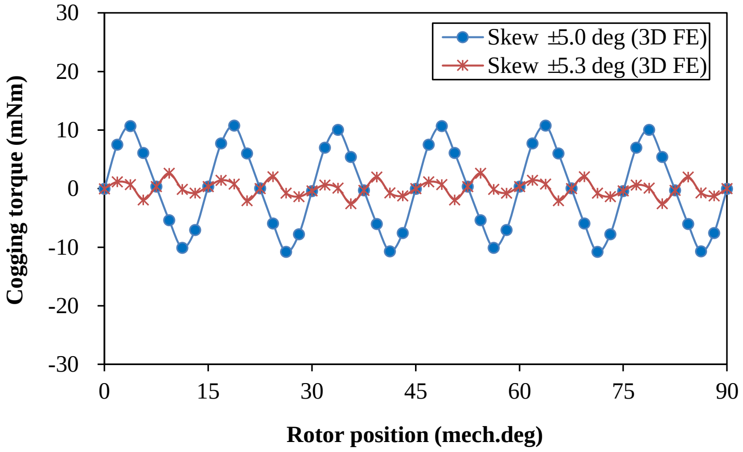

(a) Waveforms (1/4 revolution, 3D FE, 0.1mm axial gaps)

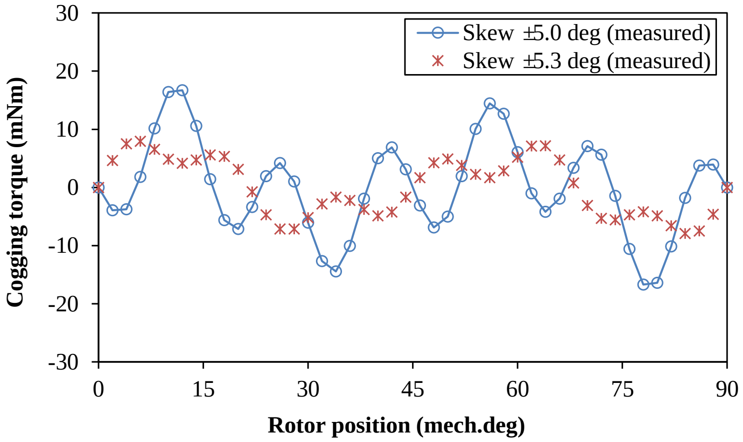

(b) Waveforms (1/4 revolution, measured)

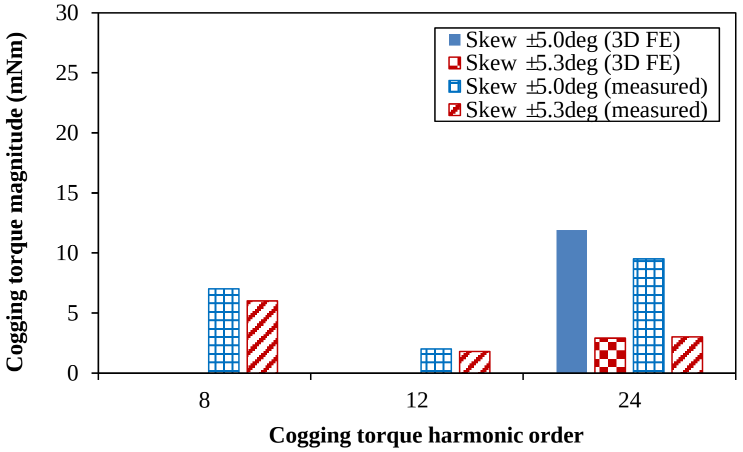

(c) Harmonics

Fig. 2.32 Comparison of cogging torque between 3D FE and measured results.

2.6 Conclusion

In this chapter, the conventional step-skewing method for cogging torque reduction in IPM machines has been investigated firstly, and it is found that the cogging torque cannot be eliminated due to the end leakage flux and the axial flux interaction between adjacent rotor steps. Then, two optimal methods have been proposed, (a) step-skewing rotor with optimal skewing angles, and (b) step lengths to compensate the 3-dimensional effect and minimize the residual cogging torque. Furthermore, the influence of machine materials (silicon-steel laminations and PMs) and rotor contours with different eccentric distances has been analyzed, which indicates that the residual cogging torque closely relates to core saturation level. In addition, the influence of manufacturing tolerance (axial assembling gaps between rotor steps) has been also investigated, which requires further corrections on the proposed methods. Prototypes have been fabricated and tested, and the foregoing analyses have been verified.

Although the 24th cogging torque is effectively reduced, it should also be noted that the 8th and the 12th orders of cogging torque components still exist, and it is necessary to investigate the origins of this components in the following chapters.

CHAPTER 3 INVESTIGATION ON COGGING TORQUE OF INTERIOR PERMANENT MAGNET MACHINES ACCOUNTING FOR MANUFACTURING TOLERANCES

3.1 Introduction

According to the prototype tests in Chapter 2, it can be found that the actual cogging torque of the 12-slot/8-pole IPM design is composed of different orders of harmonics, e.g. the 8th and the 12th orders, in addition to the original 24th order. Different from the ideal conditions, manufacturing tolerances are usually inevitable in actual machine products. Therefore, it is necessary to investigate the corresponding influence on cogging torque performance, in order to avoid sensitive cases of tolerances during the manufacturing process.

Based on the foregoing 12-slot/8-pole IPM design (other IPM machine designs will be investigated in Chapter 4), four typical types of tolerances are investigated in this chapter:

Type 1: PM diversity (including uneven PM remanence and non-uniform PM thickness)
Type 2: Assembling eccentricities (including the static and the dynamic cases)
Type 3: Stator out-of-roundness (tooth-bulges may be introduced during the assembling)
Type 4: Step-skewing angles tolerance (the rotor steps are not precisely skewed)

Due to the random distribution of non-ideal PMs and tooth-bulges, potential combinations are analyzed respectively, in order to obtain the most sensitive sequences of non-ideal PMs and tooth-bulges.

In addition, comparison of the cogging torque performance is carried out between designs with and without step-skewing (i.e. 3 rotor steps) in order to clearly demonstrate the specific influence. For simplification, the 3D end effect and the axial flux interaction between adjacent rotor steps are not considered, and the 2D FE method is employed to carry out the analyses.

3.2 PM Diversity

3.2.1 Uneven PM Remanence

Due to the non-uniform PM materials and the different magnetizing quality, the PM remanence (B_r) usually exhibits different properties for different PM poles. For N45SH, the typical value of B_r is 1.32T (PMs with which are assumed to be ‘ideal’), whilst the maximum value can be as high as 1.42T (PMs with which are assumed to be ‘non-ideal’).

In order to investigate the influence of uneven PM remanence, the random sequences of non-ideal PMs for this 8-pole rotor can mainly be divided into 16 cases, with the corresponding cogging torque performance shown in Fig. 3.1. As can be seen, the 12th order of cogging torque may be motivated by the PM diversity. However, different sequences of the non-ideal PMs may influence the cogging torque differently. According to the magnitudes of the motivated cogging torque, the 16 types of PM sequences can be divided into 3 categories: sequences without obvious influence, sequences with moderate influence and sequences with severe influence, which will be introduced as follows, respectively.

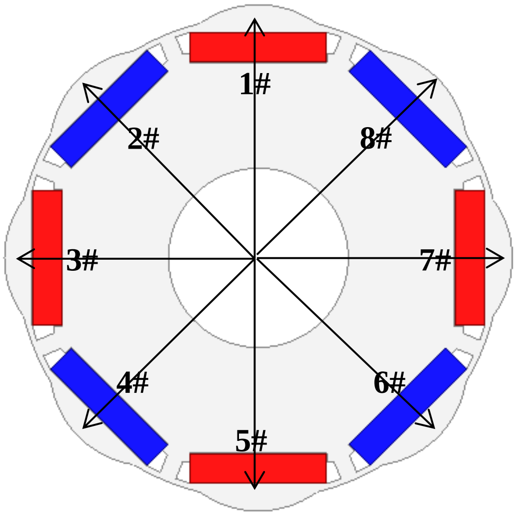

(a) PM distribution of the 8-pole rotor

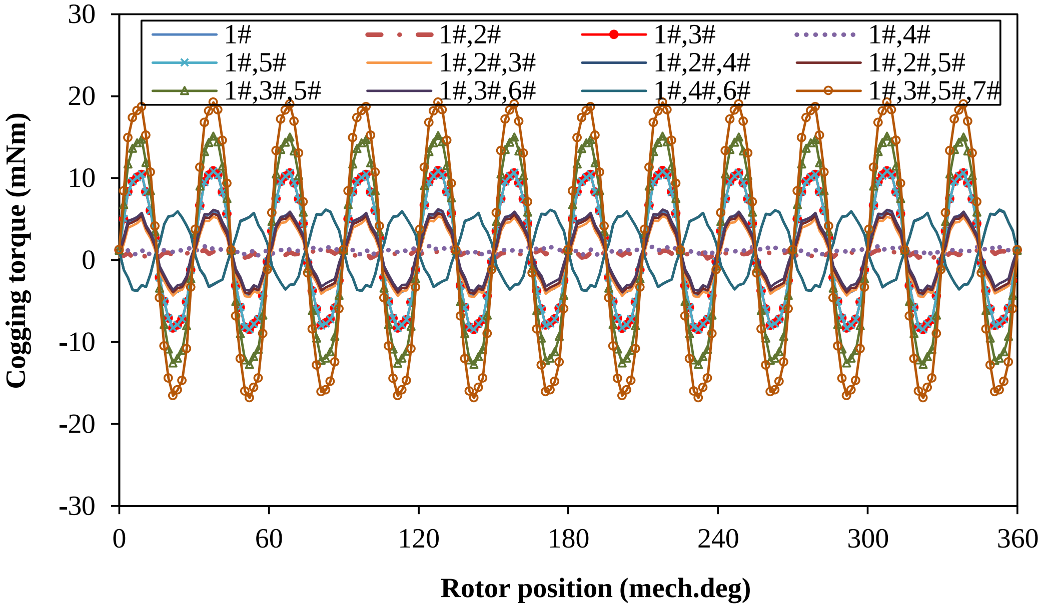

(b) Cogging torque with different sequences of non-ideal PMs considered (with skewing)

Fig. 3.1 Cogging torque with PM diversity considered (uneven remanence).

A. Non-ideal PM sequences without obvious influence

As can be seen from Fig. 3.1(b), certain non-ideal PM sequences will not obviously influence the cogging torque performance, even with PM diversity considered. As shown in Fig. 3.2(a), the fundamental features of such PM sequences can be described as: an odd number and an even number of non-ideal PMs (marked by the red color). It can be seen from Fig. 3.2(b) that no obvious component of the 12th order exists in the cogging torque with only a little increase of the 24th order which can be effectively eliminated by the step-skewing rotor. Therefore, the influence of this type is negligible. Actually, it can be deduced that all the PM sequences with equal numbers of odd and even non-ideal PMs will not obviously influence the cogging torque of the 12-slot/8-pole design, in addition to the two distributions shown in Fig. 3.2(a).

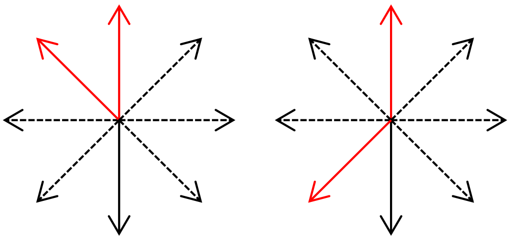

(a) Typical non-ideal PM sequence without obvious influence

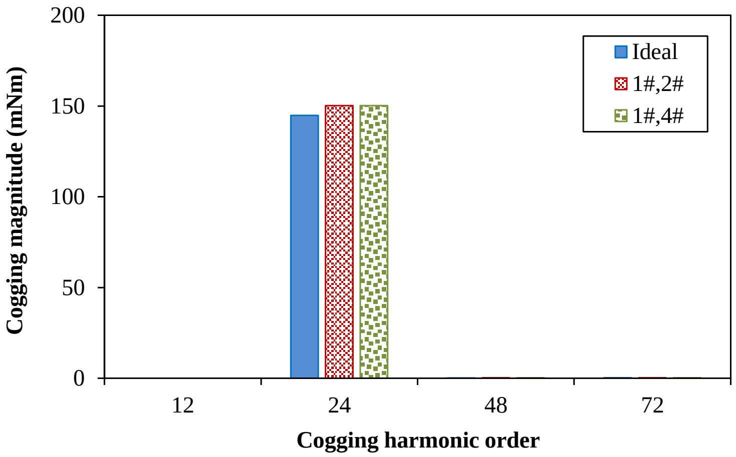

(b) Cogging harmonics (without skewing)

Fig. 3.2 Cogging torque with insensitive sequences of non-ideal PMs.

B. Non-ideal PM sequences with moderate influence

Also, it can be found in Fig. 3.1(b) that moderate influence may be introduced by certain non-ideal PM sequences, which can be generalized and shown in Fig. 3.3(a). Amongst these PM sequences, the numbers of odd and even non-ideal PMs differ by 1. It can be seen from Fig.

3.3 (b) that the 12th order of cogging harmonics are introduced by these sequences of non-ideal PMs, with the magnitude of 7.2mNm. With the skewing method employed, the 12th cogging is reduced to 4.8mNm, as shown in Fig. 3.3(c). In addition, although the 24th cogging is slightly increased, it can be eliminated by the skewing rotor.

Therefore, under these sequences of non-ideal PMs, the 12th order of cogging is introduced even the skewing method is employed, the magnitude of which is 4.8mNm.

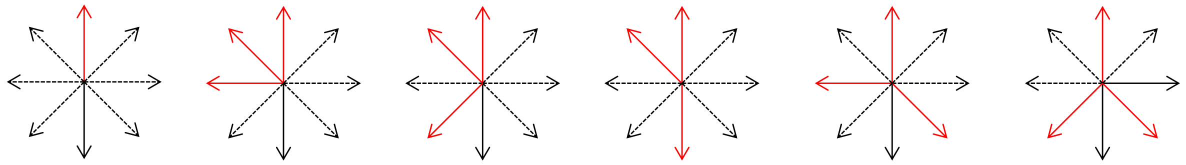

(a) Typical non-ideal PM sequences with moderate influence

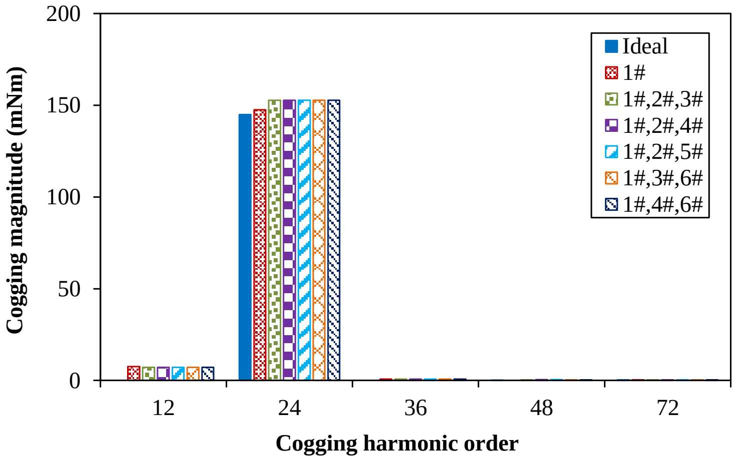

(b) Cogging torque harmonics (without skewing)

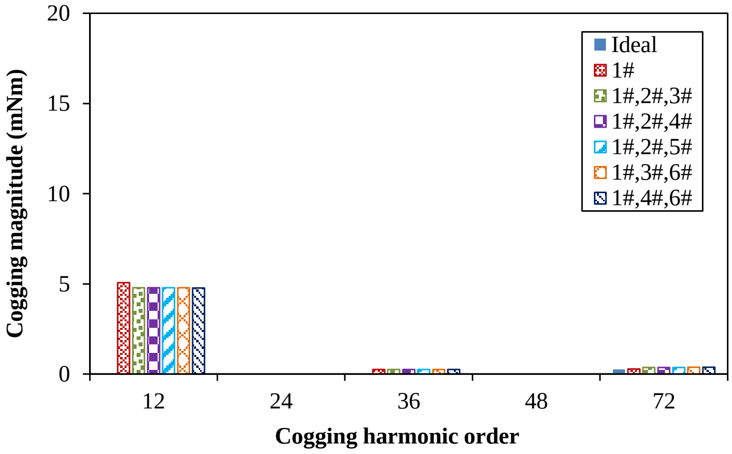

(c) Cogging torque harmonics (with skewing)

Fig. 3.3 Cogging torque with moderate sequences of non-ideal PMs.

C. Non-ideal PM sequences with severe influence

In addition to the two PM sequences described above, more severe influence on cogging torque may be introduced by the non-ideal PM sequences as shown in Fig. 3.4(a). The feature of such PM sequences can be described as ‘consequent’ non-ideal PM distributions, with the corresponding cogging torque harmonics shown in Figs. 3.4 (b) and (c). As can be seen, the 12th order of cogging torque is significantly motivated, of which the potential peak value can be as high as 27.9mNm. Even with skewing rotor employed, this value can still be 18.6mNm due to the limited effect on the 12th cogging by skewing. Therefore, severe influence to the cogging performance will be caused by such distributions of non-ideal PMs, which should be avoided during the manufacturing process.

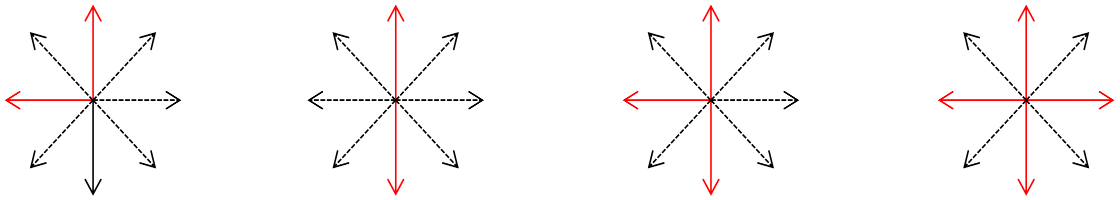

(a) Typical non-ideal PM sequences with severe influence

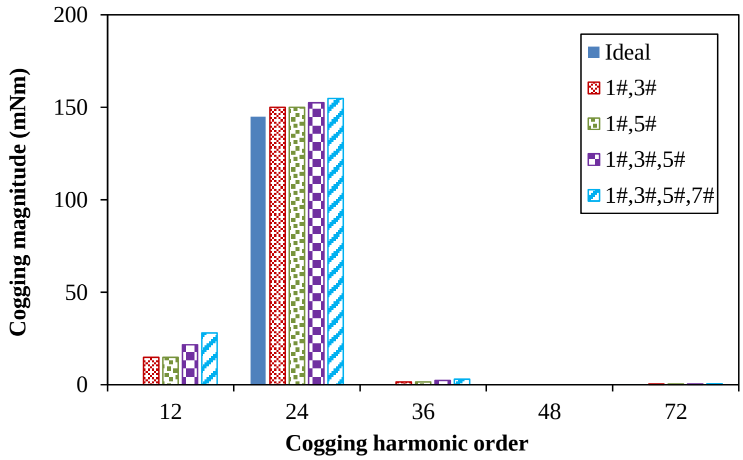

(b) Cogging torque harmonics (without skewing)

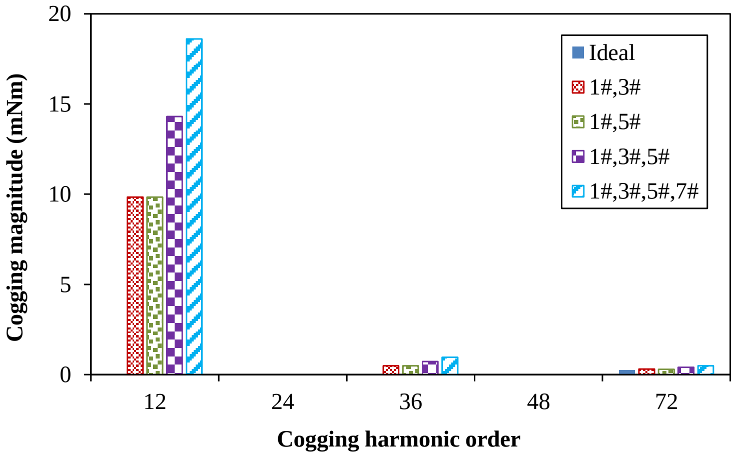

(c) Cogging torque harmonics (with skewing)

Fig. 3.4 Cogging torque with severe sequences of non-ideal PMs.

The influence of PM diversity (uneven PM remanence) on cogging torque has been investigated for the 12-slot/8-pole machine, and it is found that the 12th order of cogging torque component may be introduced, which cannot be effectively eliminated by the conventional step-skewing method. According to the feature of cogging torque harmonic order (the 12th), the influence of different non-ideal PMs is obtained, as shown in Fig. 3.5. It can be seen that negative cogging torque vectors are motivated by the non-ideal PMs of odd and even numbers. Therefore, with the PM diversity considered, the most sensitive case proves to be the consequent distribution of non-ideal PMs, the cogging torque magnitude (the 12th order) of which is four times of that by one single non-ideal PM.

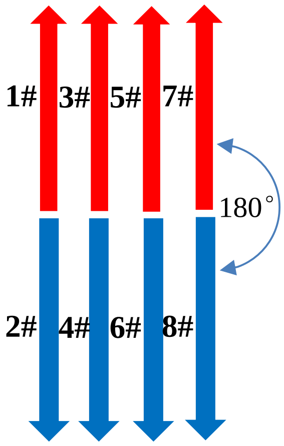

Fig. 3.5 Cogging torque vectors (the 12th) motivated by PM diversity in 12-slot/8-pole machines.

3.2.2 PM Thickness Tolerance

The second case of PM diversity is mainly caused by the tolerances of PM dimensions, e.g. thickness along magnetization, of which the typical value is 2.61mm and the maximum value is as high as 2.67mm, as shown in Fig. 3.6. PMs with the magnetization thickness of 2.67mm are assumed to be non-ideal. According to the influence of PM diversity described in Fig. 3.5, different PM sequences will not be discussed respectively and the analysis will focus on the non-ideal PM sequences shown in Fig. 3.4 (a), which represent the most severe distributions of non-ideal PMs. As shown in Fig. 3.7, the 12th order of cogging torque is produced by PM diversity on magnet thickness. With the skewing method employed, the maximum value of potential cogging torque will be 6.6mNm.

Based on the above analyses, the 12th order of cogging torque would be produced by PM diversity, including the non-uniform PM remanence and the magnet thickness. The most severe distributions of non-ideal PMs are demonstrated, which should be avoided in the manufacturing process.

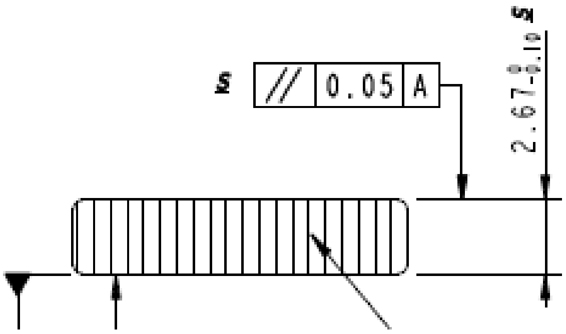

Fig. 3.6 PM diversity on magnet thickness.

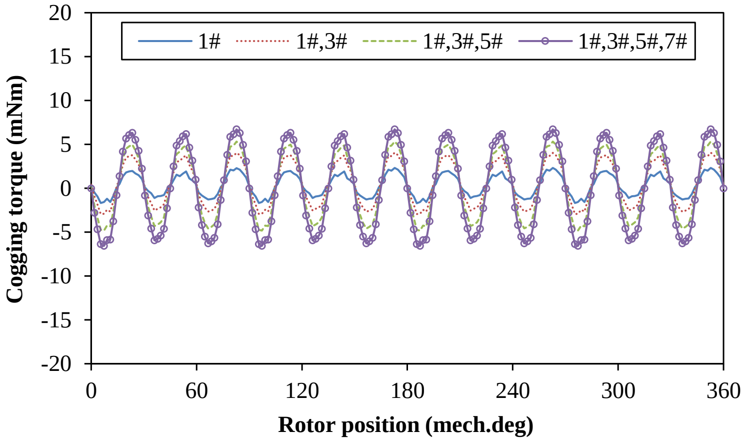

(a) Waveforms (with skewing)

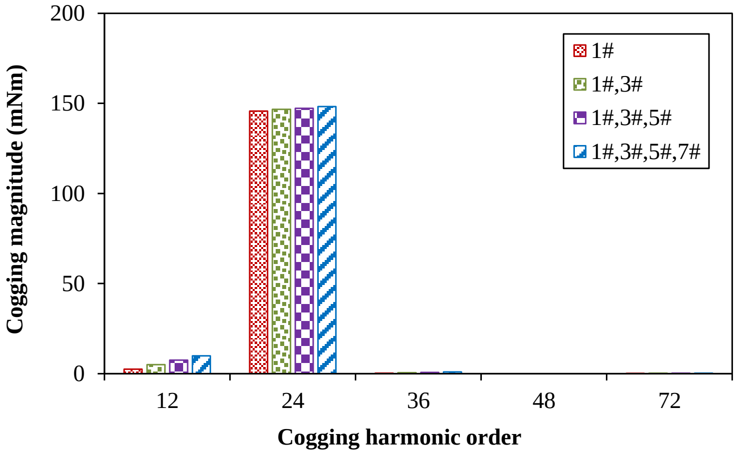

(b) Harmonics (without skewing)

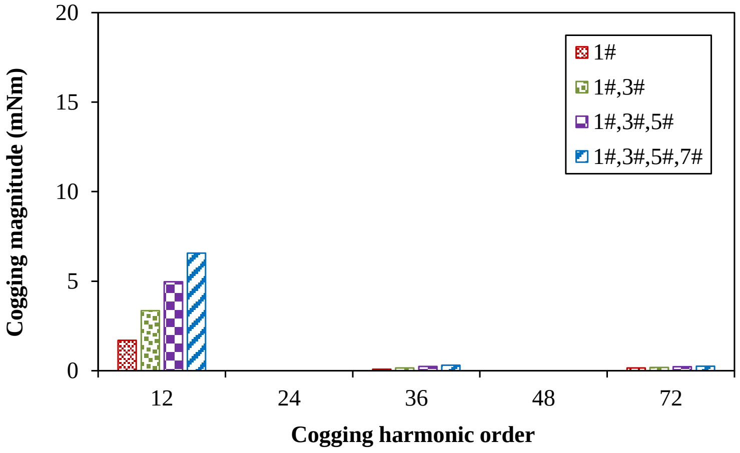

(c) Harmonics (with skewing)

Fig. 3.7 Cogging torque with PM diversity on magnet thickness considered.

3.3 Assembling Eccentricity

As a common issue for electrical machines, the assembling eccentricity is usually difficult to avoid during the manufacturing process. Therefore, it is necessary to investigate the specific influence on cogging torque. As it is well known, the eccentricity can be divided into two types: static and dynamic, which will be discussed respectively.

3.3.1 Static Eccentricity

Static eccentricity in electrical machines is mainly due to the separate end caps and the frame, in which the misaligned stator and rotor axes are reflected, as shown in Fig. 3.8 (a). In order to evaluate the influence on cogging torque, different values of static eccentricity are employed and analyzed, increasing from 0 to 0.14mm – a typical range of the static eccentricity.

As shown in Figs. 3.8 (b) and (c), the cogging torque will not be obviously influenced by static eccentricity, only with a negligible increase on the 8th order of cogging torque component.

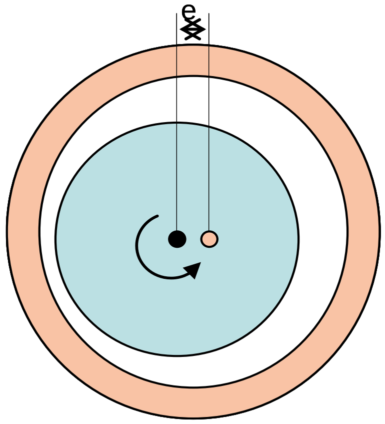

(a) Static eccentricity

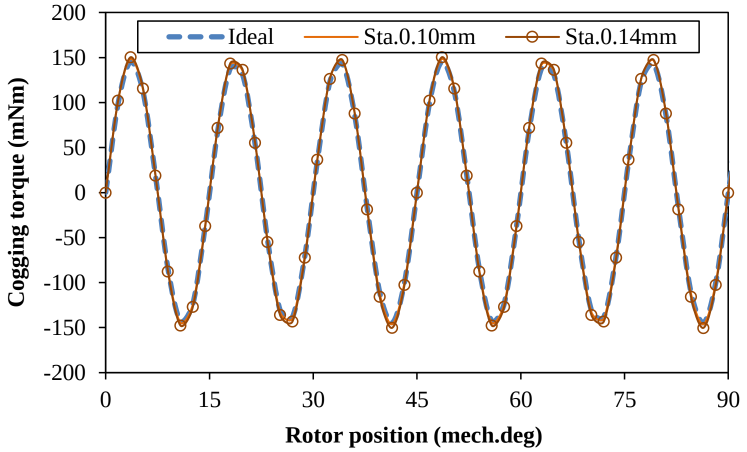

(b) Waveforms (1/4 revolution)

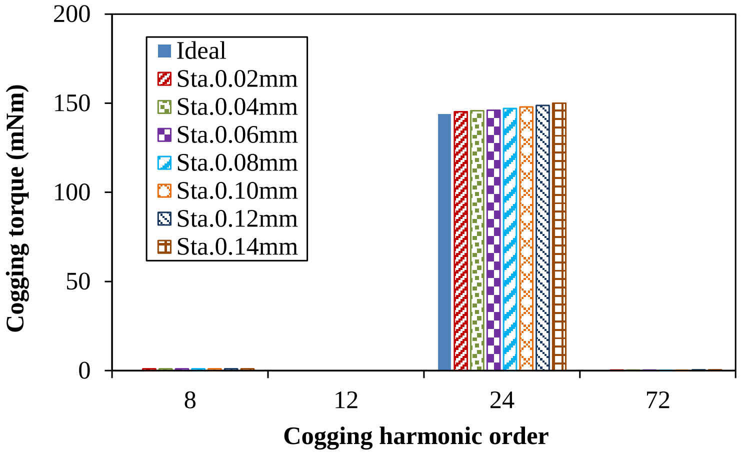

(c) Harmonics

Fig. 3.8 Cogging torque with static eccentricity considered (without skewing).

3.3.2 Dynamic Eccentricity

The other type of assembling eccentricity is the dynamic case, which is usually caused by the tolerance between the rotor and the shaft. As shown in Fig. 3.9 (a), the misaligned rotating axis and the rotor axis are reflected. Actually, the dynamic eccentricity is much easier to control during the fabrication, compared with the static type.

As shown in Figs. 3.9 (b) and (c), the influence of dynamic eccentricities on cogging torque is illustrated. It can be seen that no obvious cogging torque is introduced when the eccentricity changes from 0mm to 0.14mm.

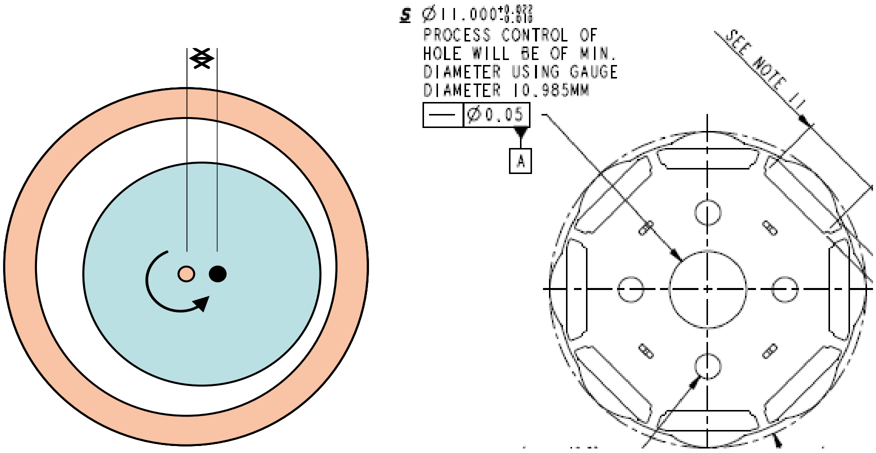

(a) Dynamic eccentricity and a potential source

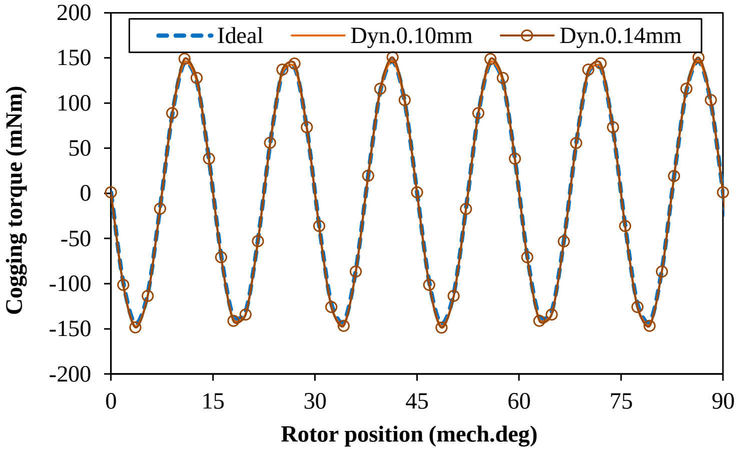

(b) Waveforms (1/4 revolution)

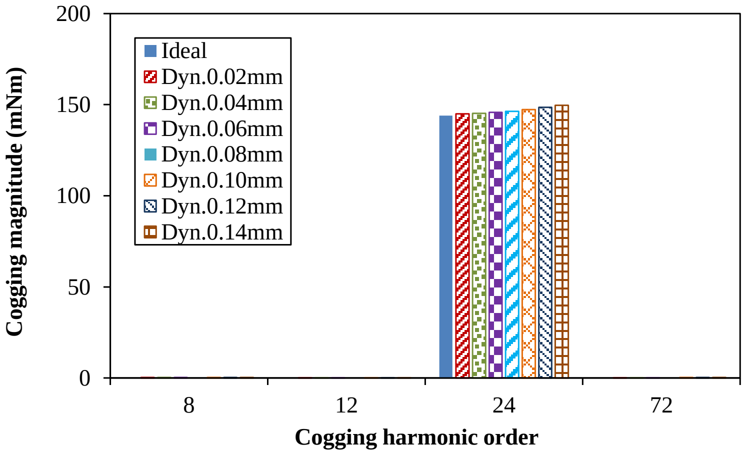

(c) Harmonics

Fig. 3.9 Cogging torque with dynamic eccentricity considered (without skewing).

According to the analyses, it can be deduced that the 12-slot/8-pole IPM machine model is not very sensitive to the assembling eccentricities and no obvious additional cogging torque harmonics are introduced. In the following chapter, the influence will also be compared between different IPM designs in order to evaluate the sensitivity.

3.4 Stator Out-of-Roundness

Due to the convenient winding fabrication, the modular stator techniques are increasingly used in fractional-slot PM machines. However, the corresponding issues would be caused by these tooth segments, e.g. the tooth-bulges by undesirably assembled tooth segments, as shown in Fig. 3.10 (marked by red line). In this part, the influence of non-ideal stator out-of-roundness caused by tooth-bulges will be investigated.

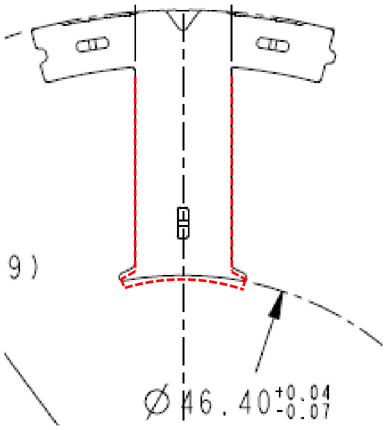

Fig. 3.10 Non-ideal stator out-of-roundness caused by tooth-bulge.

Similar to the analyses of PM diversity, it can also be deduced that the 8th order of cogging torque component will be motivated by the stator tooth-bulges, and the corresponding cogging torque vector diagram is obtained, as shown in Fig. 3.11. As can be seen, when tooth-bulges exist in the 1st, the 4th, the 7th, and the 10th teeth (4 symmetrically distributed tooth-bulges belonging to the same phase), the 8th order of cogging torque will have the highest magnitude.

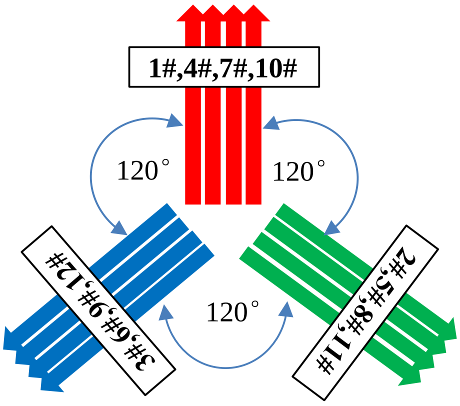

Fig. 3.11 Cogging torque vectors motivated by tooth-bulges in 12-slot/8-pole machine.

In order to verify the vector diagram described in Fig. 3.11, the influence of different numbers of tooth-bulges on cogging torque is investigated, with the bulge distances changing from 0.01mm to 0.03mm.

A. One tooth-bulge

First, as shown in Fig. 3.12(a), one tooth-bulge is analyzed, with the corresponding cogging torque and harmonics shown in Figs. 3.12(b) and (c). It can be seen that the 8th order of cogging torque is produced, in addition to the original 72nd order (which cannot be eliminated by the 3-step-skewing rotor). When the bulge distance changes from 0.01mm to 0.03mm, the 8th order of cogging torque increases from 2.8mNm to 7.95mNm, even with the skewing rotor employed.

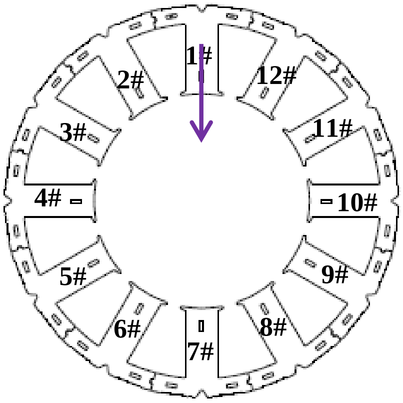

(a) One tooth-bulge

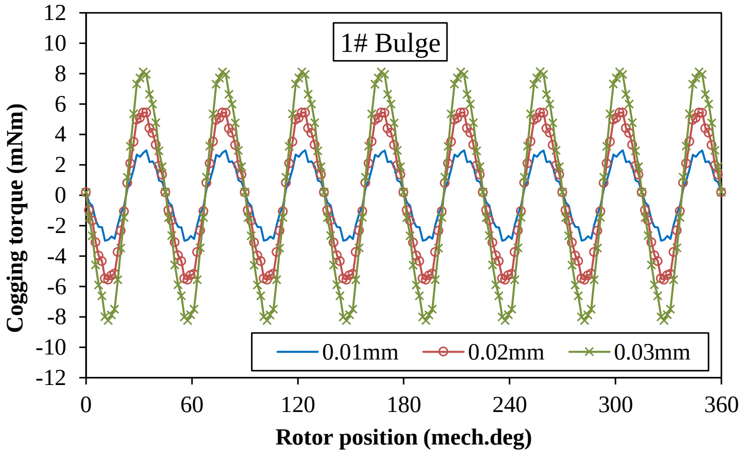

(b) Waveforms (with skewing)

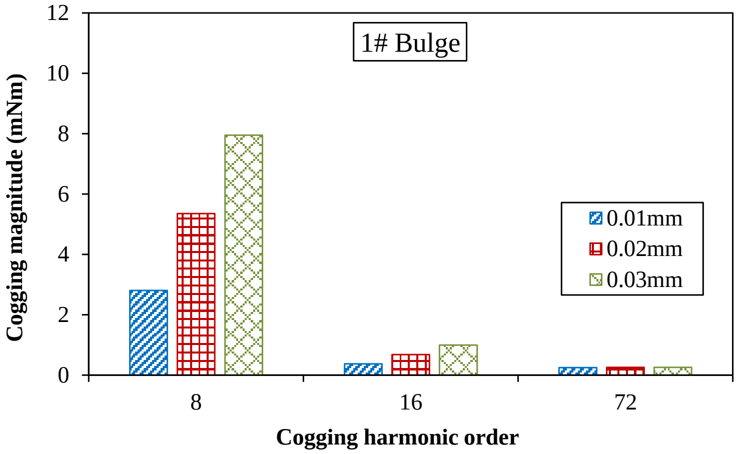

(c) Harmonics (with skewing)

Fig. 3.12 Cogging torque with one tooth-bulge considered.

B. Two sensitive tooth-bulges (opposite or perpendicular)

When two tooth-bulges (opposite or perpendicular, Fig. 3.13 (a)) occur, the cogging torque performance is obtained, as shown in Figs. 3.13 (b) and (c). It can be seen that the 8th order of cogging torque increases from 5.33mNm to 15.6mNm when the bulge distance changes from 0.01mm to 0.03mm, which proves to be twice of the cogging torque with one tooth-bulge.

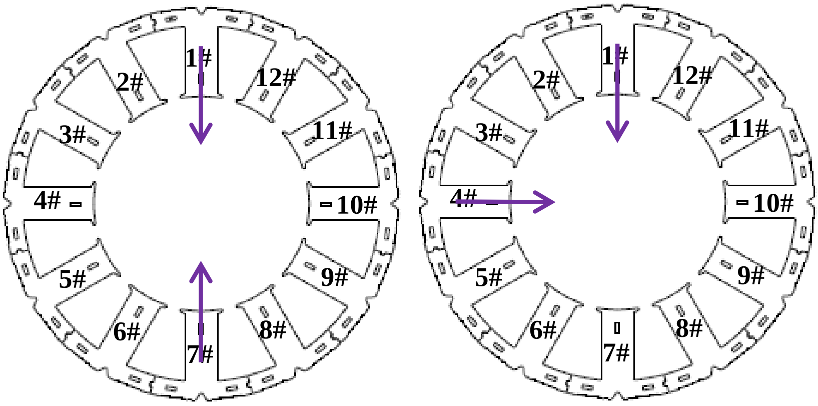

(a) Two sensitive tooth-bulges

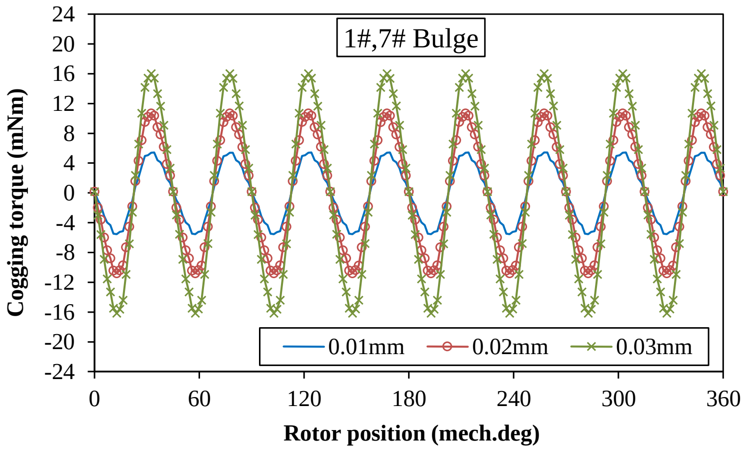

(b) Waveforms (with skewing)

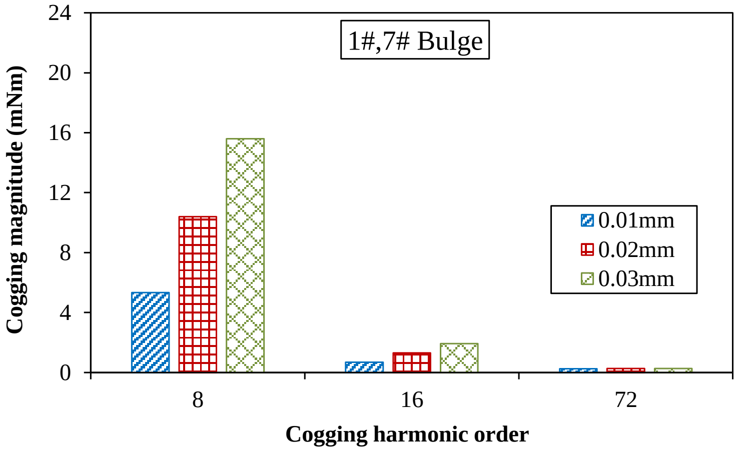

(c) Harmonics (with skewing)

Fig. 3.13 Cogging torque with two sensitive tooth-bulges considered.

C. Three sensitive tooth-bulges (two opposite and one perpendicular)

With three sensitive tooth-bulges (two opposite and one perpendicular, shown in Fig. 3.14(a)) considered, much higher cogging torque is generated, as shown in Figs. 3.14 (b) and (c). It can be seen that the 8th order of cogging torque component increases from 7.86mNm to 23.2mNm, nearly three times of that with one tooth-bulge.

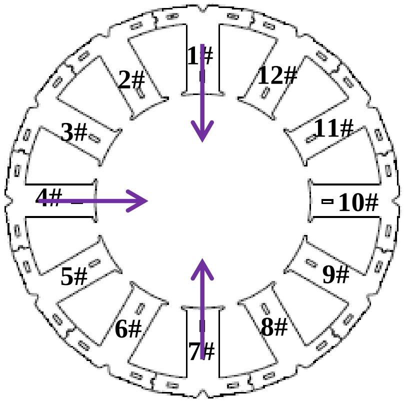

(a) Three sensitive tooth-bulges

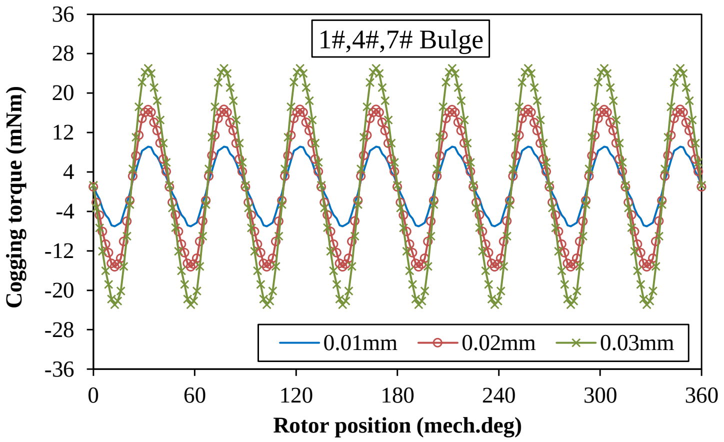

(b) Waveforms (with skewing)

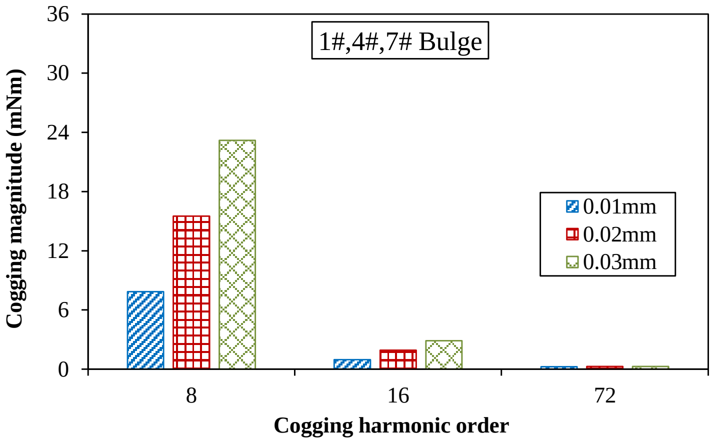

(c) Harmonics (with skewing)

Fig. 3.14 Cogging torque with three sensitive tooth-bulges considered.

D. Four sensitive tooth-bulges (symmetrically distributed on stator circumference)

As the most sensitive distribution, four symmetrically distributed tooth-bulges on stator circumference are analyzed, which significantly increase the cogging torque, as shown in Fig. 3.15. It can be seen that the 8th order of cogging torque increases to 30.9mNm with the 0.03mm of bulge distance considered, almost four times of that with one tooth-bulge.

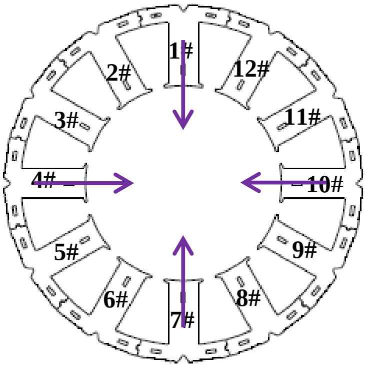

(a) Four sensitive tooth-bulges

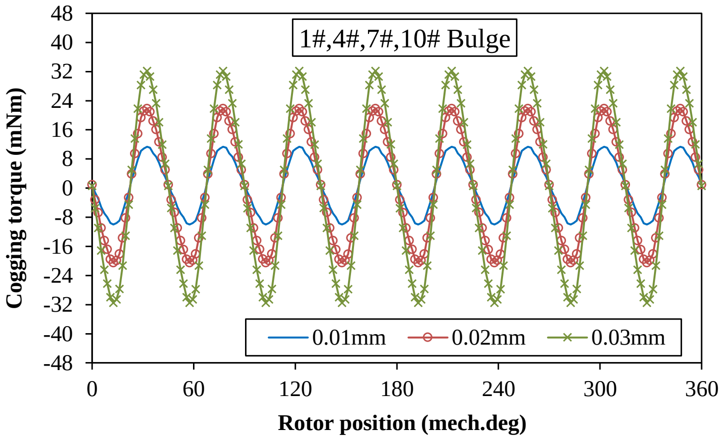

(b) Waveform (with skewing)

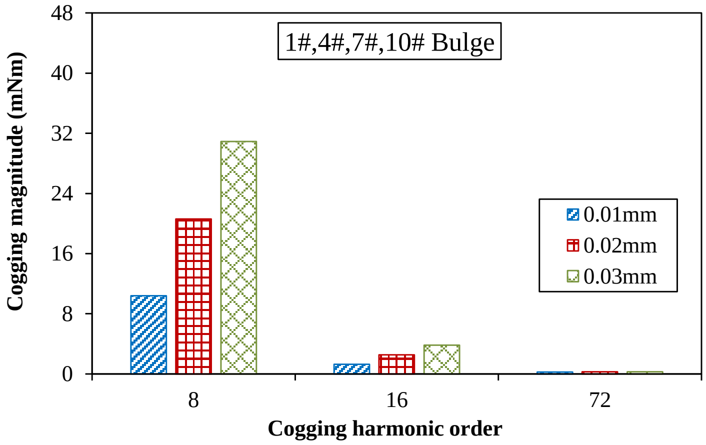

(c) Harmonics (with skewing)

Fig. 3.15 Cogging torque with four sensitive tooth-bulges considered.

The influence of tooth-bulges on cogging torque performance has been investigated, and it can be found that non-ideal stator out-of-roundness significantly deteriorates the cogging torque and introduces the 8^{th} order of cogging torque in the 12-slot/8-pole IPM design, which also verifies the vector diagram shown in Fig. 3.11. Based on the analyses, the four symmetrically distributed tooth-bulges belonging to the same phase prove to be the worst case of non-ideal stator out-of-roundness.

Due to the sensitive influence, it is proposed that the stator roundness should be strictly guaranteed, especially the following distributions of tooth-bulges during the assembling of modular stator segments for the 12-slot/8-pole machine:

(1) Two opposite or perpendicular tooth-bulges;

(2) Two opposite and one perpendicular tooth-bulges;

(3) Four symmetrically distributed tooth-bulges.

3.5 Skewing Angles Tolerances

For the 12-slot/8-pole machine, the 24th order is the fundamental component of cogging torque, which can be theoretically eliminated by 3-step-skewing rotor (skewed by +5 °, 0 °and -5 °, as shown in Fig. 3.16). However, during the manufacturing process, tolerances are usually introduced for the step skewing angles (due to the fit tolerances between the positioning holes and stakes). Therefore, it is necessary to investigate the influence of non-ideal skewing angles on cogging torque. Distinguished from the analyses on axial flux interaction, the 2D FE method is employed in this part and the cogging torque is obtained by superposition of the results due to different rotor steps, with three different cases considered respectively.

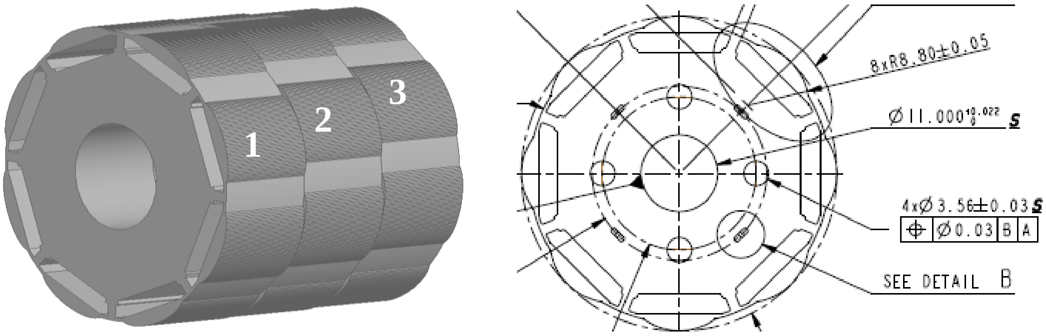

Fig. 3.16 3-step-skewing rotor.

A. Two side steps with identical tolerances

For the first case, the two side steps are skewed by identical angle tolerances. As can be seen from Fig. 3.17, the 24th order of cogging torque increases from 0.5mNm to 7.63mNm when the skewing angle tolerance changes from 0 °to -0.2 °. Similarly, when the angle tolerance changes to 0.2 °, the corresponding cogging torque increases to 7.0mNm.

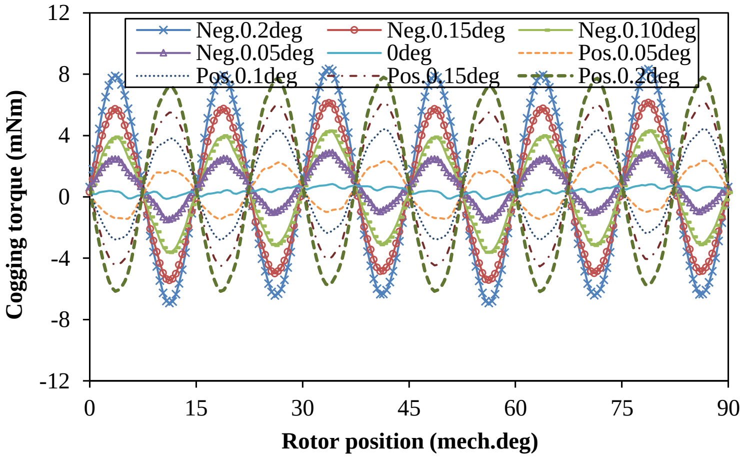

(a) Waveforms (1/4 revolution)

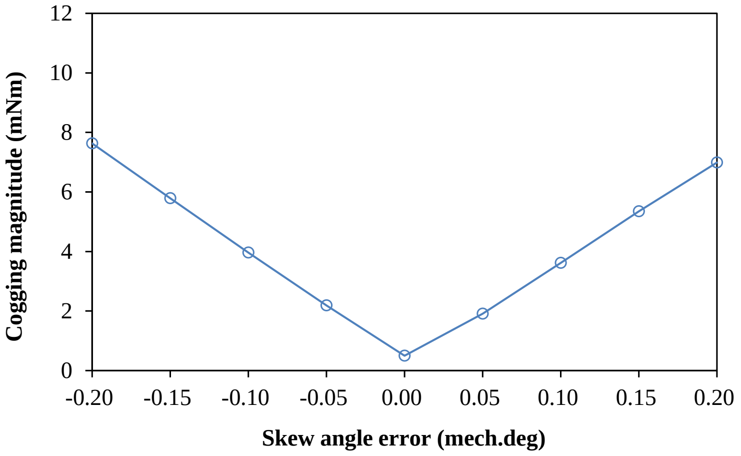

(b) Magnitudes

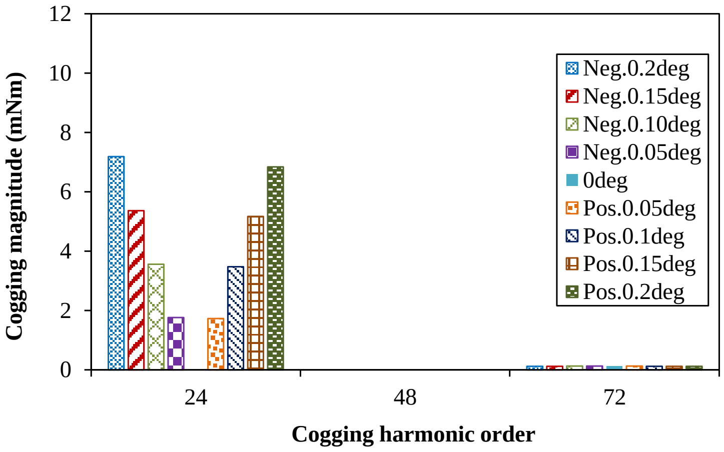

(c) Harmonics

Fig. 3.17 Cogging torque caused by non-ideal skewing angles (two side steps with identical tolerances).

B. One side step precisely skewed and the other with tolerances

Secondly, one side step is assumed to be precisely skewed, and -0.2°~0.2° tolerances are introduced to the skewing angle of the other side step. Fig. 3.18 illustrates the cogging torque performance with the angle tolerances considered. It can be seen that the magnitude of the 24th order increases to 4.38mNm when one side step is skewed with tolerances of ±0.2°. Compared with the first case, the 24th order of cogging torque is relatively lower.

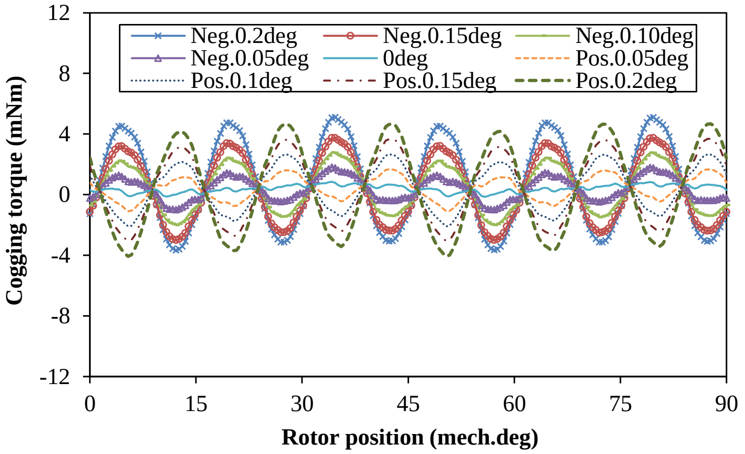

(a) Waveforms (1/4 revolution)

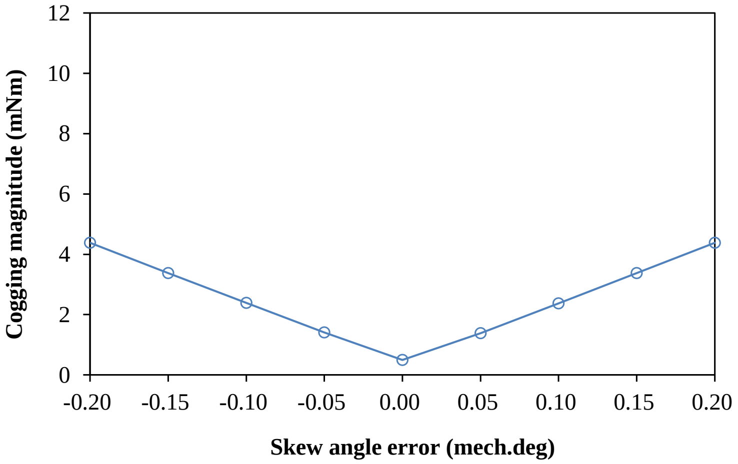

(b) Magnitudes

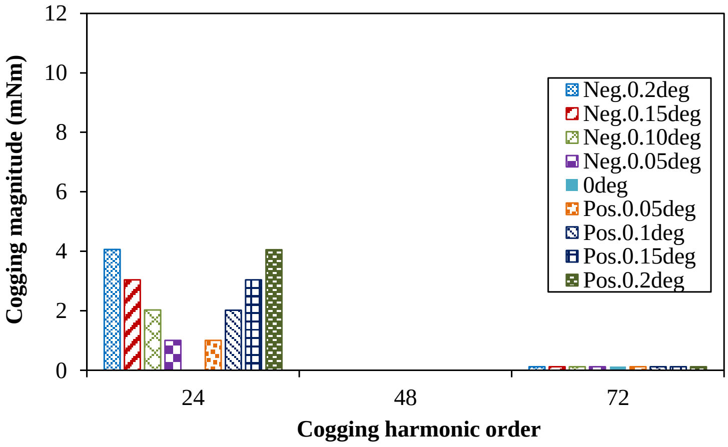

(c) Harmonics

Fig. 3.18 Cogging torque caused by non-ideal skewing angles (one side step without tolerances).

C. One side step with maximum tolerance and the other with different tolerances

The third case refers to that one side step is skewed with maximum tolerance (+0.2 °), and the influence of the skewing angle tolerance with the other side step is investigated. As can be seen from Fig. 3.19, the 24th order of cogging torque increases from 4.0mNm to 7.0mNm. This analysis also indicates that the two side steps should be skewed by adverse tolerances, through which the influence of skewing tolerances could be reduced.

By using the 2D FE method, the influence of skewing angle tolerances on cogging torque has been investigated without considering the axial flux interaction between rotor steps. Compared with the cogging torque shown in Fig. 2.8, it can be found that the 3D effect contributes to a major value of residual cogging torque (the 24th) whilst the skewing angle tolerances introduce minor influence.

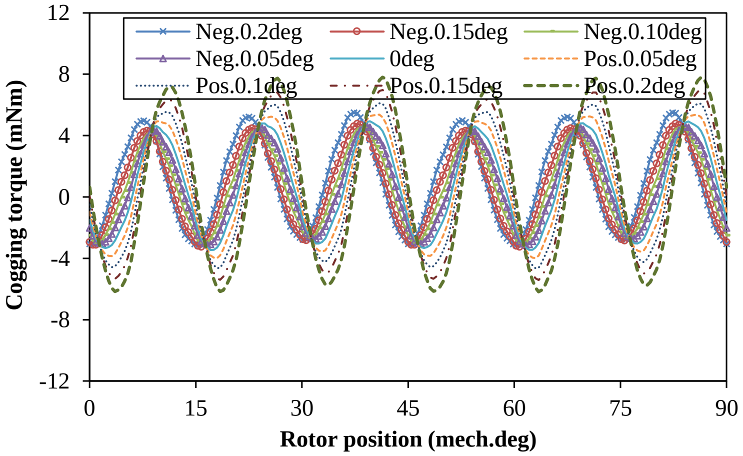

(a) Waveforms (1/4 revolution)

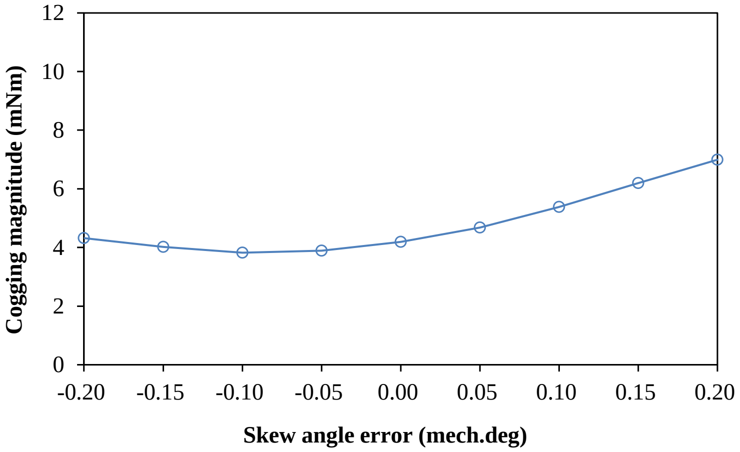

(b) Magnitudes

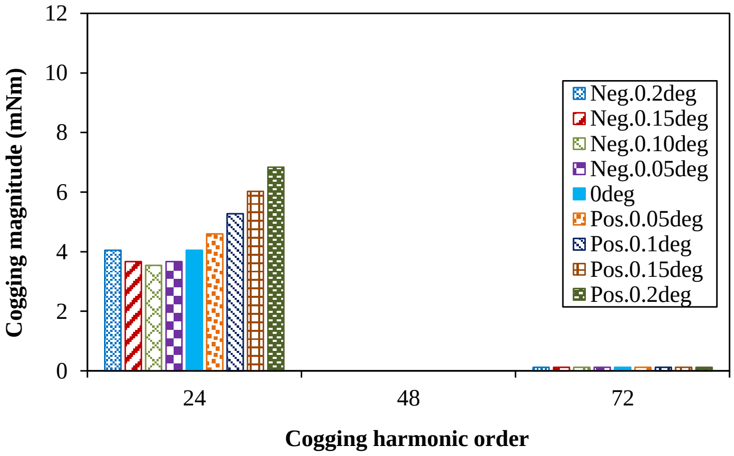

(c) Harmonics

Fig. 3.19 Cogging torque caused by non-ideal skewing angles (one side step with max. tolerances).

3.6 Conclusion

In this chapter, the influence of different types of manufacturing tolerances on cogging torque has been investigated for the 12-slot/8-pole IPM machine, including the PM diversity, the assembling eccentricity, the stator out-of-roundness and the non-ideal skewing angles. It can be found that the 8th and the 12th orders of additional cogging torque harmonics would be introduced respectively when stator tooth-bulges and PM diversity (uneven PM remanence, unequal PM thickness) occur, which also verifies the origins of cogging torque harmonics in the prototypes shown in Chapter 2. Moreover, it is proposed that the symmetrical distributions of stator tooth-bulges (belonging to the same phase) and the consequent distributions of non-ideal PMs should be avoided during the manufacturing process in order not to significantly deteriorate the cogging torque. Furthermore, when the rotor steps are not precisely skewed, the 24th order of cogging torque cannot be eliminated, and it is proposed that the two side steps should be skewed by adverse tolerances, through which the influence can be reduced. In addition, the 12-slot/8-pole design proves to be not very sensitive to the assembling eccentricities, which should also be compared with other machine configurations.

The influence of slot/pole number combinations and rotor contour designs on the cogging torque will be investigated in Chapter 4, together with prototypes and tests. In addition to the cogging torque, the influence of manufacturing tolerances on other key electromagnetic performance, i.e. the back EMF and the on-load torque, will also be analyzed and compared in Chapter 4.

CHAPTER 4 SENSITIVITY OF MANUFACTURING TOLERANCES ON ELECTROMAGNETIC PERFORMANCE IN DIFFERENT INTERIOR PERMANENT MAGNET MACHINES

4.1 Introduction

The influence of manufacturing tolerances on cogging torque has been investigated in Chapter 3 based on the 12-slot/8-pole IPM machine by eccentric rotor contour. In addition to the foregoing design, various IPM machines have been employed in industrial applications. However, different machine configurations may exhibit different sensitivities to these manufacturing tolerances. Therefore, it is necessary to investigate and compare the specific influence, as a reference for selecting proper designs for applications with strict requirements on cogging torque. Before the analyses, several basic IPM machine designs are presented, i.e. designs by different rotor contours and different slot/pole combinations.

A. Designs by Different Rotor Contours

Different from the aforementioned eccentric design, the sinusoidal rotor contour is also frequently employed, of which the pole shoe is formed by an inverse cosine function, as shown in Fig. 4.1 (b).

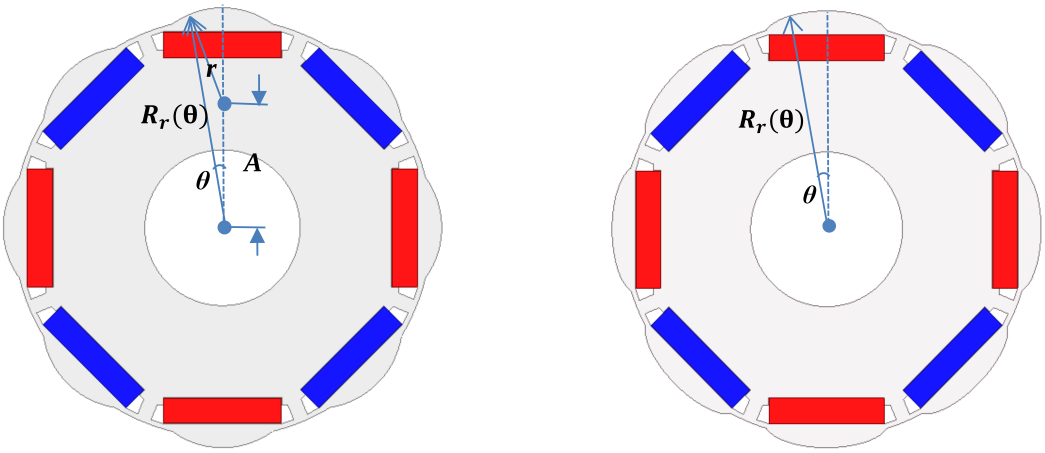

(a) Eccentric design

(b) Sinusoidal design

Fig. 4.1 12-slot/8-pole designs by different rotor contours (stator not shown) [EVA10].

Usually, the minimum air-gap length is defined, and the outer radius of the rotor pole shoe can be expressed by:

$$R_r(\theta) = R_s - \frac{\delta_{min}}{\cos(p\theta)} \quad \left(-\frac{\pi}{2p} < \theta < \frac{\pi}{2p}\right) \tag{4. 1}$$

where R_s and δ_{min} represent the stator inner radius and the minimum air-gap length respectively, p is the number of pole pairs. It can be seen that the rotor pole shoe of sinusoidal design is defined by the minimum and maximum (corresponds to maximum θ) air-gap lengths.

According to the basic parameters shown in Table 2.1, two 12-slot/8-pole IPM machine models by the same stator are established using the different rotor contours. For comparison, the minimum and maximum air-gap lengths, PM dimensions and locations, as well as the PM grooves remain the same and unchanged in the two machine models, as shown in Fig. 4.2.

As fundamental machine performance, the back EMF and the rated torque of the two designs are firstly illustrated, as shown in Fig. 4.3. It can be seen that the design by the sinusoidal rotor contour produces a little higher average torque than the eccentric design – 4.62Nm and 4.51Nm respectively, whilst the torque ripple obviously decreases from 10.8% to 5.9% with the sinusoidal design employed.

Without the manufacturing tolerances considered, the cogging torques of the two ideal models are obtained by employing the 2D FE method, as shown in Fig. 4.4. It can be seen that obviously different cogging torques are produced by the two IPM designs. For the eccentric design, the 24th order of cogging torque is introduced, the magnitude of which is as high as 144mNm. With the sinusoidal design employed, the 24th order of cogging torque is significantly reduced to 4.8mNm, whilst 9.6mNm of the 48th cogging torque is produced. However, both the 24th and the 48th cogging torque components in the two 12-slot/8-pole IPM machines can be theoretically eliminated by a step-skewing approach, e.g. a 3-step-skewing rotor by skewing ±5°. As shown in Fig. 4.4 (b), favorable cogging torque performance can be achieved by both of the two rotor designs with the step-skewing approach employed.

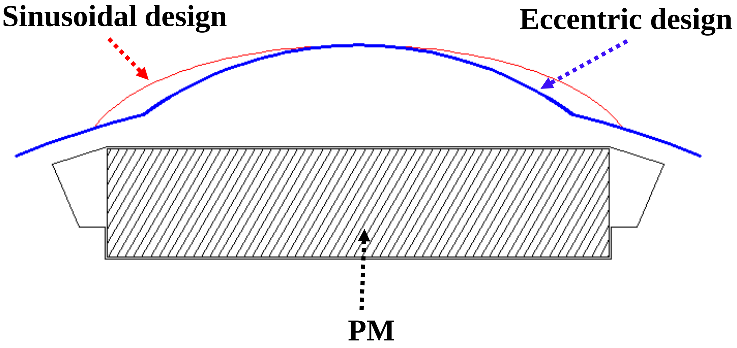

Fig. 4.2 Comparison of rotor laminations between eccentric and sinusoidal designs.

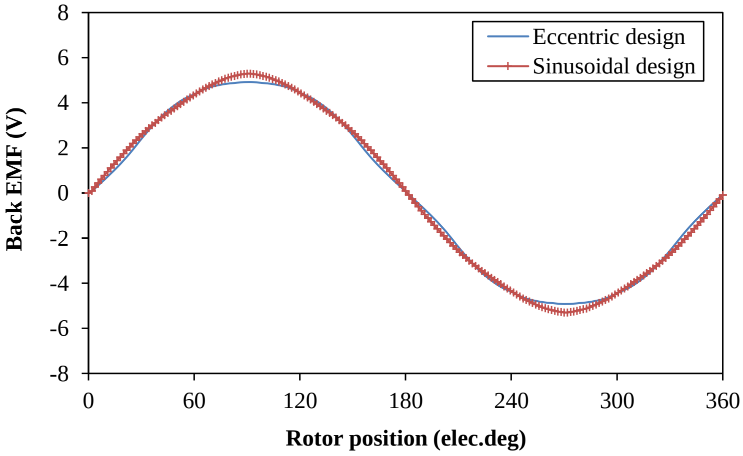

(a) Back EMF (1500rpm)

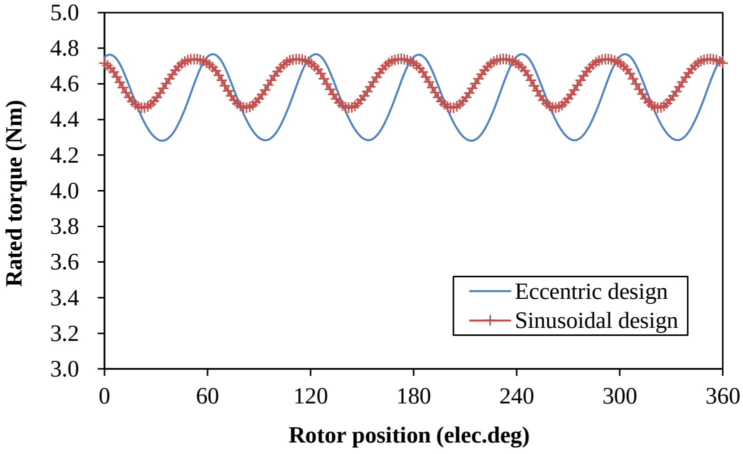

(b) On-load torque (95A, I_d=0)

Fig. 4.3 Comparison of electromagnetic performance of 12-slot/8-pole designs with different rotor contours (without skewing).

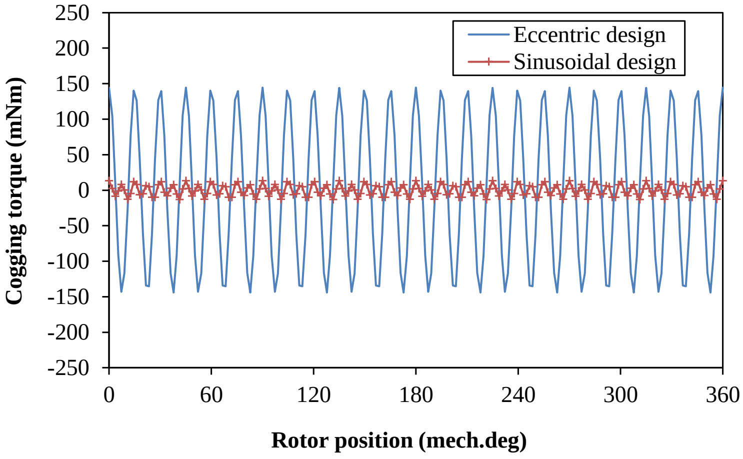

(a) Waveforms

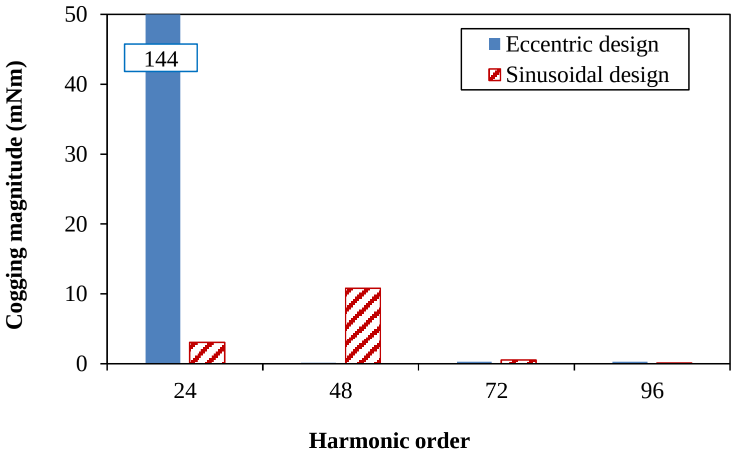

(b) Harmonics

Fig. 4.4 Comparison of cogging torque of 12-slot/8-pole designs with different rotor contours (without skewing).

B. Designs by Different Slot/Pole Combinations

In addition to the 12-slot/8-pole design, another conventional PM machine configuration is the 12-slot/10-pole machines, which have become strong candidates for many industrial applications [ISH06], [LI14], [RED12], e.g. the servo motor, the EPS motor, etc. Similar to the foregoing 12-slot/8-pole design, a 12-slot/10-pole machine model using the eccentric rotor contour is established, as shown in Fig. 4.5 (b). For comparison, the PM consumption (PM length and depth unchanged, PM width decreased by 8/10), the maximum and minimum air-gap lengths and the eccentric distance (*A*) remain the same and unchanged at the first step. As an extension, the influence of eccentric distance will be investigated and compared between the two slot/pole combinations considering those sensitive cases of manufacturing tolerances.

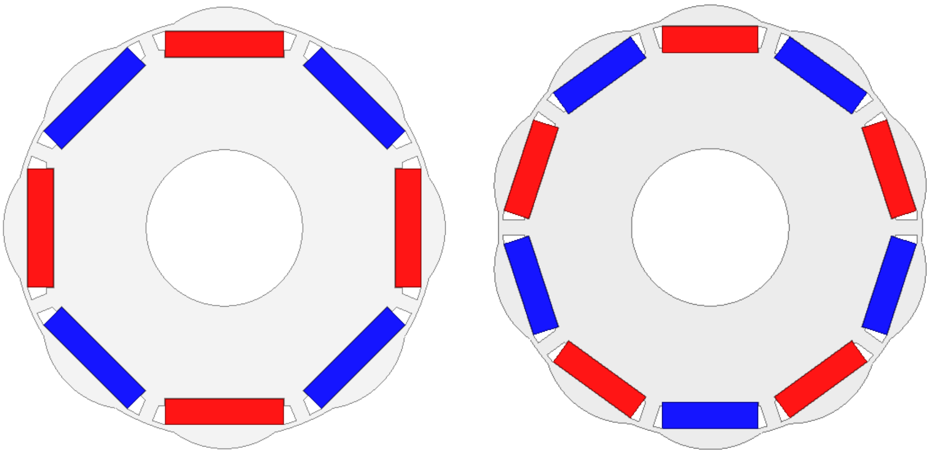

(a) 12-slot/8-pole (b) 12-slot/10-pole

Fig. 4.5 Eccentric designs by different slot/pole combinations (identical stator, not shown).

First, the back EMF and the rated torque of the two machine designs by conventional windings are obtained, as shown in Fig. 4.6. It can be seen that the average torque of the 10-pole machine is a little lower than that of the 8-pole design – 4.40Nm and 4.51Nm respectively, which is mainly due to the more leakage flux in the 10-pole rotor. However, the torque ripple can be significantly reduced by the 10-pole machine, decreasing from 10.8% to 1.5%.

Moreover, comparison of the cogging torque performance is also carried out between the two designs, as shown in Fig. 4.7. It can be seen that the cogging torque can be significantly reduced from 144mNm to very low extent with the 10-pole design employed, even without the need of skewing. However, it should be noted that the results shown in Fig. 4.7 is obtained under ideal conditions and the influence of manufacturing tolerances should be further investigated and compared between the two different slot/pole combinations.

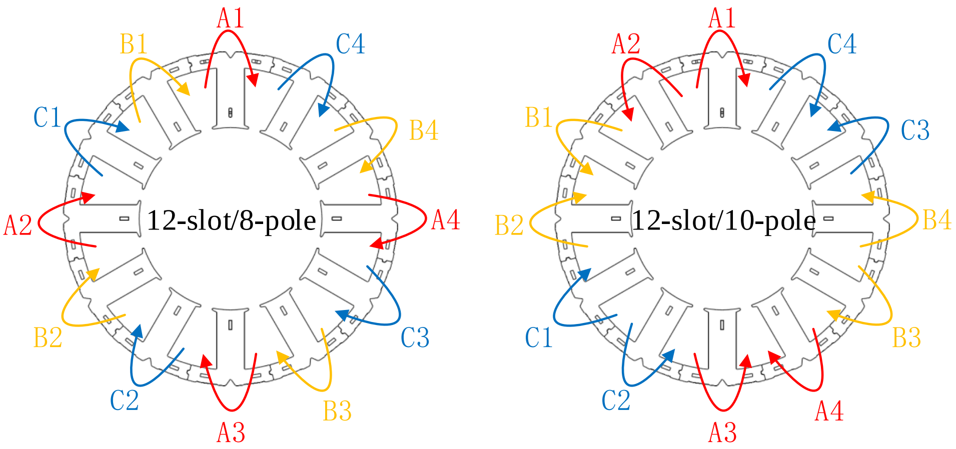

(a) Winding distribution

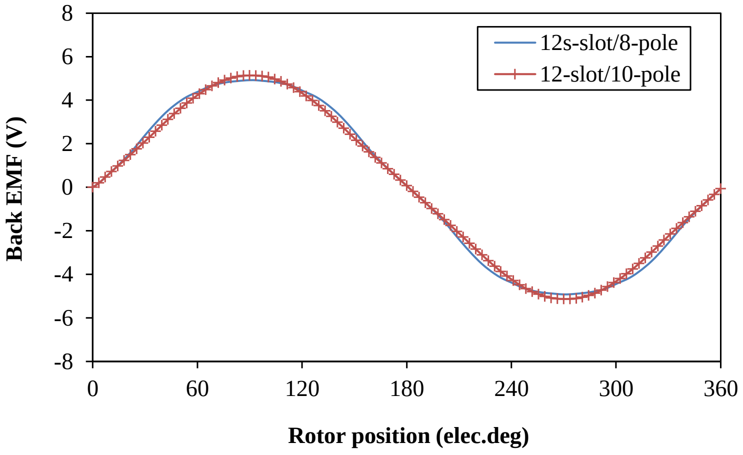

(b) Back EMF (1500rpm)

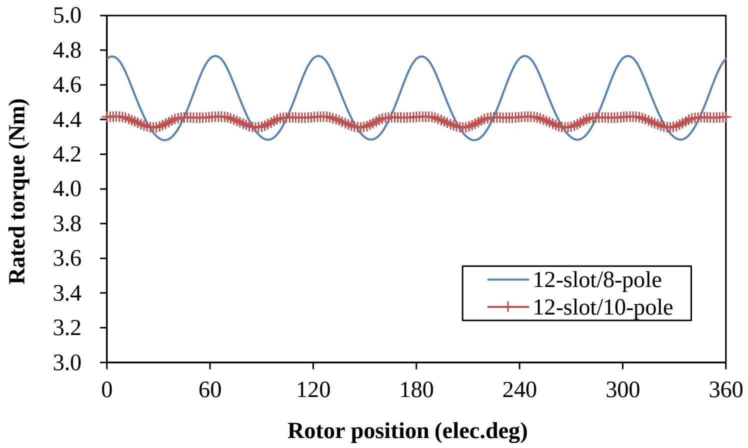

(c) On-load torque (95A, I_d=0)

Fig. 4.6 Comparison of electromagnetic performance between 12-slot/8-pole and 12-slot/10-pole designs (without skewing).

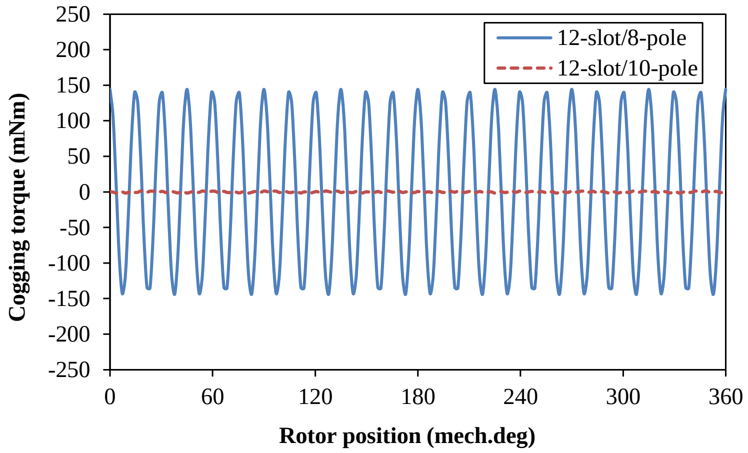

(a) Waveforms

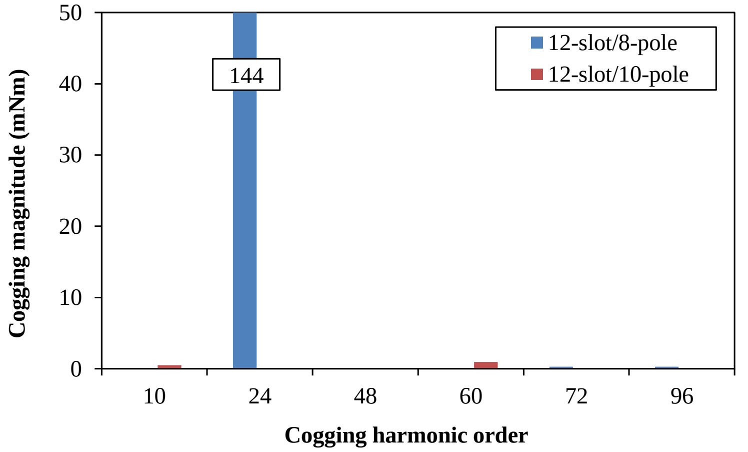

(b) Harmonics

Fig. 4.7 Comparison of cogging torque between 12-slot/8-pole and 12-slot/10-pole designs (without skewing).

4.2 Analyses of IPM Machines with Different Rotor Contours

The cogging torques of the two 12-slot/8-pole IPM designs by eccentric and sinusoidal rotor contours have been investigated under ideal conditions, which indicate that both of the two designs can reduce the cogging torques to very low extent by conventional skewing. In this section, the influence of manufacturing tolerances on cogging torques of the two designs is further investigated and compared, especially on lower orders of additional cogging torque components. Before the comparison, the cogging torque of the sinusoidal design is firstly analysed with the aforementioned tolerances considered, similar to the analyses of the eccentric design in Chapter 3. In addition, the FE analyses of PM diversity, assembling eccentricity and stator out-of-roundness are carried out without the skewing approach, in order to exclude the skewing effect.

4.2.1 Sinusoidal Design

A. PM Diversity (ideal PM: B_r=1.32T, non-ideal PM: B_r=1.42T)

As the most sensitive case of PM diversity in 12-slot/8-pole machines, the consequent distributions of non-ideal PMs are investigated for the sinusoidal design, and Fig. 4.8 illustrates the corresponding cogging torques with different numbers of non-ideal PMs (i.e. one, two, three and four) considered. It can be seen that the 12th order of cogging torques are introduced – 3.34mNm, 6.48mNm, 9.47mNm and 12.3mNm respectively, and the maximum value is 12.3mNm with four non-ideal PMs considered. In addition, the quantitative relation of the 12th cogging torques between cases by different numbers of non-ideal PMs also verifies the vector diagram shown in Fig. 3.5.

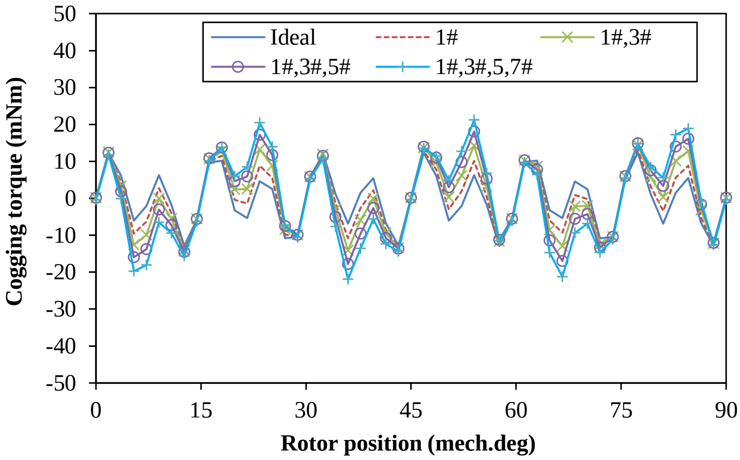

(a) Waveforms (1/4 revolution)

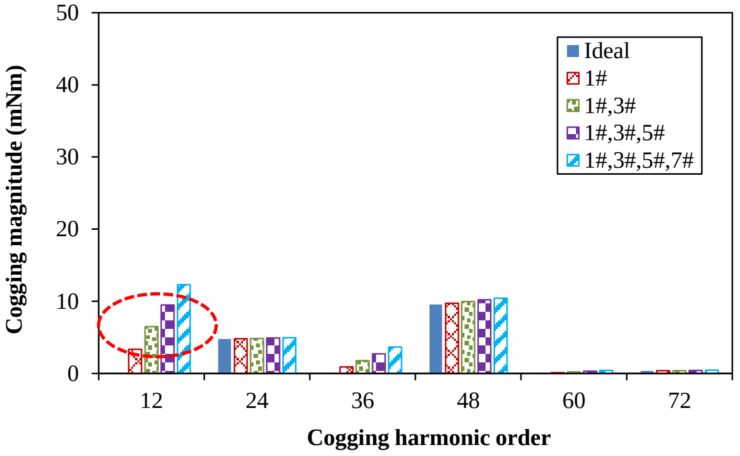

(b) Harmonics

Fig. 4.8 Cogging torque performance of sinusoidal design with PM diversity (uneven PM remanence) considered (without skewing).

B. Assembling Eccentricities

Considering the inevitable assembling eccentricities, it is also necessary to investigate the specific influence on cogging torque performance, including the static and the dynamic cases. As shown in Fig. 4.9 and Fig. 4.10, the influence of static and dynamic eccentricities in the sinusoidal design is obtained. It can be seen that the cogging torque almost remains stable when the eccentricity increases from 0 to 0.14mm, which indicates that the 12-slot/8-pole sinusoidal design is not sensitive to assembling eccentricities.

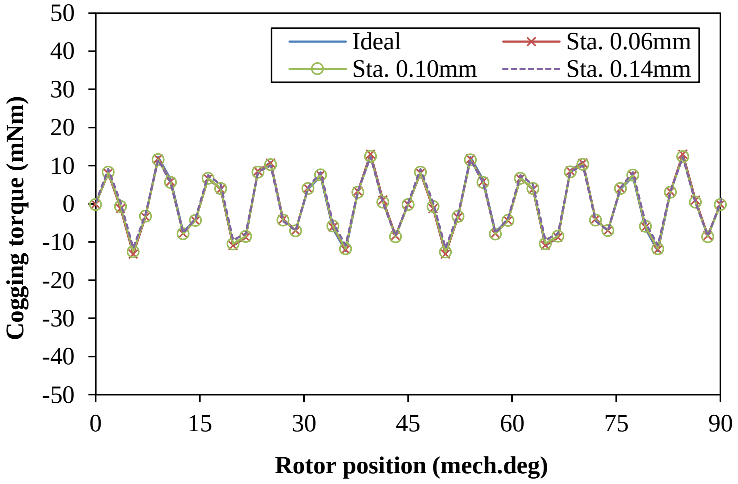

(a) Waveforms (1/4 revolution)

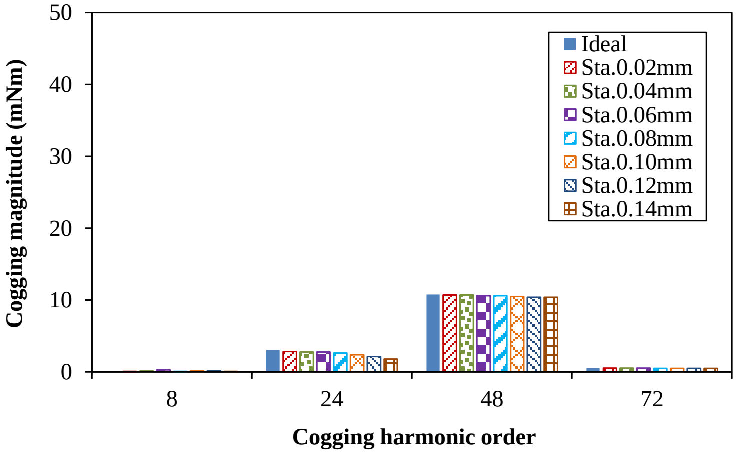

(b) Harmonics

Fig. 4.9 Cogging torque performance of sinusoidal design with static eccentricity considered (without skewing).

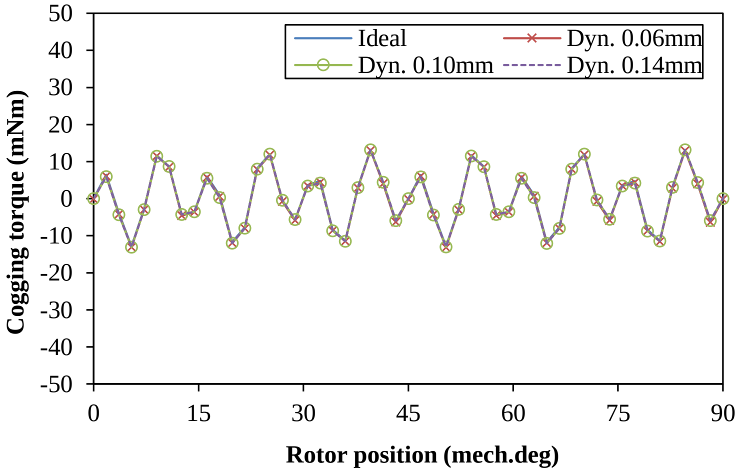

(a) Waveforms (1/4 revolution)

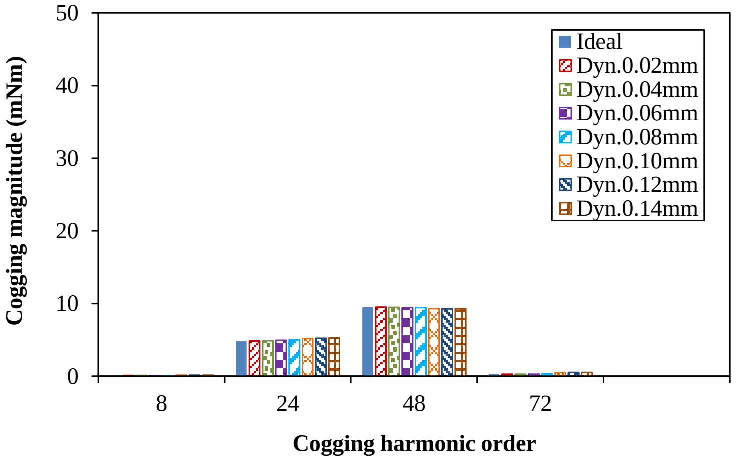

(b) Harmonics

Fig. 4.10 Cogging torque performance of sinusoidal design with dynamic eccentricity considered (without skewing).

C. Stator Out-of-Roundness

For fractional-slot PM machines by the modular stator techniques, it is difficult to guarantee the stator out-of-roundness and tooth-bulges are usually inevitable. As illustrated in Fig. 3.5, the maximum value of the 8th additional cogging torque will be produced in 12-slot/8-pole machines when the four tooth-bulges belonging to the same phase occur. For the sinusoidal design, the cogging torques considering different numbers of tooth-bulges in one phase are illustrated and the magnitudes of the 8th additional components are 5.43mNm, 10.7mNm, 16mNm and 21.2mNm respectively, as shown in Fig. 4.11. Therefore, the 8th order of additional cogging torque in the sinusoidal design will be 21.2mNm with the worst case of tooth-bulges considered.

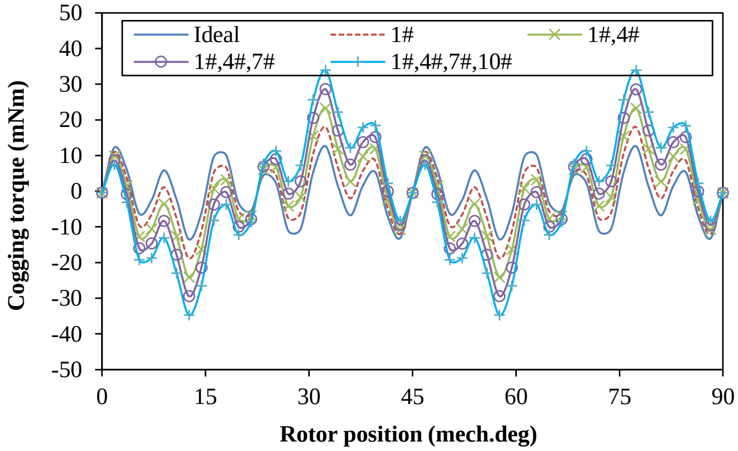

(a) Waveforms

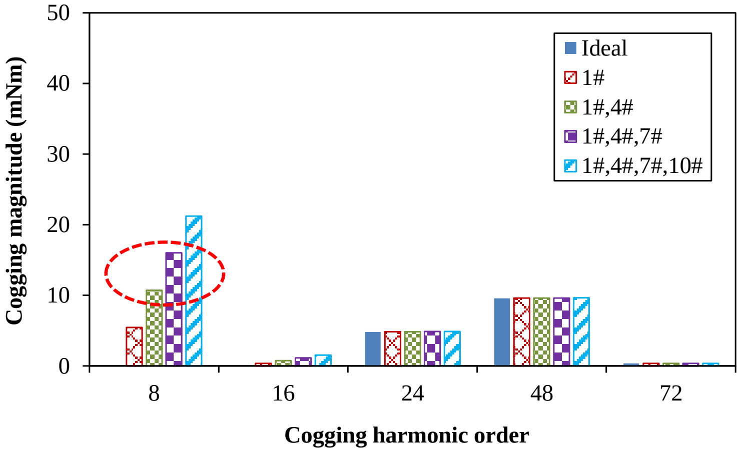

(b) Harmonics

Fig. 4.11 Cogging torque performance of sinusoidal design with stator tooth-bulges (0.02mm tooth-bulges, without skewing).

D. Skewing Angle Tolerances

For the sinusoidal design, the cogging torque can be further reduced by employing the step-skewing approach, e.g. 3-step rotor by skewing $\pm 5^{o}$. During the fabrication the skewing rotor, skewing angle tolerances may exist. Suppose that the two side steps are skewed with identical tolerances, the corresponding cogging torques are obtained, as shown in Fig. 4.12. It can be seen that the fundamental cogging torque (48th) is below 1.2mNm when the skewing angle tolerances changes from -0.2^{o} to 0.2^{o}, which is mainly due to the low original cogging torque. In addition, the 72nd component almost remains stable at 0.5mNm, due to the invalid effect of the 3-step-skewing approach on this harmonics order.

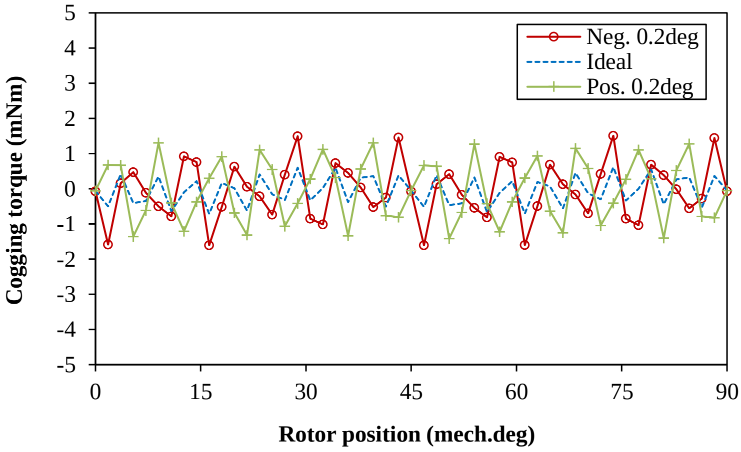

(a) Waveforms

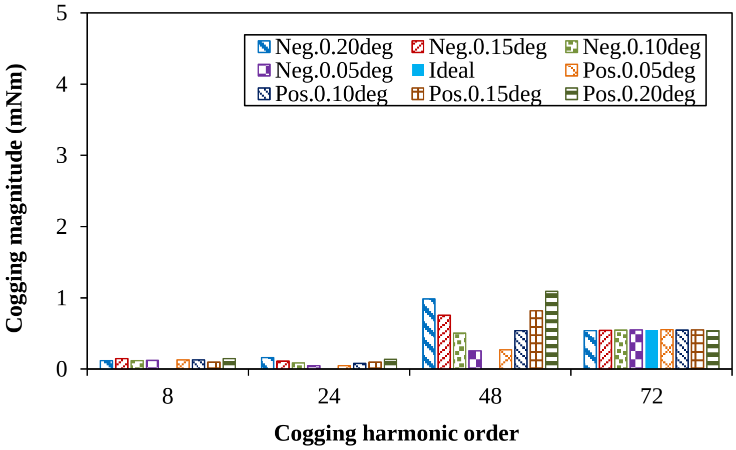

(b) Harmonics

Fig. 4.12 Cogging torque performance of sinusoidal design with skewing angle tolerances considered.

4.2.2 Comparison between Eccentric and Sinusoidal Designs

The influence of manufacturing tolerances on cogging torque has been investigated for the eccentric (Chapter 3) and the sinusoidal designs. In this section, comparison of the influence is carried out in order to illustrate the different sensitivities to manufacturing tolerances between the two different rotor designs.

A. PM Diversity

With the consequent distributions of four non-ideal PMs considered, the cogging torques of the two designs are illustrated, as shown in Fig. 4.13. It can be seen that the 12th order and multiples of cogging torque components are introduced in the two designs. However, the eccentric design produces much higher value of the 12th cogging torque than the sinusoidal design, 27.9mNm and 12.3mNm respectively. In order to guarantee the torque capability, the skewing method by a conventional skewing angle (mech. 15° for 12-slot/8-pole machines) proves to be not so effective in reducing lower orders (e.g. the 12th) of cogging torque harmonics [ZHU12]. Therefore, it can be deduced that the eccentric design usually suffers from a higher value of additional cogging torque activated by PM diversity, even with the skewing method employed.

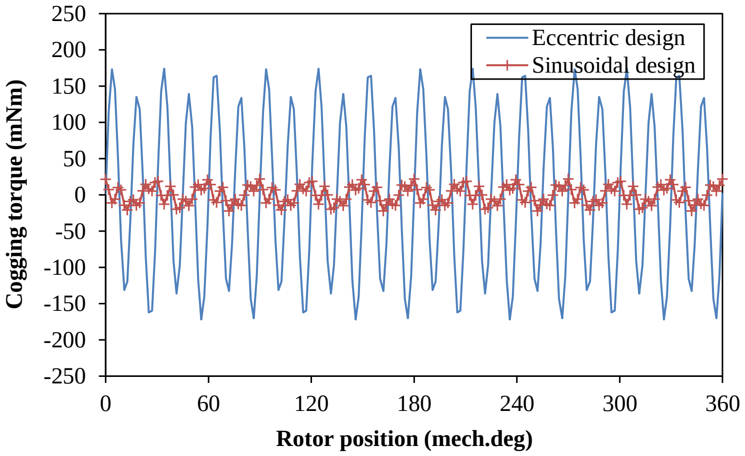

(a) Waveforms

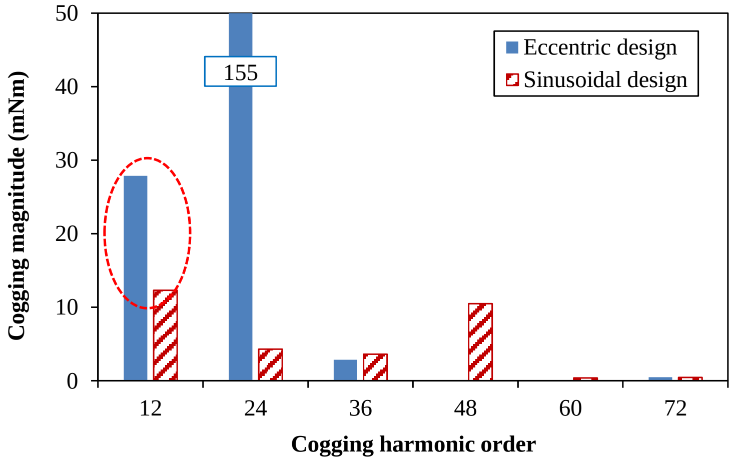

(b) Harmonics

Fig. 4.13 Comparison of cogging torque between eccentric and sinusoidal designs with four consequent-distributed non-ideal PMs (uneven remanence) considered (without skewing).

B. Assembling Eccentricities

Based on the two IPM machine models, the influences of 0.10mm static and dynamic eccentricities have been investigated by FE analyses respectively, with the cogging torque performance shown in Fig. 4.14. It can be seen that no obvious additional cogging torque component is introduced with the assembling eccentricities considered. Therefore, it can be deduced that neither of the eccentric and the sinusoidal designs is sensitive to this tolerance in 12-slot/8-pole PM machines.

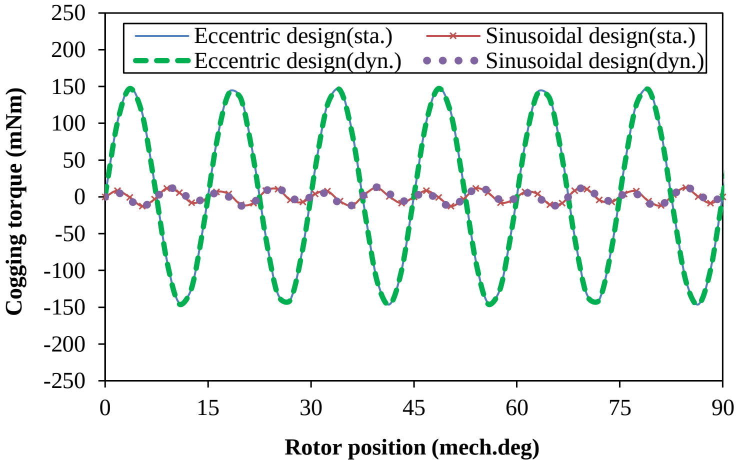

(a) Waveforms (1/4 revolution)

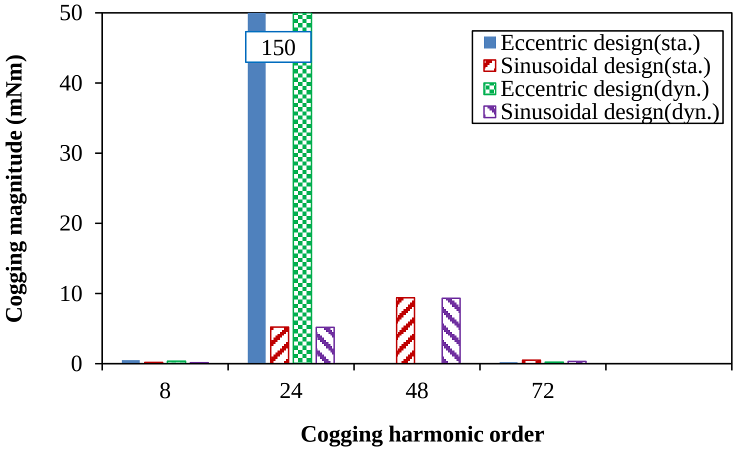

(b) Harmonics

Fig. 4.14 Comparison of cogging torque between eccentric and sinusoidal designs with static and dynamic eccentricities (0.10mm) considered (without skewing).

C. Stator Out-of-Roundness

With four assembling tooth-bulges (0.02mm, belonging to the same phase) considered, the corresponding cogging torques of the two rotor designs are illustrated, as shown in Fig. 4.15. It can be seen that the 8th order of cogging torques are introduced in both of the two designs, the magnitudes of which are 24.4mNm and 21.2mNm respectively. Due to the low harmonic order (the 8th), it is unrealistic to eliminate the component by skewing in a real machine product. Therefore, it can be deduced that both of the two rotor designs are sensitive to the assembling tooth-bulges, especially when four tooth-bulges belonging to the same phase occur. Based on the analyses, it is required that the stator out-of-roundness should be strictly guaranteed in the mass production of fractional-slot machine by modular stator techniques.

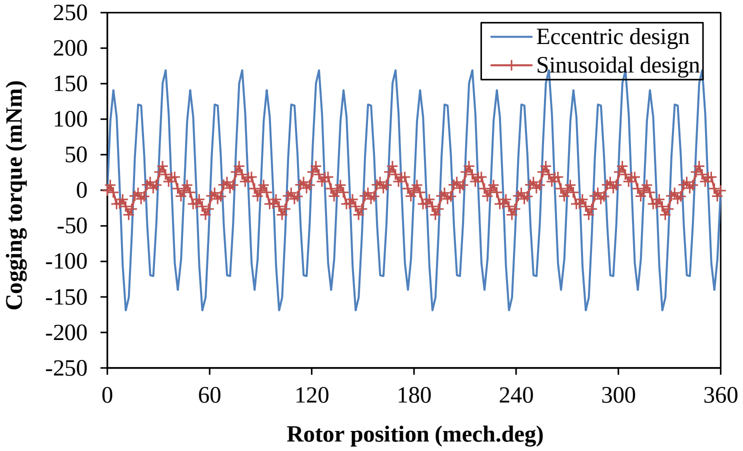

(a) Waveforms

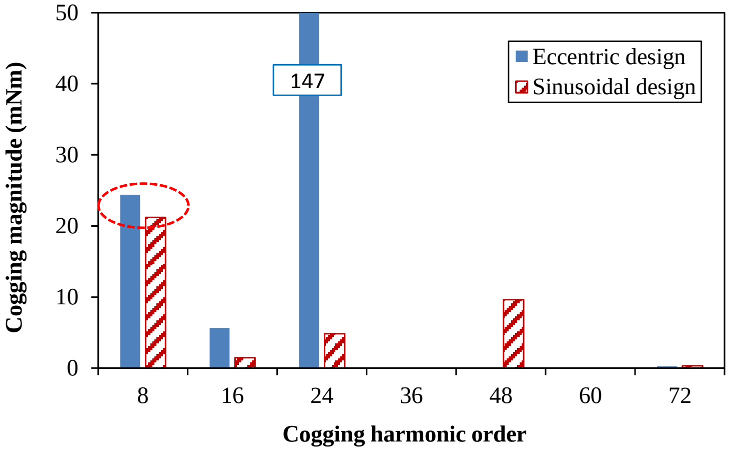

(b) Harmonics

Fig. 4.15 Comparison of cogging torque between eccentric and sinusoidal designs with four tooth-bulges (0.02mm, belonging to the same phase) considered (without skewing).

D. Skewing Angle Tolerances

In order to reduce the cogging torque, the step-skewing methods are frequently employed, e.g. 3-step-skewing rotor. Suppose that the two side steps of the 3-step rotor are skewed by the same tolerances, a comparison of the influence by skewing angle errors is carried out between the eccentric and the sinusoidal designs, as shown in Fig. 4.16. It can be seen from Figs. 4.16 (a) and (b) that the 24th order of residual cogging torque in the eccentric design is 7.7mNm with a -0.2° (actual skewing angle ±4.8°) skewing angle error considered. However, the sinusoidal design suffers from much lower residual cogging torques, even with the same skewing angle tolerance considered. In addition, Fig. 4.16 (c) illustrates the magnitudes of residual cogging torques when the skewing angle error changes in the range of -0.2°~0.2°. It can also be seen that the eccentric design is much more sensitive to the skewing angle error, which is mainly due to the much higher magnitude of the original 24th cogging torque.

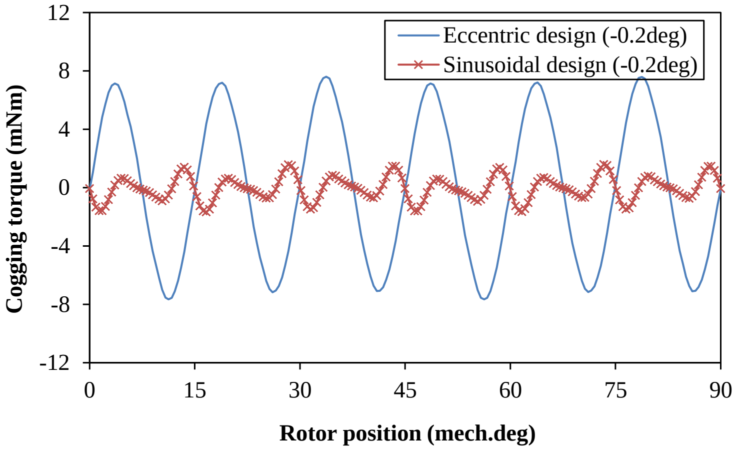

(a) Waveforms (skewing error: -0.2°)

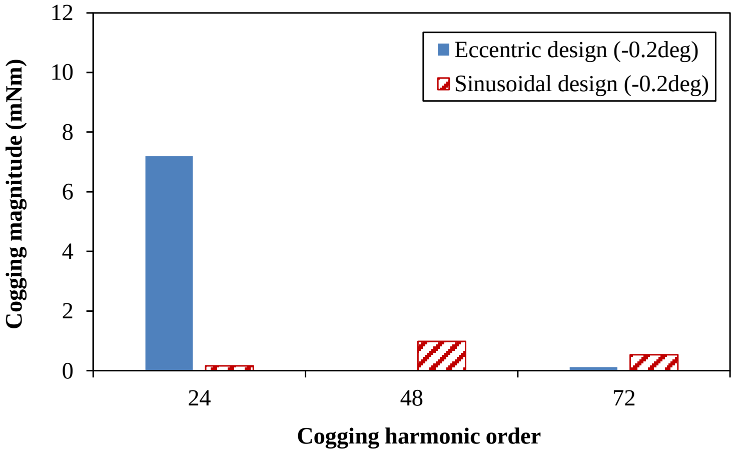

(b) Harmonics

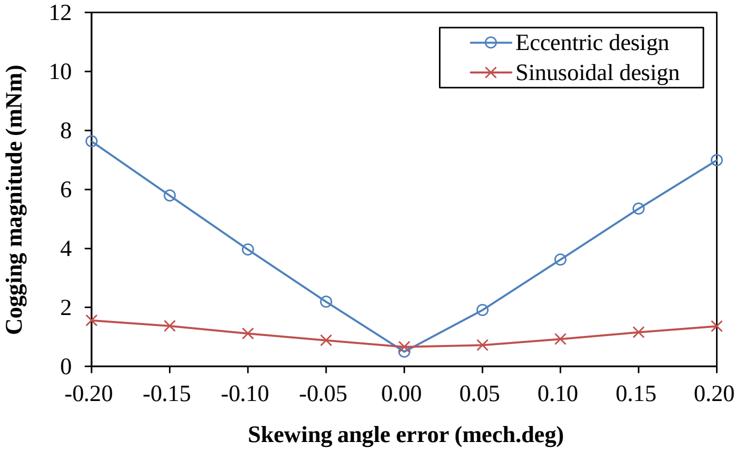

(c) Magnitudes by different skewing angle errors

Fig. 4.16 Comparison of cogging torque between eccentric and sinusoidal designs with skewing angle errors considered.

4.2.3 Verification by Spatial Field Harmonics under Different Conditions

In the foregoing analyses, comparison of the cogging torque performance accounting for the manufacturing tolerances has been carried out between the eccentric and the sinusoidal designs. As the source of cogging torque, the spatial field harmonics in the air-gap will be further investigated and compared to demonstrate the differences between the two rotor designs.

As a basic theory, the cogging torque can be analytically calculated by the Maxwell stress tensor, based on air-gap flux density components [ZHU14]:

$$T_c = \sum_k T_{ck} = (1/\mu_0)\pi L_{ef} {r_\delta}^2 \sum_k B_{rk} B_{tk} \cos(\alpha_{rk} - \alpha_{tk}) \tag{4. 2}$$

where the cogging torque component T_{ck} is produced by the k$^{\text{th}}$ order of radial (B_{rk}) and circumferential (B_{tk}) air-gap flux density components. The symbols of α_{rk} and α_{tk} represent the angles of the two flux density components respectively. L_{ef}, r_δ and μ_0 represent the effective axial length, the air-gap radius and the permeability of vacuum. According to (4.2), it can be found that the cogging torque is only produced by the same orders of radial and circumferential field harmonics. Moreover, the cogging torque magnitude not only depends on the field intensity, but also the phase angle difference between the two flux density components.

It has been found that the eccentric and the sinusoidal designs present obviously different cogging torques, especially when the ideal conditions and the tolerance of PM diversity are considered. Therefore, the corresponding spatial field harmonics will be further investigated and compared considering the two conditions respectively.

A. Spatial Field Harmonics without Manufacturing Tolerances Considered

Without the manufacturing tolerances considered, the radial and circumferential air-gap flux density components (at the relative stator / rotor position where the maximum cogging torque exists) are obtained respectively for the two designs by the FE method, as shown in Fig. 4.17 (a). Based on the waveforms, the spatial field harmonics for the two flux density components can be obtained, with the magnitudes and phase angle differences shown in Figs. 4.17 (b) and (c) respectively. Due to the decreasing magnitudes, higher orders (>44) of harmonics are not shown. It can be seen that both of the radial and circumferential flux density components have 4n (n=1, 2, 3…) orders of spatial harmonics, which are mainly due to the 8-pole PM field modulated by the 12-slot openings.

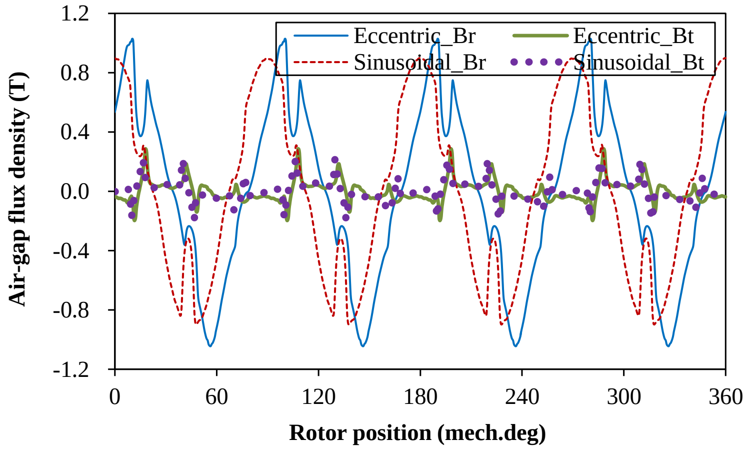

(a) Waveforms

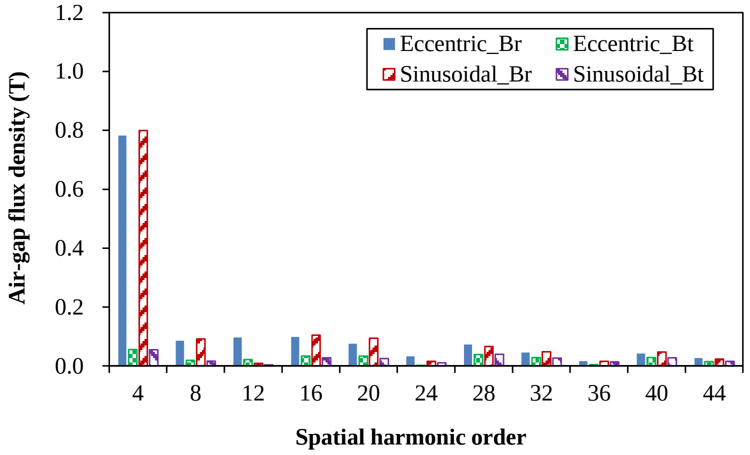

(b) Harmonics

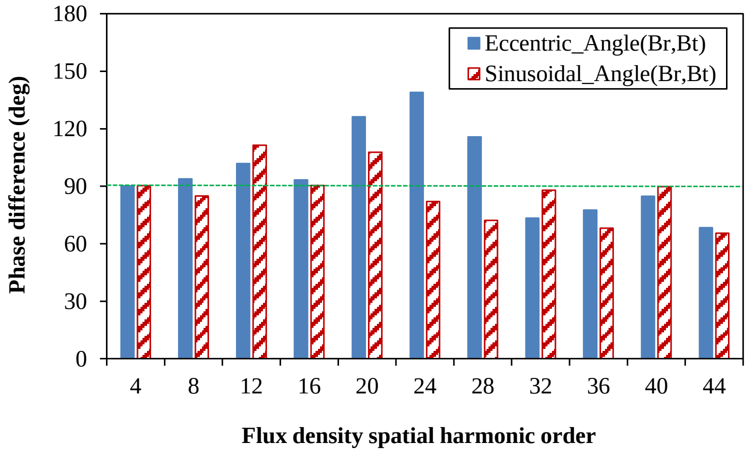

(c) Phase angle difference between radial and circumferential components

Fig. 4.17 Comparison of air-gap flux density between eccentric and sinusoidal designs under ideal conditions.

However, by comparison with the eccentric design, it can be found that higher radial field harmonics are generated by the sinusoidal design whilst its circumferential field harmonics are relatively lower. Moreover, the sinusoidal design establishes more orthogonal radial and circumferential field harmonics, which can be reflected by the phase angle differences shown in Fig. 4.17 (c). By employing (4.2), the cogging torque components produced by these spatial field harmonics can be calculated for the two designs respectively, as shown in Fig. 4.18 (a). It can be seen that the synthetic cogging torque of the eccentric design is much higher than that of the sinusoidal design, which verifies the different cogging torques shown in Fig. 4.4. Furthermore, in order to verify the effectiveness of skewing method, the 3-step-skewing method (skewing by ±5°) is employed and the cogging torque harmonics corresponding to the three relative positions are calculated respectively. By superposition, the equivalent cogging torque harmonics produced by different orders of spatial harmonics can be obtained, as shown in Fig. 4.18 (b). It can be seen that the skewing method is effective under ideal conditions for both of the two designs, which reduces the cogging torques to very low extent.

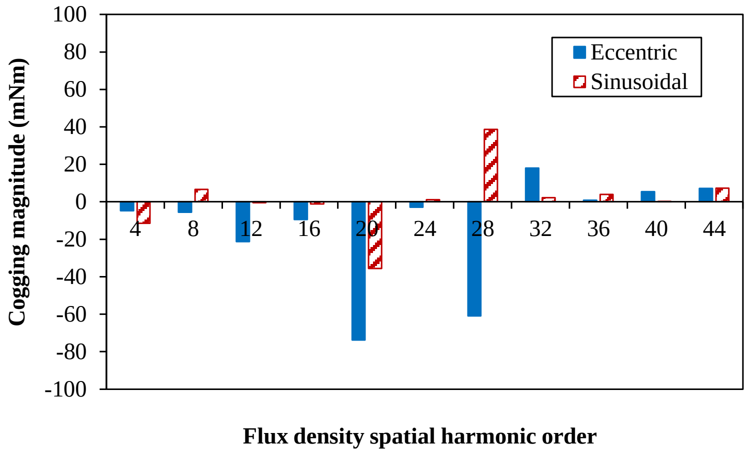

(a) Without skewing

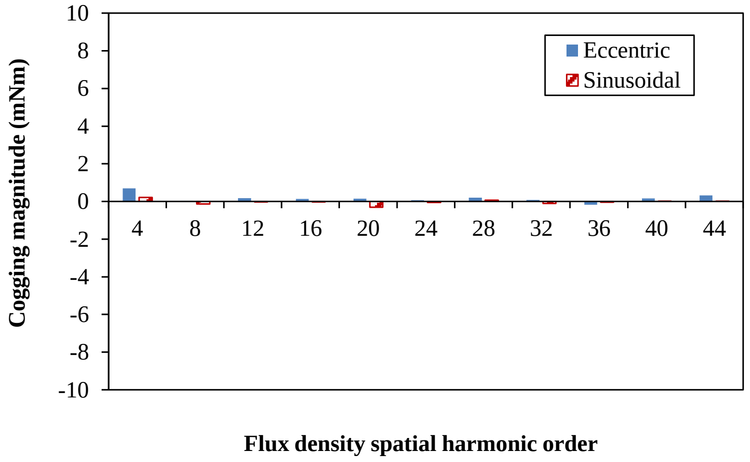

(b) With skewing

Fig. 4.18 Comparison of cogging torque activated by spatial field harmonics between eccentric and sinusoidal designs under ideal conditions.

B. Spatial Field Harmonics with PM Diversity Considered

With the manufacturing tolerances considered, the eccentric design proves to be much more sensitive to the PM diversity than the sinusoidal design. In order to clearly demonstrate the difference, the radial and circumferential field spatial harmonics are also analyzed and compared, based on the relative stator/rotor position where the maximum additional cogging torque (the 12th order) exists, as shown in Fig. 4.19. With 7.5° rotor position considered, the maximum value of the 12th additional cogging torque is obtained whilst the original 24th and the 48th components disappear. Based on the magnitudes and phase angle differences of the field spatial harmonics, the cogging torque components of the two designs can be obtained respectively, as shown in Fig. 4.20. It can be seen that the additional cogging torques are mainly activated by the 4th, the 8th and the 16th spatial harmonics. Despite the higher magnitudes of the 4th and 8th radial flux densities in the sinusoidal design, the circumferential components are relatively lower and the phase differences are closer to 90°, resulting in lower cogging torque components. In addition, the larger phase difference of the 16th field harmonics leads to higher negative component and further decreases the additional cogging in the sinusoidal design.

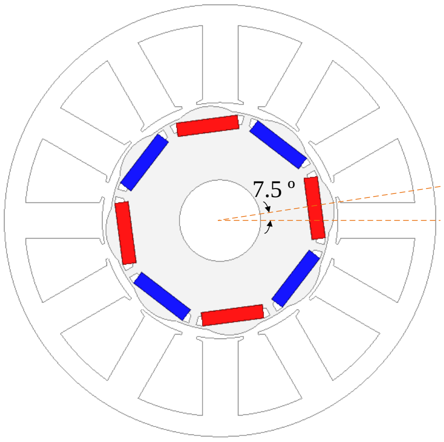

(a) Relative rotor position for maximum additional cogging torque

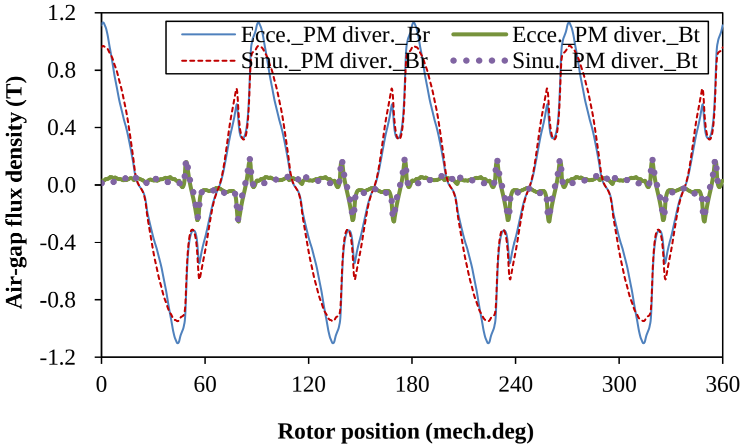

(b) Waveforms

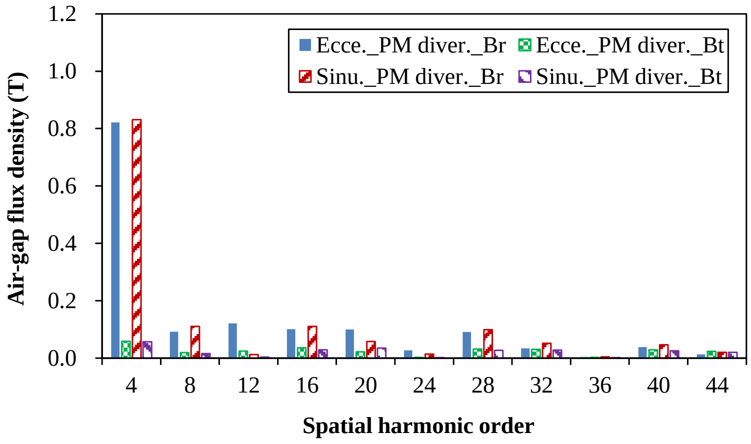

(c) Harmonics

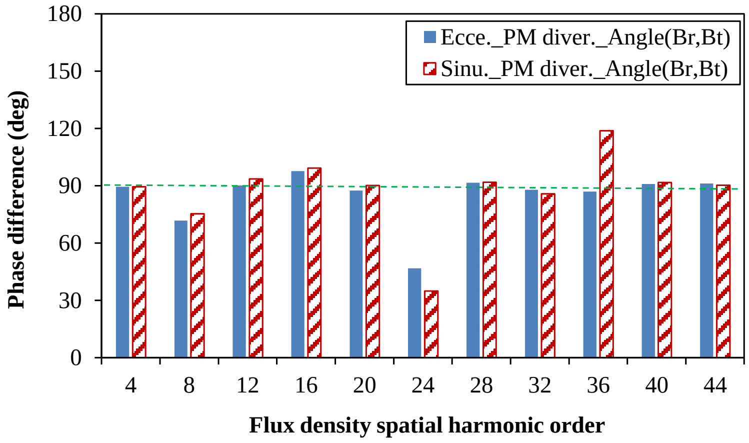

(d) Phase angle difference between radial and circumferential components

Fig. 4.19 Comparison of air-gap flux density between eccentric and sinusoidal designs with PM diversity considered.

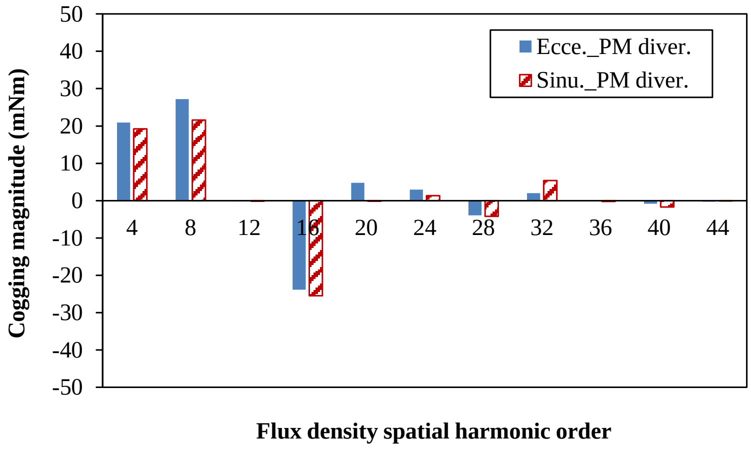

Fig. 4.20 Comparison of cogging torque activated by spatial field harmonics between eccentric and sinusoidal designs with PM diversity considered.

4.3 Analyses of IPM Machines with Different Stator Slot and Rotor Pole Combinations

Compared with the 12-slot/8-pole machine, the 12-slot/10-pole design can significantly reduce the cogging torque under ideal conditions, even without the need of the step-skewing method. In this section, the influence of manufacturing tolerances on cogging torque of the 12-slot/10-pole design will be further investigated, followed by a comparison of the influences between the two slot/pole combinations.

4.3.1 12-Slot/10-Pole Design

Before the comparison, the influence of typical manufacturing tolerances on cogging torque of the 12-slot/10-pole design is analyzed, i.e. PM diversity, assembling eccentricity and stator out-of-roundness. Based on the analyses, several sensitive cases of tolerances for this slot/pole combination will be highlighted.

A. PM Diversity (ideal PM: B_r=1.32T, non-ideal PM: B_r=1.42T)

In real machine products, the PM diversity usually occurs, due to the non-uniform PM material and magnetizing quality. However, it is difficult to predict the sequences of non-ideal PMs which are randomly generated in mass production. Therefore, sensitive distributions of non-ideal PMs should be derived in order to evaluate the potential influence on cogging torque.

Suppose one non-ideal PM exists, it can be deduced that the 12th order of additional cogging torque is introduced for the 12-slot machine. For the 10-pole rotor, the mechanical angle between adjacent PMs is 36^{o}. Therefore, a vector diagram can be employed to illustrate the additional cogging torque vectors (the 12th order) activated by non-ideal PMs, as shown in Fig. 4.21. Through the diagram, it can be easily deduced that the maximum values of additional cogging torque may be produced by the adjacent four vectors, e.g. the 1st, the 2nd, the 6th and the 7th, which indicates that the most sensitive case of PM diversity in 12-slot/10-pole machine is the distribution of four non-ideal PMs by two adjacent and their opposite.

According to the vector diagram shown in Fig. 4.21, the influence of four sensitive sequences of non-ideal PMs on cogging torque is investigated, representing the most severe cases for one, two, three and four non-ideal PMs respectively, as shown in Fig. 4.22. It can be seen that the 12th order of additional cogging torque is introduced and the magnitudes corresponding to the four different cases are 10.9mNm, 22.1mNm, 27.5mNm and 35.7mNm respectively, which also agrees with the quantitative relations reflected by the vector diagram.

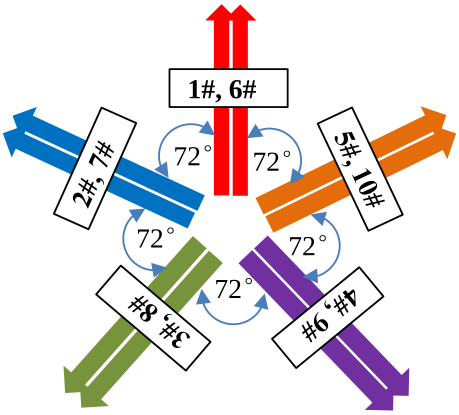

Fig. 4.21 Cogging torque vectors (12th) motivated by PM diversity in 12-slot/10-pole machine.

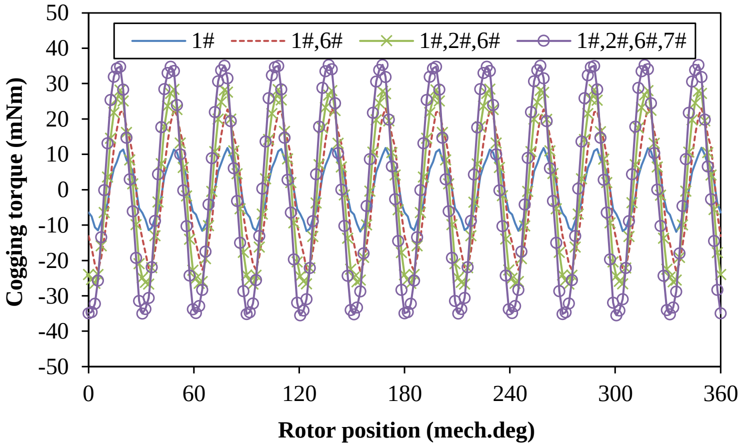

(a) Waveforms

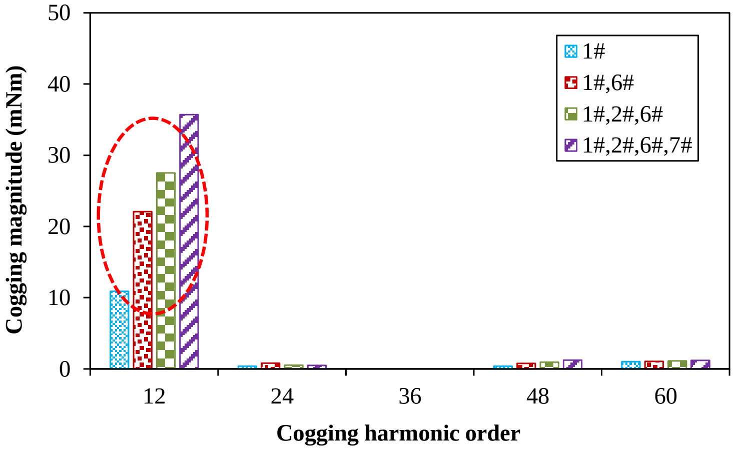

(b) Harmonics

Fig. 4.22 Cogging torque performance of 12-slot/10-pole design with PM diversity (uneven PM remanence) considered (without skewing).

B. Assembling Eccentricity

The influence of assembling eccentricities on cogging torque is investigated, including the static and the dynamic cases, as shown in Fig. 4.23 and Fig. 4.24 respectively. With the static eccentricity considered, the 10th order of additional cogging torque is introduced, the magnitude of which increases to 5.87mNm by 0.14mm static eccentricity. When the dynamic eccentricity occurs, the 12th order of additional cogging torque is produced – 7.25mNm by 0.14mm dynamic eccentricity.

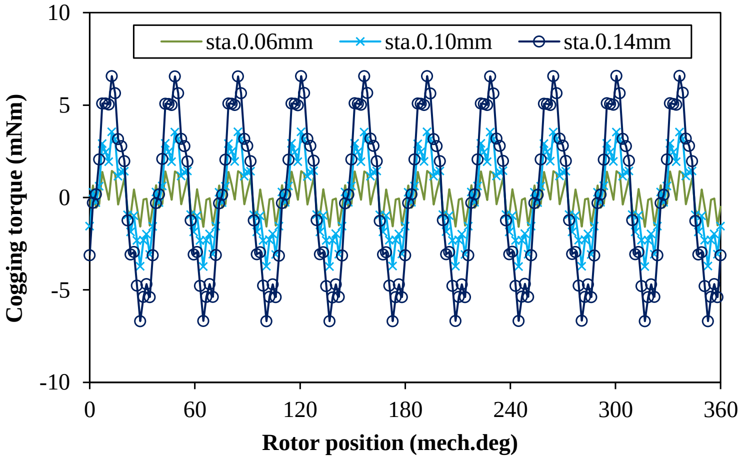

(a) Waveforms

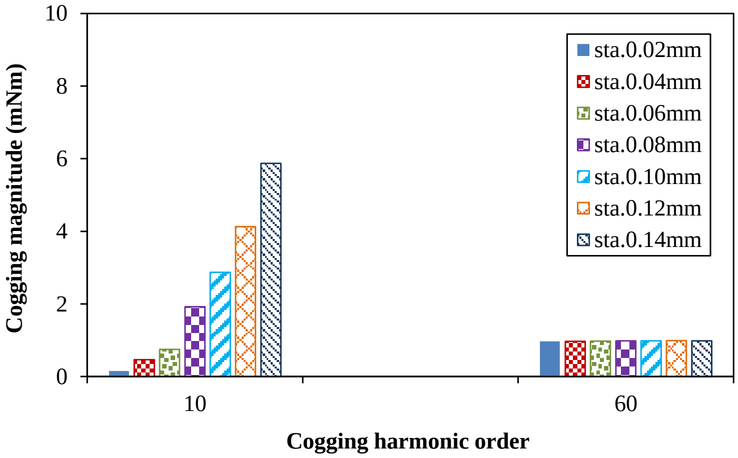

(b) Harmonics

Fig. 4.23 Cogging torque performance of 12-slot/10-pole design with static eccentricity considered (without skewing).

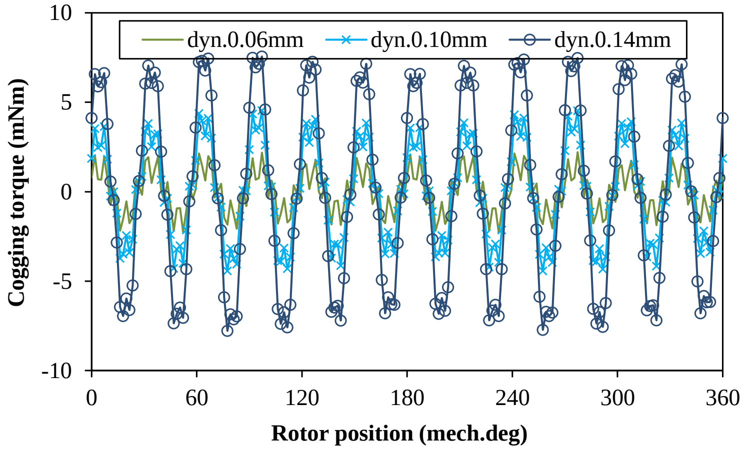

(a) Waveforms

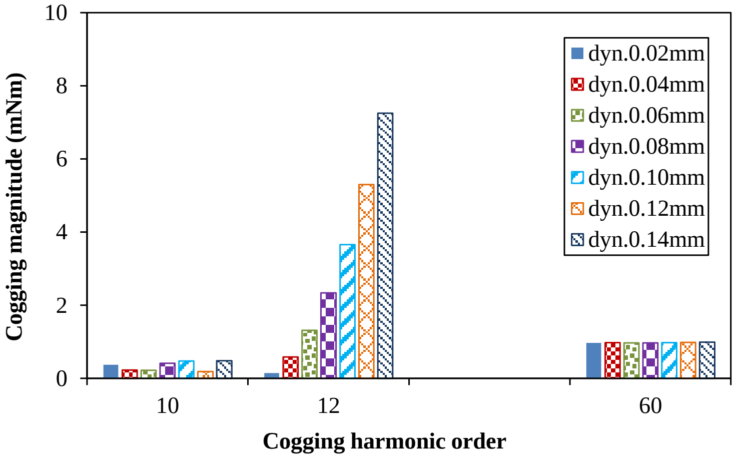

(b) Harmonics

Fig. 4.24 Cogging torque performance of 12-slot/10-pole design with dynamic eccentricity considered (without skewing).

C. Stator Out-of-Roundness

For 12-slot/10-pole PM machines, the modular stator techniques is also very frequently employed in order to ease the winding fabrication process, whilst the stator out-of-roundness usually deteriorates due to the potential tooth-bulges during the assembling of separated stator teeth. Considering the random distribution of tooth-bulges in real products, it is necessary to identify the most sensitive cases first. With one tooth-bulge considered, it can be obviously deduced that the 10th order of additional cogging torque is produced in the 10-pole machine. For the 12-slot stator, the mechanical angle between adjacent teeth is 30°. Therefore, the 10th cogging torque vectors activated by tooth-bulges can be obtained, as shown in Fig. 4.25. With the cases of four tooth-bulges considered, it can be found from the vector diagram that the most sensitive distribution in 12-slot/10-pole machines is the four tooth-bulges belonging to the same phase, which results in the maximum value of the 10th additional cogging torque (Actually, the synthetic cogging torque by adjacent six vectors is a little higher than that by the four vectors. Considering the small difference and the future comparison with the 12-slot/8-pole design, investigation will be carried out on the sensitive case of four tooth-bulges).

Based on the vector diagram, four distributions of sensitive tooth-bulges (typical value: 0.02mm) are analyzed, i.e. one tooth-bulge, two tooth-bulges, three tooth-bulges and four tooth-bulges of the same phase, with the corresponding cogging torques shown in Fig. 4.26. It can be seen that the 10th additional cogging torque increases to 11.4mNm with four tooth-bulges considered.

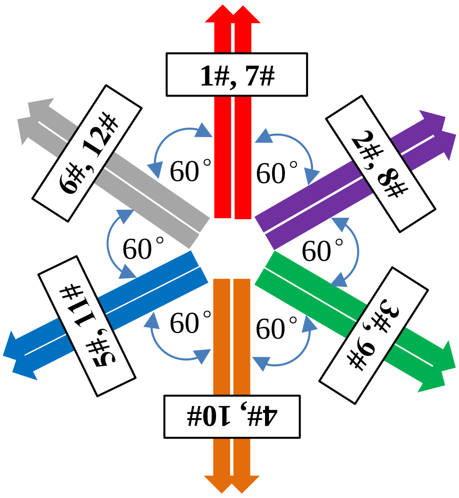

Fig. 4.25 Additional cogging torque vectors (10th) motivated by tooth-bulges in 12-slot/10-pole machine.

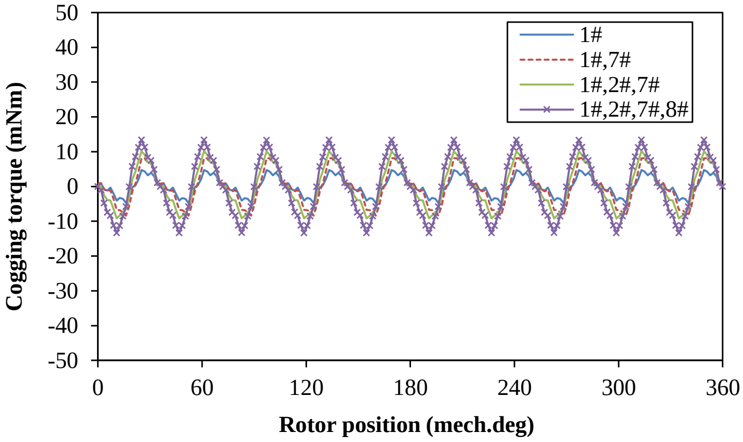

(a) Waveforms

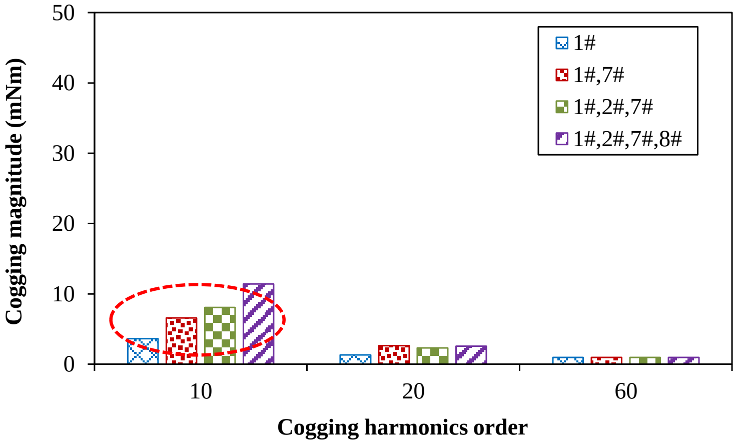

(b) Harmonics

Fig. 4.26 Cogging torque performance of 12-slot/10-pole design with 0.02mm tooth-bulges considered (without skewing).

4.3.2 Comparison between 12-Slot/8-Pole and 12-Slot/10-Pole Designs

The influence of manufacturing tolerances on cogging torque has been investigated for the two slot/pole combinations. In order to evaluate the different sensitivities, comparison of specific influences is carried out between the two designs.

A. PM Diversity (ideal PM: B_r=1.32T, non-ideal PM: B_r=1.42T)

With the PM diversity considered, the 12th order of additional cogging torque is introduced in the two designs, and the vector diagrams have been obtained, as shown in Fig. 4.27. For the 8-pole design, the consequent distributions of four non-ideal PMs prove to be the most sensitive cases of PM diversity. However, for the 10-pole design, the most severe cases are the distributions of four non-ideal PMs by two adjacent and their opposite, as shown in Fig. 4.28.

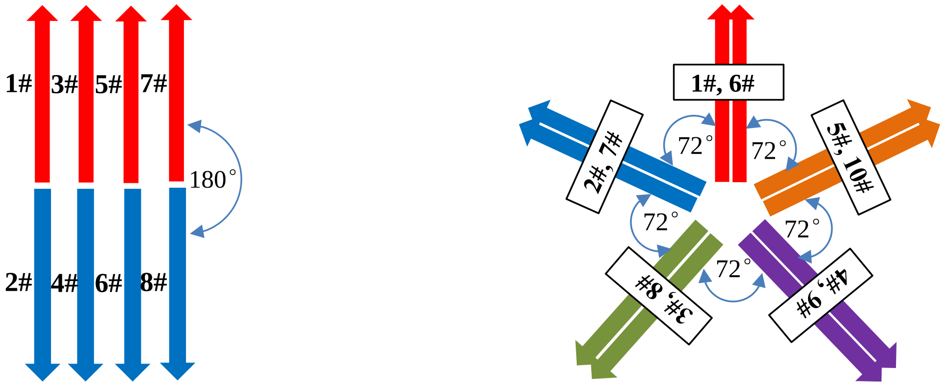

(a) 12-slot/8-pole (b) 12-slot/10-pole

Fig. 4.27 Additional cogging torque vectors (12th) activated by PM diversity in different slot/pole combinations.

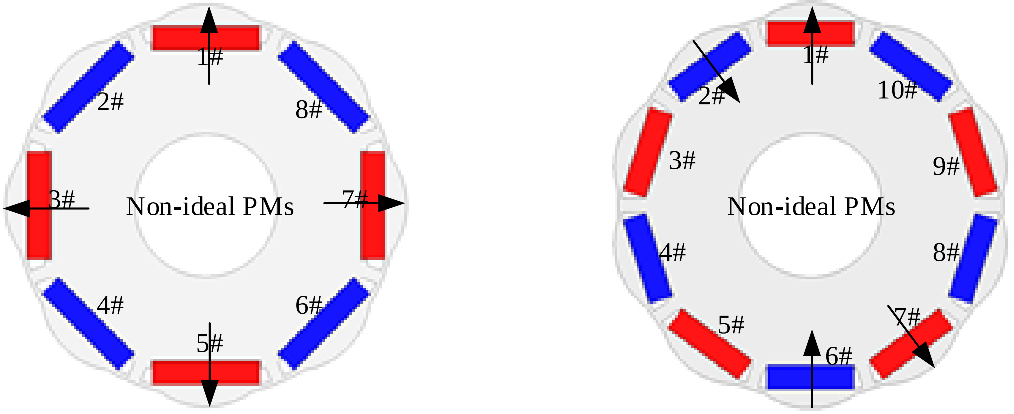

(a) 12-slot/8-pole (b) 12-slot/10-pole

Fig. 4.28 Most sensitive cases of PM diversity in in different slot/pole combinations.

As shown in Fig. 4.29, a comparison of the cogging torque is carried out between the 12-slot/8-pole and the 12-slot/10-pole designs accounting for the most sensitive case of PM diversity. Compared with the 8-pole machine, the 10-pole design produces higher value of the 12th cogging torque – 27.9mNm and 35.7mNm respectively.

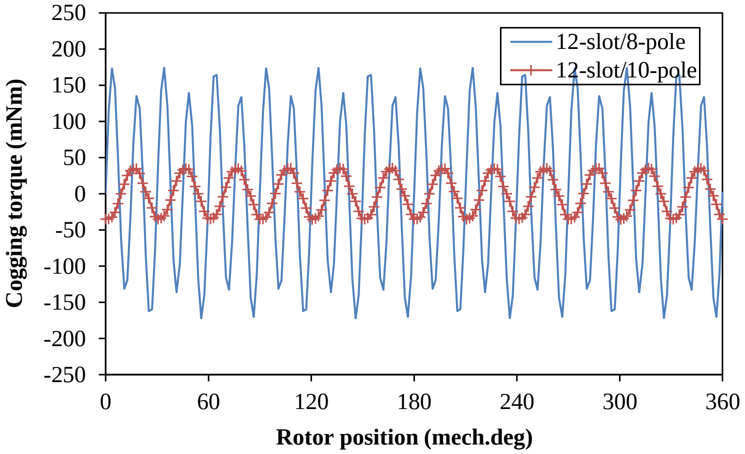

(a) Waveforms

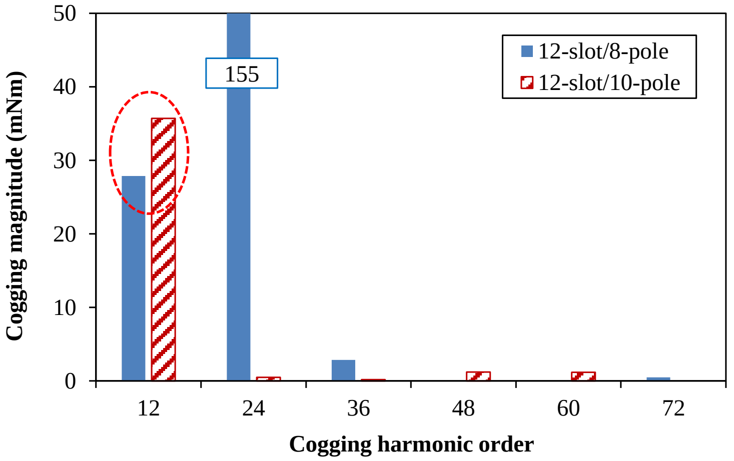

(b) Harmonics

Fig. 4.29 Comparison of cogging torque in 12-slot/8-pole and 12-slot/10-pole machines with PM diversity considered (without skewing).

In addition to the existing rotor pole shoes, the influence of eccentric distance is also investigated and compared between the two combinations, as shown in Fig. 4.30. It can be found that the 10-pole design produces higher values of the 12th additional cogging torque when the eccentric distance *A* changes in a wide range (12mm ~ 15mm). Therefore, it can be deduced that the 12-slot/10-pole design is more sensitive to PM diversity than the 12-slot/8-pole design.

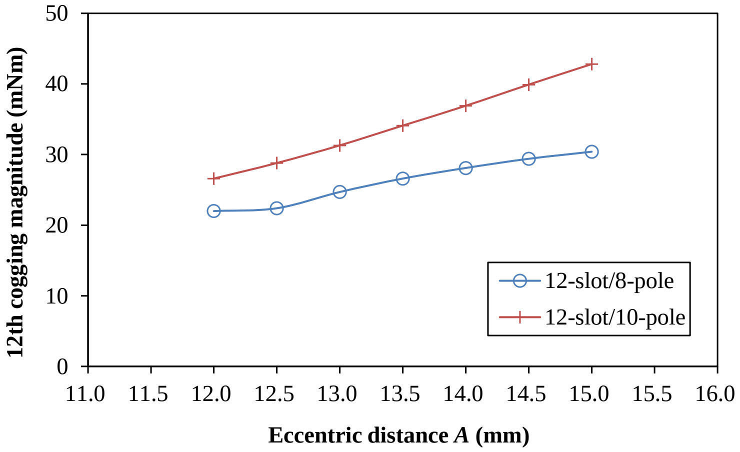

Fig. 4.30 Comparison of the 12th cogging torque activated by PM diversity in12-slot/8-pole and 12-slot/10-pole machines by different eccentric distances *A* (without skewing).

B. Assembling Eccentricity

A comparison of the cogging torque between the 12-slot/8-pole and the 12-slot/10-pole machines is carried out accounting for the influence of assembling eccentricities (the static and the dynamic types), as shown in Fig. 4.31. With a 0.10mm static eccentricity considered, the 10th order of additional cogging torque component (2.87mNm) is introduced in the 12-slot/10-pole design whilst the 8th order component in the 12-slot/8-pole machine is negligible. When a 0.10mm dynamic eccentricity exists, the additional cogging torque components in the 10-pole and the 8-pole design are 3.7mNm (the 12th order) and 5.5mNm (the 1st order) respectively. Nevertheless, considering the low magnitudes of the additional components, it can be deduced that the cogging torque performance of the two designs are not so sensitive to assembling eccentricities.

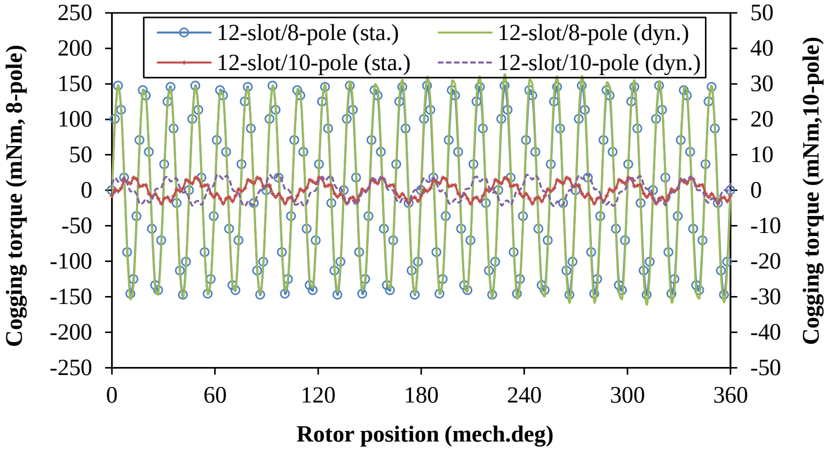

(a) Waveforms

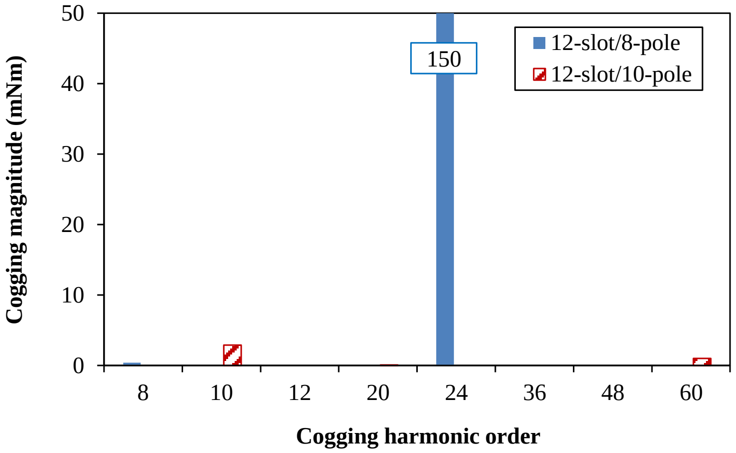

(b) Harmonics (static)

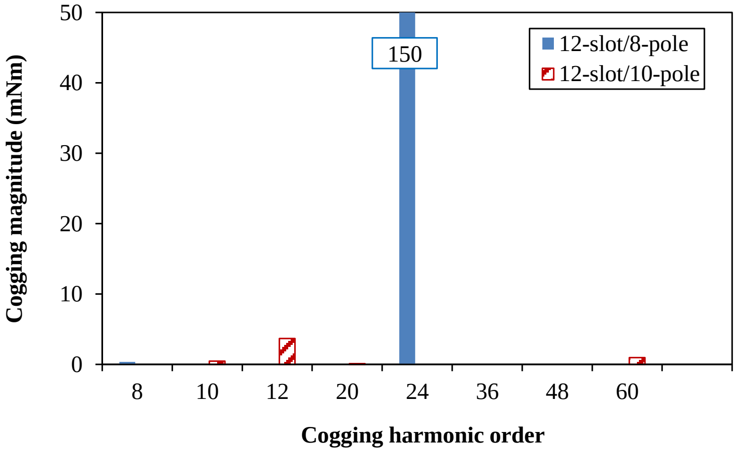

(c) Harmonics (dynamic)

Fig. 4.31 Comparison of cogging torque in 12-slot/8-pole and 12-slot/10-pole machines with static and dynamic eccentricities (0.10mm) considered (without skewing).

C. Stator Out-of-Roundness

The stator out-of-roundness usually deteriorates due to the tooth-bulges during the assembling of modular stator teeth, and the influence of tooth-bulges has been investigated, with the additional cogging torque vector diagrams of the two designs shown in Figs. 4.32 (a) and (b) respectively. It can be deduced that the most sensitive cases for both of the two designs prove to be the four tooth-bulges belonging to the same phase.

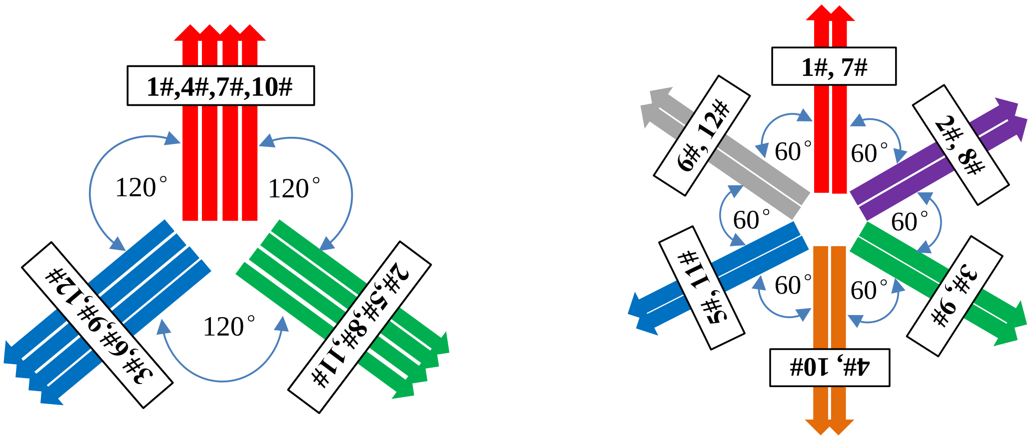

(a) 12-slot/8-pole (8th) (b) 12-slot/10-pole (10th)

Fig. 4.32 Additional cogging torque vectors activated by tooth-bulges in different slot/pole combinations.

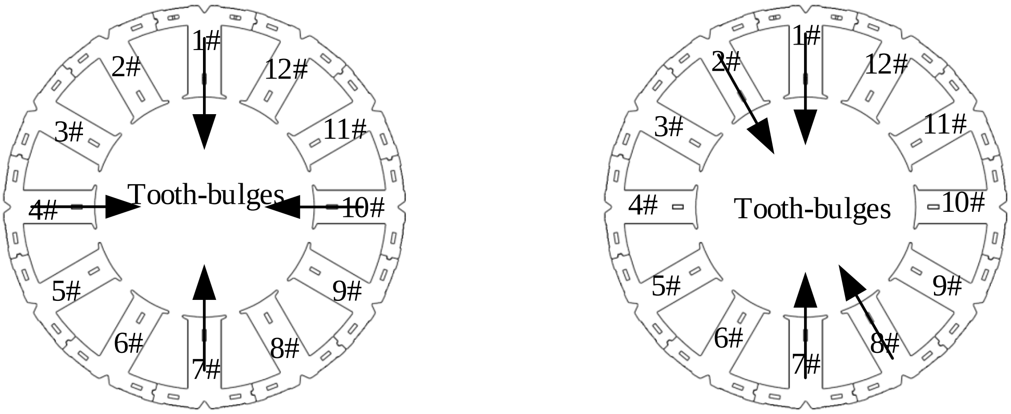

(a) 12-slot/8-pole (b) 12-slot/10-pole

Fig. 4.33 Most sensitive cases of tooth-bulges in different slot/pole combinations.

With the most sensitive distributions of four tooth-bulges considered, the cogging torques of the two designs are illustrated for comparison, as shown in Fig. 4.34. It can be seen that the 8th order of additional cogging torque in the 12-slot/8-pole machine is much higher than the 10th additional cogging torque produced in the 12-slot/10-pole design, 24.4mNm and 11.4mNm respectively. In addition to the two existing models, the influence of eccentric distance (*A*) is also investigated and compared between the two slot/pole combinations accounting for the sensitive tooth-bulges, as shown in Fig. 4.35. It can be seen that the additional cogging torques of the two designs almost remain stable respectively when the eccentric distance changes in a wide range (12mm ~ 15mm). However, the 12-slot/8-pole design proves to be much more sensitive to tooth-bulges and higher magnitudes of additional cogging torque usually exist. Therefore, the stator out-of-roundness should be strictly guaranteed for designs by this slot/pole combination in order not to activate too high additional cogging torques.

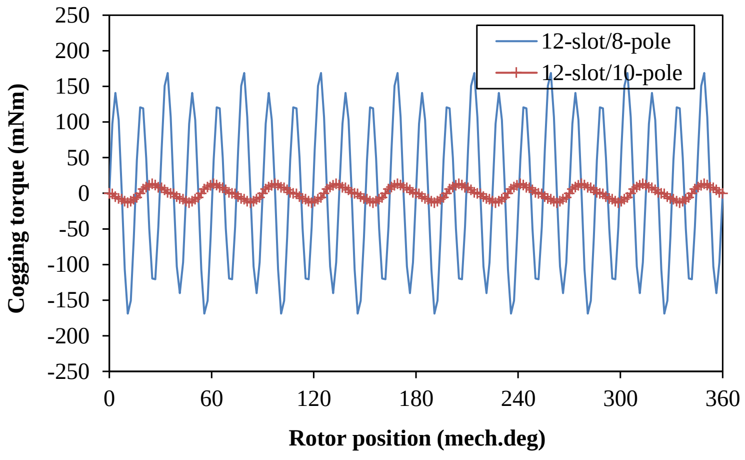

(a) Waveforms

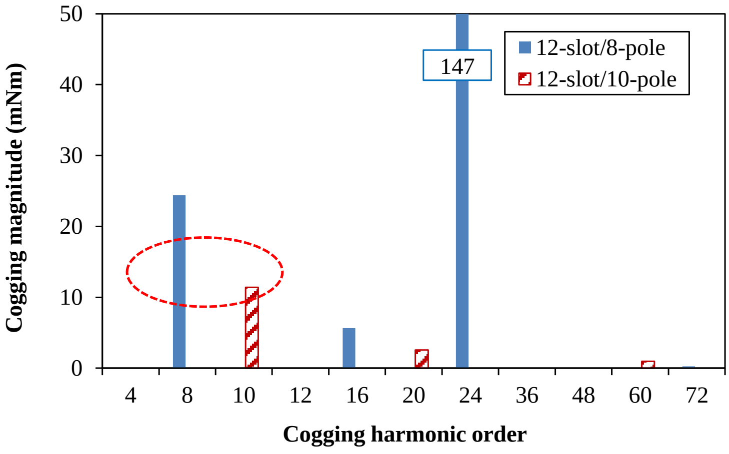

(b) Harmonics

Fig. 4.34 Comparison of cogging torque in 12-slot/8-pole and 12-slot/10-pole machines with tooth-bulges considered (without skewing).

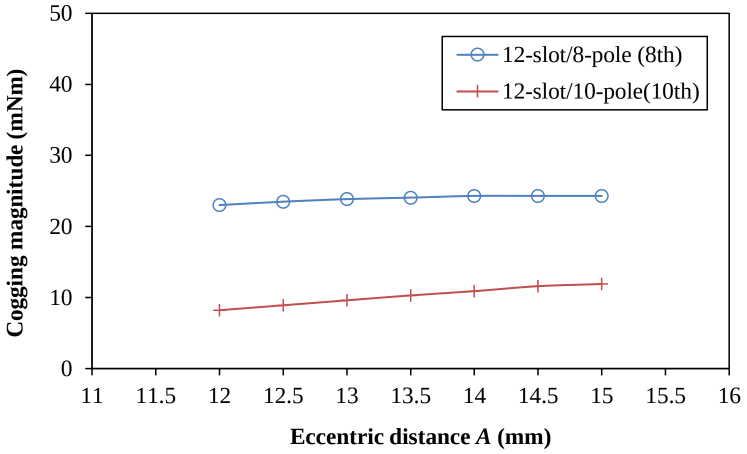

Fig. 4.35 Comparison of the 12th cogging torque activated by tooth-bulges in12-slot/8-pole and 12-slot/10-pole machines by different eccentric distance *A* (without skewing).

4.3.3 Verification by Spatial Field Harmonics under Different Conditions

Based on the foregoing analyses, the 12-slot/8-pole and the 12-slot/10-pole designs exhibit different sensitivities to the tolerances of PM diversity and tooth-bulges. As a verification, the spatial field harmonics are investigated, as well as the resultant cogging torque components.

A. Spatial Field Harmonics with and without PM Diversity Considered

First, the radial and circumferential air-gap flux density components (at the relative stator and rotor position where the maximum cogging torque exists) in the 12-slot/10-pole design are obtained respectively by the FE method with and without PM diversity considered, as shown in Fig. 4.36 (a). Further, the spatial field harmonics (due to the decreasing magnitudes, higher orders of harmonics are not shown) and the phase angle differences between the radial and circumferential components are obtained, as shown in Figs. 4.36 (b) and (c) respectively.

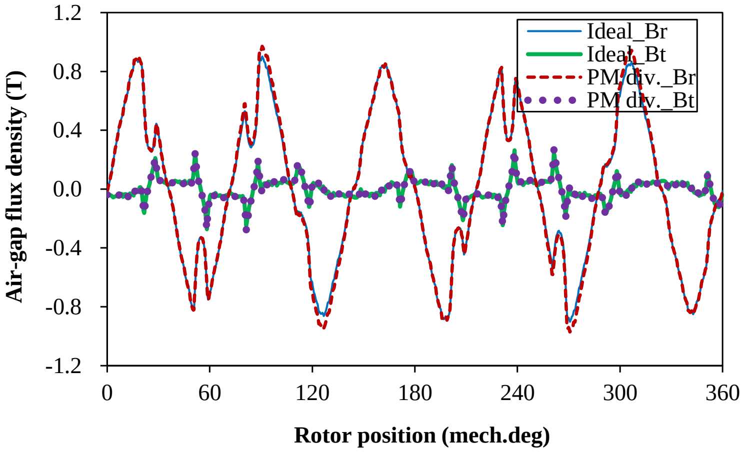

(a) Waveforms

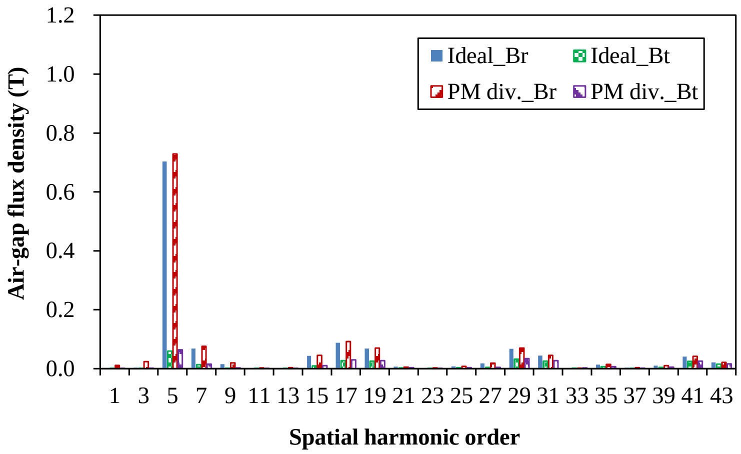

(b) Harmonics

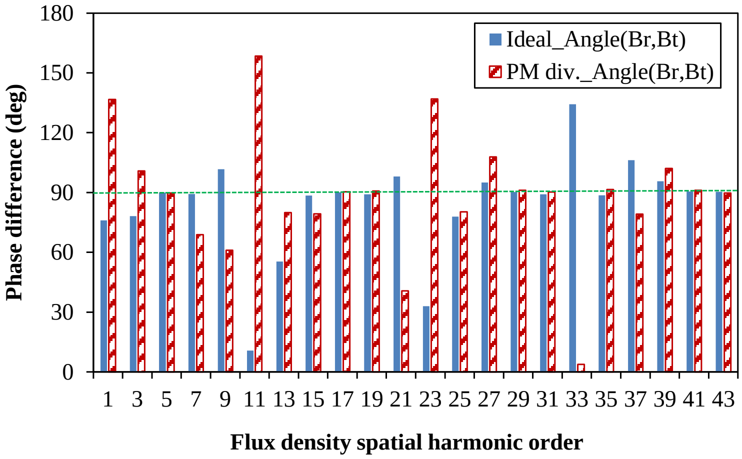

(c) Phase difference between radial and circumferential components

Fig. 4.36 Comparison of air-gap flux densities in 12-slot/10-pole design with and without PM diversity considered.

As can be seen, the flux density magnitudes slightly increase with the PM diversity considered. Moreover, the phase angle differences between the two components exhibit obvious variation, e.g. the 5th, the 7th, the 9th and the 15th spatial field harmonics. Therefore, additional cogging torque components are activated by these spatial field harmonics in the 12-slot/10-pole design, as shown in Fig. 4.37. Despite the very low cogging torque under ideal conditions, the synthetic cogging torque activated by these changed spatial field harmonics significantly increases to 35.6mNm, which agrees well with the foregoing analyses shown in Fig. 4.29.

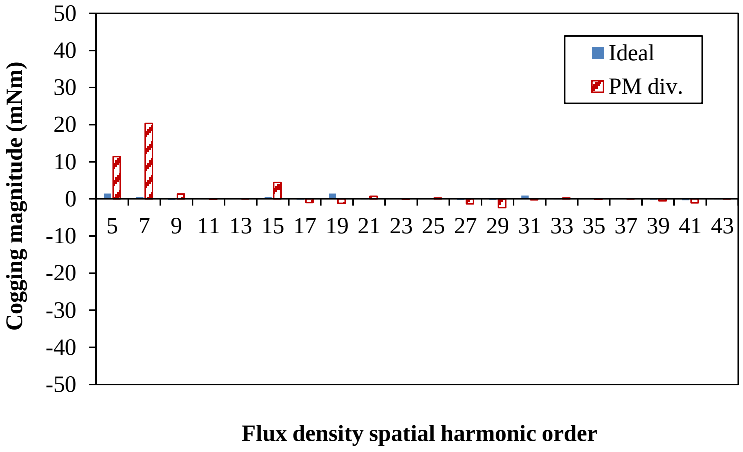

Fig. 4.37 Comparison of cogging torque activated by spatial field harmonics in 12-slot/10-pole design with and without PM diversity considered.

For comparison, the additional cogging torque components activated by spatial field harmonics in the 12-slot/8-pole design are also illustrated according to Fig. 4.18 and Fig. 4.20, as shown in Fig. 4.38. At the 7.5° rotor position, it can be seen that the original 24th cogging torque in the 8-pole design disappears and the maximum additional component (mainly the 12th order) -28mNm - is activated by the 4th, the 8th and the 16th (negative) field spatial harmonics.

Therefore, the analyses of cogging torque by way of spatial field harmonics verify the additional cogging torque components activated by PM diversity in the two machine designs, which indicate that the 12-slot/10-pole machine is more sensitive to the tolerance of PM diversity than the 12-slot/8-pole design.

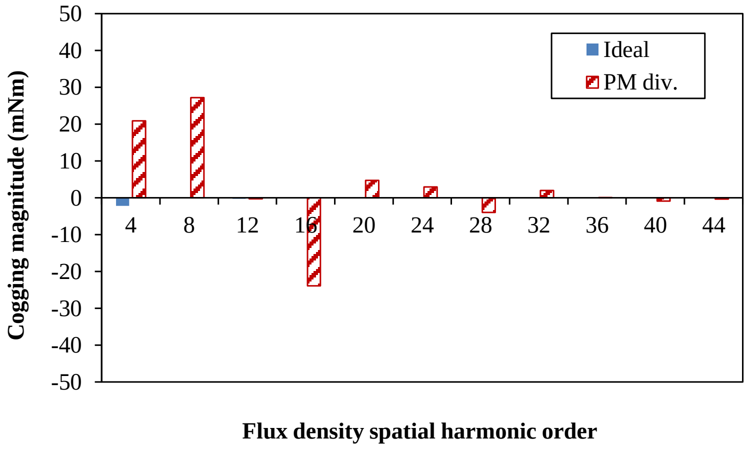

Fig. 4.38 Comparison of cogging torque activated by spatial field harmonics in 12-slot/8-pole design with and without PM diversity considered (7.5° rotor position).

B. Spatial Field Harmonics with and without Tooth-Bulges Considered

Similarly, the method by spatial field harmonics can be also employed to analyze the influence of tooth-bulges on cogging torque. First, the radial and circumferential air-gap flux density components in the 12-slot/10-pole design with and without considering tooth-bulges are obtained by FE method, as shown in Fig. 4.39 (a). Based on the waveforms, the spatial harmonic components and the phase angle differences between the radial and circumferential components can be obtained, as shown in Figs. 4.39 (b) and (c) respectively. Although the magnitudes of field harmonics remain stable, the variation of phase angle differences between the radial and circumferential spatial components cannot be neglected, especially the 5th order of spatial harmonics – changing from 89.96° to 89.69° with the tooth-bulges considered. Considering the highest magnitudes, an additional cogging torque component (11.1mNm) is produced by the 5th order of spatial field harmonics, as shown in Fig. 4.40, which verifies the analyses shown in Fig. 4.34.

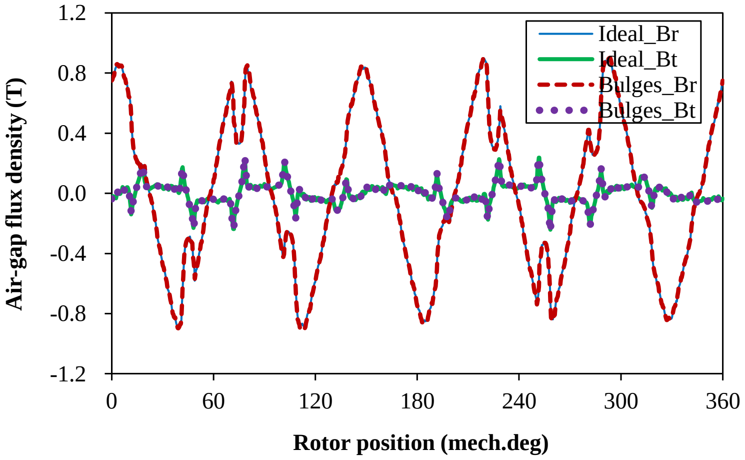

(a) Waveforms

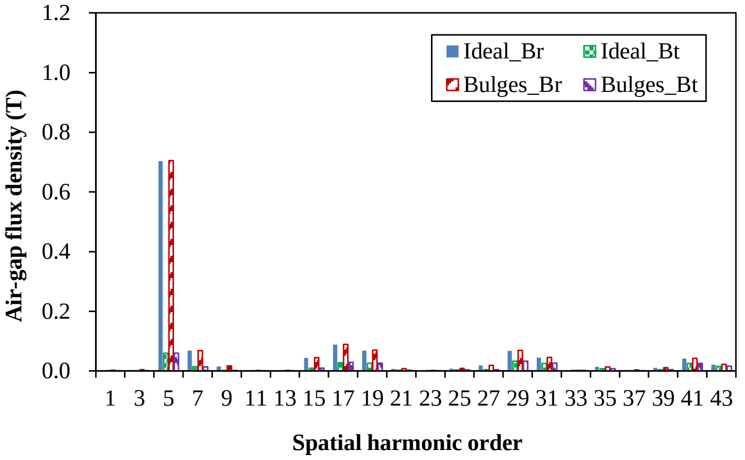

(b) Harmonics

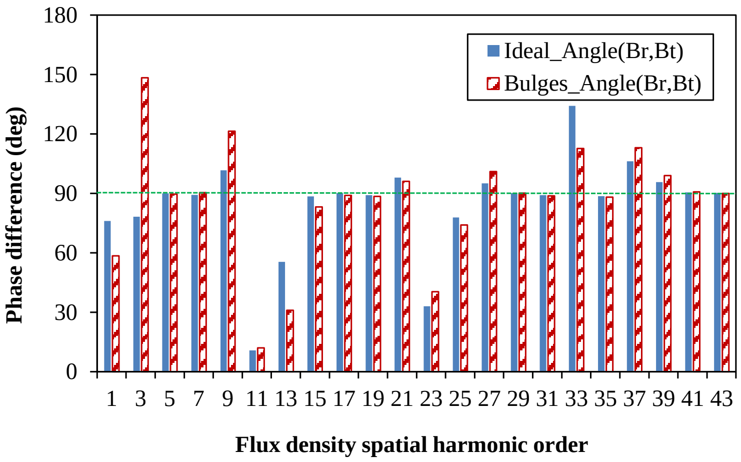

(c) Phase difference between radial and circumferential components

Fig. 4.39 Comparison of air-gap flux densities in 12-slot/10-pole design with and without tooth-bulges considered.

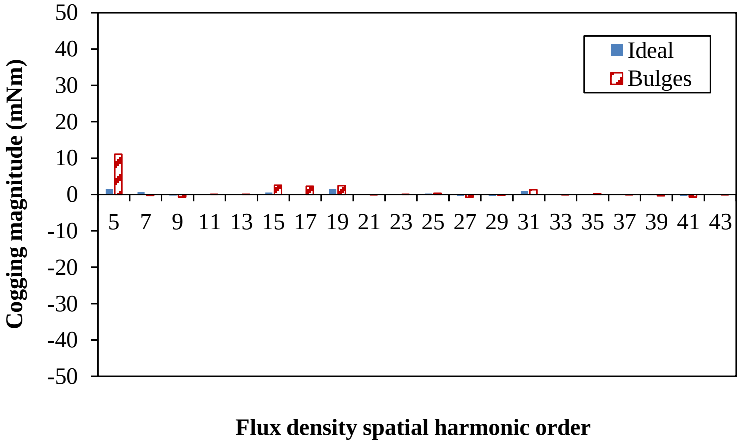

Fig. 4.40 Comparison of cogging torque activated by spatial field harmonics in 12-slot/10-pole design with and without tooth-bulges considered.

For comparison, the radial and circumferential flux density components are also investigated in the 12-slot/8-pole machine with and without tooth-bulges considered, as shown in Fig. 4.41. Despite the minor influence on the flux density magnitudes, the phase angle differences between the radial and circumferential spatial field harmonics exhibit a series of obvious changes with the tooth-bulges considered, as shown in Fig. 4.41 (c). Therefore, the changes of phase angle differences result in additional cogging torque components, as shown in Fig. 4.42 (a). In order to clearly illustrate the additional cogging torque components (the 8th time harmonics), the step-skewing method (2 step by skewing 7.5°) is employed to remove the original cogging torque (the 24th time harmonic), as shown in Fig. 4.42 (b). Comparing Fig.

4.42 and Fig. 4.40, it can be seen that the additional cogging torques in the 8-pole and 10-pole designs are mainly activated by the 4th and the 5th field spatial harmonics respectively. However, the 12th field spatial harmonic also contributes to the 8-pole design, resulting in a higher additional cogging torque although the step-skewing method is employed (skewing coefficient: 0.75). Therefore, it can be deduced that the 12-slot/8-pole design is more sensitive to tooth-bulges than the 12-slot/10-pole design, which agrees with the foregoing analyses.

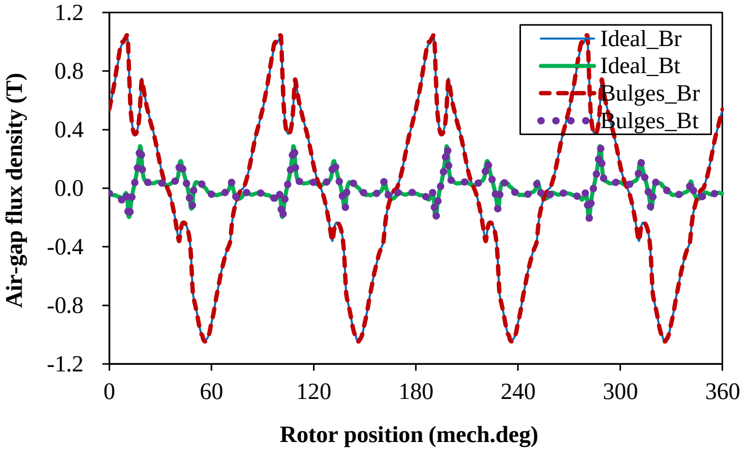

(a) Waveforms

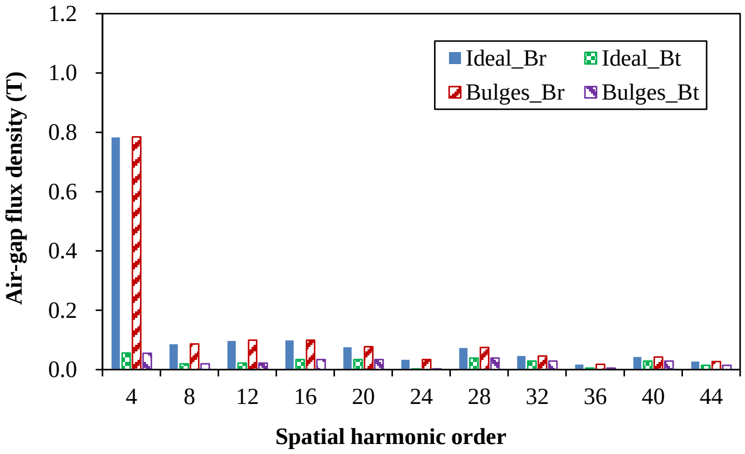

(b) Harmonics

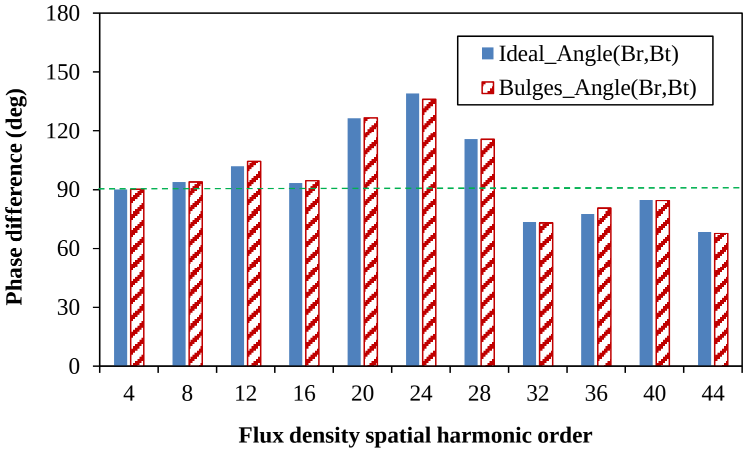

(c) Phase difference between radial and circumferential components

Fig. 4.41 Comparison of air-gap flux density in 12-slot/8-pole design with and without tooth-bulges considered.

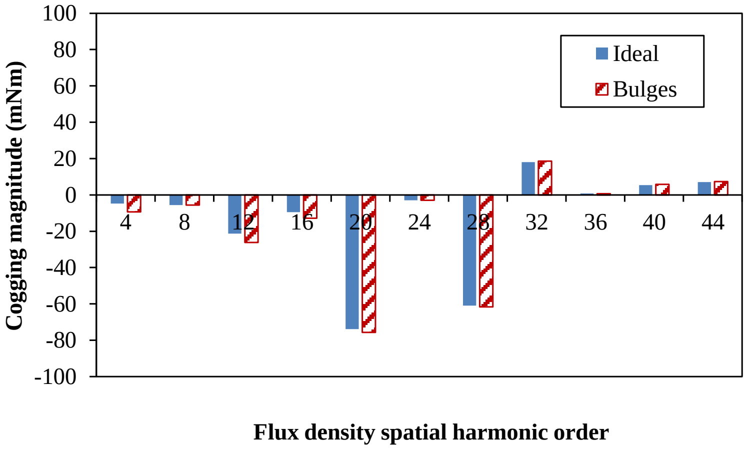

(a) Without skewing

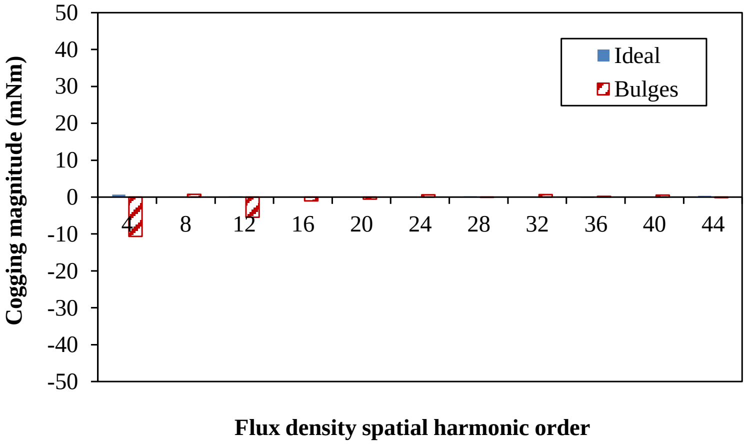

(b) With skewing

Fig. 4.42 Comparison of cogging torque activated by spatial field harmonics in 12-slot/8-pole design with and without tooth-bulges considered.

4.4 Influence of Manufacturing Tolerances on Other Electromagnetic Performance in Different Interior Permanent Magnet Machines

The influence of manufacturing tolerances on cogging torque has been investigated and compared amongst different IPM machine designs. As the key electromagnetic performance, the back EMF and the on-load torque are also analyzed for these IPM machines, according to the aforementioned sensitive cases of PM diversity (ideal PM: B_r=1.32T, non-ideal PM: B_r=1.42T) and tooth-bulges (0.02mm). For comparison, all the harmonics are noted by the orders corresponding to one whole revolution.

4.4.1 Back-EMF

A. PM Diversity

First, the back EMF performance of the 12-slot/8-pole machines with different rotor contours is investigated and compared accounting for the tolerance of PM diversity, as shown in Fig. 4.43. It can be seen that low magnitudes of the 8th (and the 16th) voltage harmonics are introduced – 0.11V and 0.09V for the eccentric and sinusoidal designs respectively, which are mainly due to the asymmetric magnetic fields in the air-gap. Moreover, the back EMF performance is also analyzed for the 12-slot/10-pole design, as shown in Fig. 4.44. With the PM diversity considered, the 7th order of harmonic is introduced in the back EMF with the magnitude of 0.12V, which is a little higher than the 8th harmonic in the 8-pole design.

Therefore, it can be deduced that no significant influence is introduced in the back EMF performance by the tolerance of PM diversity for these IPM machine designs, although low magnitudes of additional harmonics are produced by the asymmetric magnetic fields.

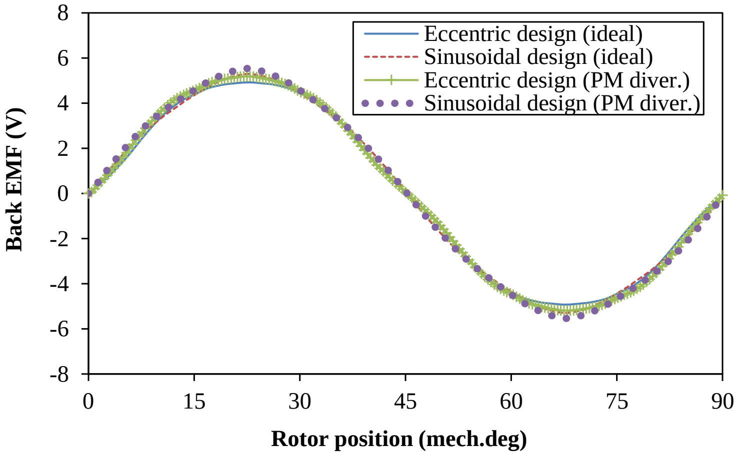

(a) Waveforms (1/4 revolution)

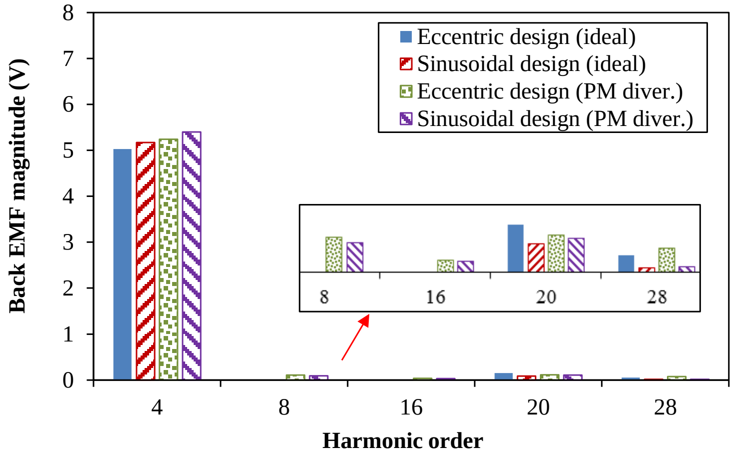

(b) Harmonics

Fig. 4.43 Influence of PM diversity on back-EMF in IPM machines with different rotor contours (1500rpm).

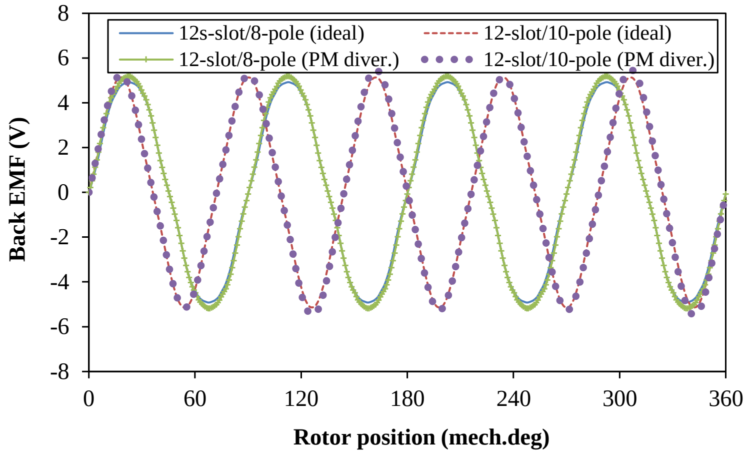

(a) Waveforms (1 revolution)

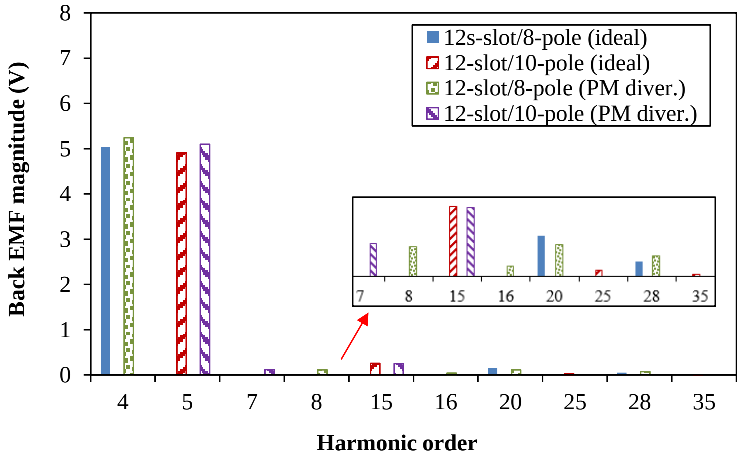

(b) Harmonics

Fig. 4.44 Influence of PM diversity on back-EMF in IPM machines with different slot/pole combinations (1500rpm).

B. Tooth-bulges

Moreover, the influence of assembling tooth-bulges on the back EMF performance is also investigated and compared amongst different IPM machine designs, as shown in Fig. 4.45 and Fig. 4.46 respectively. According to the back EMF harmonics, it can be seen that no additional components are introduced in the IPM designs with assembling tooth-bulges considered, except for minor variation on the original back EMF components. Therefore, the influence of tooth-bulges on the back EMF performance is negligible, which proves to be applicable for the IPM machines with different rotor contours and slot/pole combinations.

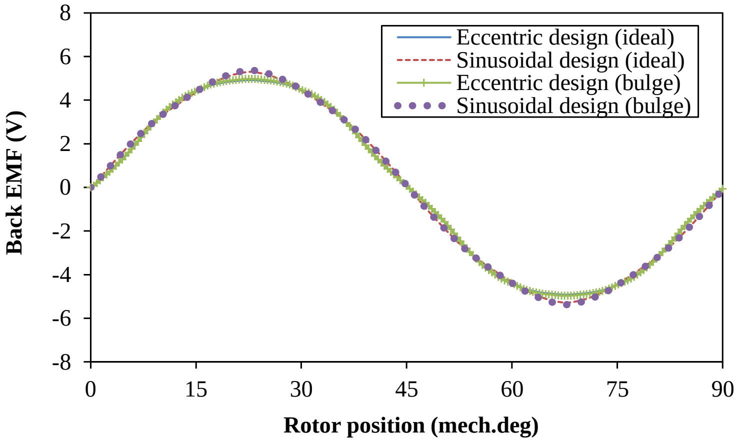

(a) Waveforms (1/4 revolution)

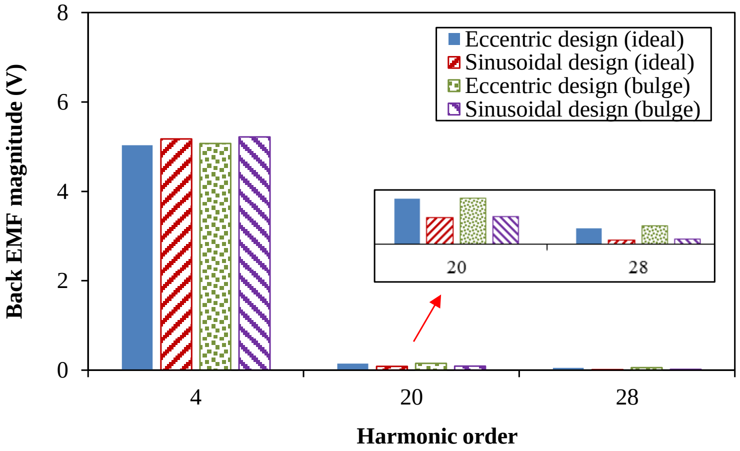

(b) Harmonics

Fig. 4.45 Influence of tooth-bulges on back-EMF in IPM machines with different rotor contours (1500rpm).

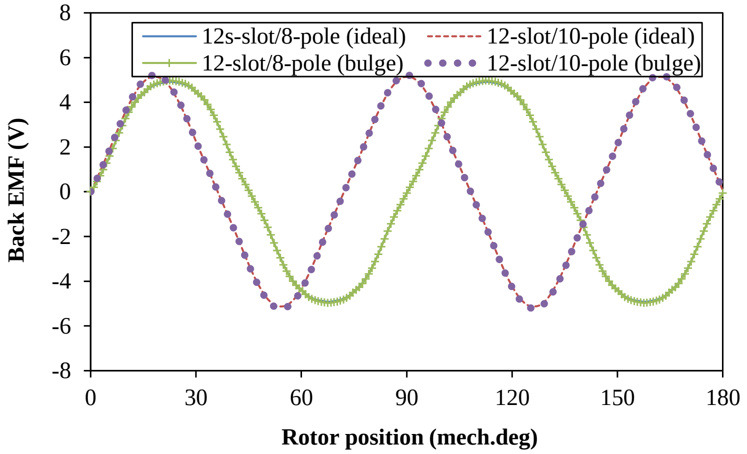

(a) Waveforms (1/2 revolution)

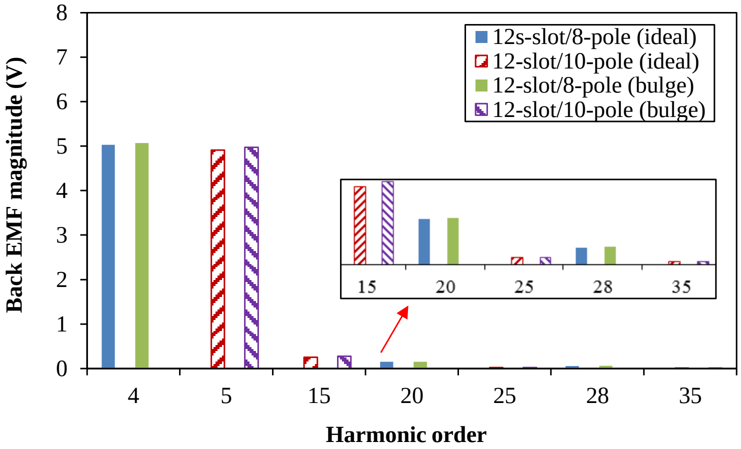

(b) Harmonics

Fig. 4.46 Influence of tooth-bulges on back-EMF in IPM machines with different slot/pole combinations (1500rpm).

4.4.2 On-load Torque

A. PM Diversity

For the IPM machines with different rotor contours, the influence of PM diversity on the torque quality is investigated, as shown in Fig. 4.47. It can be seen that the torque ripple of the eccentric design increases from 10.7% to 12.5%, whilst the sinusoidal design increases from 5.9% to 8.0%. More specifically, the 12th order of additional torque harmonics are introduced – 0.086Nm and 0.072Nm for the eccentric and sinusoidal designs respectively, which are mainly due to the 8th additional back EMF harmonics and the foregoing 12th additional cogging torque components.

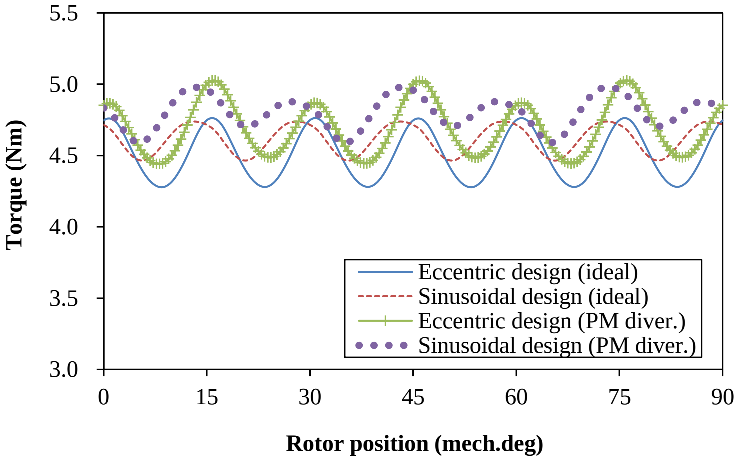

(a) Waveforms (1/4 revolution)

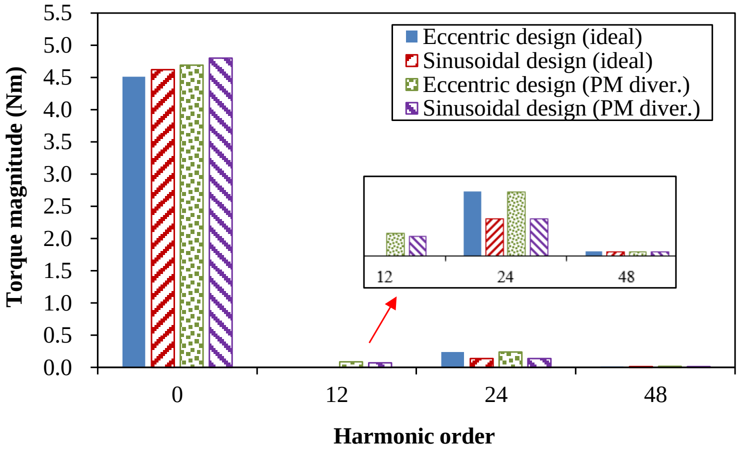

(b) Harmonics

Fig. 4.47 Influence of PM diversity on torque quality in IPM machines with different rotor contours (95A, I_d=0).

Moreover, the torque quality is also compared between the 12-slot/8-pole and 12-slot/10-pole IPM machines, as shown in Fig. 4.48. It can be seen that the torque ripple of the 10-pole design increases significantly from 1.4% to 6.1%. Actually, the 12th additional torque harmonic is introduced - 0.118Nm, which is mainly caused by the 7th order of additional back EMF harmonic and the 12th additional cogging torque component. Therefore, the 12-slot/10-pole design proves to be more sensitive to the tolerance of PM diversity than the 12-slot/8-pole design (similar to the different sensitivities on cogging torque), although the torque ripple of the 10-pole design is still lower.

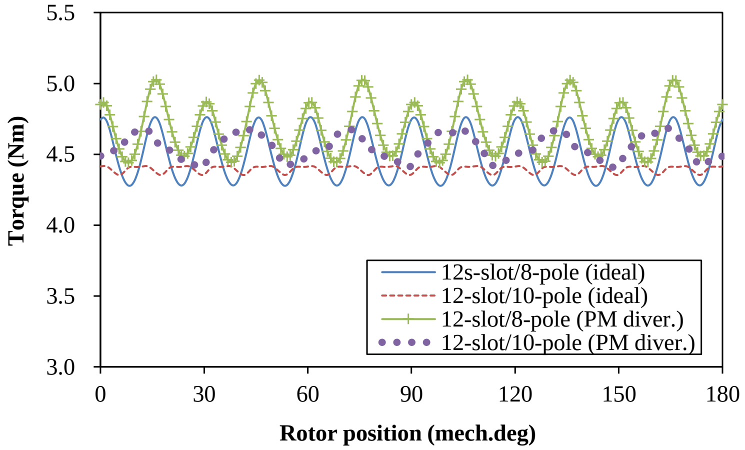

(a) Waveforms (1/2 revolution)

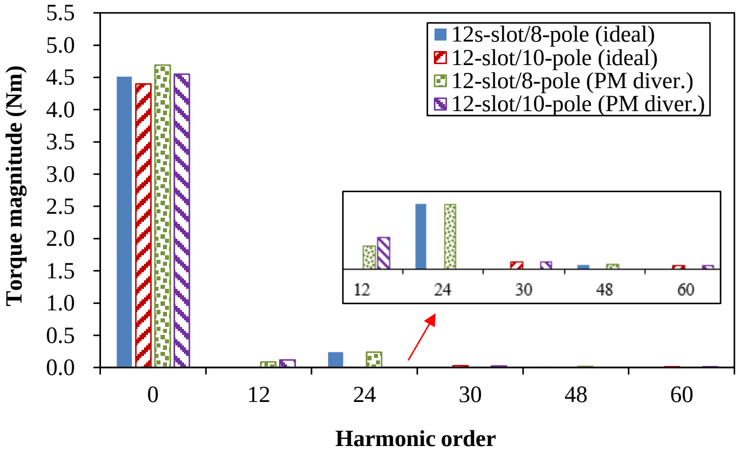

(b) Harmonics

Fig. 4.48 Influence of PM diversity on torque quality in IPM machines with different slot/pole combinations (95A, I_d=0).

B. Tooth-bulges

Similarly, the influence of tooth-bulges on torque quality is also investigated for different IPM machines, as shown in Fig. 4.49 and Fig. 4.50. For the 12-slot/8-pole machines with the eccentric and sinusoidal rotor contours, similar additional torque harmonics of the 8th order are introduced, being 0.035Nm and 0.039Nm respectively, which are mainly due to the 8th order of additional cogging torque components in the two machine designs. However, the influence by tooth-bulges can be ignored, compared with the influence of PM diversity.

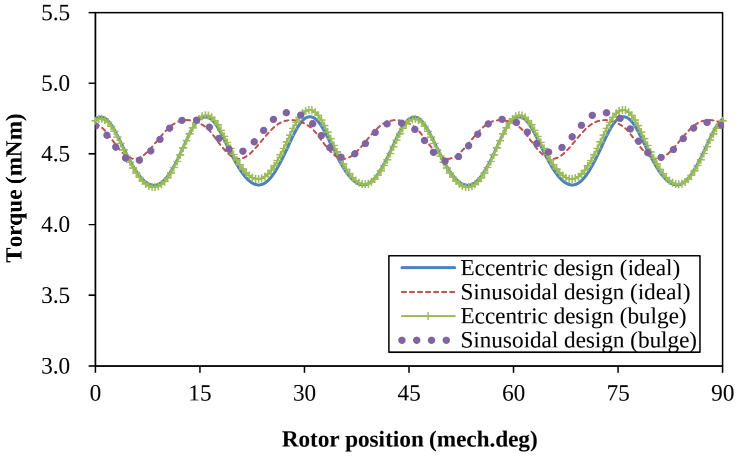

(a) Waveforms (1/4 revolution)

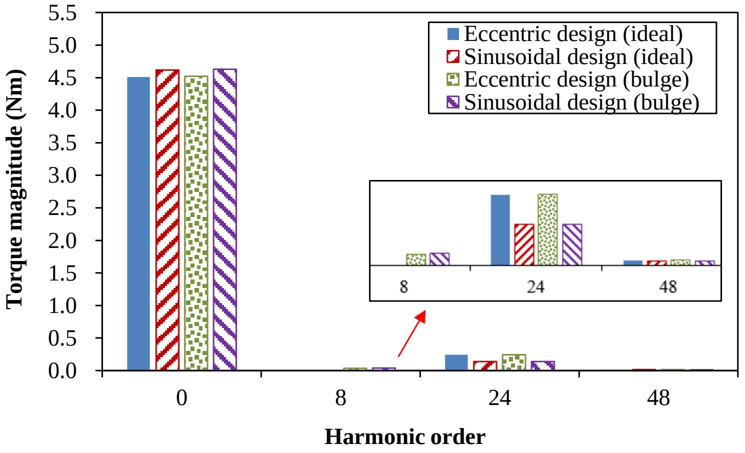

(b) Harmonics

Fig. 4.49 Influence of tooth-bulges on torque quality in IPM machines with different rotor contours (95A, I_d=0).

Moreover, a comparison of the torque quality is also carried out between the 12-slot/8-pole and the 12-slot/10-pole designs with the tooth-bulges considered, as shown in Fig. 4.50. It can be seen that the 8th and the 10th additional torque harmonics are introduced in the two designs

- 0.035Nm and 0.025Nm respectively, which are also due to the additional cogging torque components. Despite this, the torque ripples of the two designs are not obviously influenced, with the low magnitudes of additional torque harmonics considered.

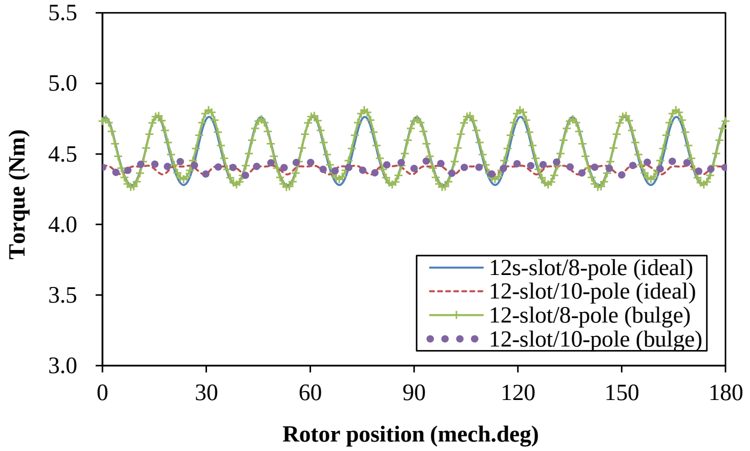

(a) Waveforms (1/2 revolution)

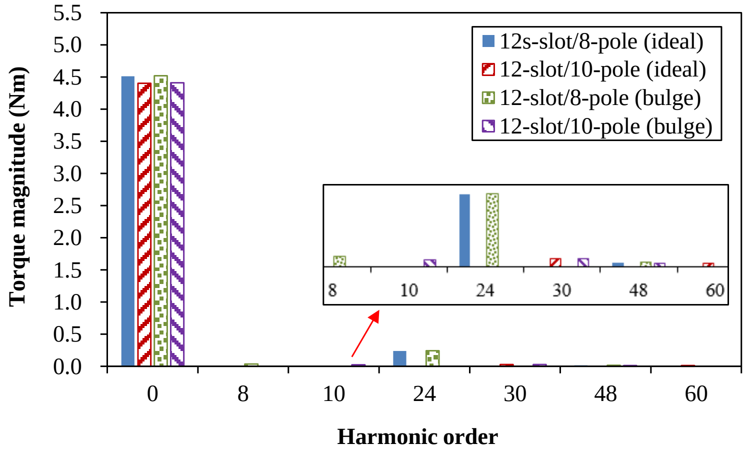

(b) Harmonics

Fig. 4.50 Influence of tooth-bulges on torque quality in IPM machines with different slot/pole combinations (95A, I_d=0).

Based on the analyses, it can be seen that the additional cogging torque components by manufacturing tolerances are reflected in the on-load torque performance and increase the torque ripple as a consequence. Moreover, the influence of PM diversity on the torque ripple proves to be more obvious than that of tooth-bulges, which is mainly due to the more obvious additional back EMF harmonics. However, the influence of manufacturing tolerances on the performance of back EMF and on-load torque is relatively lower when compared with that on cogging torque.

4.5 Prototypes and Tests

A. Prototypes with Different Rotor Contours

It has been found that the cogging torques of IPM machines by the eccentric and sinusoidal rotor contours exhibit different sensitivities to manufacturing tolerances, especially when the PM diversity occurs. In order to verify the different influences by manufacturing tolerances and avoid the complicated sampling tests on numerous bulk products, prototypes are fabricated with amplified tolerances, as shown in Fig. 4.51. On the one hand, different types of PMs (sintered and bonded NdFeB materials, one type is assumed to be non-ideal) are employed to verify the influence of PM diversity, with the PM magnetic properties shown in Table 4.1. On the other hand, an ideal stator and a non-ideal stator with one 0.2mm tooth-bulge are fabricated, in addition to the two different rotors.

(a) Ideal stator

(b) Stator with one tooth-bulge

(c) Eccentric rotor

(d) Sinusoidal rotor

Fig. 4.51 12-slot/8-pole IPM machine prototypes with different rotor contours (3-step-skewing by 5°, 0° and -5°).

TABLE 4.1

COMPARISON OF MAGNETIC PROPERTIES BETWEEN TWO TYPES OF PMS

PM types	PM remanence (T, 20 ℃)	Coercive force (kA/m)
Sintered NdFeB	1.32	972.6
Bonded NdFeB	0.83	610

In order to measure the cogging torque, the test platform on basis of a lathe is established, as shown in Fig. 2.31. When the rotor rotates, the cogging torque values at different rotor positions can be reflected by the scale [ZHU09]. First, the cogging torque of the ideal prototypes (with sintered NdFeB magnets) is tested, as shown in Fig. 4.52. It can be seen that the magnitudes of the cogging torque are within ±17mNm for both of the two designs, despite some additional components introduced.

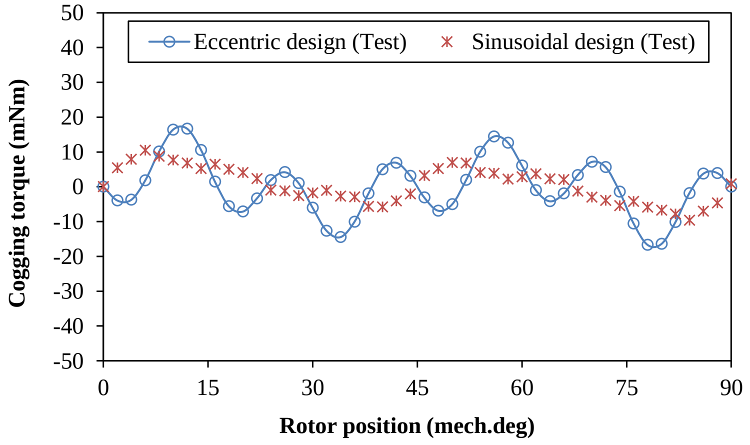

(a) Waveforms (1/4 revolution)

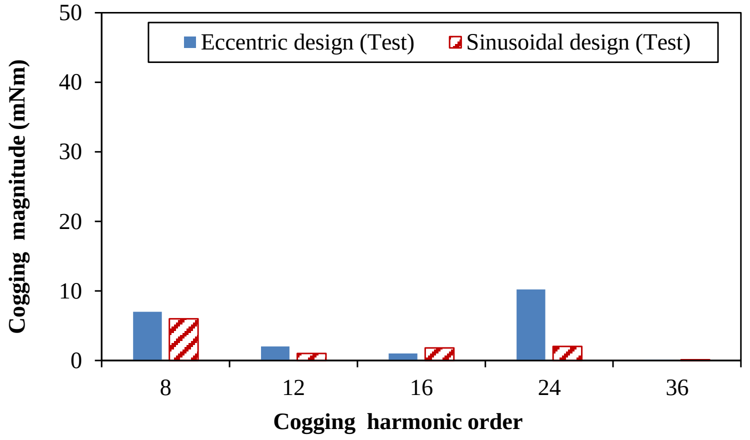

(b) Harmonics

Fig. 4.52 Comparison of cogging torques between eccentric and sinusoidal designs under ideal conditions (3-step-skewing by 5°, 0° and -5°).

Then, the cogging torques of the prototypes with consequent distributions of sintered and bonded NdFeB PMs are tested and compared, with the waveforms and harmonics shown in Figs. 4.53 (a) and (b) respectively. In addition, the 3-dimensional (3D) FE results are also illustrated for comparison (2D FE results are also provided in the Appendix of this chapter). It can be seen that the 12th order of cogging torque exists in both of the two prototypes, although the conventional 3-step-skewing method is employed. Moreover, the eccentric design presents much higher values of the 12th cogging torque than the sinusoidal design – 60mNm and 31mNm respectively, which verifies that the cogging torque of the eccentric design is much more sensitive to the PM diversity during the manufacturing process.

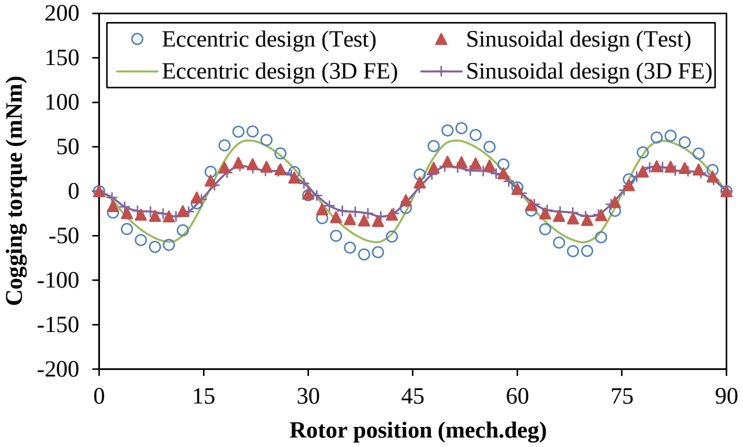

(a) Waveforms (1/4 revolution)

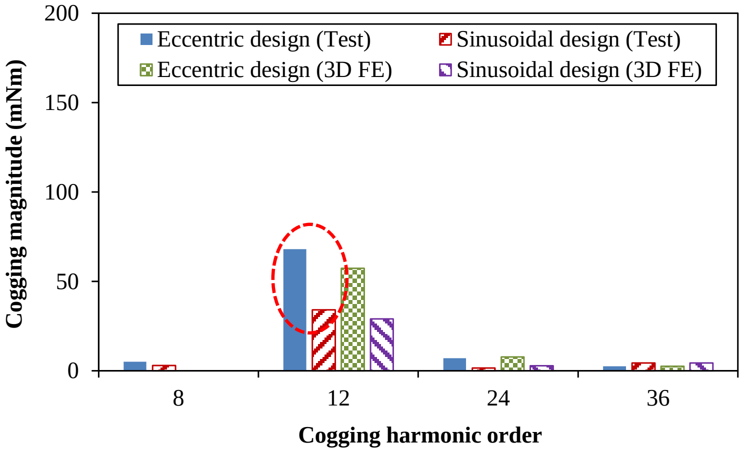

(b) Harmonics

Fig. 4.53 Comparison of cogging torques between eccentric and sinusoidal designs with consequent distribution of 4 non-ideal PMs (3-step-skewing by 5°, 0° and -5°).

Moreover, the cogging torques of the prototypes with the non-ideal stator and ideal rotors are also tested in order to identify the influence of non-ideal stator out-of-roundness, as shown in Fig. 4.54. It can be seen that the 8th order of additional cogging torque components are introduced in the eccentric and sinusoidal designs, 46mNm and 34mNm respectively.

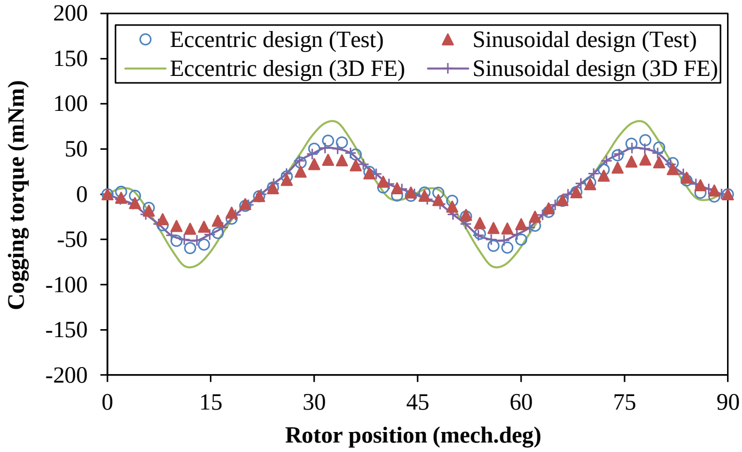

(a) Waveforms (1/4 revolution)

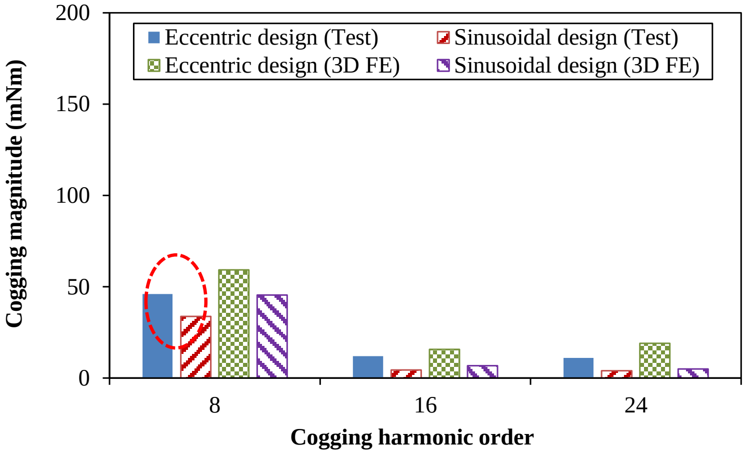

(b) Harmonics

Fig. 4.54 Comparison of cogging torques between eccentric and sinusoidal designs with one 0.2mm tooth-bulge (3-step-skewing by 5 °, 0 °and -5 °).

Although the potential PM diversity and tooth-bulges in real products will not have such severe tolerances as presented, the employed test methods can avoid the complicated sampling tests on numerous products and the results can still verify the different sensitivities between the two designs of rotor contours. Therefore, particular considerations should be made on the eccentric rotor contour (especially the eccentric distance), in order to reduce the sensitivity to manufacturing tolerances.

B. Prototypes with Different Slot/Pole Combinations

The influence of manufacturing tolerances on cogging torque has been investigated and compared between the 12-slot/8-pole and the 12-slot/10-pole designs, which shows that the two IPM designs exhibit different sensitivities to the tolerances. As verification, prototypes of the two designs are fabricated, as shown in Fig. 4.55. Similarly, in order to reflect the influence of PM diversity, the two different materials of PMs are provided (with properties shown in Table 4.1), distributed according to the most sensitive cases of the two designs respectively (as shown in Fig. 4.28). Moreover, the non-ideal stator by one 0.2mm tooth-bulge is also employed to verify the influence of non-ideal stator out-of-roundness.

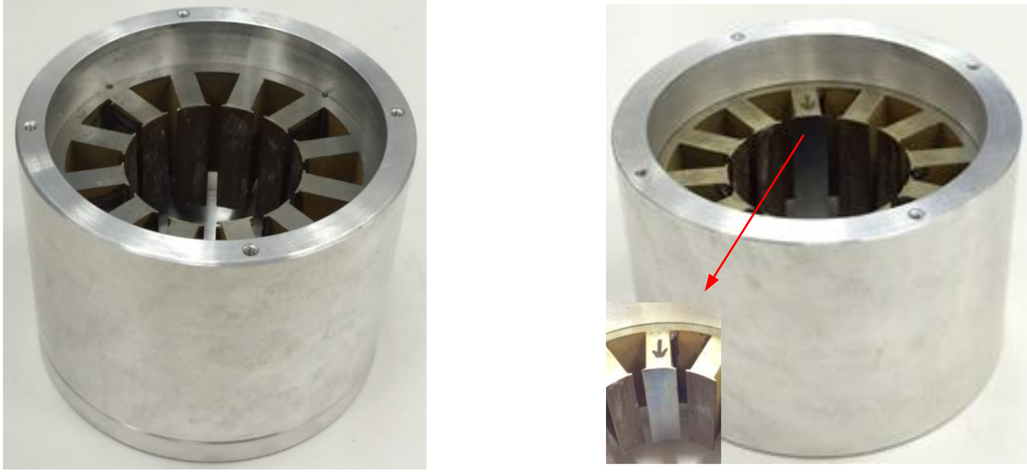

(a) Stator (ideal)

(b) Stator (one 0.2mm tooth-bulge)

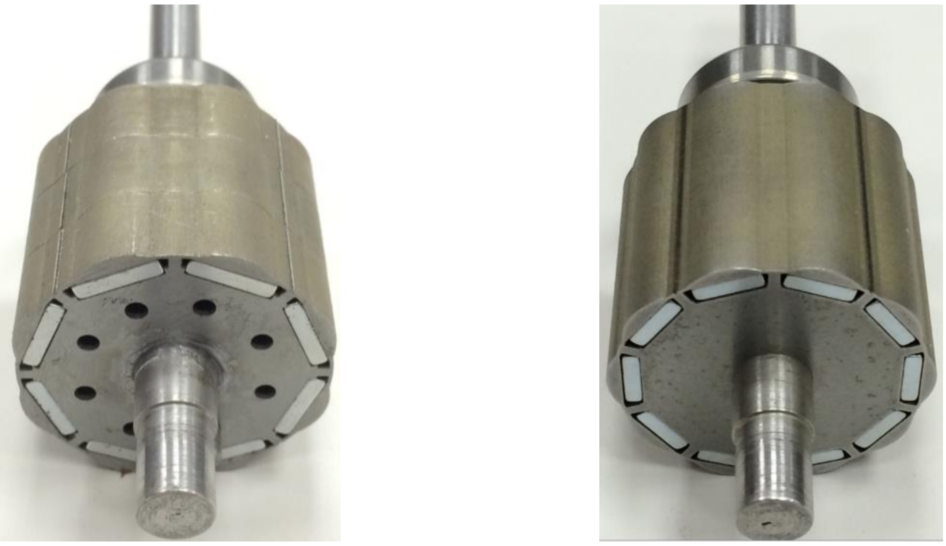

(c) 8-pole rotor

(d) 10-pole rotor

Fig. 4.55 12-slot/8-pole and 12-slot/10-pole IPM machine prototypes with eccentric rotor contours (A=13.8mm).

First, the 8-pole and 10-pole prototypes are tested under ideal conditions (without PM diversity or tooth-bulge), with the cogging torques shown in Fig. 4.56. It can be seen that no obvious additional cogging torque components are introduced. Despite the high magnitude (as high as 135mNm), the 24th order of cogging torque of the 8-pole design can be effectively reduced by employing the step-skewing method.

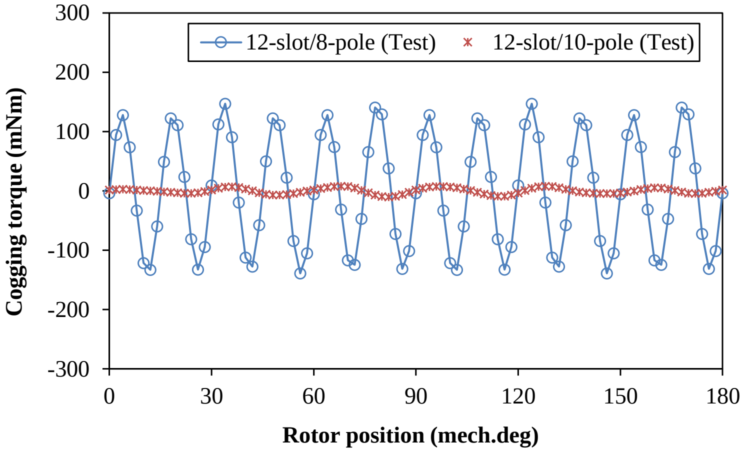

(a) Waveforms

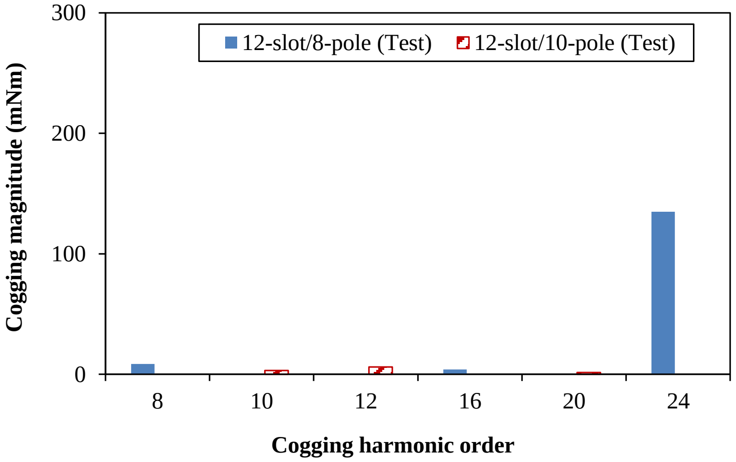

(b) Harmonics

Fig. 4.56 Comparison of cogging torques between 12-slot/8-pole and 12-slot/10-pole designs under ideal conditions.

Then, the prototypes by the ideal stator and non-ideal 8-pole and 10-pole rotors (different materials of PMs inside, according to the most sensitive distributions of non-ideal PMs respectively) are tested, with the cogging torques shown in Fig. 4.57. As can be seen, the 12th order of additional cogging torque components are introduced in both of the two designs, 101mNm and 135mNm respectively. Therefore, the 12-slot/10-pole design proves to be more sensitive to the PM diversity than the 12-slot/8-pole design, which agrees with the foregoing analyses.

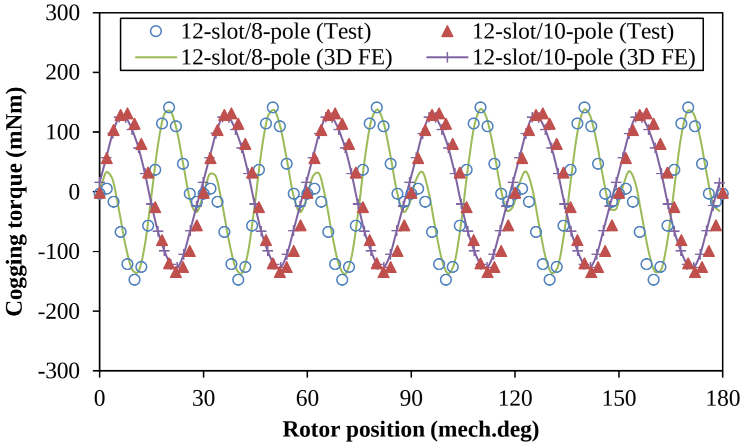

(a) Waveforms

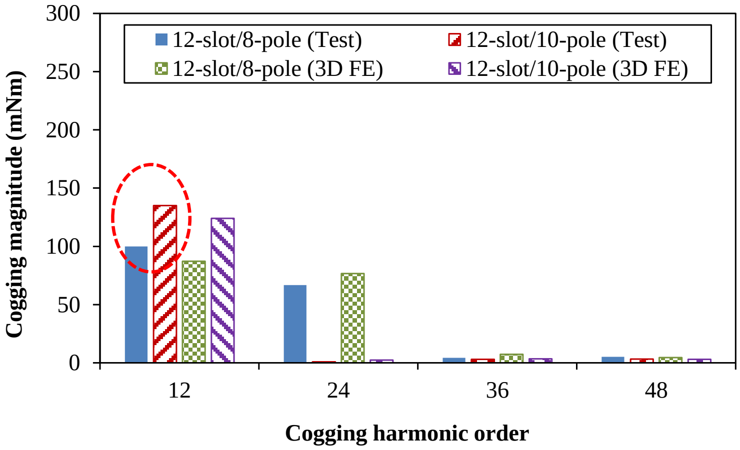

(b) Harmonics

Fig. 4.57 Comparison of cogging torques between 12-slot/8-pole and 12-slot/10-pole designs with the most sensitive distributions of non-ideal PMs.

Moreover, the prototypes by the non-ideal stator (with one 0.2mm tooth-bulge) and the ideal rotors are also tested, with the cogging torques shown in Fig. 4.58. It can be seen that the 8th order of additional cogging torque in the 8-pole machine are much higher than the 10th cogging torque in the 10-pole machine, 55mNm and 27mNm respectively. Considering the low harmonic orders, it is unrealistic to reduce the additional cogging torques by skewing. Therefore, the 12-slot/8-pole design proves to be much more sensitive to the assembling tooth-bulges than the 12-slot/10-pole design, which verifies the aforementioned different sensitivities of the two designs.

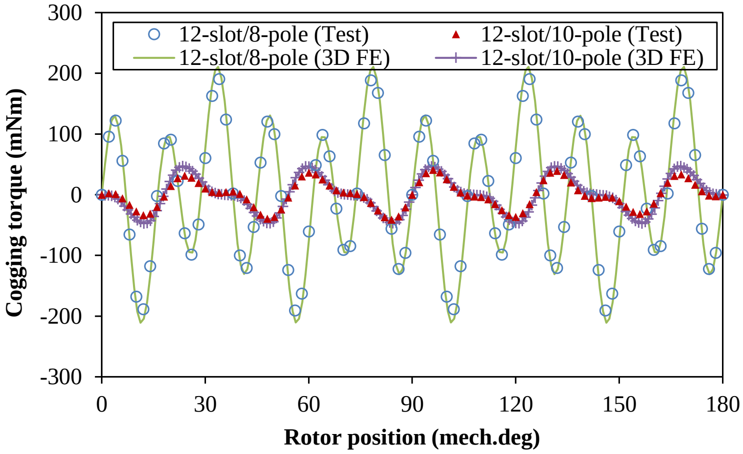

(a) Waveforms (1/2 revolution)

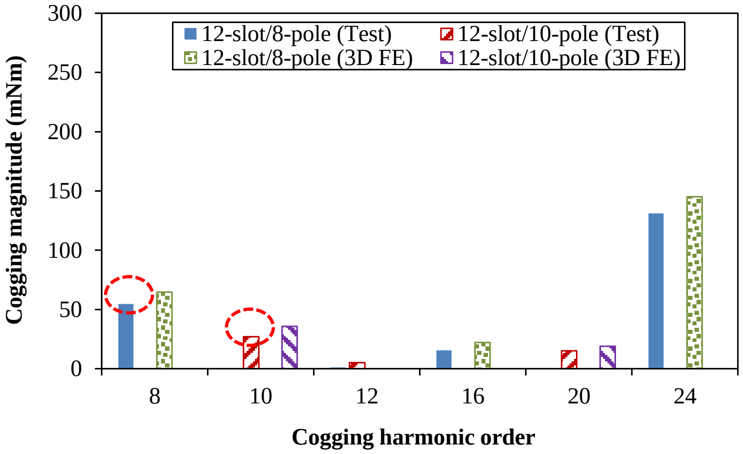

(b) Harmonics

Fig. 4.58 Comparison of cogging torques between 12-slot/8-pole and 12-slot/10-pole designs with one tooth-bulge (0.2mm).

4.6 Conclusion

12-slot/8-pole IPM machines with the eccentric and the sinusoidal rotor contours have firstly been presented, based on which the influence of the four typical manufacturing tolerances on cogging torque has been investigated and compared. Based on the most sensitive case of PM diversity, the influence by consequent distribution of abnormal PMs is analyzed, which introduces much higher cogging torque (the 12th order) in the eccentric design than in the sinusoidal design. Moreover, both of the two rotor designs prove to be sensitive to the tooth-bulges during the assembling of modular stator teeth, resulting in additional cogging torques (the 8th order), especially when four tooth-bulges belonging to the same phase exist.

Compared with the 12-slot/8-pole machine, the 12-slot/10-pole design exhibits different sensitivities to the tolerances. With the PM diversity considered, the most sensitive case in the 12-slot/10-pole design proves to be the two adjacent non-ideal PMs and their opposite, which introduces higher additional cogging torque component (the 12th). However, the 12-slot/10-pole design is much less sensitive to the tooth-bulges, and the maximum additional cogging torque is also introduced by the four tooth-bulges belonging to the same phase.

In addition, it has also been proven that the sensitivity to PM diversity in eccentric designs can be reduced by adjusting the eccentric distance whilst no obvious effect is achieved on reducing the influence of tooth-bulges.

For verification, the spatial field harmonics under ideal and non-ideal conditions have been analyzed respectively, followed by the tests on different prototypes.

Appendix - Comparison of cogging torque between 2D and 3D FE results

A. IPM designs with different rotor contours

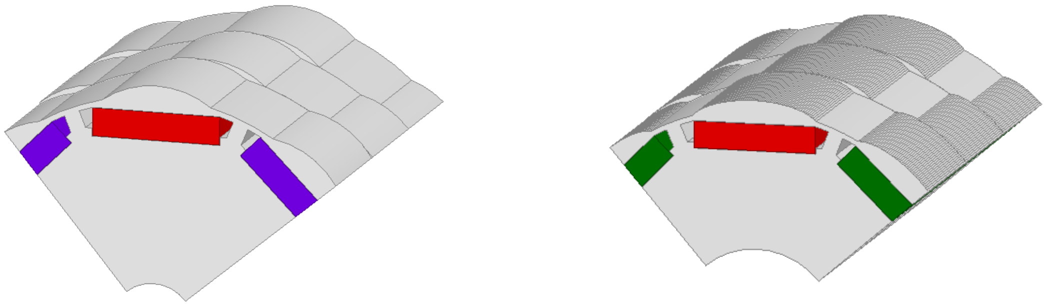

(a) 3D models of Eccentric (left) and sinusoidal (right) designs (stator not shown)

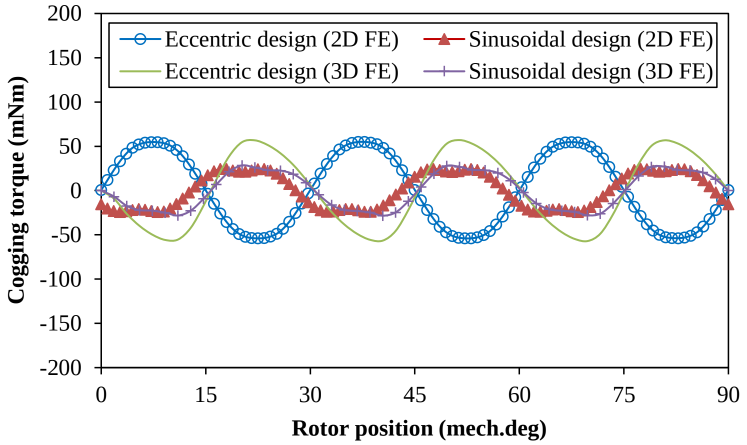

(b) Waveforms

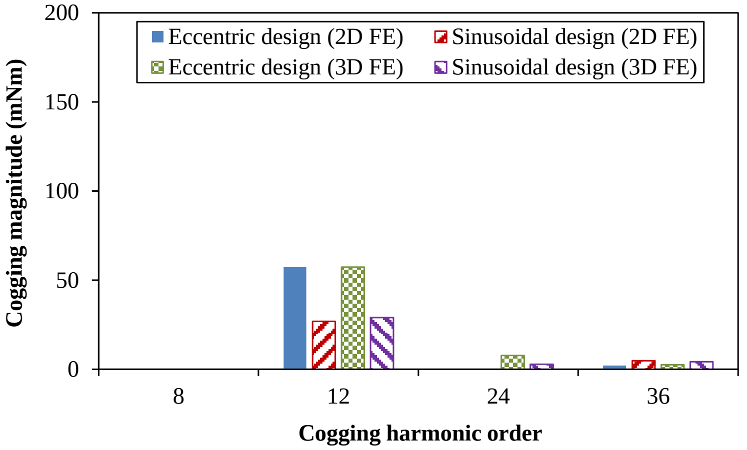

(c) Harmonics

Fig. 4.A.1 Cogging torques of eccentric and sinusoidal designs with consequent distribution of 4 non-ideal PMs (3-step-skewing by 5 °, 0 ° and -5 °).

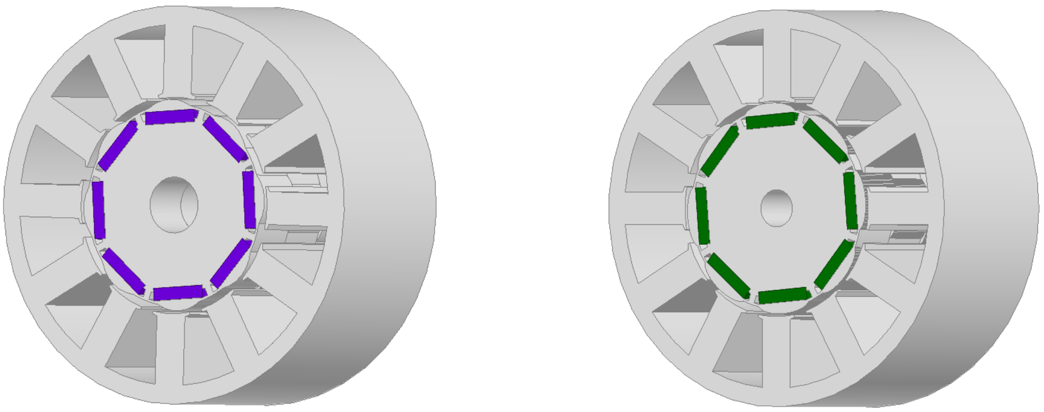

(a) 3D models of Eccentric (left) and sinusoidal (right) designs

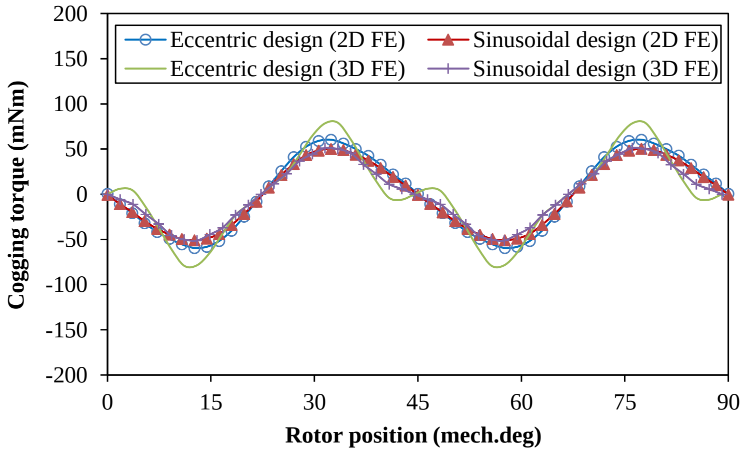

(b) Waveforms

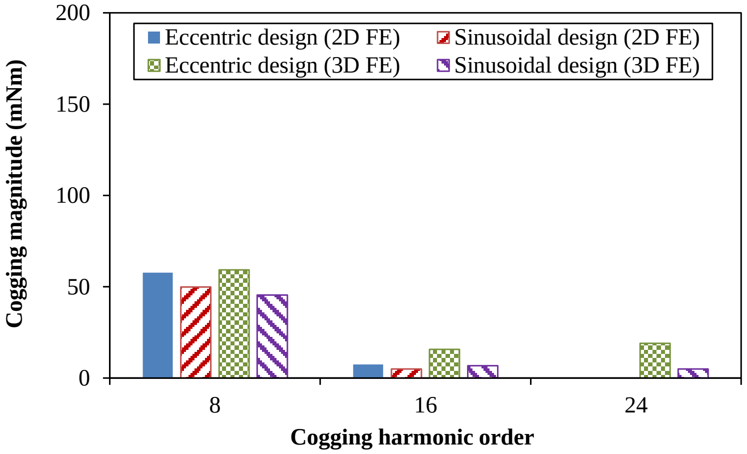

(c) Harmonics

Fig. 4.A.2 Cogging torques of eccentric and sinusoidal designs with one 0.2mm tooth-bulge (3-step-skewing by 5 °, 0 ° and -5 °).

B. IPM designs with different slot/pole combinations

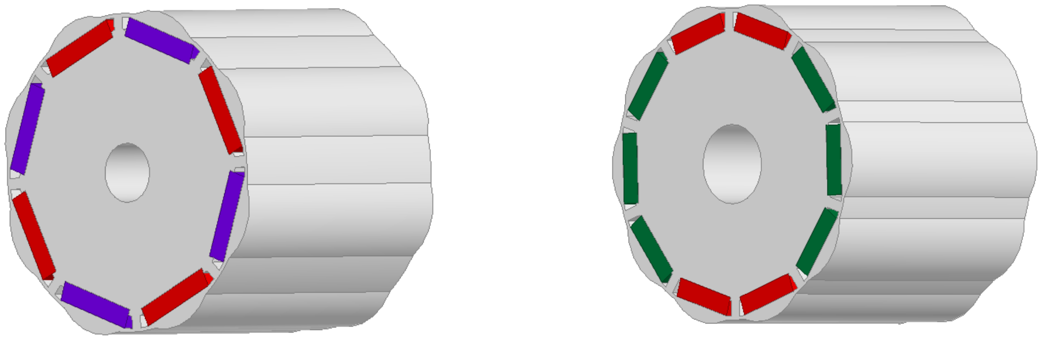

(a) 3D models of 12-slot/8-pole (left) and 12-slot/10-pole (right) designs (stator not shown)

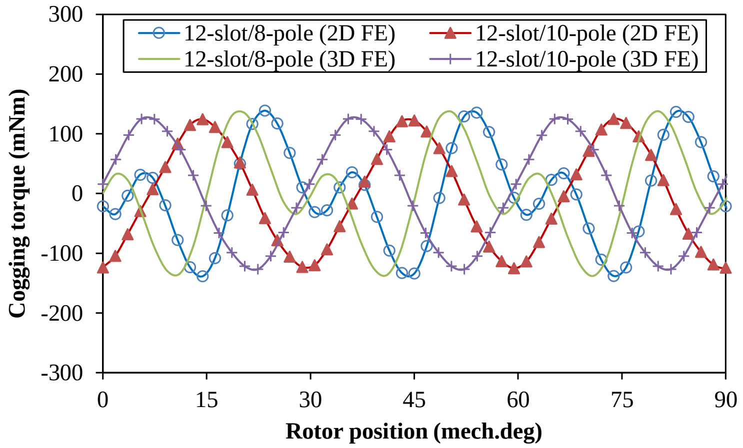

(b) Waveforms

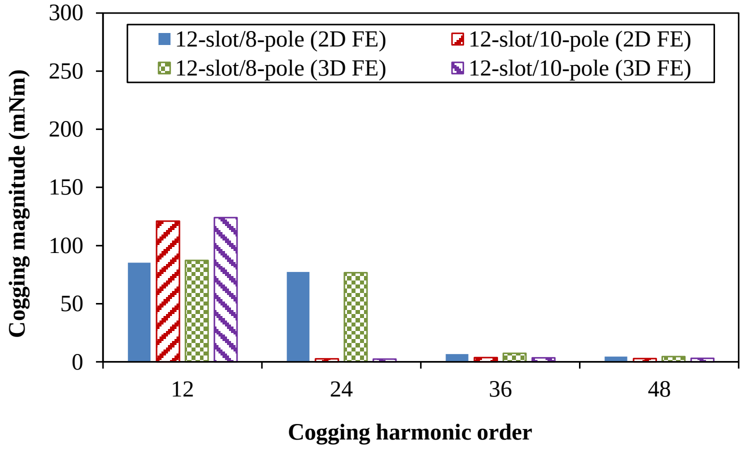

(c) Harmonics

Fig. 4.A.3 Cogging torques of 12-slot/8-pole and 12-slot/10-pole designs with most sensitive distributions of non-ideal PMs.

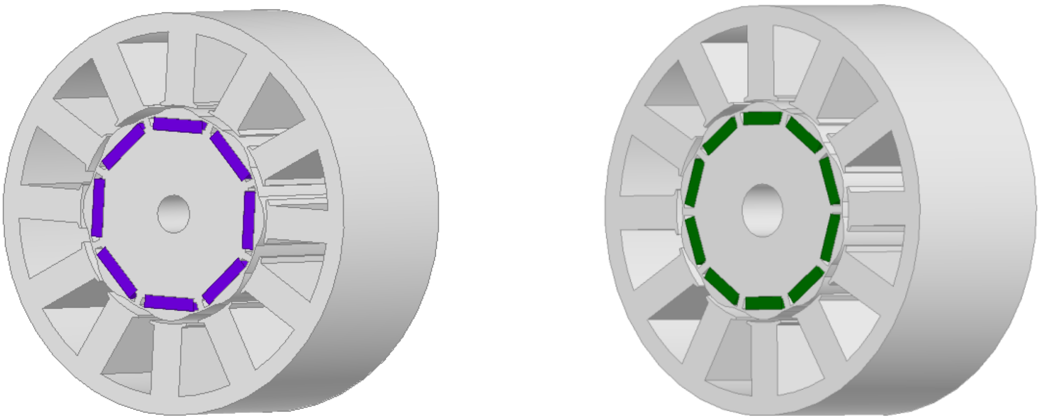

(a) 3D models of 12-slot/8-pole (left) and 12-slot/10-pole (right) designs

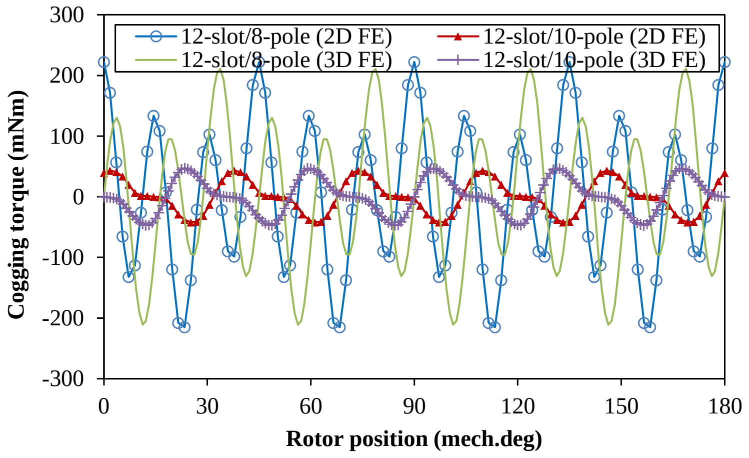

(b) Waveforms

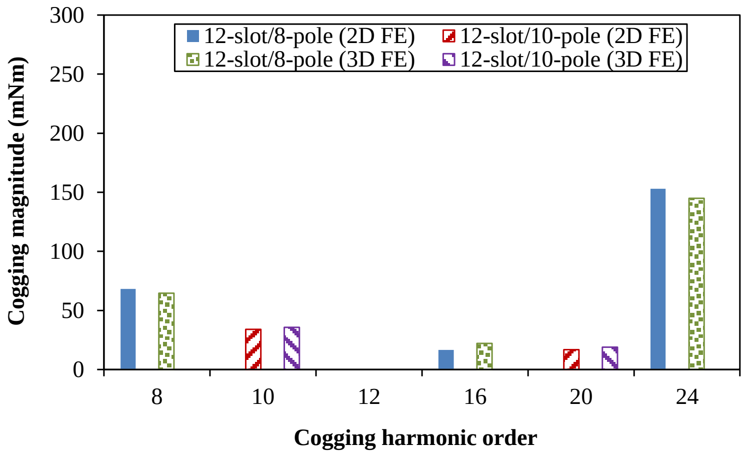

(c) Harmonics

Fig. 4.A.4 Cogging torques of 12-slot/8-pole and 12-slot/10-pole designs with one 0.2mm tooth-bulge.

CHAPTER 5 ANALYSIS OF WINDINGS IN VARIABLE RELUCTANCE RESOLVERS

5.1 Introduction

In order to realize precise control of electric machines, the rotor positions should be accurately estimated and provided to the driver. Amongst various position sensors, the variable reluctance (VR) resolvers are frequently employed in industrial applications, especially in vehicles, due to several significant advantages [SUN04], [SUN08], [KIM09], [KIM10], [KIM13b], [CUI12], e.g. the high reliability, the short axial dimension and easy integration, and the high detection accuracy, etc.

In this chapter, the basic structure and the operating principle of a conventional VR resolver will be introduced first. As important components of the VR resolver, three sets of windings are wound on the stator teeth, i.e. the exciting, the SINE and Cosine windings, which closely relate to performance of this sensor (Compared with three-phase designs, two-phase resolvers are much more frequently used in recent decades, through which the production cost of windings and decoding chips can be obviously reduced). The specific research work will begin with the analyses of resolver windings - a base condition for further development.

Fig. 5.1 illustrates a typical model of conventional VR resolver [SUN04]. Three sets of coils are located on each stator tooth, and the rotor contour is particularly designed in order to make the air-gap permeance close a sinusoidal variation. More specifically, the exciting winding is composed of several uniform coils with alternate polarities, while the SINE and COSINE output windings are both sinusoidally distributed and electrically perpendicular to each other, as can be seen from Fig. 5.1 (b). It should also be noted that the output coils adjust the polarities every other tooth due to the alternate polarities of the exciting coils, which are not shown in Fig. 5.1. The most significant difference in operating principle between the wound-field (WF) type and the VR type of resolvers can also be deduced from the structures. For the former, the air-gap length is basically constant and the sinusoidal air-gap flux density is established through the sinusoidal magnetomotive forces (MMF) produced by the exciting winding which is arranged in sinusoidal distribution. However, for the latter, the exciting winding is composed of several uniform coils and the sinusoidal air-gap flux density is established through sinusoidal air-gap permeance, which can be obtained by the rotor contour (different air-gap lengths at different rotor positions). As no winding is located on the rotor, no brush is required for VR resolvers.

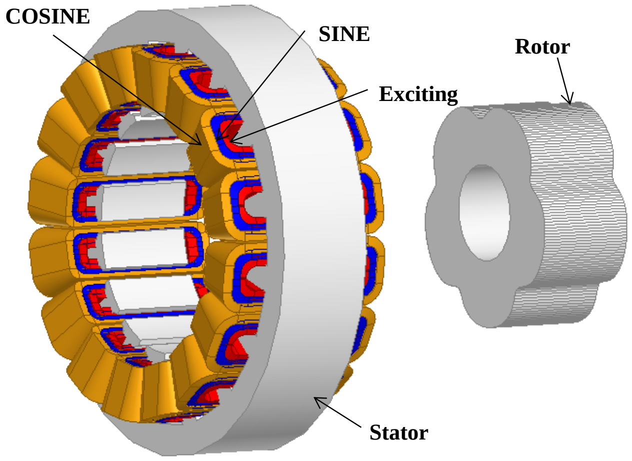

(a) Basic structure

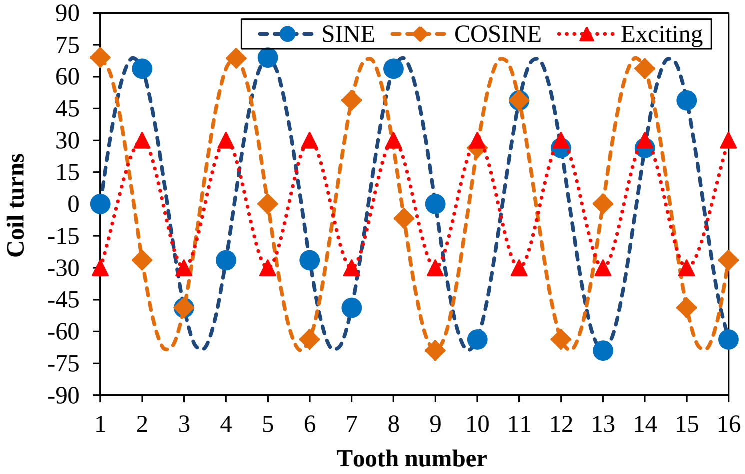

(b) Typical winding distribution

Fig. 5.1 Conventional VR resolver (5 rotor saliencies).

5.2 Analytical Derivation of Operating Principle for VR Resolvers

In this section, the relationship between the numbers of stator teeth Z, rotor saliencies p and output winding polarities $2p_w$, is established, together with the description of basic operating principles. Based on the air-gap function of a conventional VR resolver and with the higher-order permeance harmonics ignored, the air-gap permeance facing to the k^{th} stator tooth can be described as [SUN08], [CUI12]:

$$P_k = P_0 + P_{m1}\cos(p\theta - \alpha_k) \tag{5. 1}$$

$$\alpha_k = \left[(k-1)\frac{2\pi p}{Z}\right] \tag{5. 2}$$

where θ represents the rotational angle, P_0 is the constant component of air-gap permeance and P_{m1} is the amplitude of sinusoidal component, and α_k is the electrical angle difference between the first and the kth stator teeth. With the polarity considered, turns of exciting coil on the kth stator tooth can be expressed by:

$$N_{ek} = N_{e0}\cos[(k-1)\pi] \tag{5. 3}$$

where N_{e0} represents the absolute value of turns per stator tooth. Take the SINE phase for example, the winding is arranged in sinusoidal distribution, and turns of coil on the kth stator tooth can be presented by:

$$N_{sk} = N_{s0}\sin\left[(k-1)\frac{2p_w\pi}{Z}\right] = N_{s0}\sin\left(\frac{p_w}{p}\alpha_k\right) \tag{5. 4}$$

Here, N_{s0} represents the maximum number of coil turns. Different from the derivation in the previous papers [SUN08], [CUI12], p_w is introduced in this formula in order to distinguish winding pole pairs from rotor saliencies.

Before the derivation of output voltages, it is necessary to describe the feature of input impedance. Based on the magnetic circuit, this parameter can be obtained by:

$$X_{in} = \sum_{k=1}^{Z} 2\pi f N_{e0}^2 P_k = 2\pi f N_{e0}^2 Z P_0 \tag{5. 5}$$

where f is the frequency of exciting voltage. It can be seen from (5.5) that the input impedance is constant, independent of rotational angle. With the permeance of some higher-order harmonics considered, slightly varying components will exist. However, the amplitude of the corresponding permeance is much lower and can be ignored. As a result, the amplitude of exciting current will keep constant as well, when a sinusoidal voltage of high frequency is applied to the exciting winding.

Without considering the motional electromotive force (this component will be further investigated in the Chapter 6), the voltage induced in the output coil on the kth stator tooth can be described as:

$$E_{sk} = -\frac{\mathrm{d}\psi_{sk}}{\mathrm{dt}} = -N_{sk}N_{ek}P_k\frac{\mathrm{d}I_m}{\mathrm{dt}} \tag{5. 6}$$

where ψ_{sk} is the flux-linkage of the output coil on the kth stator tooth and I_m represents the exciting current. As a result, the output voltage of SINE output winding will be:

$$E_s = \sum_{k=1}^{Z} E_{sk} = -N_{e0}N_{s0}\frac{\mathrm{d}I_m}{\mathrm{dt}}\sum_{k=1}^{Z}\cos[(k-1)\pi] \cdot \sin\left(\frac{p_w}{p}\alpha_k\right)\{P_0 + P_{m1}\cos[p\theta - \alpha_k]\} \tag{5. 7}$$

It is obvious that P_0 will not contribute to the synthetic voltage of SINE phase, and (5.7) can be rewritten as:

$$E_s = -N_{e0}N_{s0}P_{m1}\frac{\mathrm{d}I_m}{\mathrm{dt}}\sum_{k=1}^{Z}\cos[(k-1)\pi].\sin\left(\frac{p_w}{p}\alpha_k\right) \cdot \{\cos(\alpha_k)\cos(p\theta) + \sin(\alpha_k)\sin(p\theta)\} \tag{5. 8}$$

The exciting current proves to be a signal with constant amplitude and the same frequency as the exciting voltage, independent of the rotational angle. As a result, it can be deduced that when the number of stator teeth, rotor saliencies and output winding polarities meet the requirement expressed by (5.9), the output voltages of the SINE winding will present a sinusoidal variation corresponding to p times of the rotational angle θ.

$$p_w = p \text{ or } \frac{Z \pm 2p_w}{2} = p \tag{5. 9}$$

Then the output voltage of SINE phase will be:

$$E_s = \pi f N_{e0}N_{s0}P_{m1}ZI_m\sin(p\theta) \tag{5. 10}$$

Comparing (5.10) with (5.5), the ideal transformation ratio of resolver can be described as:

$$\varepsilon = \frac{N_{s0}P_{m1}}{2N_{e0}P_0} \tag{5. 11}$$

Similarly, the same conclusion can be obtained for the output signal of COSINE phase, which will not be duplicated here.

As can be seen from (5.9), the pole pairs of output windings are not necessarily equal to rotor saliencies, and other stator slot and rotor pole combinations can also be adopted in the design of a VR resolver. Further explanation of stator slot and rotor pole combination as well as potential applications will be discussed in the following parts.

In order to clearly describe of the operating principle, a FE model of 5 rotor saliencies (designated as 5-X) resolver with 8 stator teeth is made, and voltages induced in each coil of SINE phase are decoded and shown in Fig. 5.2 (a), with the synthetic voltages presented in Fig.

5.2 (b). According to (5.4), there is no coil on the 1st and the 5th stator teeth, and the SINE phase winding has 6 coils in total, which can be divided into two groups: the positive and the negative. For a single coil, the output voltage is not a sinusoidal waveform, but also contains a cosine and a DC components, which can be reflected in (5.8). However, the synthetic voltage of positive coils will present a sinusoidal variation, together with a DC component. When the synthetic voltage of negative coils is added, the DC component will be eliminated and an ideal sine waveform is generated.

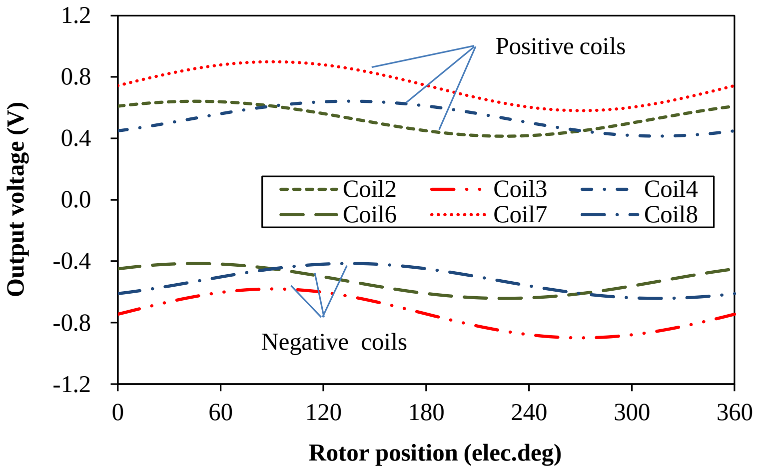

(a) Output voltage in each coil

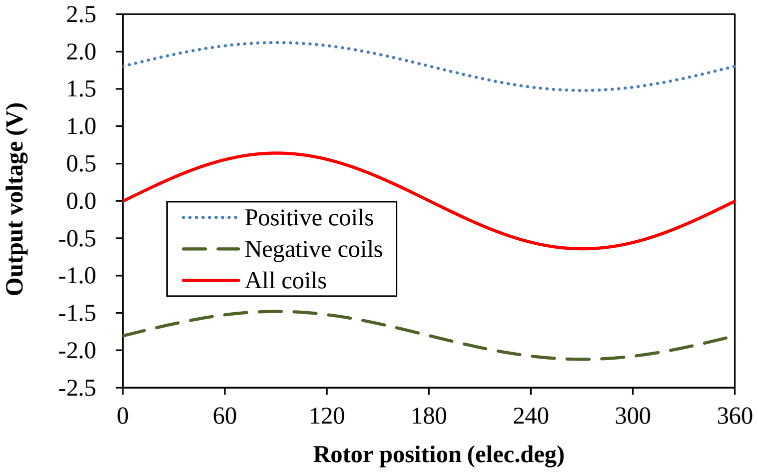

(b) Synthetic output voltages

Fig. 5.2 Decoded output voltage in coils of SINE winding (Z=8, p=5, obtained by FE analyses).

5.3 Stator Slot and Rotor Pole Combination

The analytical derivation and FE verification have been given to demonstrate the operating principle of VR resolver as well as the relationship of stator slot and rotor pole combinations. In this part, a comparison between 2-pole, 6-pole and 10-pole winding distributions is made, as an example to further explain the essence of this relationship.

5.3.1 Identical Stator and Windings for Different Poles of Resolvers

According to (5.9), 2-pole output winding can be used in 1-X, 3-X and 5-X VR resolvers which have 8 stator teeth. Also, 3-X and 5-X resolvers can be realized through 6-pole and 10-pole of windings, respectively. Fig. 5.3 illustrates the distributions of three different poles of windings.

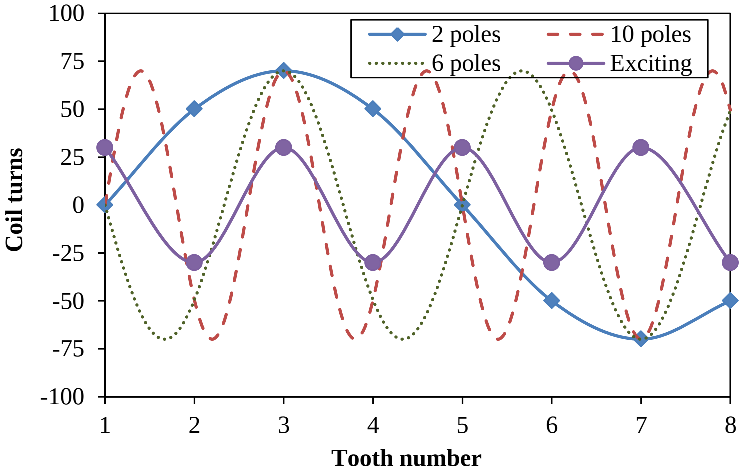

Fig. 5.3 Comparison of 2-pole, 10-pole and 6-pole winding distributions under 8 stator teeth.

It can be seen that the number of turns for each coil of 10-pole winding is equal to that of 6-pole winding. As the coil polarity should be reversed every alternate tooth in order not to eliminate the output voltage, the two windings become the 2-pole winding. It means that for 8 stator teeth, 5-X and 3-X resolvers have identical winding distribution, which is similar to that of 2-pole winding.

As a verification of the above analysis, an FE model of 8 stator teeth is made with 2-pole output windings plotted in Fig. 5.3, and then the 3-X and the 5-X rotors are attached to the model respectively, as shown in Figs. 5.4 (a) and (b). The output of SINE phase winding is examined when the rotor rotates for 1 revolution. It can be seen from Fig. 5.4 (c) that the two combinations present 6-pole and 10-pole sinusoidal signals respectively, which indicates the feasibility of identical stator and winding to be shared by different poles of resolvers.

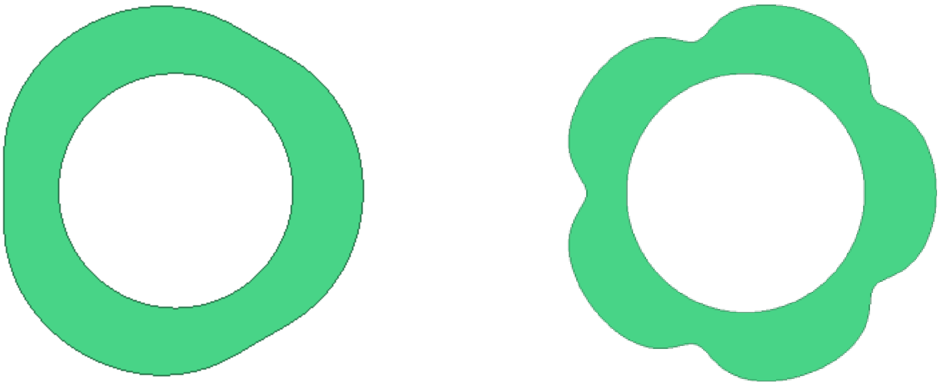

(a) 3-X rotor (b) 5-X rotor

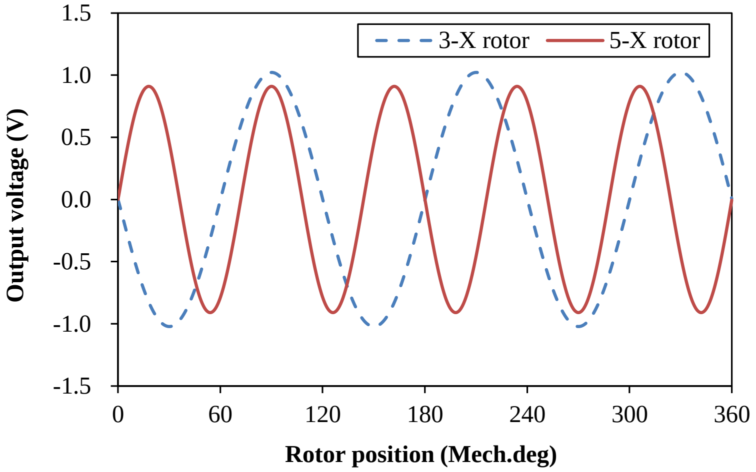

(c) Output voltages (SINE phase)

Fig. 5.4 Output voltages for 3-X and 5-X resolvers with identical stator and windings.

Based on above analyses, a summary of conventional stator slot and rotor pole combinations can be summarized in Table 5.1, from which some conclusions can be obtained. First, a certain number of stator teeth can be used for an arbitrary number of resolver poles, (for example, all of 2-X, 3-X, 4-X, 6-X, 7-X and 8-X resolvers can be realized through 10 stator teeth), which is beneficial to serialization products. Second, identical stator with its winding can be shared by two resolvers with different numbers of rotor saliencies, (for example, 5-X and 7-X rotors can share a 12-tooth stator and its winding), and the sum of rotor saliencies is equal to the number of stator teeth.

It is proposed that the number of stator teeth should be carefully selected in order to cover two potential designs. Actually, there are other considerations in choosing this number, which will be discussed in the following part.

TABLE 5.1

IDENTICAL STATOR AND WINDINGS FOR RESOLVERS WITH VARIANT ROTOR SALIENCIES

Stator teeth Z	Rotor saliencies p		
	(p_W=1)	(p_W=2)	(p_W=3)
8	3, 5	2,6	1,7
10	4,6	3,7	2,8
12	5,7	4,8	3,9
14	6,8	5,9	4,10
16	7,9	6,10	5,11
18	8,10	7,11	6,12
20	9,11	8,12	7,13

5.3.2 Selection of Slot and Pole Combinations for Minimum Voltage Harmonics

According to the foregoing analyses, there are multiple choices for the number of stator teeth during design of a resolver, and it is recommended by previous papers that the number should be increased in order to reduce harmonics in output voltages which will influence position detection accuracy [SUN08]. However, the number of stator teeth is always restricted to the resolver size with mechanical strength considered, especially for multi-polar resolvers.

If the number of stator teeth cannot be more than 4 times of rotor saliencies, a parameter q is defined in this thesis, as shown in (5.12), in order to help the designer to make an initial evaluation of harmonics for potential stator slot and rotor pole combinations. Essentially, this parameter represents the actual average number of stator teeth allocated for each pole of output winding, which cannot be judged simply by $Z/2p$. It is proposed that the value of this parameter q should be selected as high as possible.

$$q = \frac{Z}{|Z - 2p|} \qquad (Z \neq 2p, Z \leq 4p\ ) \tag{5. 12}$$

For verification, 5 different numbers, i.e. 12, 14, 16, 18 and 20, of stator teeth are selected for the 5-X resolver separately in order to investigate the influence of this number on harmonics. Some basic conditions are defined in order for fair comparison:

(a) constant exciting current and frequency;

(b) identical rotor;

(c) same outer and inner diameters of stator;

(d) identical number of exciting coils per tooth;

(e) same maximum number of output coils per tooth.

In addition, other dimensions, for example the tooth width, are inversely proportional to the number of stator teeth. With respect to the requirement of automatic winding fabrication, there is always a minimum value for the slot opening of stator, and this value is fixed as 1.4mm in the following comparison. Common parameters of the five models are shown in Table 5.2.

In order to simplify the analysis, a 50mA sine current with the frequency of 10 kHz is applied to the exciting coils in Maxwell 2D, and the envelope of the output voltage in SINE or COSINE winding is collected for FFT analysis. Major harmonic components for the five designs are shown in Fig. 5.5. It should be noted that only some major harmonics are listed, and in fact there are still some other higher orders of harmonics which are not shown.

TABLE 5.2

COMMON PARAMETERS FOR DIFFERENT DESIGNS

Parameters	Values
Stator outer diameter	37mm
Stator inner diameter	20mm
Core axial length	8 mm
Stator slot opening width	1.4mm
Min. and Max. air-gap length	0.5mm, 1.61mm
Exciting coil turns per tooth	30
Max. of output coil turns per tooth	70
Exciting signal	0.05A (10kHz)

As can be seen from Fig. 5.5, THD values of the output voltages increase from 0.02% to 0.049%, when the number of stator teeth changes from 12 to 18. It indicates that increasing the stator teeth will not reduce harmonics in the output signals. In contrast, values of the parameter q keep decreasing, which are 6, 3.5, 2.7 and 2.25 respectively. Moreover, when this number is selected as 20 (one conventional design of VR resolver with simplified manufacturing process, which will be further investigated), 4 times of rotor saliencies, there will be a significant increase for the THD value, which is mainly caused by the 3rd and 5th tooth harmonics. The FE results illustrate that it is the parameter q defined by (5.12) that actually reflects the level of harmonics in output voltage of resolver, rather than the number of stator teeth itself, which verifies the above conclusion.

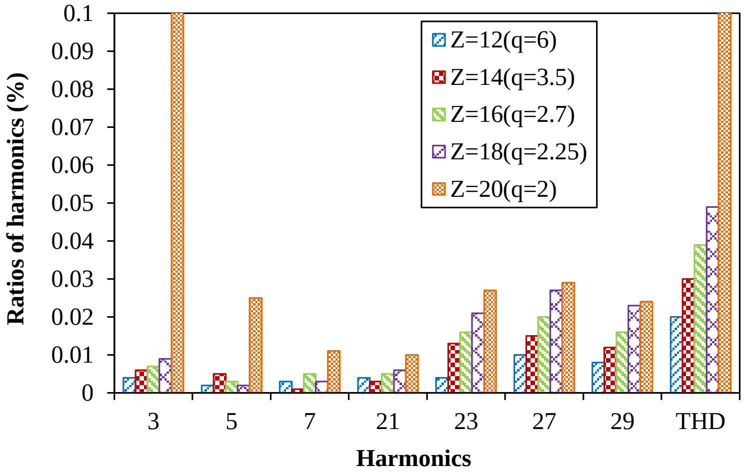

Fig. 5.5 Voltage harmonics for 5-X resolvers with different numbers of stator teeth (obtained by FE analysis).

It can be further deduced that the VR resolver in which the number of stator teeth *Z* approaches two times of rotor saliencies 2*p* usually has a lower content of harmonics. The design according to this concept can be designated as ‘close-slot-pole’ design, which is often adopted in the design of permanent magnet machines. In addition to low content of harmonics in the output voltages, there are also some other advantages for the ‘close-slot-pole’ design. From one hand, the number of coils is reduced, which simplifies the winding fabrication; from the other hand, small-scale resolver can be realized due to the reduced number of stator teeth with mechanical strength considered.

5.4 Improvement of VR Resolvers by Alternate Tooth Windings

It is well known that a conventional VR resolver always has 3 sets of coils on each of the stator teeth (except a series of particular slot and rotor pole combinations – $Z=4p$), i.e. exciting coils, SINE coils and COSINE coils, which are arranged in certain sequence during production. In fact, the process of manufacture is very complicated and the quality is usually difficult to guarantee. First, coil locations cannot be kept symmetrical due to the 3 layers of coils on each stator tooth, thus yielding to DC components in output signals. Second, insulation of these slender wires can be easily damaged by multiple winding processes. Both of the two cases will degrade the position detection accuracy of resolver. Furthermore, output windings are always in sinusoidal distribution and coil turns are different from tooth to tooth, which makes the winding process even more complicated.

The main purpose of the research work in this section is to investigate potential improvements on resolver winding arrangement in order to simplify the winding fabrication and to solve the problems described above.

5.4.1 Alternate Tooth Windings for Particular Slot and Pole Combinations

Among various stator slot and rotor pole combinations, there are a series of particular combinations, of which the numbers of stator teeth and rotor saliencies exhibit a 4 times relationship, for example, a 5-X resolver with 20 stator teeth as described above.

According to (5.4) and (5.9), alternate tooth windings with identical coil turns can be adopted in the 5-X resolver, as shown in Fig. 5.6. It can be seen that the SINE and COSINE output windings are both composed of 10 identical coils, which are located on the even numbers and the odd numbers of stator teeth, respectively. Separation of the SINE and COSINE output windings can be realized in such combinations. Moreover, these coils all have identical number of turns, which further simplify the manufacturing process. However, the quality of output signals should be evaluated.

As it is well known, the numbers of stator teeth and rotor saliencies have a close relationship with tooth harmonics which cannot be eliminated by the winding itself. For the 5-X resolver with 20 stator teeth, high percentages of the 3rd and 5th harmonics exist in the output voltages, as described in Fig. 5.5. Fig. 5.7 illustrates the position error caused by the harmonics. It can be seen that for ideal production and application environment the angle error of the 5-X resolver will be within ±0.2°, which will become even higher due to asymmetry and eccentricity during the process of production and instalment. Therefore, further improvement should be made to increase the accuracy (which will be further investigated in following chapters).

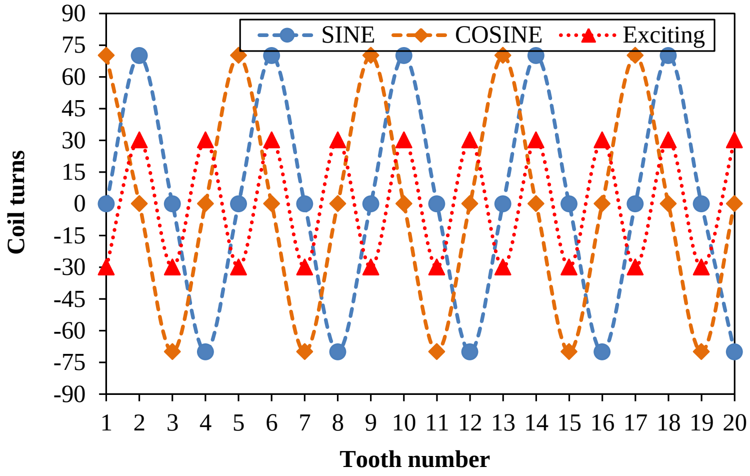

Fig. 5.6 Winding distributions of a conventional 5-X resolver with 20 stator teeth.

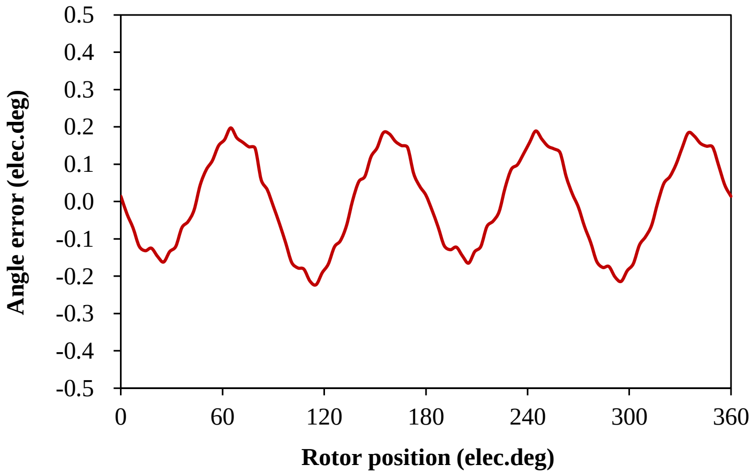

Fig. 5.7 Position errors of 5-X resolver with 20 stator teeth (obtained by FE analysis).

5.4.2 Alternate Tooth Windings for General Slot and Pole Combinations

It has been described above that alternate tooth windings can be employed in resolvers with particular combinations of which the number of stator teeth is 4 times of rotor saliencies. However, the angle error is still a barrier for widespread application of this design. As a matter of fact, alternate tooth windings can be adopted for resolvers with optional slot/pole combinations, based on the basic operating principle of resolver and the voltage distributions in each of the output coils. By way of example, analysis of a 5-X resolver with 16 stator teeth has been made in order to verify the feasibility of alternate tooth windings being used in general combinations and to further investigate specific performance, i.e. the angle error. Fig. 5.8 illustrates the laminations and windings of the 5-X resolver. Compared with resolvers with conventional windings shown in Fig. 5.1, the number of coils is significantly reduced.

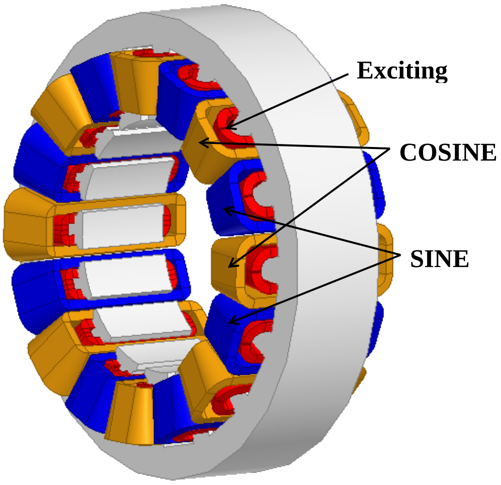

(a) Stator with alternate output windings

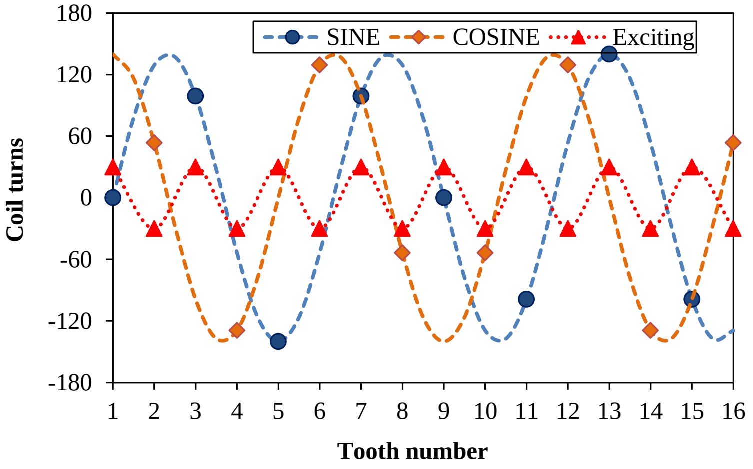

(b) Distribution of alternate tooth windings with different coils

Fig. 5.8 A design of VR resolver with alternate tooth windings (Z=16, p=5).

Since the perpendicular nature of the two output windings is unchanged, the two output signals still keep the phase angle difference of 90 electrical degrees, which is verified by FE result, as shown in Fig. 5.9. Considering the removal of half output coils, attention should be paid to the adjustment of coil turns in order to make the output voltage maintain proper amplitude for signal processing by resolver-to-digital (R/D) conversion integrated circuit (IC).

In addition to the verification of perpendicular characteristics, it is also necessary to make a comparison on the distribution of harmonics between resolvers with conventional and alternate tooth windings. Fig. 5.10 (a) illustrates the differences of harmonics distributions between the two designs. It can be seen that THD value of the output voltage has a slight increase from 0.039% to 0.045%. Differences in electric errors between conventional and alternate tooth windings have also been compared, as shown in Fig. 5.10 (b). The error increases from ±0.033 ° to ±0.06 °, which will not significantly deteriorate the accuracy of resolver.

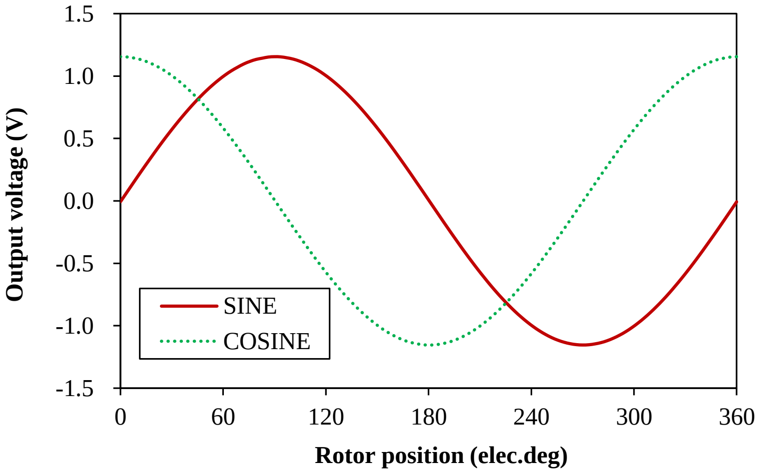

Fig. 5.9 Output voltages by alternate tooth windings (Z=16, p=5, obtained by FE analysis).

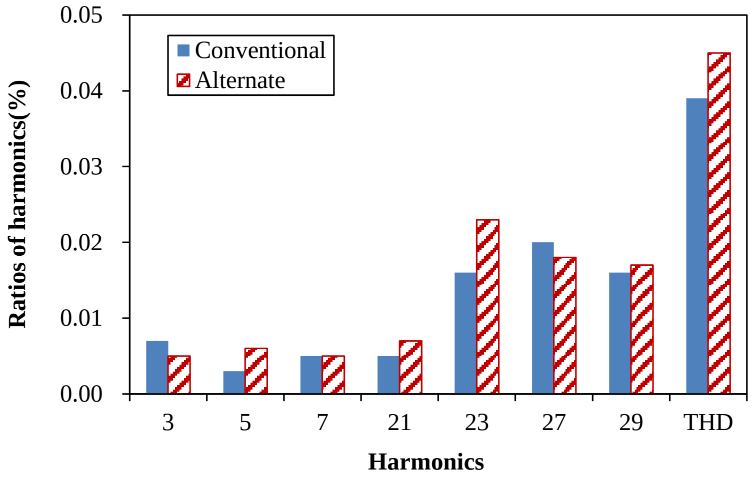

(a) Voltage harmonics

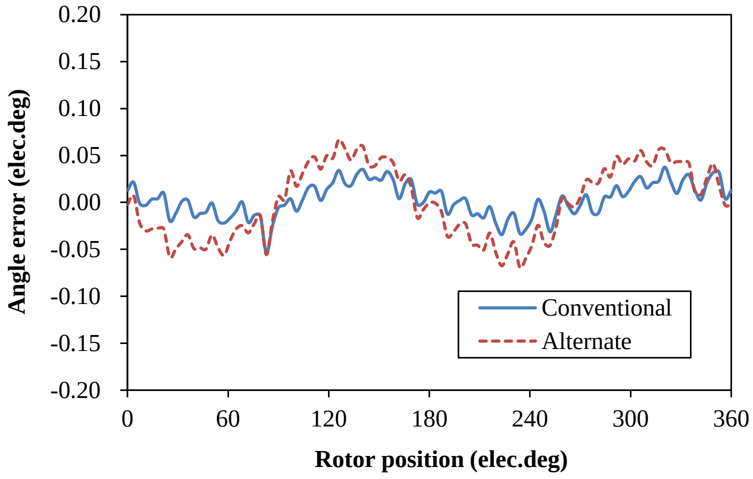

(b) Electric angle errors

Fig. 5.10 Comparison of voltage harmonics and position errors between conventional and alternate tooth windings (*Z*=16, *p*=5, obtained by FE analysis).

According to the above analysis, alternate tooth windings can be adopted, not restricted to some particular stator slot and rotor pole combinations such as 20 stator slots and 5 rotor saliencies. Moreover, the angle error can be significantly reduced by the design with 16 stator slots and 5 rotor saliencies, which is mainly due to the decrease of the 3rd and 5th harmonics.

In summary, alternate tooth windings can partially solve the problems described above without significant influence on position detection accuracy. However, the coil turns are still different from tooth to tooth.

5.4.3 Alternate Tooth Windings with Uniform Coils

In this part, alternate tooth windings by using uniform coils will be introduced and applied to resolvers in order to further simplify the manufacturing process.

A design with 12 stator teeth for the 5-X resolver is shown in Fig. 5.11 (a). In order to make an efficient and effective comparison, parameters are also based on the previous design, as shown in Table 5.2. In addition, the winding distributions are shown in Fig. 5.11 (b). It can be seen that the SINE and the COSINE windings both have 4 uniform coils which have 122 turns each, while the stator teeth of 1, 4, 7 and 10 only have exciting coils on them. Although these coils have identical number of turns, they still have the same function as windings in sinusoidal distributions, which can be deduced from (5.4).

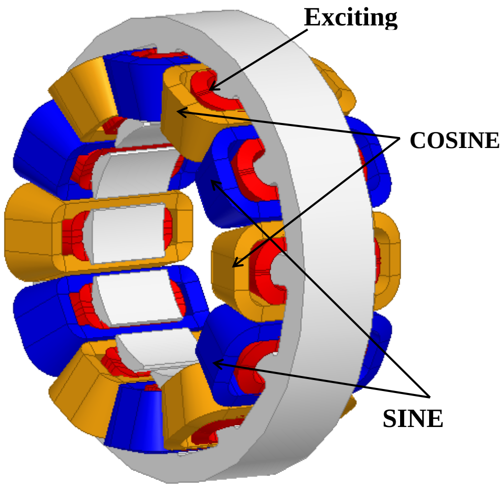

(a) Stator with alternate output windings

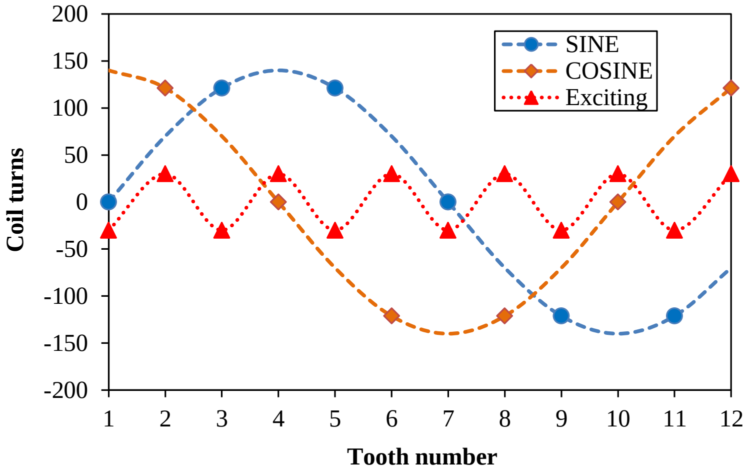

(b) Distribution of alternate tooth windings with uniform coils

Fig. 5.11 A design of VR resolver with alternate tooth windings (Z=12, p=5).

Similarly, harmonics in the output voltages have been compared between conventional and alternate tooth windings for the 5-X resolver, as shown in Fig. 5.12 (a). It can be seen that the THD of the output voltage increases from 0.02% to 0.031%. Also, a comparison on position errors caused by the two winding arrangements is made, as shown in Fig. 5.12 (b). The angle error changes from ±0.016 °to ±0.03 °, both much lower than that of previous designs.

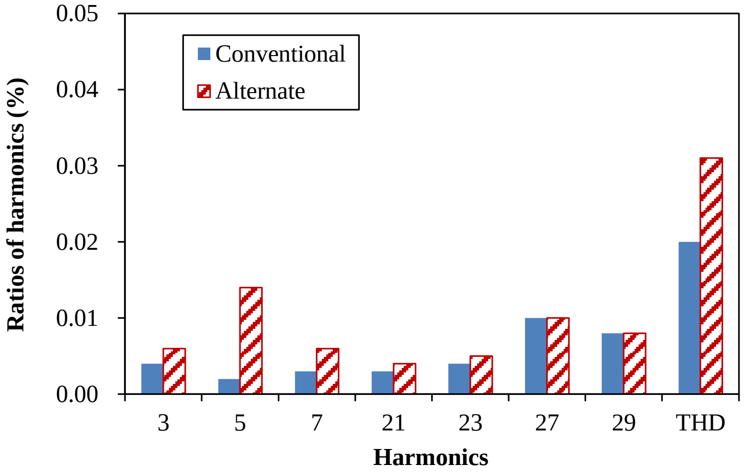

(a) Voltage harmonics

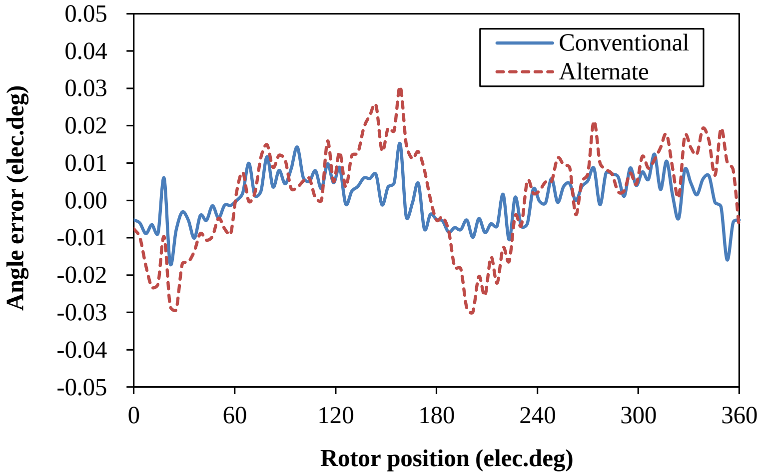

(b) Electric angle error

Fig. 5.12 Comparison of voltage harmonics and position errors between conventional and alternate tooth windings (Z=12, p=5, obtained by FE analysis).

As an extension, this concept can be applied to other stator slot and rotor pole combinations, which are generalized and shown in Table 5.3. Theoretically, an arbitrary number of resolver poles will have a certain number of stator teeth to form a number of combinations for applying this design method. However, it is necessary to make an overall consideration in actual applications, for example, the size and mechanical strength of stator teeth, cost, etc. Fortunately, PM machines with 12-slot/10-pole and 12-slot/14-pole designs are widely used in industrial applications such as servo motors, EPS motors, due to their unique advantages, and resolvers for these motors can be designed according to the concept proposed in this part.

From the above analyses, it can be seen that 12 stator teeth will be an ideal selection for 5-X resolver. Not only does this combination have low harmonics, but also alternate tooth windings by using uniform coils can be adopted, thus significantly simplifies the manufacturing process. Moreover, the stator and winding can be adopted for both 5-X and 7-X resolvers, as position sensors for PM machines of 12-slot/10-pole and 12-slot/14-pole designs respectively.

TABLE 5.3

COMBINATIONS AVAILABLE FOR ALTERNATE TOOTH WINDINGS USING UNIFORM COILS

Stator teeth Z	Output winding polarities $2p_w$	Rotor saliencies p
12	2	1, 5, 7
24	4	2, 10, 14
36	6	3, 15, 21
48	8	4, 20, 28
12n (n=1, 2, 3…)	2n	n, 5n, 7n

5.5 Prototype and Test

In order to verify the proposed resolver, a prototype with alternate tooth windings is fabricated, as shown in Fig. 5.13 (a). Main parameters of the prototype are listed in Table 5.4. To carry out the test, the prototype is integrated to a PM motor, with the stator fixed inside the end cap and the rotor attached to the shaft, as shown in Fig. 5.13 (b). In addition, the end shaft of the PM motor is equipped with a 5000-revolution encoder, which provides relatively accurate position signals for comparison.

TABLE 5.4

MAIN PARAMETERS OF 5-X PROTOTYPE WITH 12 STATOR TEETH

Parameters	Values
Stator outer diameter	37 mm
Stator inner diameter	20mm
Stator yoke depth	2.5mm
Stator tooth width	2.4mm
Stator slot-opening width	1.4mm
Core axial length	8 mm
Min. and Max. air-gap length	0.4mm, 2mm
Exciting winding turns	30*12
SINE-phase stator tooth No.	3, 5, 9, 11
COSINE-phase stator tooth No.	2, 6, 8, 12
Output winding turns of one phase	105*4
Wire diameter	0.1mm

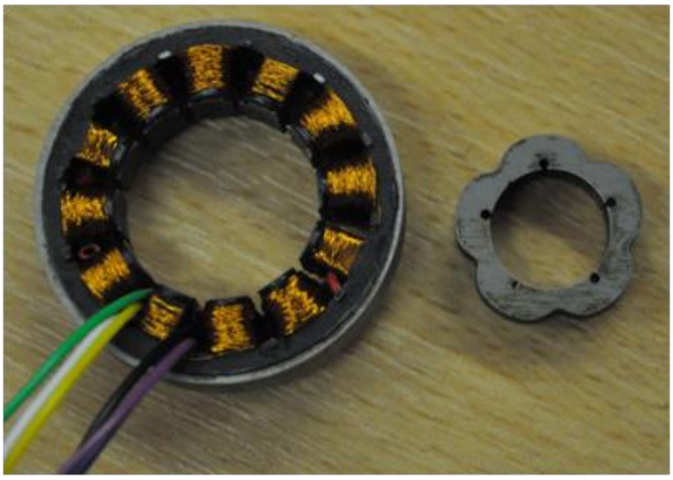

(a) Resolver prototype

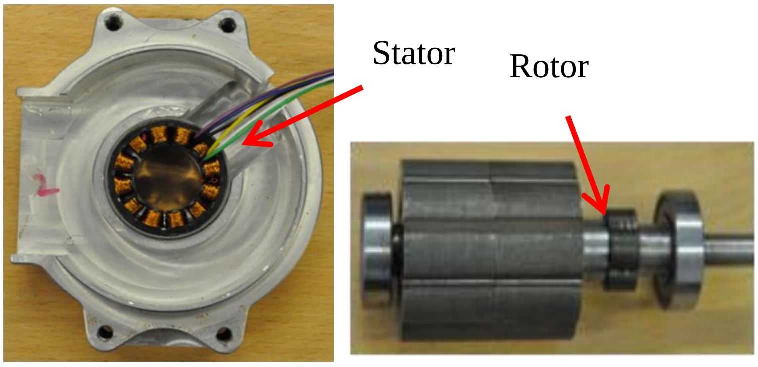

(b) Instalment of resolver stator and rotor

Fig. 5.13 Prototype and instalment of resolver stator and rotor.

A test platform is established on basis of dSPACE DS1005 system, as shown in Fig. 5.14. Besides the main test system, the PM motor is driven by the power converter shown in Fig. 5.14, and dSPACE I/O board is used to collect position signals produced by the prototype and the encoder respectively, which are transmitted to the processor board shown in Fig. 5.14 (b) for data processing. In addition, the supply of exciting signal and the process of output signals of resolver are performed by way of an R/D conversion IC (AU6802n1) [TAM02]. Fig. 5.15 illustrates the decode module with this IC, through which A, B and Z position signals produced by the prototype can be obtained.

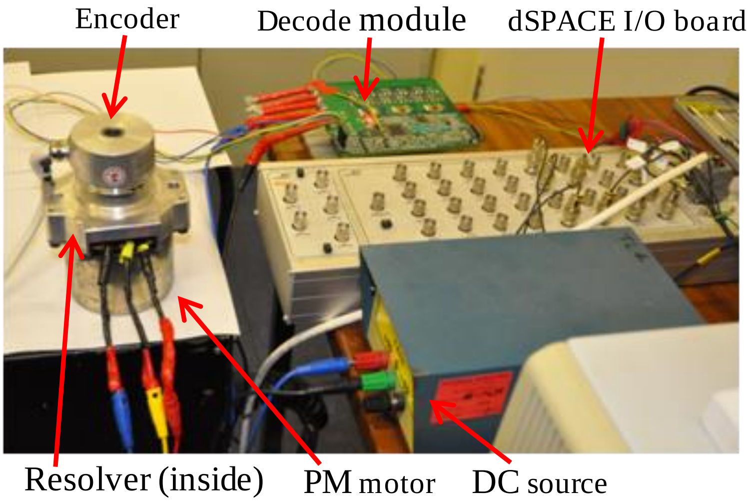

(a) Main test system

(b) dSPACE processor board

(c) Machine power converter

Fig. 5.14 Test platform and devices.

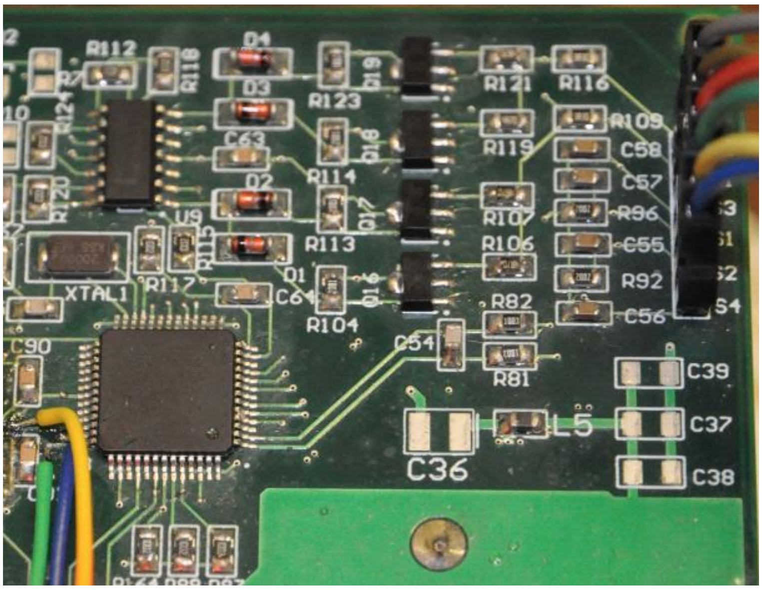

Fig. 5.15 Decode module for resolver (AU6802n1).

Before comparison of the position detection accuracy between the two sensors, a preliminary check on the prototype is made. When the PM motor rotates at a constant speed, the analog output voltages of the prototype are captured and plotted in Fig. 5.16. It can be seen that the two phases of output signals are symmetrical and no obvious constant components exist, which basically guarantees the prototype with normal operating characteristics. In addition, both of the two phases of output voltages have the amplitudes of about 1.0V, which satisfies the requirement of signal processing by the IC described above.

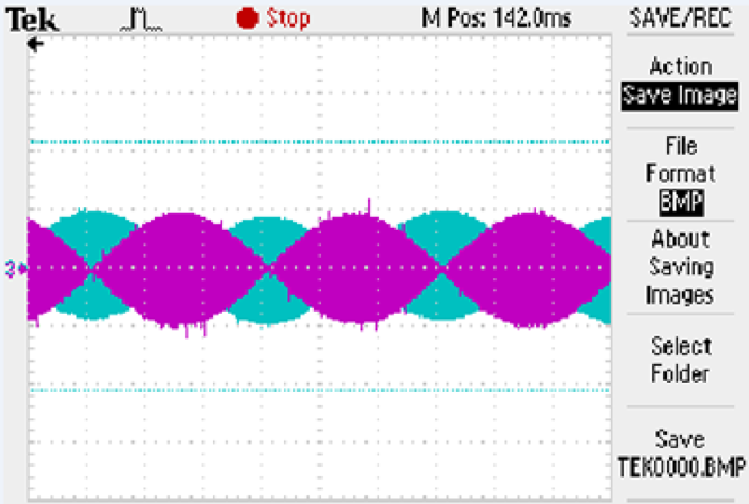

Fig. 5.16 Analog output voltages of the prototype.

When the PM motor is driven at a constant speed of 180 rpm, A, B and Z signals generated by the encoder are directly input to dSPACE. Meanwhile, another set of A, B and Z signals produced by the prototype as well as the R/D conversion IC are also input to dSPACE for comparison. Rotor positions estimated by the encoder and the resolver can be easily obtained, as illustrated in Fig. 5.17 (a). It should be noted that the results are captured using dSPACE software, and then plotted with Excel in order to make a clear comparison. Basically, the two estimated positions have a good coincidence with each other.

Position errors are also demonstrated in order to make a clear verification on the detection accuracy of the proposed design, as shown in Fig. 5.17 (b). It can be seen that the electric angle error is within ±1.4 °, which will not influence the motor current control for most of industrial applications. However, this error is still higher than the designed value. As a device of high accuracy, several factors which will degrade this index may be involved in fabrication and instalment of the prototype, i.e. off-centre stator and rotor, asymmetric coils, etc.

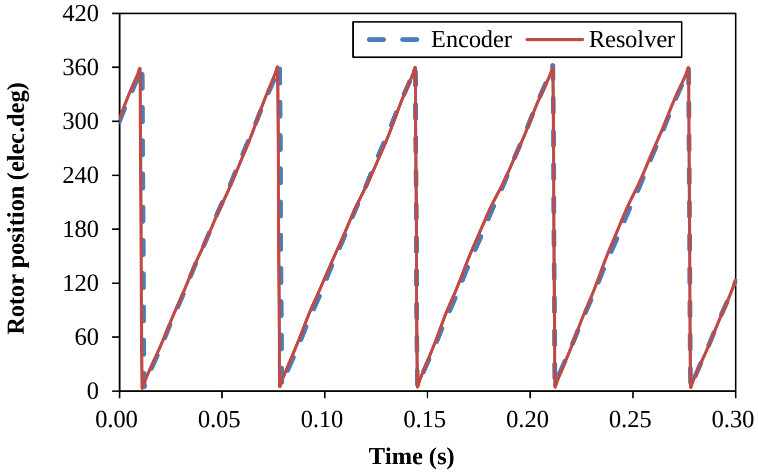

(a) Position signals

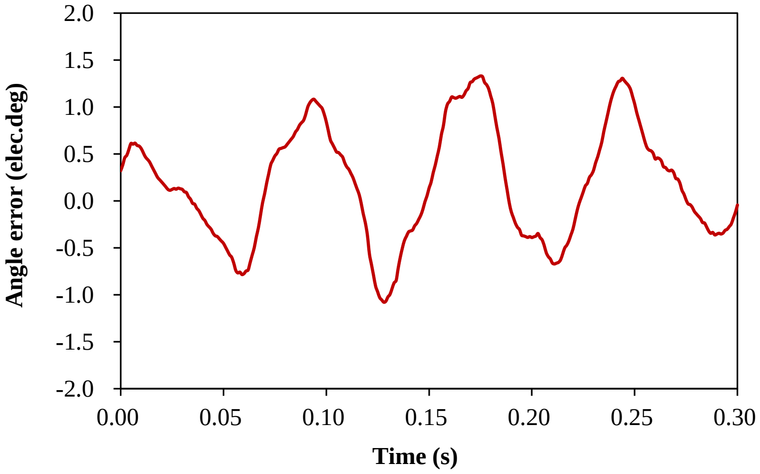

(b) Electric angle error

Fig. 5.17 Position detection accuracy of the resolver prototype.

5.6 Conclusion

Winding characteristics of the conventional VR resolvers have been analysed in this chapter, including the exciting, the SINE and COSINE windings.

According to the winding distributions of conventional VR resolver, the operating principle has been verified by analytical derivation and FE analyses, from which main parameters can also be calculated, including the input/output impedance and the transformation ratio.

Based on the analytical derivation, the relationship between stator slot and rotor pole combinations has been established, which enables identical stator and windings to be commonly used by different poles of resolvers. Also, harmonic levels amongst designs with different stator slot and rotor pole combinations can be effectively evaluated through an index q defined in this paper. As a deduction, the ‘close-slot-pole’ concept is proposed for the design of multi-polar resolvers.

In order to simplify the winding fabrication, alternate output windings have been proposed for general stator slot and rotor pole combinations, in addition to special combinations ($Z=4p$). As a further improvement, alternate output windings with uniform coils have been proposed for a series of slot/pole combinations, which can significantly simplify the output winding fabrication without obvious deterioration on the position detection accuracy.

A 5-X resolver prototype according to the proposed design has been fabricated and tested, as a verification of the foregoing analyses.

CHAPTER 6 NOVEL VARIABLE RELUCTANCE RESOLVERS WITH NON-OVERLAPPING TOOTH-COIL WINDINGS

6.1 Introduction

The analyses of windings in VR resolvers have been investigated in Chapter 5, and it has been proven that alternate tooth windings can be employed to simplify the fabrication of output windings. For the special slot/pole combinations (Z=4p), separated SINE and COSINE output windings by uniform coils can be achieved. However, the tooth harmonics in output voltages are introduced, which cannot be eliminated by the winding itself and deteriorates the detection accuracy as a consequence. Actually, alternate tooth windings can also be employed in general slot/pole combinations, whilst the coil turns no longer remain stable. In order to solve the problems of tooth harmonics and non-uniform output coils, a series of slot/pole combinations are identified, through which separated output windings by uniform coils become available in VR resolvers without obvious deterioration on the detection accuracy.

Compared with conventional VR resolvers, the number of coils on each stator tooth is reduced from three to two by employing the alternate tooth windings technology, which simplifies the winding fabrication to some extent. However, the exciting coils and one phase of output coils are still overlapping. For further simplification, a novel VR resolver with non-overlapping tooth-coil windings (NTWVRR) is proposed in this chapter.

First, the basic operating principle of NTWVRR is illustrated based on a fundamental slot/pole combination (5-X resolver by 12 stator slots), followed by the optimization on major dimensions. Further, main parameters are analytically derived, including the input/output impedance and the transformation ratio. Moreover, the feasibility of identical stator and windings being used in different poles of resolvers is investigated.

Due to the simplified manufacturing process, a 2-X resolver of the proposed topology is designed for the HEV/EV applications, of which the winding fabrication duration is compared with an existing product. With the actual application conditions considered, the position detection accuracy is investigated and compared by the FE method, including the typical operating speed range and the potential assembling eccentricities. In addition, the voltage difference amongst three different poles of resolvers with the identical stator is analysed. For verification, several prototypes are fabricated and tested.

6.2 Basic Operating Principle of NTWVRR and Optimization

Winding distributions and the operating principle of NTWVRR are introduced in this section, followed by optimization of major dimensions.

6.2.1 Winding Distributions and Basic Operating Principle

Winding arrangements between the conventional and proposed designs are compared in Figs. 6.1 (a) and (b). It can be seen that, in the conventional VR resolver, all windings, including the exciting winding and two phases of output windings, are wound on the same teeth. Meanwhile, in the proposed VR resolver, the exciting winding and the two phases of output windings are located on different stator teeth and each stator tooth only has one single coil, thus the three sets of windings are non-overlapping from one another.

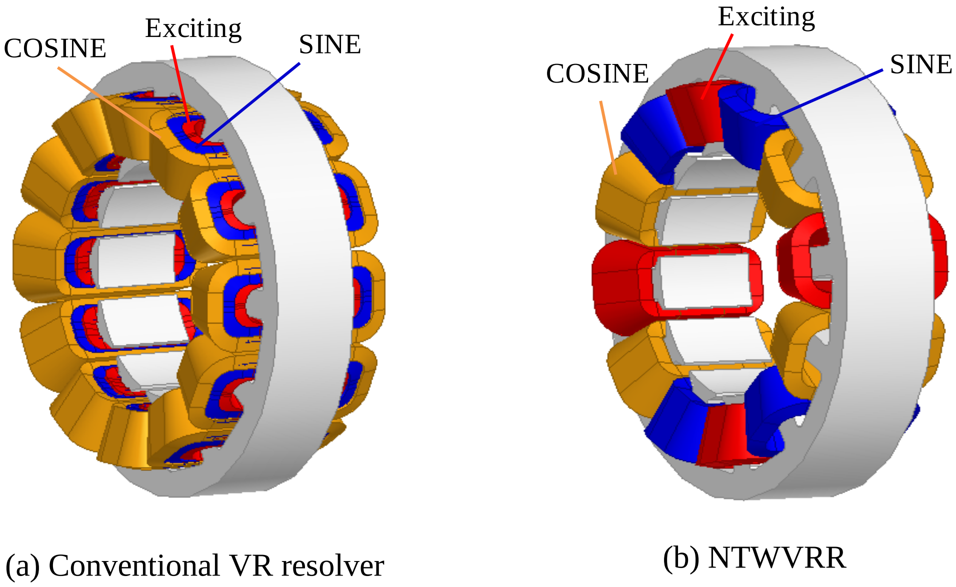

(a) Conventional VR resolver

(b) NTWVRR

Fig. 6.1 VR winding arrangements of conventional VR resolver and NTWVRR.

As a typical application, a 5-X resolver with 12 stator slots is investigated, with its main parameters shown in Table 6.1. Actually, this type of 5-X resolver products of this size are widely used in EPS motors. For the proposed 5-X resolver, winding distributions are illustrated in Fig. 6.2. Compared with the conventional VR resolver, the major features of the winding arrangements can be summarized. Firstly, each stator tooth has one single coil, and the three sets of windings are non-overlapping, as described above. Secondly, each output winding is composed of uniform coils, which have the same number of turns, identical for SINE and COSINE output windings. Thirdly, the 4 exciting coils are of the same polarities.

TABLE 6.1

MAIN PARAMETERS OF RESOLVER MODEL

Parameters	Values
Stator outer diameter (mm)	37
Lamination axial length (mm)	8
Air-gap length (mm)	0.4 (Min.), 2 (Max.)
Stator slots	12
Rotor saliencies	5

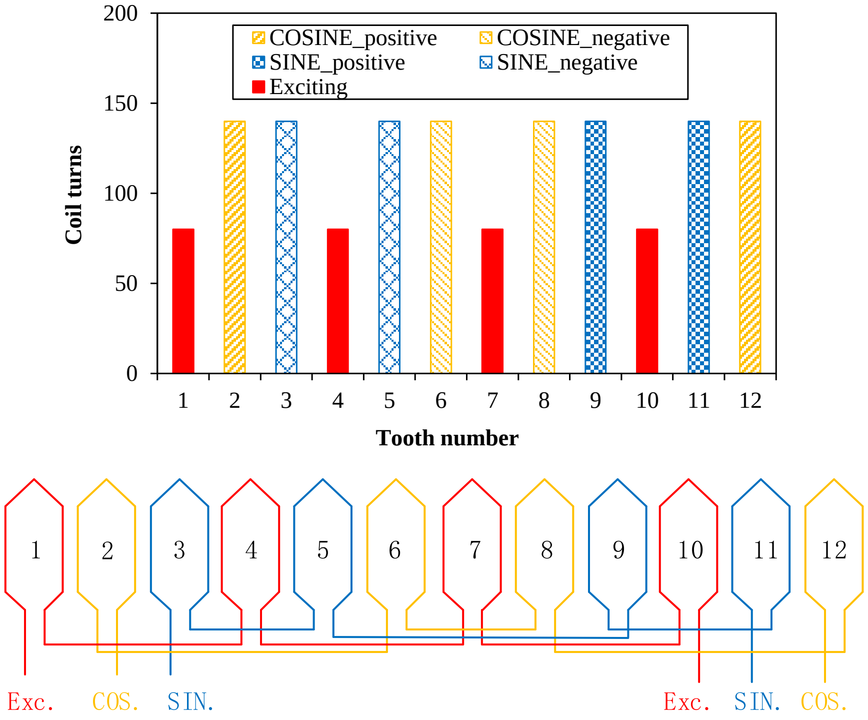

Fig. 6.2 Distributions of non-overlapping uniform windings in the proposed VR resolver.

According to the winding distributions, the basic performance of the novel resolver can be verified by 2-dimensional FE analysis. Fig. 6.3 (a) illustrates the flux distribution in the stator and the rotor laminations when a 10 kHz sinusoidal signal is applied to the exciting winding. It can be seen that there are four real exciting poles with identical polarity, while the other eight stator poles provide the main path for exciting flux, which is different from that of conventional VR resolver. Voltages can be induced in output coils on the 8 stator poles, as shown in Fig. 6.3 (b) which indicates that two phases of orthogonal output voltages can be obtained. However, it should be noted that the voltage waveforms reflect the envelopes of actual output signals which have the same frequency as the exciting signal, and the sampling operation is always performed by aforementioned decoding chips.

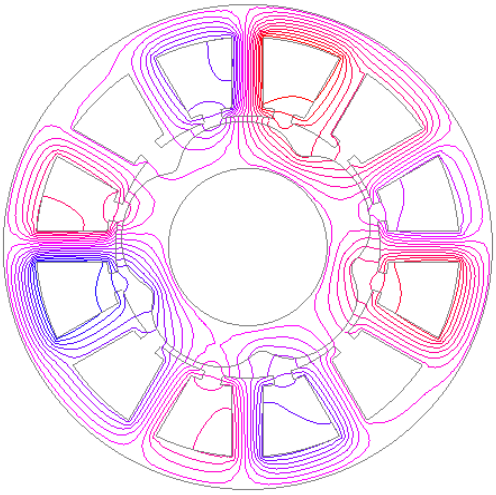

(a) Flux distribution

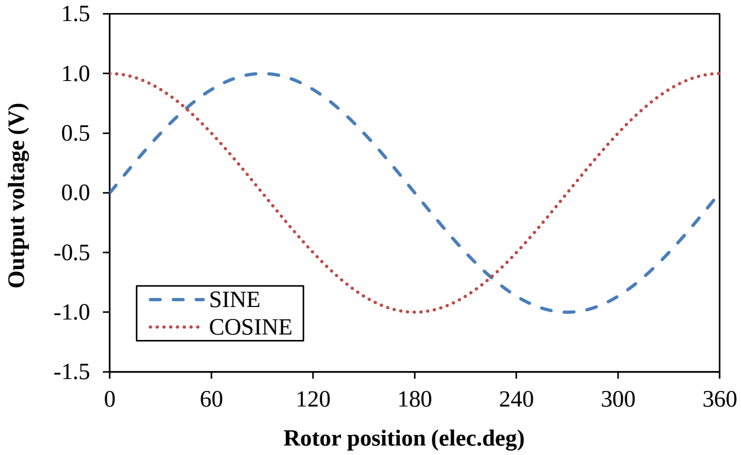

(b) Output voltages

Fig. 6.3 Flux distribution and output voltages (envelope) of NTWVRR.

FFT analysis is also made in order to investigate the harmonics in output voltages, as shown in Table 6.2. It can be seen that the 3rd order of harmonics is the most significant component – with amplitude of 0.36% - compared with that of the fundamental wave. In fact, there are also other higher-order harmonics with even lower amplitudes, which are ignored and not listed. As it is well known, the electric angle error is an important index of the resolver, which is caused by various factors in the process of design, manufacturing and mounting. Under ideal conditions, harmonic components will directly determine the value of this index. According to the output voltages in Fig. 6.3, the rotor position can be calculated by an arc tangent operation of the SINE and COSINE voltages. By comparing the calculated rotational angle with the actual rotor position, an error will be generated, defined as the electric angle error, which represents the position detection accuracy of the resolver, as shown in Fig. 6.4. It can be seen that the calculated rotor position by the 5-X resolver will have an error of ±0.22 electric degree over an electric cycle.

TABLE 6.2

HARMONICS DISTRIBUTION BY NTWVRR

Harmonics	1^{st}	3^{rd}	5^{th}	7^{th}	9^{th}	11^{th}	13^{th}
Ratios (%)	100	0.36	0.002	0.004	0.004	0.002	0.002

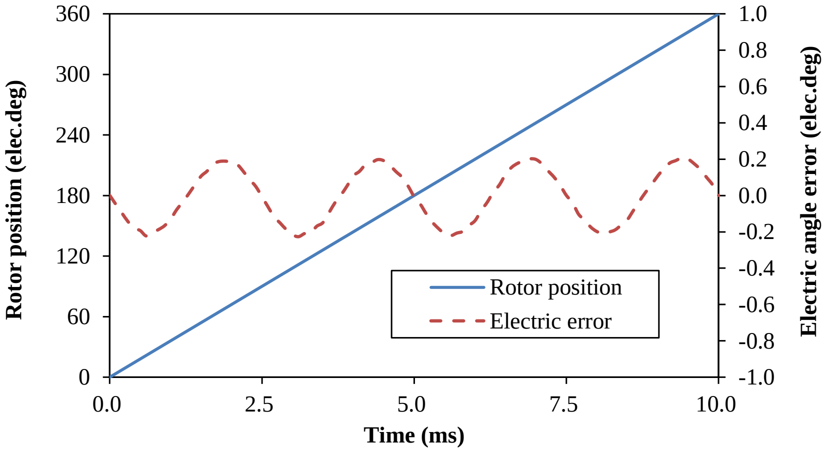

Fig. 6.4 Electric angle error caused by harmonics.

6.2.2 Design Optimization

After the introduction of the basic operating principle, it can be seen that the position detection accuracy is subject to the output voltage harmonics, and optimization of major dimensions is carried out to reduce the corresponding electric angle error.

A. Air-gap length function

Firstly, the influence of rotor contour is investigated, with the air-gap length expressed by:

$$\delta = \frac{a}{b + \cos(p\theta)} \tag{6. 1}$$

where a is the length factor and b represents the shape factor.

In the first step, the influence of the length factor a in the air-gap function is analysed while the shape factor keeps constant. Fig. 6.5 illustrates the THD value of the output voltage and the electrical angle error under different length factors. It can be seen that the THD value decreases from 0.36% to 0.07% when the length factor increases from 1 to 1.5. The corresponding electrical angle error presents similar variation, reducing from ±0.22 ° to ±0.052 °. This consequence is mainly due to the increase of actual air-gap length, which significantly reduces the voltage harmonics.

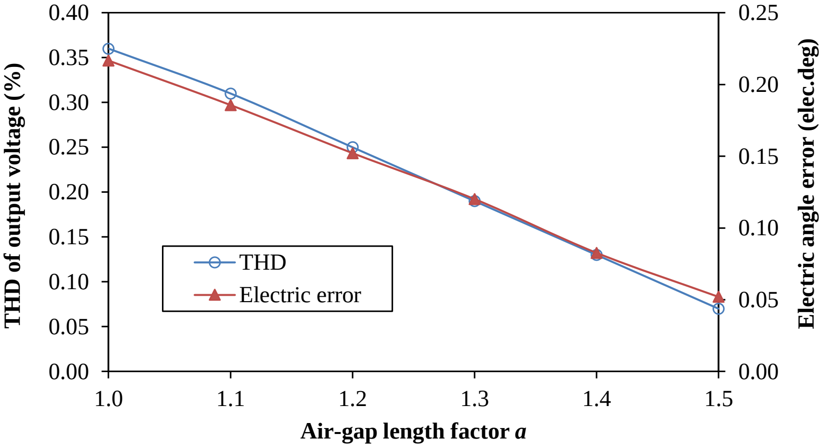

Fig. 6.5 Influence of air-gap length factor (*b*=1.5).

Larger air-gap length usually requires more winding turns, thus increasing the manufacturing cost. In the next step, the influence of air-gap shape factor *b* will be investigated with the minimum air-gap length fixed as 0.52mm. It is also necessary for the length factor to make corresponding variation, in order to maintain the minimum air-gap length. As illustrated in Fig. 6.6, the THD value of output voltage changes from 0.26% to 0.02% when the shape factor *b* decreases from 1.8 to 1.3. There will be a similar trend for the electric angle error, reducing from ±0.163 °to ±0.015 °. The reason for this variation is that smaller shape factor represents a higher ratio of fundamental-wave permeance, which can significantly reduce other harmonics.

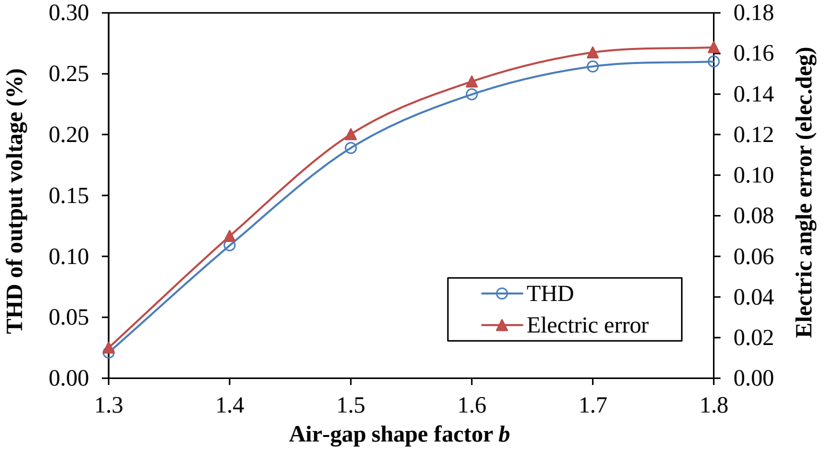

Fig. 6.6 Influence of air-gap shape factor.

For a certain inner diameter of stator, the rotor contour is defined by the air-gap function. Therefore, the mechanical strength of rotor core should also be taken into account while choosing this function. Too small a shape factor will lead to too big a maximum air-gap length, and the inner diameter of rotor might be too small. With a combined consideration of these aspects, 1.3 and 1.5 are selected as the length factor and the shape factor of the air-gap function respectively while corresponding angle error will be ±0.12° for this design. The following optimization work upon other parameters will be done on basis of this rotor.

B. Slot-opening width

The slot-opening width of stator is another factor which significantly influences the harmonics of the output voltages. This part will demonstrate its influence on the variation of THD value, together with electric angle error.

In order to make a convenient parametric analysis, tooth arc angle is introduced to represent the width of tooth tip. For the proposed 5-X resolver with 12 slots, the tooth arc angle will be 30° if a close slot is adopted. As shown in Fig. 6.7, the THD value decreases from 0.25% to 0.06% when the tooth arc angle increases from 20° to 26°, and then this value keeps an upwards trend, rising to 0.1% at the tooth arc angle of 28°. Similar variation is also reflected by the electric angle error, which has the lowest value of ±0.057° at the tooth arc angle of 26°.

Also, the potential requirement of automatic winding machine in production has to be taken into account when this parameter is selected. The angle of 24° proves to be an appropriate selection for tooth arc angle of the proposed resolver, which is equivalent to 1mm slot opening.

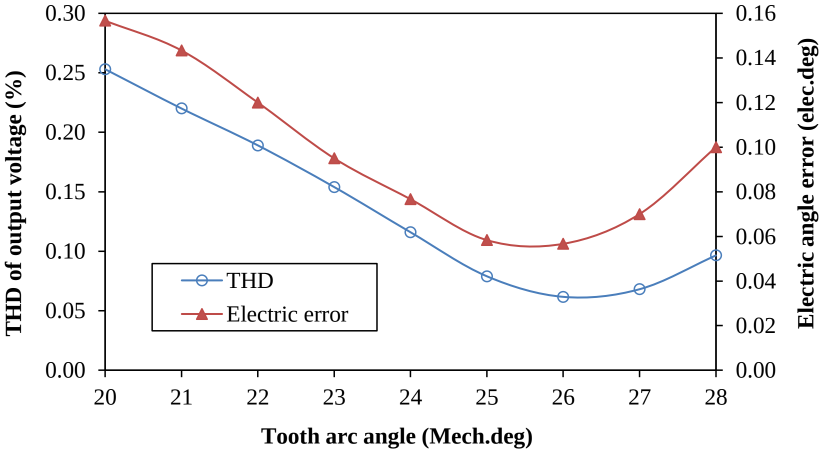

Fig. 6.7 Influence of tooth arc angle.

Based on the above analyses, it can be seen that the variation of electrical angle error has a good correlation with that of THD value, which can be considered as an effective index for evaluation of position detection accuracy. In addition, influences of these major dimensions on output voltage magnitudes are not discussed, which directly relates to the winding fabrication cost and will be investigated in Chapter 7.

6.3 Analytical Derivation of Main Parameters

Generally, the signal processing of the resolver is performed by way of an R/D conversion IC, e.g. AU6802, AD2S80 and corresponding subseries. It should be noted that there are always certain recommended ranges for the exciting current and output voltages. As a consequence, it is necessary to make a prediction of the impedance and the transformation ratio, in order to make reasonable designs. Compared with the analytical derivation for conventional resolver, the proposed resolver has its unique features.

6.3.1 Open-circuit Impedance

By way of example, the 5-X resolver described above will be analysed first, and the conclusion can be extended to other similar slot/pole combinations. With higher orders of harmonics ignored, the air-gap permeance corresponding to the k^{th} stator tooth can be expressed as that of a conventional resolver [CUI12]:

$$P_k = P_0 + P_{m1} \cos\left[p\theta - (k-1)\frac{2\pi p}{Z})\right] \tag{6. 2}$$

where θ is rotational angle. P_0 and P_{m1} represent the constant and sinusoidal components of the air-gap permeance respectively. Z is the number of stator slots and p is the number of rotor saliencies.

According to Fig. 6.2, an equivalent magnetic circuit of the proposed resolver can be established, as shown in Fig. 6.8 (a), where F_1, F_2, F_3 and F_4 represent magneto-motive forces (MMFs) produced by the four exciting coils respectively. Due to the identical number of turns for each exciting coil, a simplified model can be obtained in Fig. 6.8 (b), where the equivalent permeance of P_e and P_{sc} can be expressed as:

$$P_e = \sum_{k=1,4,7,10} P_k = 4 \cdot P_0 \tag{6. 3}$$

$$P_{sc} = \sum_{k=2,3,5,6,8,9,11,12} P_k = 8 \cdot P_0 \tag{6. 4}$$

In addition, F is the equivalent MMF, which has the same amplitude as F_1, F_2, F_3 and F_4.

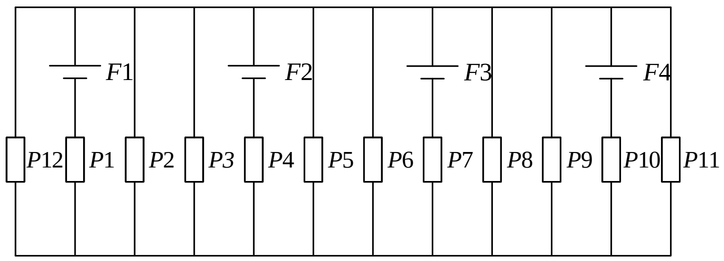

(a) Basic model

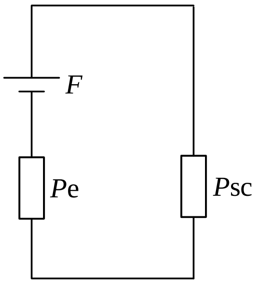

(b) Simplified model

Fig. 6.8 Equivalent magnetic circuit for the resolver (Z=12, p=5).

Based on above analysis, the open-circuit input impedance can be expressed as:

$$X_{in} = 2\pi f N_{e0}^2 \frac{P_e P_{sc}}{P_e + P_{sc}} = \frac{8}{3} \cdot 2\pi f N_{e0}^2 P_0 \qquad (6.5)$$

where f represents the frequency of exciting signal and N_{e0} is the number of turns for each exciting coil. Compared with the main reactance, the values of leakage reactance and resistance are relatively lower, which will not be considered here. Not restricted to the 5-X resolver, for general slot/pole combinations having the same topology as the proposed resolver, this impedance can be described as:

$$X_{in} = \frac{4}{9} \cdot \pi f N_{e0}^2 P_0 Z \qquad (6.6)$$

Similarly, the open-circuit output impedance can also be obtained by the same method as:

$$X_{out} = \frac{2}{3} \cdot \pi f N_{s0}^2 P_0 Z \qquad (6.7)$$

where N_{s0} is the number of turns for each output coils. It can be seen that the open-circuit impedance will remain constant at different rotor positions and consequently the exciting current will maintain a constant amplitude. This will be a basic condition for the calculation of output voltage.

6.3.2 Transformation Ratio

This transformation ratio index represents the amplitude ratio of output voltage and exciting voltage, and the priority is to theoretically calculate the output voltage. As an example, the SINE phase output will be analysed. According to the winding distribution shown in Fig. 6.2, equivalent magnetic circuit of the SINE phase winding can be described as Fig. 6.9 (a), with ideal conditions considered. A simplified model can also be obtained, as shown in Fig. 6.9 (b). Due to the constant amplitude of exciting current I_m, the output voltage in each of the four coils can be expressed as:

$$E_{sk} = -\frac{\mathrm{d}\psi_{sk}}{\mathrm{dt}} = -2\pi f N_{e0} N_{s0} I_m \frac{1}{3} P_k \sin(2\pi f\mathrm{t}) \tag{6. 8}$$

where ψ_{sk} is the flux-linkage of the output coil on the k^{th} stator tooth. According to the winding polarity, the synthetic output voltage of the SINE phase will be:

$$\begin{aligned} E_s &= -(E_{s3} + E_{s5}) + (E_{s9} + E_{s11}) \\ &= \frac{4}{3} \cdot 2\pi f N_{e0} N_{s0} I_m P_{m1} \sin(\frac{\pi}{3}) \sin(p\theta) \sin(2\pi f\mathrm{t}) \end{aligned} \tag{6. 9}$$

Also, this analytical expression can be extended to other similar slot/pole combinations with the proposed winding distribution, expressed as:

$$E_s = \frac{Z}{9} \cdot 2\pi f N_{e0} N_{s0} I_m P_{m1}\, sin\left(\frac{\pi}{3}\right) sin(p\theta)\, sin(2\pi f t) \tag{6. 10}$$

Based on (6. 6) and the exciting current, the exciting voltage can be expressed as:

$$E_{in} = \frac{4}{9} \cdot \pi f N_{e0}^2 P_0 Z I_m \sin(2\pi f\mathrm{t}) \tag{6. 11}$$

By comparing (6. 10) with (6. 11), the ideal transformation ratio for this resolver topology can be calculated by:

$$\varepsilon = \frac{\sqrt{3} N_{s0} P_{m1}}{4 N_{e0} P_0} \tag{6. 12}$$

Expressions of the impedance and the transformation ratio have been analytically derived above. However, the leakage impedance is not considered. According to the conventional winding theory, the leakage reactance can be divided into several components, such as slot leakage, harmonics leakage and end leakage, and their prediction can be obtained by empirical formulas [CHE00]. In fact, modern commercial FE software can solve the problem. A more practical way in the design of the resolver is to make a prediction of the main reactance and the transformation ratio by (6. 6), (6. 7) and (6. 12) first, from which a reasonable number of coil turns can be initially determined. Then, more accurate values of these parameters can be obtained by FE analyses.

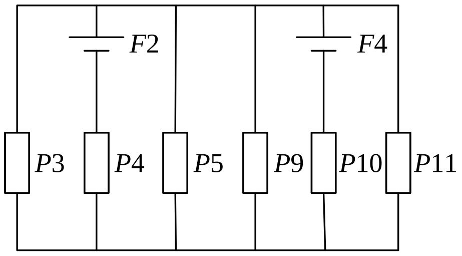

(a) Basic model

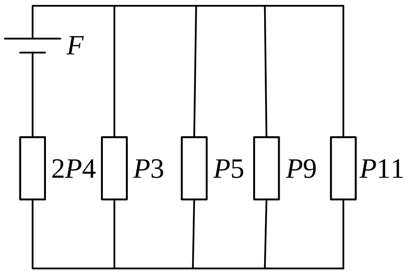

(b) Simplified model

Fig. 6.9 Equivalent magnetic model for the SINE phase winding.

6.4 Further Application in Different Slot and Pole Combinations

Besides the 5-X resolver described above, the feasibility of non-overlapping tooth-coil windings for other stator slot/rotor pole combinations will be investigated in this part.

6.4.1 NTWVRR of Different Slot and Pole Combinations

Based on the proposed resolver and its winding arrangement, the distributions of 2-pole, 10-pole and 14-pole SINE phase winding are illustrated in Fig. 6.10 (a). It can be seen that the four coils of 2-pole and 14-pole winding are the same as those of 10-pole winding with the 12-slot stator employed, which can also be verified by analytical deduction. Besides the 5-X rotor, two other rotors (1-X and 7-X) of similar dimensions are shown in Figs. 6.10 (b), (c) and (d) respectively. With identical stator and winding commonly utilized, output voltages can be obtained from FE models by the 3 different rotors. In order to evaluate their separate detection accuracy, a comparison on electric angle errors will be made.

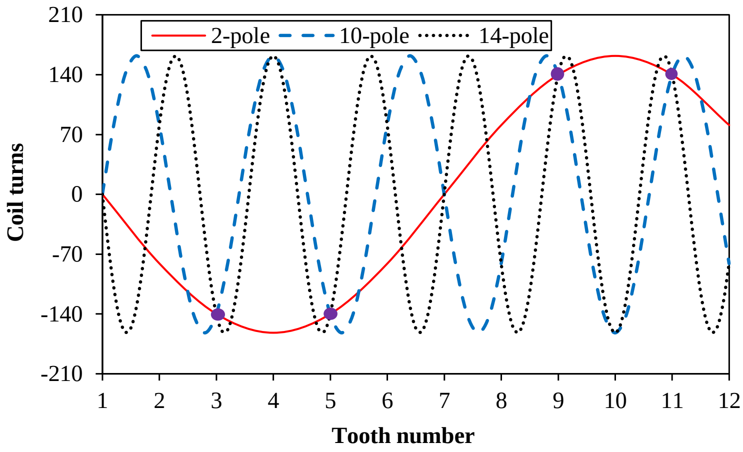

(a) Winding distributions

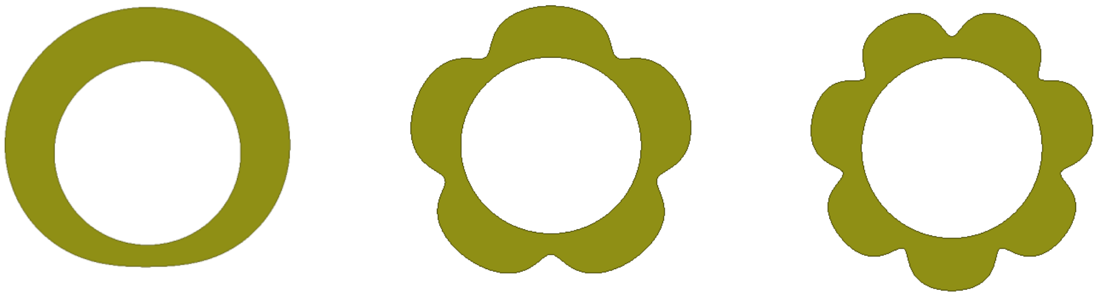

(b) 1-X rotor (c) 5-X rotor (d) 7-X rotor

Fig. 6.10 Winding distributions for different poles of resolvers.

When compared with the actual rotor position, electric angle errors are calculated for the 3 rotors respectively, as shown in Fig. 6.11. It can be seen that position errors by the 5-X and the 7-X resolvers are of similar level (±0.083°), both of which are much lower than that of the 1-X resolver (±0.616°). It can be further deduced that a higher accuracy is often obtained by increasing the number of rotor saliencies.

The foregoing analyses are all based on a 5-X resolver with 12 stator slots. However, this novel concept of VR resolver is not restricted to this stator slot/rotor pole combination only, and a series of other combinations are also possible, as shown in Table 6.3, from which two important conclusions can be drawn: First, the resolver with an arbitrary number of rotor saliencies will have a corresponding number of stator slots, and the two numbers present a relationship of 12 times. Second, identical stator and winding can be commonly utilized by resolvers of 3 variant rotor saliencies.

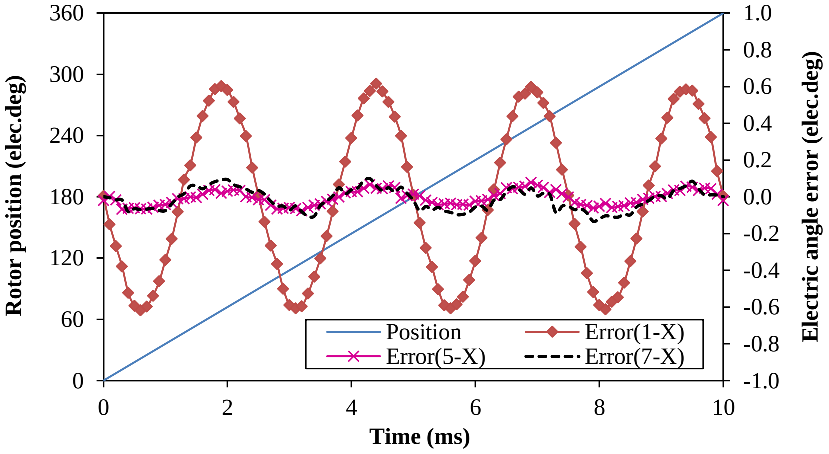

Fig. 6.11 Comparison of electric angle error between different combinations.

It should also be noted that for a 5-X resolver, the number of stator slots can also be selected as 60, besides the selection of 12. However, the number of stator slots is always restricted to the mechanical strength. In addition, too many stator slots will also involve complicated winding process, thereby increasing the total manufacturing cost. Therefore, a smaller number of stator slots will be more competitive for the manufacture of resolver.

TABLE 6.3

STATOR SLOT/ROTOR POLE COMBINATIONS FEASIBLE FOR RESOLVER WITH NON-OVERLAPPING TOOTH-COIL WINDINGS

Stator slots *Z*	Output winding polarities $2p_w$	Rotor saliencies *p*
12	2	1, 5, 7
24	4	2, 10, 14
36	6	3, 15, 21
48	8	4, 20, 28
12n (n=1, 2, 3…)	2n	n, 5n, 7n

6.4.2 Comparison of Sensitivity to Assembling Eccentricity

The foregoing analyses are carried out under ideal conditions. However, the assembling eccentricity is difficult to avoid when the resolver is integrated into a motor. The influence of this tolerance is investigated by FE analysis based on the 5-X resolver. As can be seen from Fig. 6.12, the electric angle error increases from ±0.48 °to ±2.37 °when the eccentricity changes from 0.01mm to 0.05mm.

In order to reduce the influence of eccentricity, designs by different air-gap functions are analysed with identical eccentricity of 0.03mm. As can be seen from Fig. 6.13, the electric error decreases from ±1.42 °to ±1.01 °when the air-gap length factor increases from 1.3 to 1.8. In order to further improve the detection accuracy, it is necessary to investigate winding distributions of the proposed resolver topology.

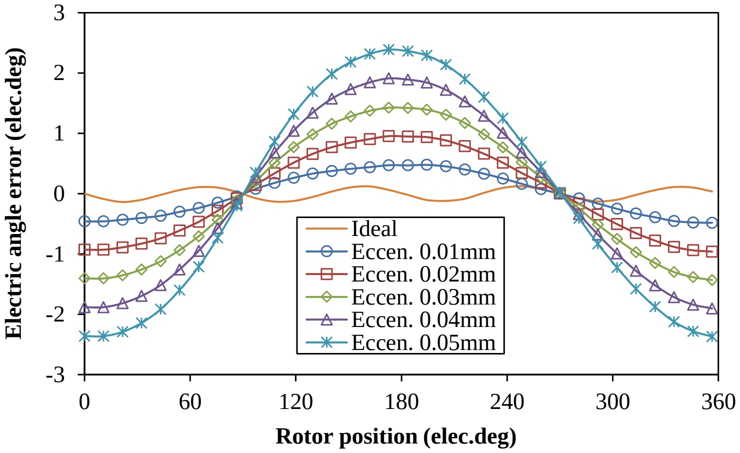

Fig. 6.12 Electrical error during one cycle with eccentricity (static) considered.

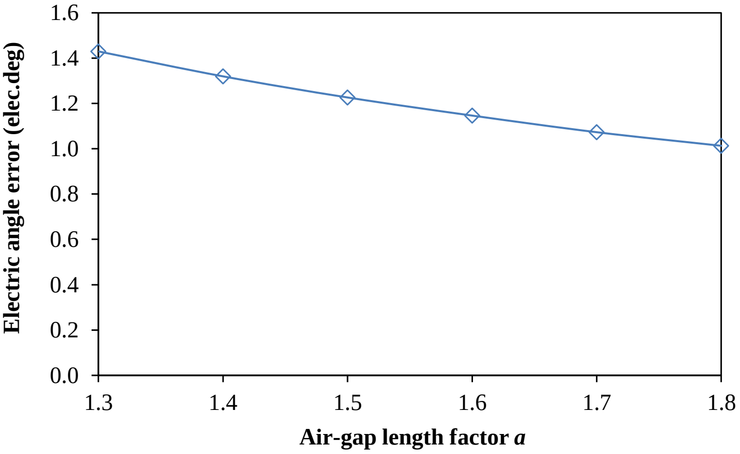

Fig. 6.13 Influence of air-gap length factor on electric angle error with 0.03mm eccentricity (static) considered.

As listed in Table 6.3, a series of slot/pole combinations can be applied for the proposed resolver topology. Fig. 6.14 illustrates the distributions of 2-polarity, 4-polarity and 6-polarity output windings respectively. It can be seen that 4-polarity and 6-polarity output windings are composed of positive and negative groups of coils, both of which are symmetrically distributed around the stator circumference. When the induced DC voltage (constant magnitude, the same frequency as the exciting signal) in some coils is increased or decreased by eccentricity, the DC voltage induced in other coils of the same group will present an adverse variation. The complimentary function makes the resolver much less sensitive to eccentricity, due to the effective restriction of DC voltages. In contrast, positive and negative coils of the 2-polarity windings are assembled within half of the stator circumference respectively, and DC voltage induced by eccentricity cannot be eliminated, which makes the 5-X resolver more sensitive to eccentricity.

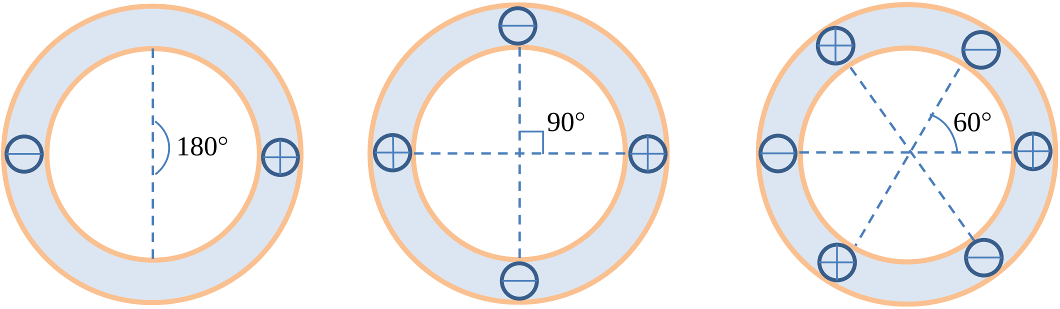

(a) 2-polarity (b) 4-polarity (c) 6-polarity

Fig. 6.14 Distribution of positive and negative output coils (one phase).

In order to verify the difference, a 24-slot-2-pole NTWVRR model is established with identical main dimensions as the 5-X design. When the eccentricity increases from 0.01mm to 0.05mm, corresponding electric errors produced by the two models are compared, as shown in Fig. 6.15. It can be seen that the detection accuracy of the 2-X resolver will not be obviously influenced by eccentricity, which is mainly due to the symmetrical distribution of its 4-polarity output coils as described above.

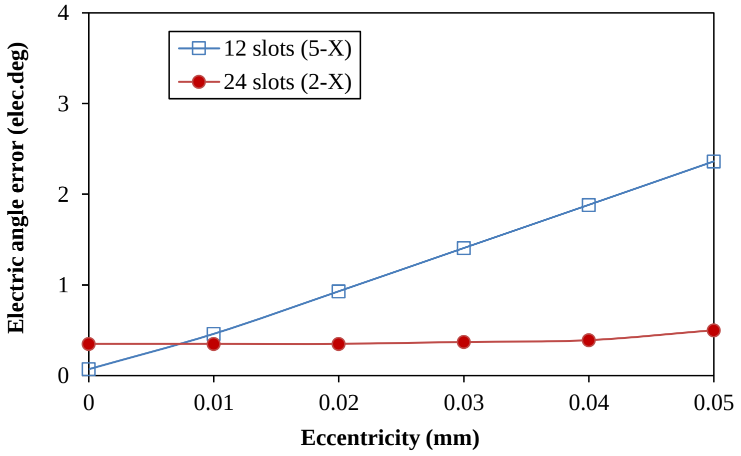

Fig. 6.15 Comparison of eccentricity (static) influence between two slot/pole combinations.

It can be deduced that only the design with 12 slots of the proposed resolver topology is sensitive to eccentricity, due to asymmetric distribution of positive and negative coils of the 2-polarity output windings. The detection accuracy of the 5-X resolver will deteriorate significantly when larger assembling eccentricity is introduced.

6.5 Prototype and Test

As a basic configuration of the proposed topology, a 5-X resolver prototype with 12 slots has been fabricated in order to verify the foregoing analyses, as shown in Fig. 6.16. Dimensions and winding distributions of the prototype are based on Table 6.1 and Fig. 6.2 respectively.

Fig. 6.16 5-X resolver prototype.

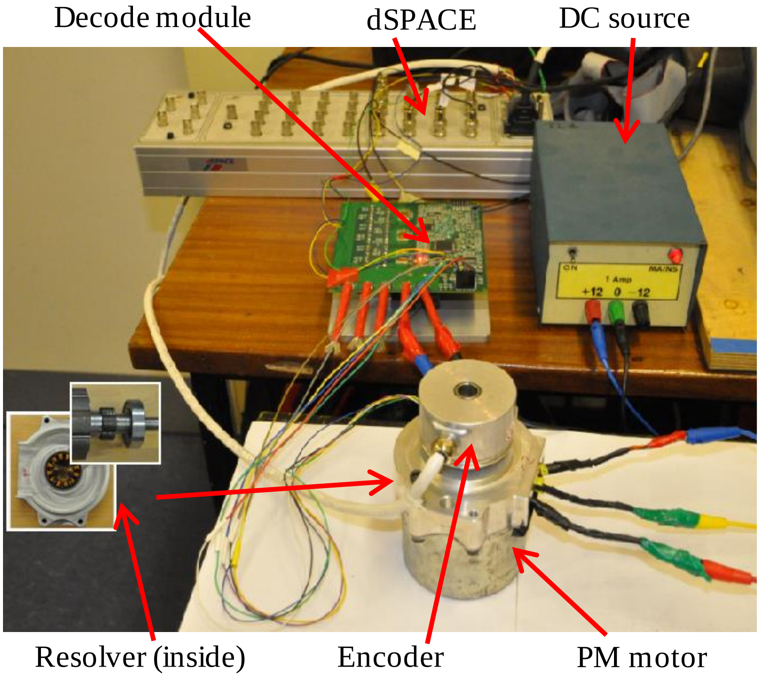

Fig. 6.17 Test platform.

The prototype is integrated into a PM motor, with the stator installed inside a pillow of the end cap and the rotor attached to the motor shaft. For comparison, a 5000-revolution optical encoder is coaxially installed at the end shaft of the motor, and the signal provided by the encoder is assumed to be the actual rotor position. A test platform is established on the basis of dSPACE DS1005 system, as shown in Fig. 6.17. In addition, the supply of exciting signal and the processing of output signals of resolver are performed through an R/D conversion IC, which can translate the analog outputs into A, B and Z signals for estimation of the rotor position. A DC source is used as power supply for the decode module.

The first step is to make a preliminary check in order to confirm whether the prototype is properly fabricated and installed, with main parameters shown in Table 6.4 and two phases of analog output voltages shown in Fig. 6.18. It can be seen that the measured values of main parameters basically agree with those designed, which verifies the aforementioned analyses. In addition, the two output signals are symmetrical and no obvious constant components exist, which preliminarily guarantees the normal operating characteristics of the prototype.

TABLE 6.4

MAIN PARAMETERS OF THE 5-X PROTOTYPE

Parameters	Measured values	Designed values
Input impedance (Ω)	139	127
Output impedance (Ω)	503	486
Transformation ratio	0.18	0.21

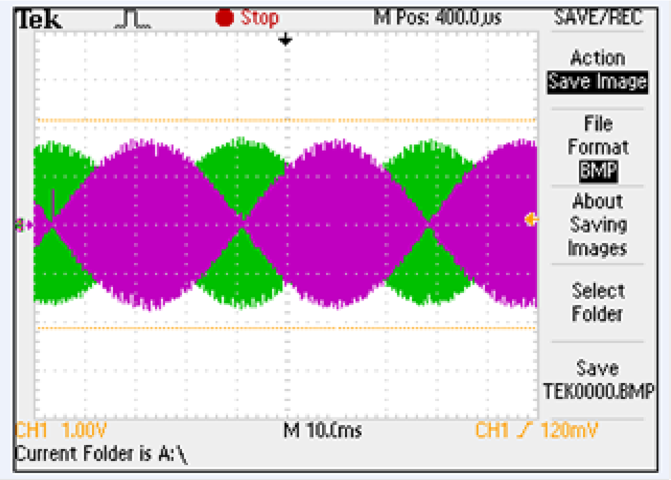

Fig. 6.18 Analog output voltages of the prototype.

The next step is to investigate the position detection accuracy of the prototype. With the PM motor driven to rotate at a constant speed of 180rpm, A, B and Z signals generated by the encoder are directly transmitted to dSPACE. Meanwhile, the other set of A, B and Z signals produced by the prototype as well as the decode module are also inputted into dSPACE for comparison. Rotor positions estimated by the two sensors can be easily obtained, as illustrated in Fig. 6.19. It should be noted that the results are captured using dSPACE software, and then plotted with Excel in order to clearly demonstrate the comparison. As can be seen, rotor positions estimated by two sensors basically agree with each other, and position error caused by the prototype is proven to be about ±2°, which is acceptable for general industrial applications. Obviously, the influence of inevitable eccentricity is reflected by the prototype, which deteriorates the detection accuracy.

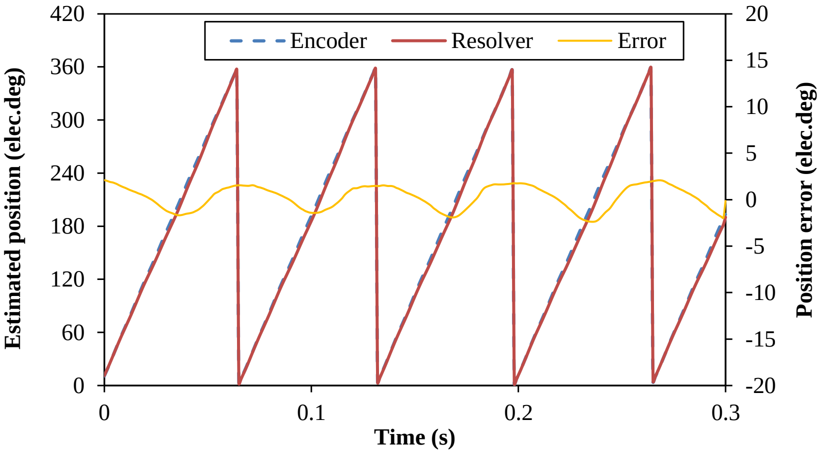

Fig. 6.19 Estimated rotor positions by encoder and resolver (180rpm).

In addition, the detection accuracy at higher speeds is investigated and compared, as shown in Fig. 6.20. It can be seen that corresponding position errors almost remain stable when the speed increases to 4000rpm (a maximum operating speed restricted by the test platform). The influence of operating speeds and assembling eccentricity will be further investigated in the following sections.

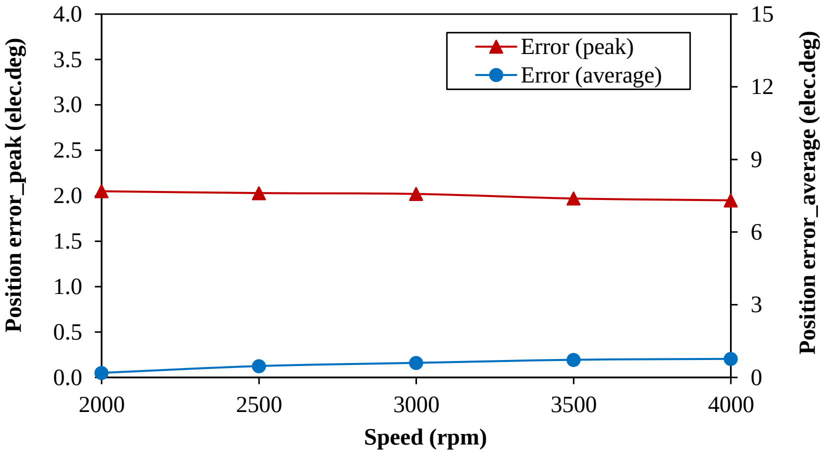

Fig. 6.20 Position errors obtained by tests at different speeds.

6.6 Typical Application of NTWVRR in HEV/EV Systems

Nowadays, VR resolvers are frequently used in HEV/EV applications [KIM10], [SHA08], [CUI12], due to the high reliability, easy installation as well as good detection accuracy. For this typical application, a design of the proposed NTWVRR is established based on dimensions of the conventional VR resolver used in Prius system, and the influence of actual application conditions will be further investigated in this section.

6.6.1 NTWVRR for HEV/EV Applications

In Toyota Prius system, VR resolvers are employed as position sensors for the traction and the integrated-starter-generator (ISG) machines, a FE model of which is established according to the main parameters shown in Table 6.4, with the winding arrangements illustrated in Fig. 6.21. It can be seen that three layers of coils are wound on each of the 14 stator teeth, and coil turns of the SINE and COSINE output windings are different. It can be deduced that the manufacturing process of such resolvers is very complicated due to the problems with overlapping sinusoidally distributed windings.

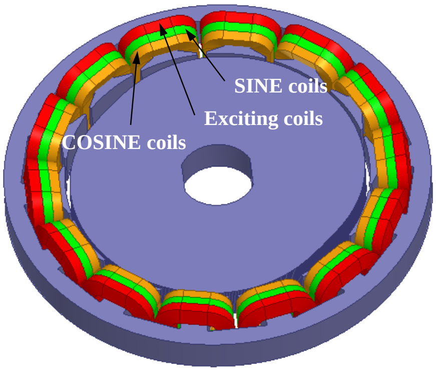

(a) Conventional VR resolver

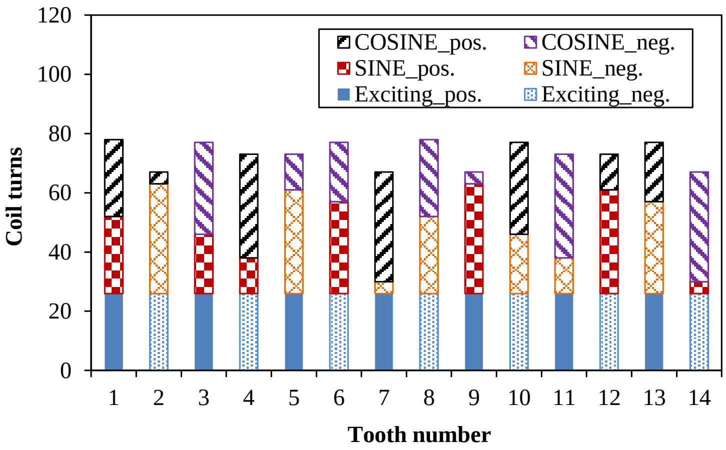

(b) Winding distribution

Fig. 6.21 Conventional VR resolver used in HEV/EV system.

TABLE 6.5

MAIN PARAMETERS OF VR RESOLVER MODEL

Parameters	Values
Stator teeth / rotor saliencies	24/2
Stator outer diameter (mm)	110
Stator inner diameter (mm)	80
Lamination axial length (mm)	8
Air-gap length (mm)	0.72 (Min.), 3.6 (Max.)

According to the proposed NTWVRR, a new design of the 2-X resolver based on the same parameters is established for the HEV system, as shown in Fig. 6.22. It can be seen that the two phases of output windings as well as the exciting winding are wound averagely on different stator teeth, and all the output coils of the 2-X resolver have an identical number of turns. In addition, unipolar exciting coils with an identical number of turns are employed to establish the exciting magnetic field.

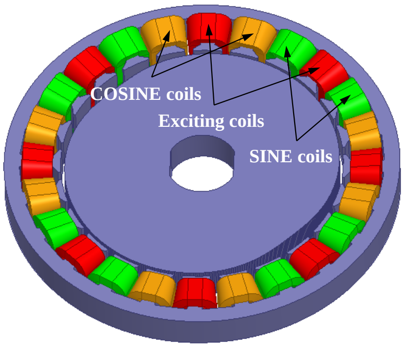

(a) 2-X NTWVRR

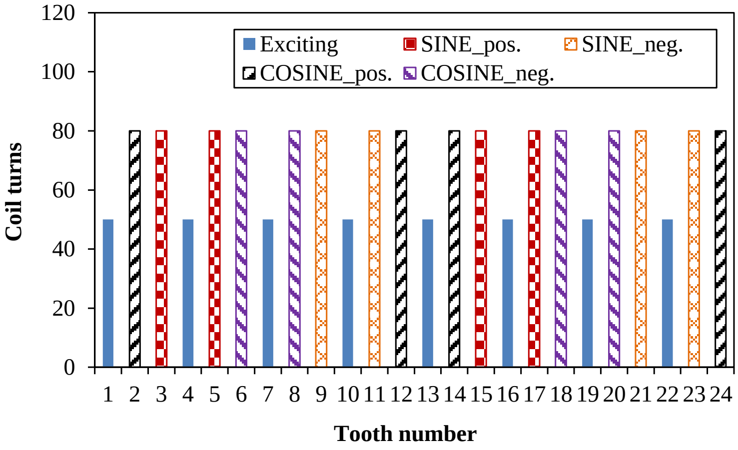

(b) Winding distribution

Fig. 6.22 NTWVRR for HEV/EV applications.

Firstly, the operating principle of the proposed design is investigated by the FE method. With a 10 kHz exciting signal applied to the exciting winding, the SINE and the COSINE output voltages can be obtained, as shown in Fig. 6.23. It can be seen that the two orthogonal output voltages and the exciting signals have the same frequency. By demodulation and an arc tangent calculation of the SINE and COSINE voltages, the rotor positions can be obtained, the task of which can be performed by a commercial decoding-chip, e.g. AU6802, AD2S80 and other subseries [TAM02], [ANA08].

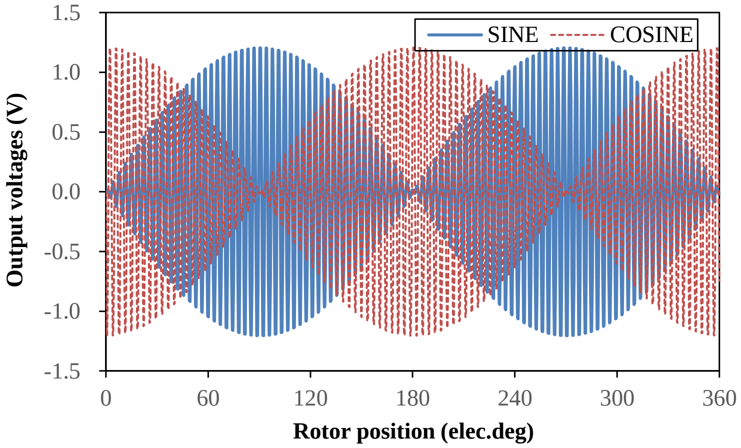

Fig. 6.23 Output signals of the proposed design.

Actually, the advantage can also be reflected on the winding fabrication duration. By employing the proposed design, the total number of coils is decreased from 42 to 24, resulting in the simplification of manufacturing steps. Usually, each winding-fabrication step includes the acceleration & deceleration process and the stator-tooth rotation process by a winding machine, which basically defines the winding-fabrication duration. Table 6.6 illustrates a comparison of action time between the two designs, which is closely related to the manufacturing cost. It can be seen that the winding-fabrication duration is significantly reduced from 210s to 120s with the novel design employed. Furthermore, short-circuit cases between different sets of coils can be avoided by the non-overlapping coils, which further improve the reliability and the rate of qualified products. Therefore, the proposed design can significantly simplify the winding fabrication process and reduce the overall cost of the products.

TABLE 6.6

COMPARISON OF WINDING-FABRICATION DURATION BETWEEN PROPOSED AND CONVENTIONAL VR RESOLVERS

Winding-fabrication index	Conventional	Proposed
Stator rotation steps	42	24
Stator rotation time per step (s)	3	3
Acceleration / Deceleration time (s)	2	2
Total duration (s)	210	120

6.6.2 Position Detection Accuracy under Actual Application Conditions

The operating principle has been verified by FE analyses, as well as the evaluation of winding-fabrication duration. In this section, the influence of actual conditions in HEV/EV applications is investigated by the FE method, including the operating speed and the assembling eccentricity. As an index of the detection accuracy, the electric angle errors under different application conditions are investigated.

A. Operating speed

The traction and the ISG machines in a HEV/EV system usually operate over a wide speed range, e.g. from 0 to 6000rpm, even as high as 12000rpm. Therefore, it is necessary to investigate the detection accuracy of the resolver sensor at different operating speeds. In order to obtain the corresponding electric errors, the output signals and its basic signal processing method should be firstly investigated. According to the operating principle, the output signals of VR resolver involve two different components: the transformer electromotive force (EMF) and the motional EMF, as shown in Fig. 6.24. It can be seen that the motional EMF has the same period cycle as the normal transformer EMF, but with different phase angles (90° electric angle in advance), due to different generation mechanisms. Actually, the transformer EMF is produced by variation of the exciting current whilst the motive EMF is established through the variation of air-gap permeance.

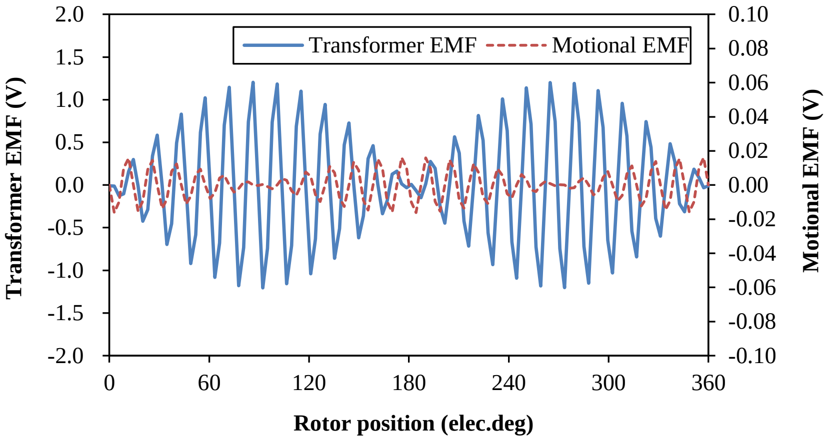

Fig. 6.24 Transformer EMF and motional EMF induced in output windings (SINE phase).

As an example, the output voltage in the SINE phase of VR resolver can be expressed by:

$$E_s = E_{st}\sin(p\theta)\cos(\omega t) + p\omega_m E_m \cos(p\theta)\sin(\omega t) \tag{6. 13}$$

where p is the number of rotor saliencies. E_{st} is the magnitude of transformer EMF and ω represents the angular frequency of exciting voltage. E_m is the magnitude of motional EMF at unit angular speed and ω_m represents the mechanical angular frequency. By demodulation, the signal is transferred to:

$$E_s{}' = E_s\cos(\omega t) = \frac{1}{2}E_{st}\sin(p\theta)\,[1+\cos(2\omega t)] + \frac{1}{2}p\omega_m E_m\cos(p\theta)\sin(2\omega t) \tag{6. 14}$$

With the high-frequency components removed by a low-pass filter, the objective position function of resolver can be obtained, which is independent of the rotating speed. Therefore, through an arc tangent operation on the envelopes of output voltages, the estimated rotor positions can be obtained, as well as the electric errors.

For the proposed VR resolver, the electric angle errors under 4 different operating speeds are investigated, as shown in Fig. 6.25. It can be seen that the electric error almost remains stable at $\pm 0.4^{\circ}$ when the speed increases from 3000rpm to 12000rpm. Therefore, accurate rotor positions can be achieved by the novel design over a wide speed range required by a typical HEV/EV system. Theoretically, no phase delay will be introduced for high-speed operations, due to the removal of motional EMF by demodulation, and the resolver itself contributes no extra detection errors, except the intrinsic error caused by voltage harmonics.

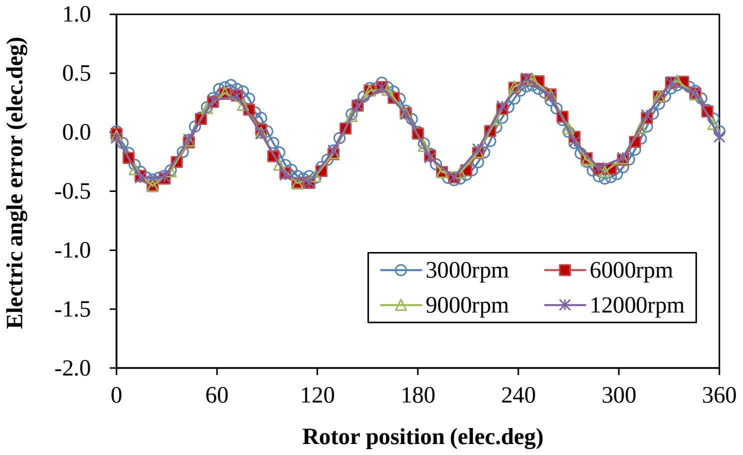

Fig. 6.25 Detection accuracy under different operating speeds.

B. Eccentricity

When integrated into the machines, the rotor eccentricity of VR resolvers, either static or dynamic, as shown in Fig. 6.26, is difficult to avoid during assembling and operating, due to its frameless design. In this section, the sensitivity to rotor eccentricity of the proposed VR resolver is investigated.

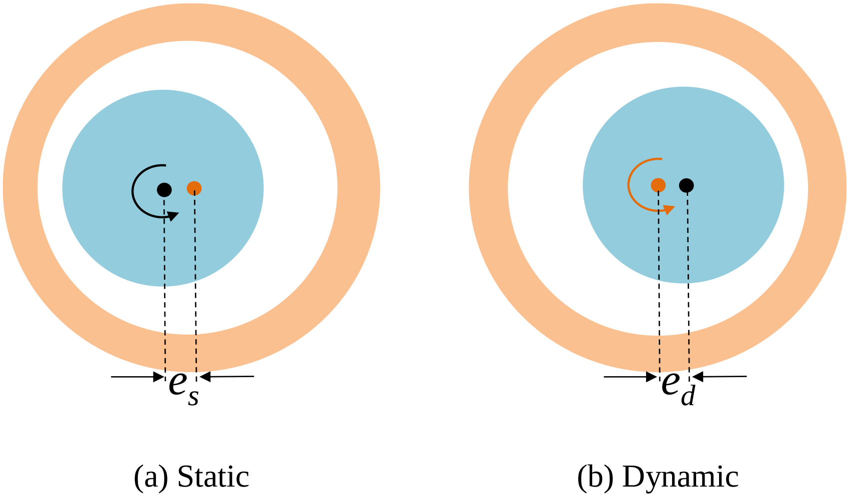

(a) Static

(b) Dynamic

Fig. 6.26 Static and dynamic eccentricities during assembling and operating.

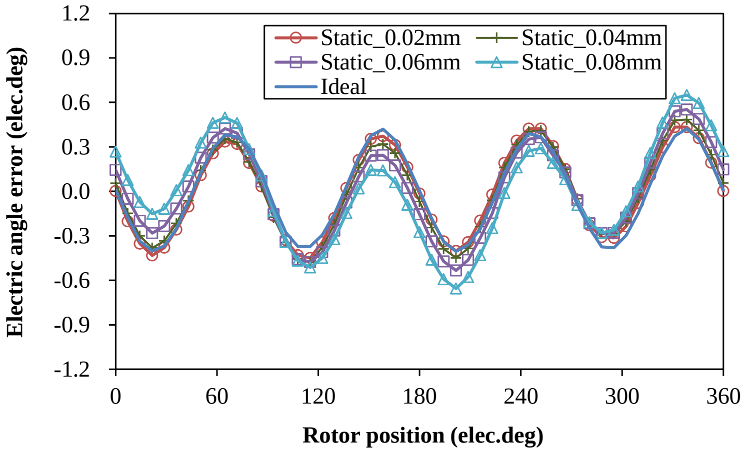

(a) Static eccentricity

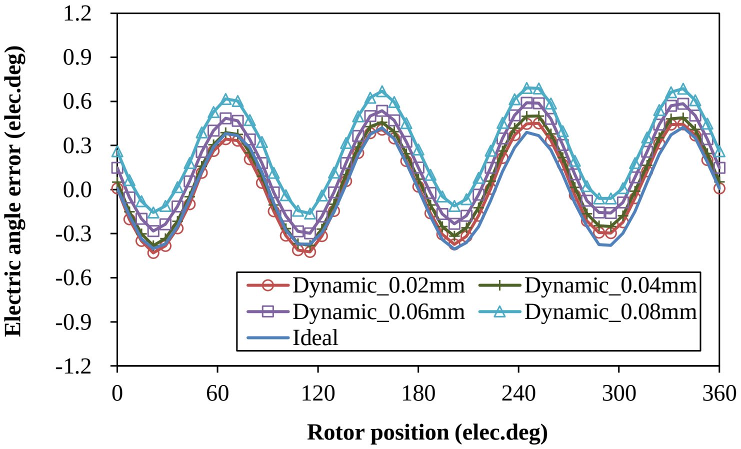

(b) Dynamic eccentricity

Fig. 6.27 Influence of eccentricities on electric angle error.

Based on the resolver model established above, the electric angle errors are investigated with different values of rotor eccentricity considered, including the static and the dynamic cases, as shown in Fig. 6.27. It can be seen that the consequent electric angle errors are within $\pm 0.6^{\circ}$ and no obvious influence is introduced to the detection accuracy when the eccentricity increases from 0 to 0.08 mm. Therefore, it can be deduced that the novel VR design is not sensitive to assembling eccentricity.

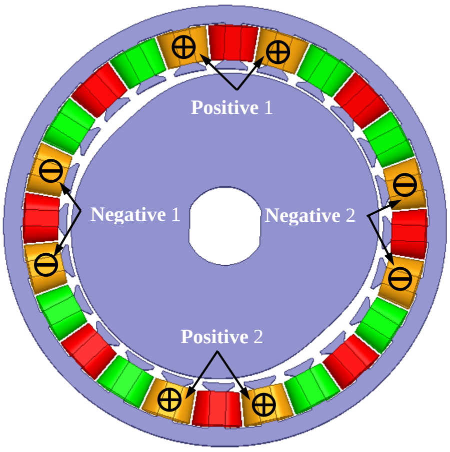

Fig. 6.28 Distributions of positive and negative coil groups for output windings (SINE phase) in the proposed 2-X VR resolver.

Actually, the insensitivity to assembling eccentricity of the proposed VR resolver is closely related to the output winding distributions. According to Fig. 6.22 (b), each output winding is composed of symmetrically distributed positive and negative coil groups, which have 4 coils each. The two coil groups of SINE phase output winding is investigated for example, as shown in Fig. 6.28. It can be seen that the positive and the negative coil groups are alternately distributed with 90^{o} mechanical angle intervals, corresponding to the number of polarities for the VR resolver.

According to the operating principle of VR resolvers, positive and negative DC components (after demodulation) exist in the output voltages of two coil groups respectively. Under ideal conditions, two DC components are of the same magnitude, which can be eliminated in the synthetic output voltage, as shown in Fig. 6.29. For the proposed VR resolver, eccentricity may increase or decrease the DC voltages in some of the coils (e.g. positive 1 or negative 1), whilst the other coils (positive 2 or negative 2) of the same group present corresponding adverse variation. Therefore, the DC component in either of the two coil groups will not be influenced, due to the complimentary function by the symmetrically distributed positive or negative coil groups. Even with eccentricity considered, no extra DC component is introduced in the synthetic output voltages. Therefore, the detection accuracy of the proposed VR resolver will not be obviously influenced by rotor eccentricities.

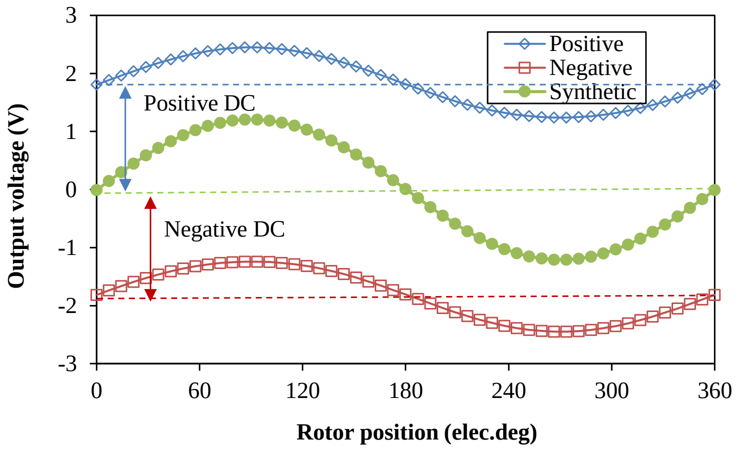

Fig. 6.29 Output voltages in positive and negative coil groups of output windings (SINE phase, after demodulation).

6.6.3 Comparison between the existing and proposed VR resolvers

The influence of operating speeds and the assembling eccentricities on the proposed resolver topology has been investigated. Further, the corresponding influence on the existing VR resolver is also analysed and compared with the proposed topology, as shown in Fig. 6.30. It can be seen that the operating speed has very limited influence on the two resolvers and the electric angle errors almost remain stable respectively when the speed increases from 3000rpm to 12000rpm. However, the existing design proves to be much more sensitive to the assembling eccentricity and the electric angle error significantly increases to ±0.3 ° with 0.08mm static eccentricity considered, which is mainly caused by the residual DC components in output voltages.

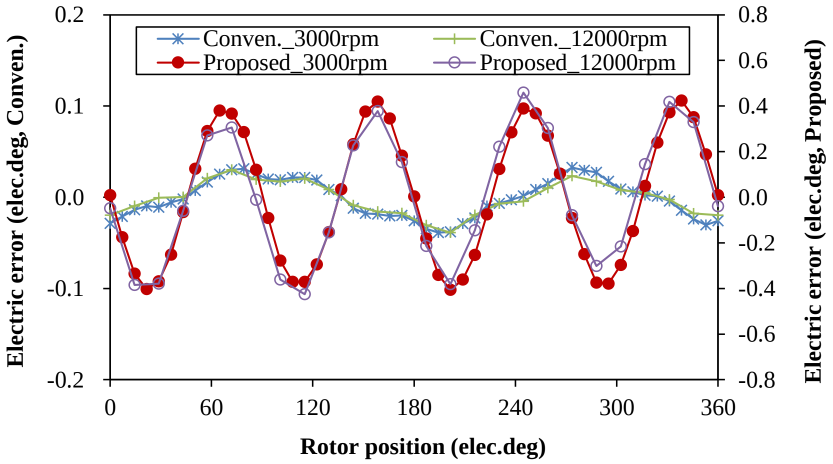

(a) Electric errors under different speeds

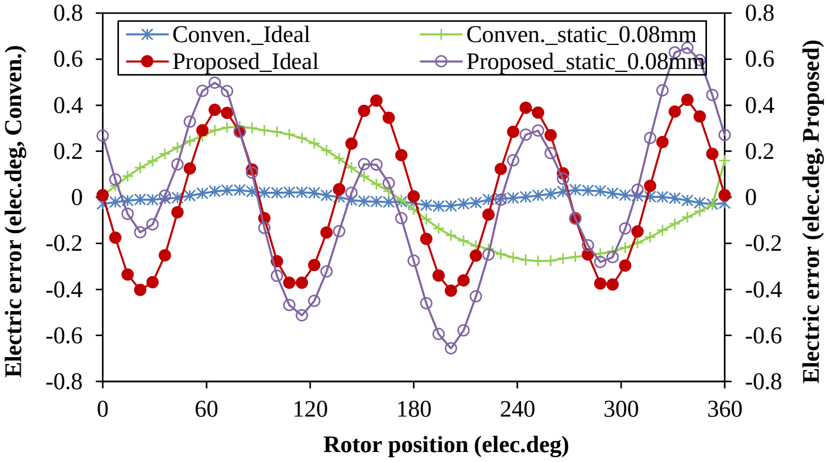

(b) Electric errors under different static eccentricities

Fig. 6.30 Comparison of electric angle errors between conventional and proposed VR resolvers with speed and eccentricity considered.

6.6.4 Identical Stator and Windings for Different Poles of Resolvers

As described in the previous section, due to similar winding distributions as in Fig. 6.22 (b), it can be further deduced that the proposed 24-slot stator and windings can also be employed in 10-X and 14-X resolvers, as shown in Fig. 6.31. In order to make comparison amongst the three combinations, sinusoidal rotors based on identical minimum (0.72mm) and maximum (3.6mm) air-gap lengths are established respectively, which share the aforementioned 24-slot stator and windings. With the FE method employed, the output voltages and corresponding electric angle errors are investigated and analysed in this section.

Based on three different combinations, envelopes of the output voltages are captured respectively, as shown in Fig. 6.32 (a). In addition, the detection accuracy is also investigated, with the electric angle errors shown in Fig. 6.32 (b). As can be seen, normal position signals can be obtained by the three combinations respectively, which is mainly due to the identical winding distributions of three resolvers. However, there are remarkable differences on the magnitudes of output voltages, which are 1.25V, 1.0V and 0.7V, respectively. Usually, the analogue voltage magnitude should be within a certain range required by commercial decoding-chips. Too high voltage may damage the decoding-chip whilst the accuracy may be deteriorated by too low signals. Therefore, it is necessary to investigate the origins of voltage differences, as a guidance to make the output voltages applicable for signal processing by decoding-chips.

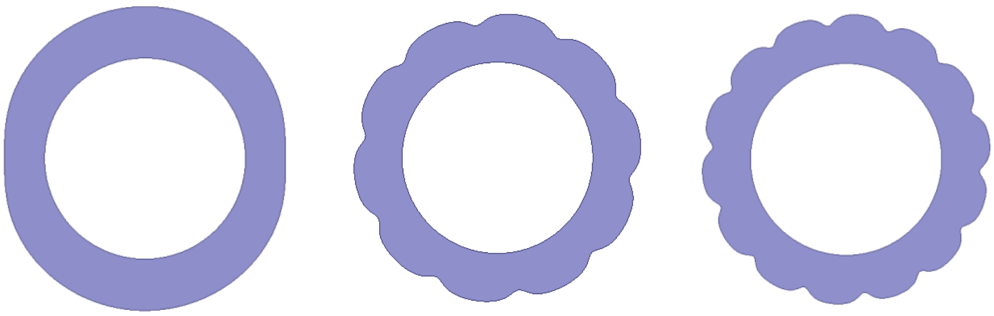

(a) 2-X rotor (b) 10-X rotor (c) 14-X rotor

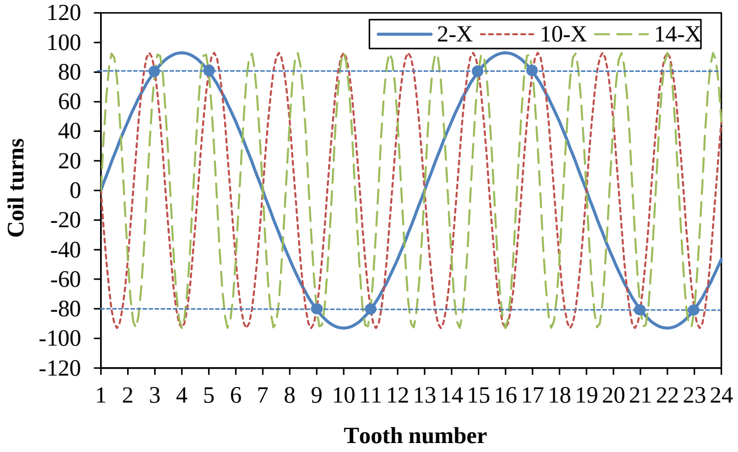

(d) Output winding distributions (SINE phase)

Fig. 6.31 Identical stator and windings for three rotors with different numbers of rotor saliencies.

For VR resolvers, it has been deduced that the output voltage is proportional to the magnitude of sinusoidal air-gap permeance within the range of one stator tooth. Before comparison of the permeance amongst the three different combinations, the air-gap length function of VR resolvers can be presented by:

$$\delta = \frac{a}{b + \cos(p\theta)} \tag{6. 15}$$

where the constants a and b represent the length factor and the shape factor, respectively. Based on the function of air-gap shown in (6.15), sinusoidal air-gap permeance can be obtained, together with a constant component. According to the relative position between the rotor and the stator shown in Fig. 6.33 and with the slot-opening effect ignored, the magnitude of sinusoidal air-gap permeance within the range of one stator tooth can be described as:

$$P_{m1} = 2\int_0^{\pi/Z} \frac{\mu_0 R_{si} L_{ef}\cos(p\theta)}{a}\,d\theta = \frac{2\mu_0 R_s L_{ef}}{ap}\sin\left(\frac{\pi p}{Z}\right) \tag{6. 16}$$

where μ_0 is the vacuum permeability, Z is the number of stator slots. R_s and L_{ef} represent the stator inner radius and the core axial length, respectively. It can be obtained from (6.16) that the magnitudes of sinusoidal air-gap permeance within one stator tooth in the 10-X and the 14-X resolvers are 0.747 and 0.533 of that in the 2-X resolver, respectively. Therefore, different values of output voltages are produced with the identical stator and windings employed in the three resolvers, due to the different sinusoidal air-gap permeance, as shown in Fig. 6.32 (a). It should also be noted that the influence of slot opening is not considered, which results in a little difference on the aforementioned theoretical factor.

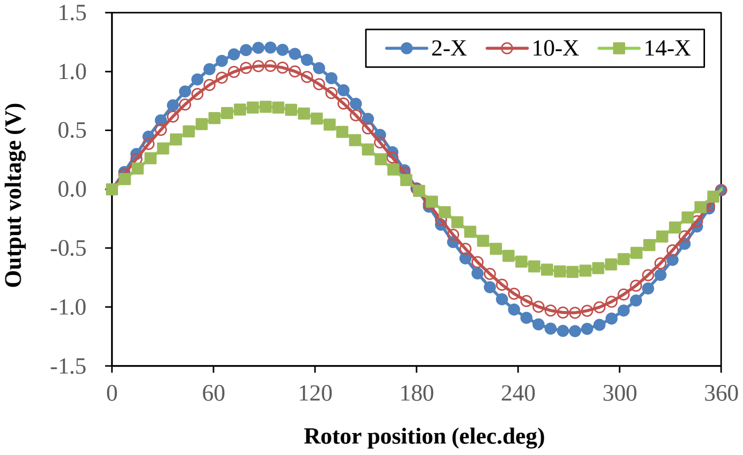

(a) Output voltages (SINE phase)

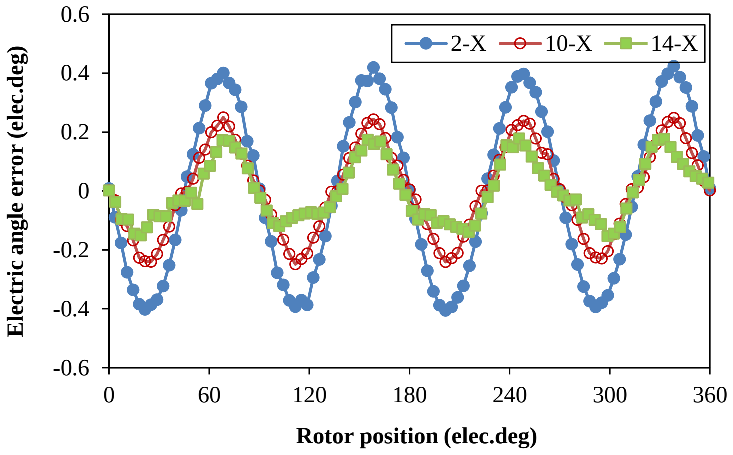

(b) Electric angle errors

Fig. 6.32 Comparison of output voltages (SINE phase) and electric errors between 2-X, 10-X and 14-X resolvers with identical stator and windings.

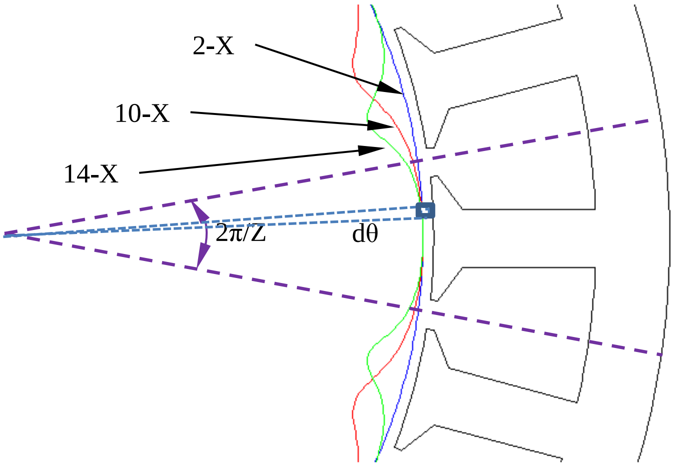

Fig. 6.33 Magnitudes of sinusoidal air-gap permeance within one stator tooth in 2-X, 10-X and 14-X resolvers.

In order to verify the influence of slot opening, the output voltages under different tooth arc widths are obtained by the FE method respectively, as shown in Fig. 6.34. On the one hand, it can be seen that different magnitudes of output voltages are produced with the identical stator and windings employed in the 2-X, 10-X and 14-X resolvers. On the other hand, the voltage difference becomes more obvious when the tooth arc angle increases, which is mainly due to the increasing difference of sinusoidal air-gap permeance within one stator tooth.

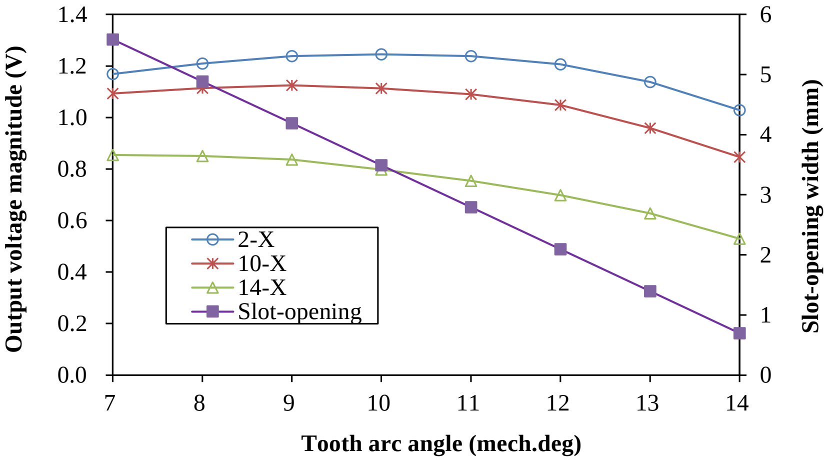

Fig. 6.34 Comparison of output voltage magnitudes under different tooth arc widths amongst 2-X, 10-X and 14-X resolvers (identical input voltage).

However, different air-gap length functions can be employed in the 10-X and the 14-X resolvers, in order to increase the component of sinusoidal air-gap permeance and consequently enhance the output voltages. As an extension of the proposed design, the 10-X and the 14-X resolvers with the identical stator and windings can be employed in related multipolar PM machines.

6.6.5 Prototype and Test

Based on the main parameters shown in Table 6.4 and the winding distributions shown in Fig. 6.33, prototypes of the proposed VR resolver are fabricated, including the 24-slot stator and the three rotors, as shown in Fig. 6.35.

In order to verify the foregoing analyses, a test platform based on the dSPACE DS1005 system is established, as shown in Fig. 6.36. The resolver prototype is attached to a PM motor and a 5000-revolution encoder is co-axially installed, the output of which is assumed to be the real rotor positions. The decoding module with a commercial decoding-chip provides a 10 kHz sinusoidal exciting signals, collects the analogue output voltages and converts into digital A, B, Z signals, which are input to the dSPACE for processing.

As shown in Fig. 6.37, the analogue output signals of the 2-X prototype are firstly investigated, the quality of which directly relates to the position detection accuracy. It can be found that no obvious signal distortion exists in either of the two output voltages, which indicates that the basic operating characteristics can be guaranteed. In addition, magnitudes of the output voltages will be analysed and compared amongst the three combinations later in this section.

(a) Stator (b) 2-X rotor

(c) 10-X rotor (d) 14-X rotor

Fig. 6.35 Prototypes of the proposed VR resolver.

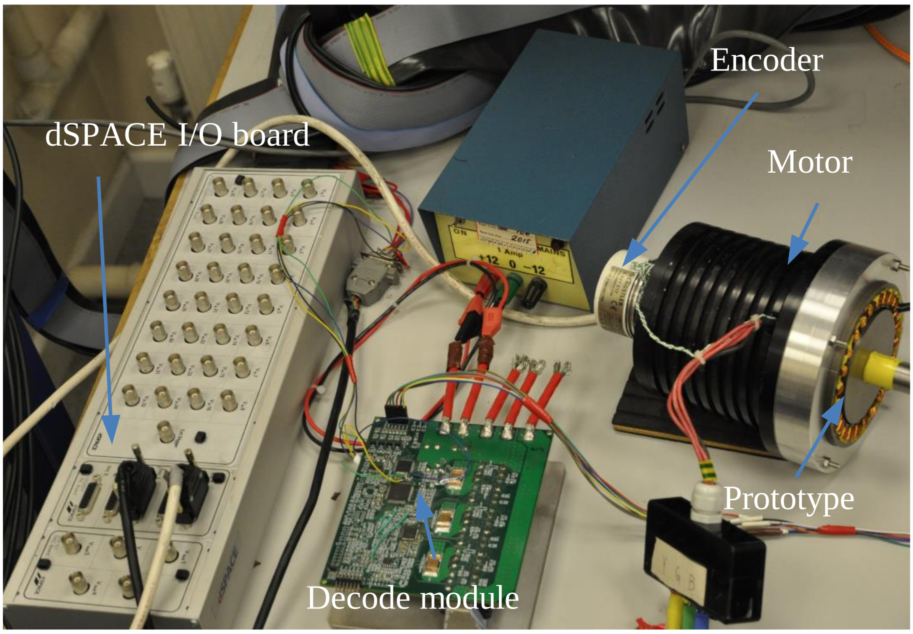

Fig. 6.36 Test platform.

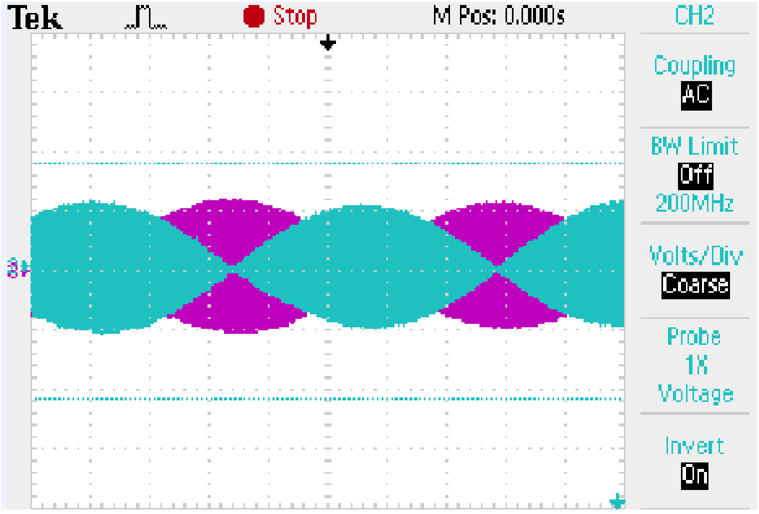

Fig. 6.37 Output voltages of the 2-X resolver.

As a position sensor, the detection accuracy is an important index, which can be obtained through the test platform. With the PM motor driven to a constant speed, the A, B and Z signals produced by the encoder and the resolver are input to the dSPACE system, through which the two estimated position signals can be obtained as well as the electric errors, as shown in Fig. 6.38. It can be seen that a good detection accuracy can be achieved by the 2-X resolver with the electric error in the range of ±1.3°, which is sufficient for the machine driven units in HEV/EV systems.

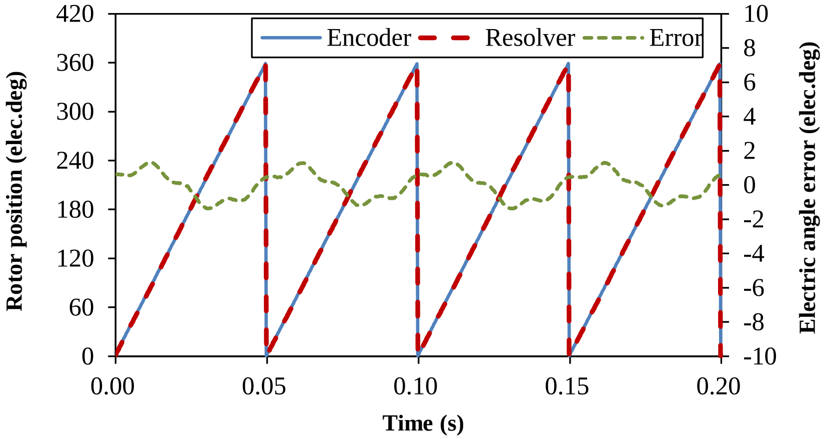

Fig. 6.38 Comparison of the estimated rotor positions between encoder and 2-X resolver prototype (600rpm).

Furthermore, the detection accuracy at different operating speeds is also investigated for the 2-X resolver, i.e. 600rpm, 1000rpm and 1600rpm (the maximum applicable speed of the test system). As shown in Fig. 6.39, the electric errors present very similar variations, including the peak-to-peak value and the average value. In addition, the fundamental period cycle of the errors (1 cycle during 360° electric angles) reflects that a little DC component is still introduced in the output voltages, caused by asymmetric coil locations during the prototype fabrication. Similar to the FE results, there are still components of the 4th order in the electric errors, which is mainly due to the intrinsic harmonics of voltages. Due to the stable electric errors, it can be deduced that no obvious influence on the detection accuracy is introduced by the resolver itself, which verifies the foregoing analyses.

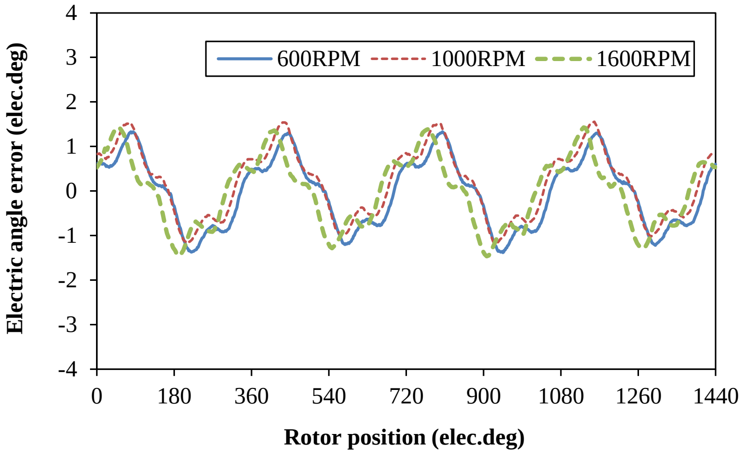

Fig. 6.39 Electric angle errors of the 2-X prototype at different speeds.

In addition, the 10-X and the 14-X prototypes are also tested with related parameters shown in Table 6.7. As can be seen, the three prototypes have very similar input inductances, i.e. 2.24 mH, 2.25 mH and 2.25 mH, which is mainly due to the identical component of constant air-gap permeance. The similarity is also reflected on the output inductances. Furthermore, the transformation ratio results indicate the magnitudes of output voltages with an identical exciting voltage employed in the three resolvers. Due to unequal values of sinusoidal air-gap permeance, different output voltages are induced, which verifies the foregoing analyses. In addition, it can also be found that the measured parameters basically agree with the 3D FE results. Actually, for the pancake designs of VR resolvers, the end effect cannot be ignored and the 3D FE method is necessary in order to make more accurate prediction of main parameters.

TABLE 6.7

INDUCTANCES AND OUTPUT VOLTAGES IN 2-X, 10-X AND 14-X RESOLVERS

Parameters	Measured results			3D FE results		
	2-X	10-X	14-X	2-X	10-X	14-X
Input inductance (mH)	2.24	2.25	2.25	2.23	2.24	2.25
Output inductance (mH)	6.63	6.69	6.77	7.0	7.22	7.34
Transformation ratio	0.14	0.11	0.07	0.17	0.14	0.09

Finally, it should also be noted that the position signals by a 2-X resolver can be automatically converted into 8-pole outputs with a simple setting in the decoding-chip [TAM02]. Therefore, the proposed VR resolver can be employed in conventional 48-slot-8-pole and 12-slot-8-pole PM machines which are frequently used in HEV/EV applications.

6.7 Conclusion

A novel VR resolver with non-overlapping tooth-coil windings (NTWVRR) has been proposed in this chapter. The most significant advantage for this design is the separation of exciting coils, SINE and COSINE output coils, which are located on different stator teeth. A further improvement is that both of the two output windings are composed of identical coils, rather than sinusoidally distributed styles, as is the case with a conventional resolver. Thus the manufacturing process is significantly simplified. The basic operating principle and key performance have been verified by FE analyses and analytical derivation, as well as related tests on a 5-X NTWVRR prototype.

Moreover, the proposed resolver topology enables identical stator and windings to be commonly utilized by 3 different poles of resolvers. In addition, feasible stator slot/rotor pole combinations for this novel topology are summarized, in order to satisfy the requirements of different applications.

As a typical application of the proposed resolver topology, a 2-X NTWVRR has been proposed for HEV/EV systems. With the influence of actual application conditions considered, i.e. the operating speeds and the installing eccentricities, a stable position detection accuracy can be achieved by the proposed design. Prototypes have been fabricated and tested, as a verification of the foregoing analyses.

CHAPTER 7 NOVEL DESIGNS OF ROTOR CONTOURS FOR VARIABLE RELUCTANCE RESOLVERS

7.1 Introduction

In addition to the stator and windings, the rotor is another key component of a VR resolver, for which a sinusoidal design of rotor contour is usually employed to eliminate field harmonics. However, the exciting magnetic flux flowing through the air-gap is not along straight lines towards the rotor centre, especially in regions with large air-gap lengths. Consequently, a series of air-gap permeance harmonics may be introduced, which bring in additional voltage harmonics and degrade the position detection accuracy. In this section, output voltage harmonics of the 2-X NTWVRR (as shown in Fig. 7.1) will be firstly investigated, followed by potential elimination solutions by optimal rotor contours, i.e. the air-gap length functions, the effectiveness of which will be further investigated in a conventional VR resolver topology.

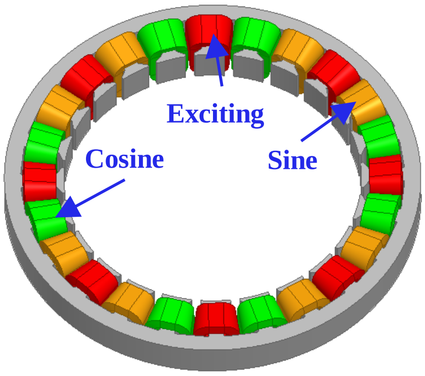

(a) Stator and windings

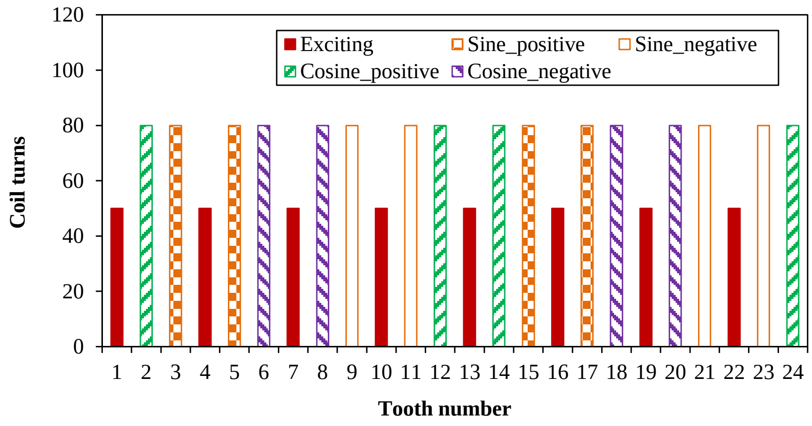

(b) Winding distributions

Fig. 7.1 Stator and windings of the 2-X NTWVRR [GE15a].

7.2 Sinusoidal Design

For the first step, the aforementioned sinusoidal design of rotor contour is investigated. In order for more convenient determination of the maximum and minimum air-gap lengths, the air-gap length function can be expressed by:

$$\delta = \frac{K\delta_{min}}{1 + (K - 1)\cos(p\theta)} \qquad (1 < K < 2) \tag{7. 1}$$

where K is defined as the fundamental wave factor and δ_{min} represents the expected minimum air-gap length. By employing different values of K, different air-gap lengths can be obtained when δ_{min} is fixed (a typical value of 0.72mm in the following analyses), with the corresponding rotor radii shown in Fig. 7.2. It can be seen that the maximum air-gap length between the stator and rotor increases from 1.68 mm to 13.68 mm when K changes from 1.4 to 1.9.

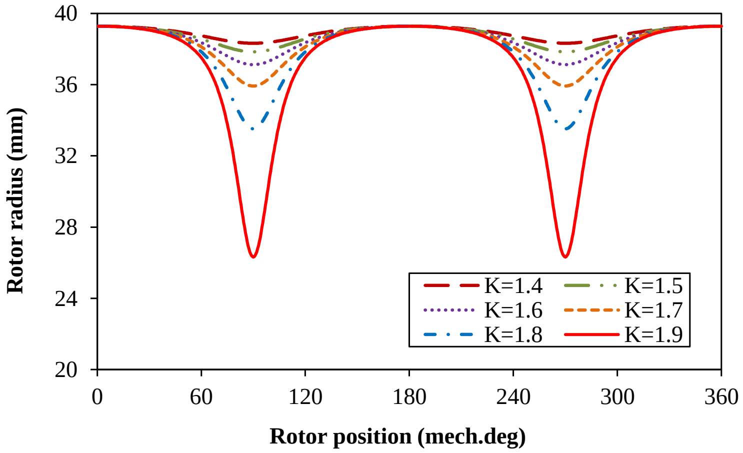

Fig. 7.2 Rotor radii by different values of fundamental wave factor *K*.

By 2D FE analyses, the output voltages of VR resolvers with identical stator and windings but different rotors are obtained, with the sine phase voltages shown in Fig. 7.3. As can be seen, the voltage magnitude increases from 0.90 V to 1.37 V when *K* increases from 1.4 to 1.9, which is mainly due to the increasing magnitudes of sinusoidal air-gap permeance within one stator tooth. According to the requirements of commercial decoding chips [TAM02], [ANA08], the output voltage of VR resolver should be within a certain range to avoid abnormal position signals during the decoding operation. Therefore, it can be further deduced that the number of coil turns can be reduced by employing rotors with higher values of *K*, which reduces the consumption of copper wires and the duration of winding fabrication, as well as the total cost.

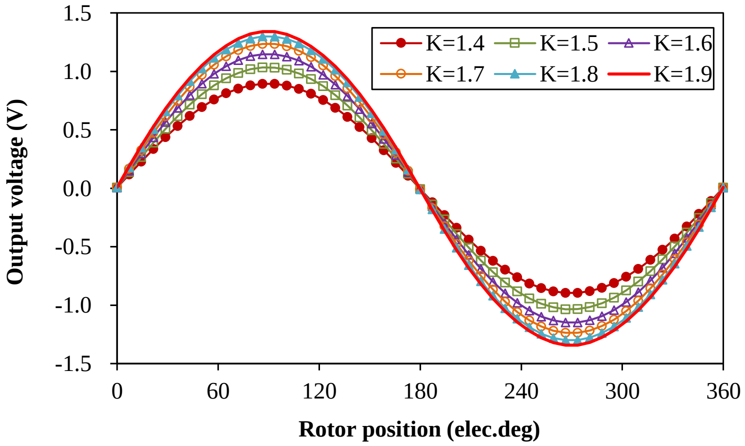

Fig. 7.3 Influence of fundamental wave factor *K* on voltage magnitudes (sine phase, after decoding operation).

As a position sensor, the position detection accuracy is an important index for VR resolvers, which is closely related to the quality of output voltages, e.g. the harmonic components. A comparison of the voltage harmonics distribution is carried out between the designs by different values of fundamental wave factor *K*, as shown in Fig. 7.4 (a). It can be seen that the third order of voltage harmonics present a more rapid increasing variation – changing from 1.45 mV to 18.2 mV – when *K* increases from 1.4 to 1.9. Similarly, the influence of voltage harmonics can be reflected on the position detection accuracy, which is represented by electric angle error between the calculated and the actual rotor positions, as shown in Fig. 7.4 (b). On the one hand, the fourth order of electric angle errors are usually introduced by the third order of voltage harmonics, which cannot be neglected. On the other hand, the electric error increases from ±0.14 °to ±1.05 °when *K* changes from 1.4 to 1.9, which is mainly due to the increasing ratios of harmonic components (the third order) in the output voltages.

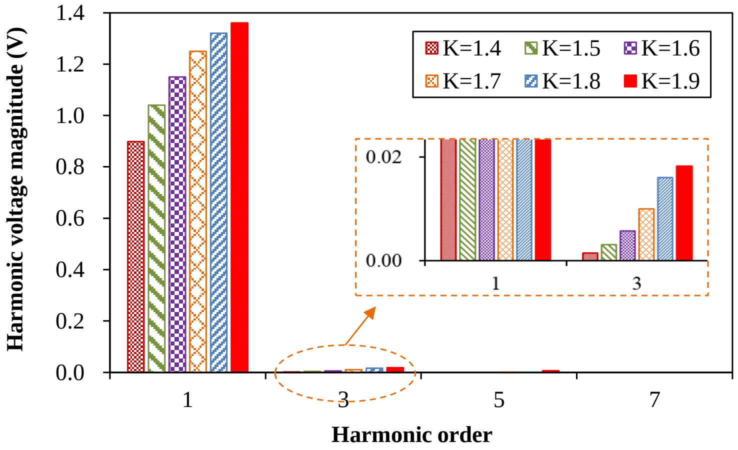

(a) Voltage harmonics

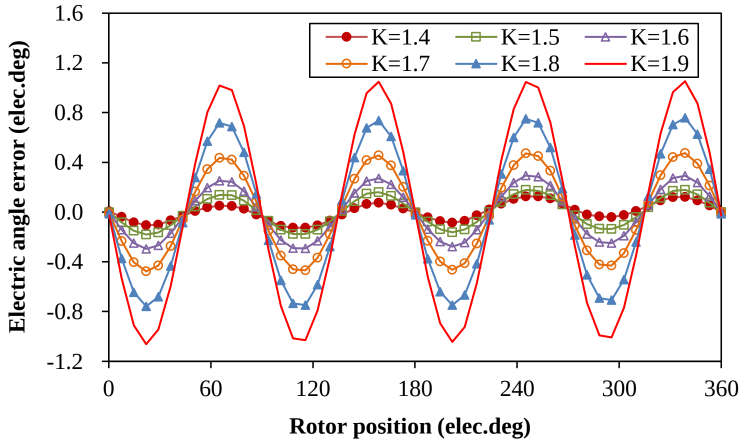

(b) Electric angle errors

Fig. 7.4 Influence of fundamental wave factor *K* on voltage harmonics and position detection accuracy.

Therefore, the fundamental wave factor *K* exhibits a conflict between the output voltage magnitude and the position detection accuracy of the aforementioned VR resolver. In order to reduce the number of coil turns as well as the cost of fabrication, VR resolver designs by higher fundamental wave factor *K* in the air-gap length function can be employed. However, the consequent voltage harmonics should be further improved.

7.3 Eccentric Design

According to the foregoing analyses in IPM machines, the eccentric design of rotor contour can also be employed to reduce the harmonics, as shown in Fig. 7.5. It can be seen that the rotor contour is composed of circle arc segments, the number of which represents the number of rotor saliencies, e.g. two circle arc segments for the 2-X rotor. In addition, a typical feature of this design is that centres of the circle arc segments are not the rotor centre, but with a displacement *A*.

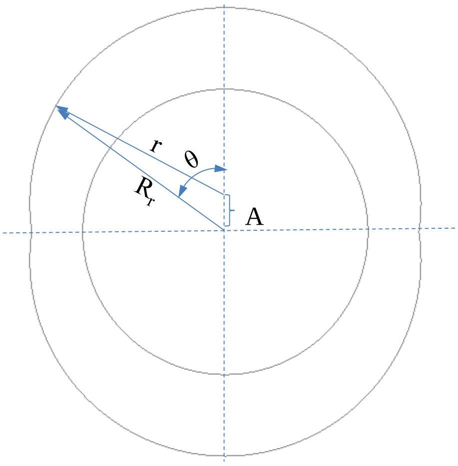

Fig. 7.5 Eccentric design of rotor contour (*p*=2).

According to the eccentric design, the rotor outer radius can be described by:

$$R_r(\theta) = \mathrm{A}\cos(\theta) + \sqrt{r^2 - (Asin(\theta))^2} \tag{7. 2}$$

where *A* is the displacement of arc centres (designated as eccentric distance) and *r* represents the radius of circle arc segments. It can be deduced that the rotor contour is only subject to the eccentric distance *A* (or the circle arc radius *r*) when the minimum air-gap length is defined (0.72mm). Therefore, optimal rotor contour of the eccentric design can be obtained by choosing a proper eccentric distance. During the optimization process, the influence of the eccentric distance on the VR resolver can be obtained, including the output voltage quality and the position detection accuracy.

With the foregoing stator and windings (shown in Fig. 7.1) employed, the influence of eccentric distance on the 2-X NTWVRR is investigated, as shown in Fig. 7.6. It can be found that the output voltage rises from 0.824V to the maximum value of 1.102V when the eccentric distance increases from 1mm to 4.5mm, and then it starts to decrease gradually. For the corresponding electric angle error, it decreases from ±0.488 ° to the minimum value of ±0.277 ° when the eccentric distance increases from 1mm to 2.5mm, followed by a rapid increasing trend – as high as ±1.256 ° for 6mm eccentric distance.

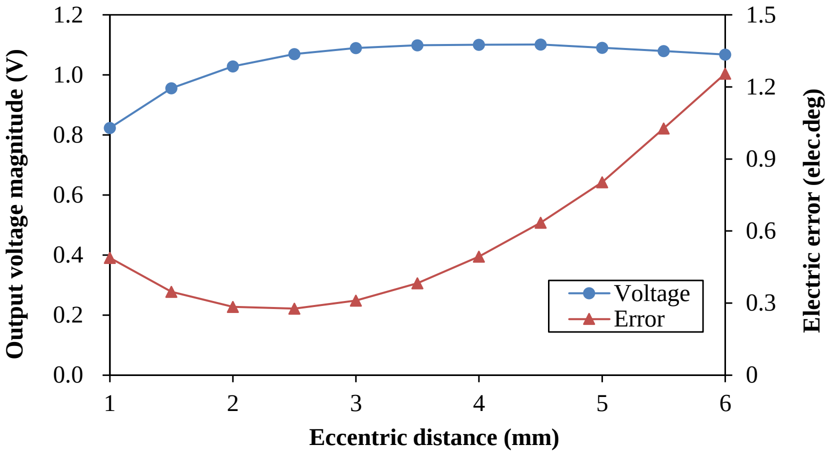

Fig. 7.6 Influence of eccentric distance on output voltage and electric error.

In order for a global evaluation of different design methods, comparison between the sinusoidal and eccentric designs is carried out. At the first step, similar maximum (2.88mm) and minimum (0.72mm) air-gap lengths are employed for the two designs, in which the fundamental wave factor *K* and the eccentric distance *A* are selected as 1.6 and 2.5mm (lowest electric angle error) respectively. Corresponding output voltages and electric angle errors are illustrated, as shown in Fig. 7.7. It can be seen that the output voltage of the sinusoidal design is 1.148V, which is a little higher than that of eccentric design (1.069V). In addition, very similar detection accuracy can be achieved by the two designs, both ±0.3 °.

According to the foregoing analyses, almost maximum output voltages can be obtained by the sinusoidal design with 1.9 of the fundamental wave factor *K* and the eccentric design with 4.5mm of eccentric distance *A* respectively. Another comparison is carried out between the two typical designs, as shown in Fig. 7.8. It can be found that 22% higher output voltage can be obtained by the sinusoidal design, which results in a smaller number of coil turns for actual products. However, the electric angle error is reduced from ±1.06 °to ±0.62 °with the eccentric design employed.

In summary, it proves to be difficult for the sinusoidal and eccentric designs to achieve both high output voltages and low electric angle errors. Therefore, further improvement is still necessary.

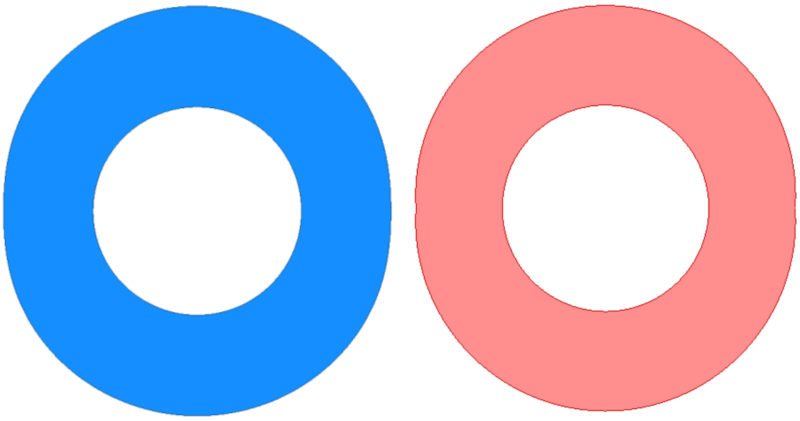

(a) Rotors with sinusoidal (left) and eccentric (right) designs

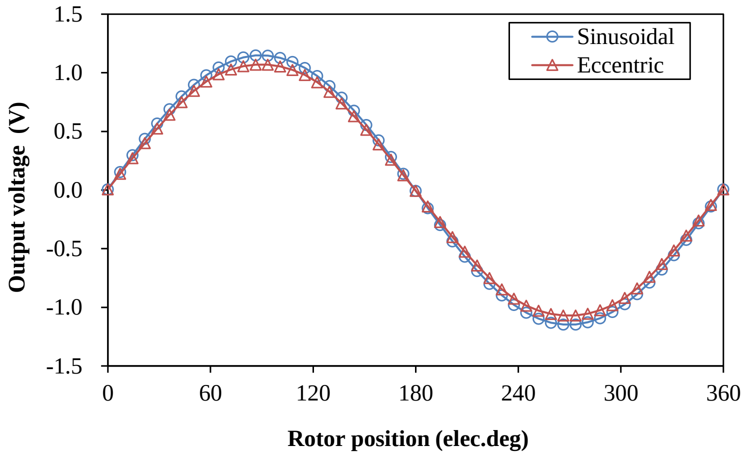

(b) Output voltages

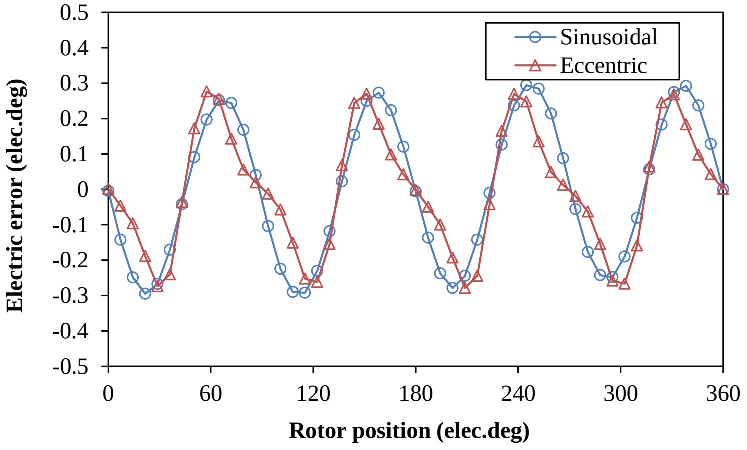

(c) Electric errors

Fig. 7.7 Comparison of designs with sinusoidal (*K*=1.6) and eccentric (*A*=2.5mm) designs.

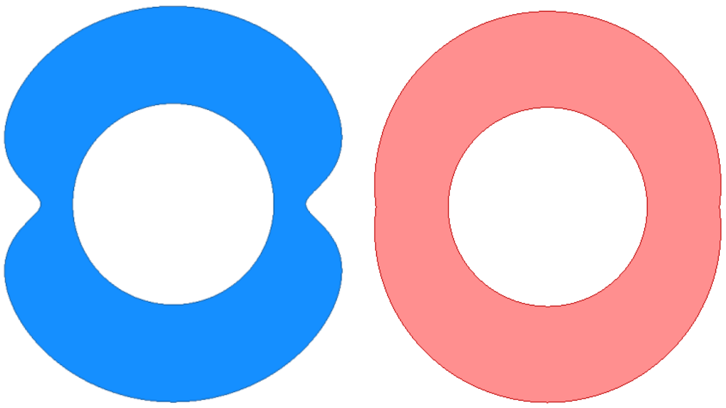

(a) Rotors with sinusoidal (left) and eccentric (right) designs

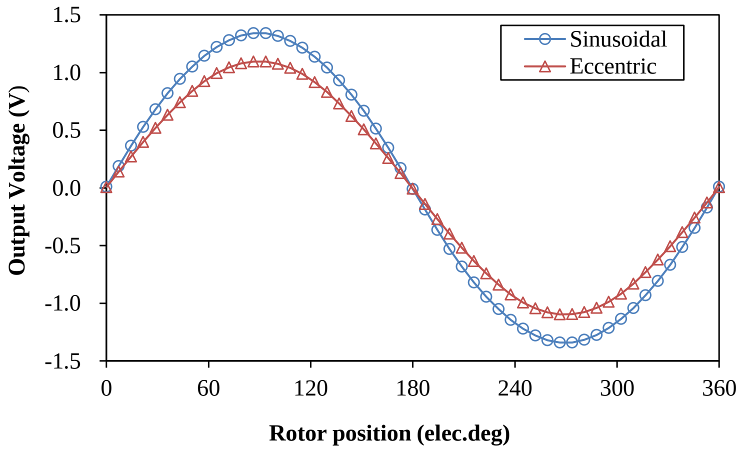

(b) Output voltages

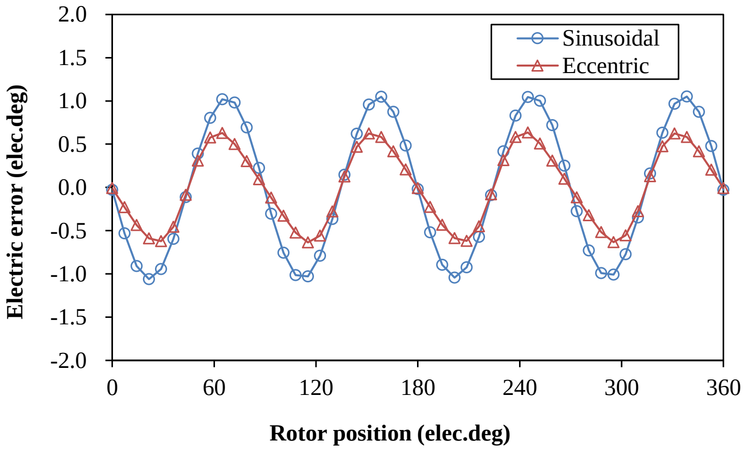

(c) Electric errors

Fig. 7.8 Comparison of designs with sinusoidal (*K*=1.9) and eccentric (*A*=4.5mm) designs.

7.4 Novel Design by Injecting Auxiliary Air-gap Permeance Harmonics (AAPH)

In order to improve the detection accuracy, the priority is to investigate the origin of the voltage harmonics. In this section, analytical derivation of the voltages in different coils of the aforementioned VR resolver will be made with different orders of air-gap permeance considered. In addition, the FE method is employed to verify the analyses.

7.4.1 Origins of Third-Order Harmonics in NTWVRR

With the air-gap length function shown in (7.1), sinusoidal air-gap permeance is expected to be established to reduce voltage harmonics. However, the magnetic flux flowing through the air-gap is not along straight lines towards the rotor centre, especially in regions with large air-gap lengths. Therefore, a series of air-gap permeance harmonics are inevitably introduced, which can be expressed by:

$$P_k = P_0 + \sum_{\gamma=1}^{\infty} P_{m\gamma} \cos\left[\gamma p \theta - (k-1)\frac{2\pi\gamma p}{Z})\right] \tag{7. 3}$$

where P_k is the air-gap permeance under the *k*-th tooth, P_0 and $P_{m\gamma}$ represent the constant and the variable components respectively, γ is the harmonic order and Z is the number of stator slots. Due to the minor values of permeance harmonics, the synthetic air-gap permeance under the exciting teeth almost remains constant, as well as that under the output teeth. Take the sine phase for example, the transformer electromotive force (EMF) in the coil of the *k*-th tooth can be described by:

$$E_{sk} = -\frac{\mathrm{d}\psi_{sk}}{\mathrm{dt}} = -\frac{2}{3}\pi f N_{e0} N_{s0} I_m P_k \sin(2\pi f \mathrm{t}) \tag{7. 4}$$

where ψ_{sk} is the flux-linkage in the coil of the *k*-th tooth, I_{m} and f represent the exciting current amplitude and frequency, N_{e0} and N_{s0} are the numbers of turns for exciting and sine phase coils, respectively. Based on the winding distributions shown in Fig. 7.1, the sine phase output voltage of the 24-slot VR resolver can be obtained by:

$$\begin{aligned} E_s &= 2(E_{s3} + E_{s5}) - 2(E_{s9} + E_{s11}) \\ &= -\frac{4}{3}\pi f N_{e0} N_{s0} I_m \sin(2\pi f t)(\sum_{k=3,5} P_k - \sum_{k=9,11} P_k) \end{aligned} \tag{7. 5}$$

In order to clearly describe the influence by different orders of permeance harmonics, transformer EMF vectors of the 4 sine-phase coils (3#, 5#, 9#, and 11#) are demonstrated, as shown in Fig. 7.9. Due to the decreasing magnitudes, only the permeance harmonics within the first 5 orders are considered. The symbol of α represents the relative electric angle between exciting teeth (4# and 10#) and β is the angle between exciting teeth and adjacent output teeth, both of which are corresponding to the orders of permeance harmonics. As can be seen, the second, the third, and the fourth orders of permeance harmonics will not contribute to the synthetic output voltage, due to the compensation effect by positive (3#, 5#) and negative (9#, 11#) coils. In contrast, the fifth order of voltage harmonic cannot be eliminated, in addition to the fundamental component, as shown in Fig. 7.9 (a) and Fig. 7.9 (c) respectively.

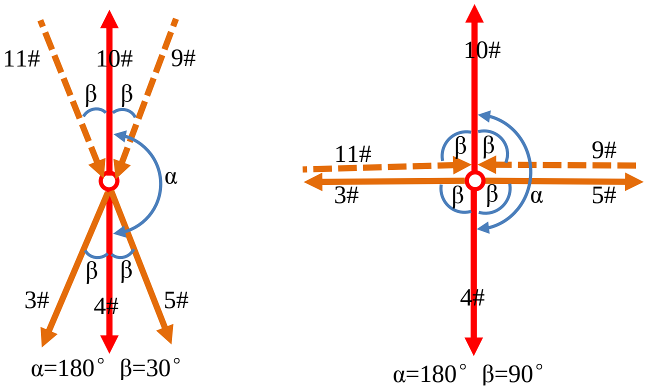

(a) Fundamental (b) Third-order (c) Fifth-order

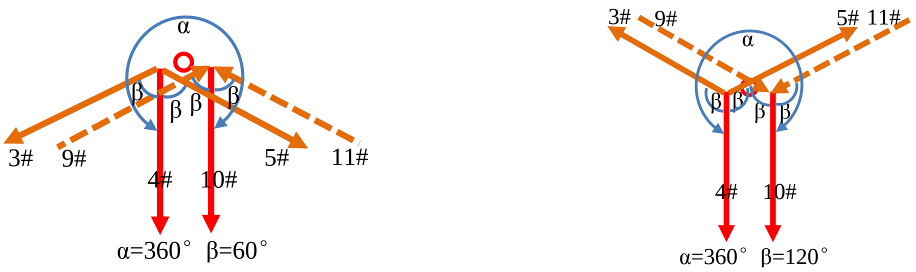

(d) Second-order (e) Fourth-order

Fig. 7.9 Transformer EMF vectors of sine phase coils induced by different orders of air-gap permeance harmonics.

However, it should also be noted that the exciting teeth distribution of the resolver with non-overlapping tooth-coil windings is in consequent-pole styles, which is different from that of a conventional VR resolver. Therefore, it is still necessary to further investigate the corresponding influence. Actually, a significant feature of a consequent-pole design has proven to be the different pole arc widths of 'active pole' and 'iron pole' [WU14], [CHU15], which can also be reflected on the pole arc width of the aforementioned VR resolver (each ‘active pole’ corresponding to two ‘iron poles’), as shown in Fig. 7.10. It can be seen that the angle of β is slightly increased by Δβ, with this feature considered.

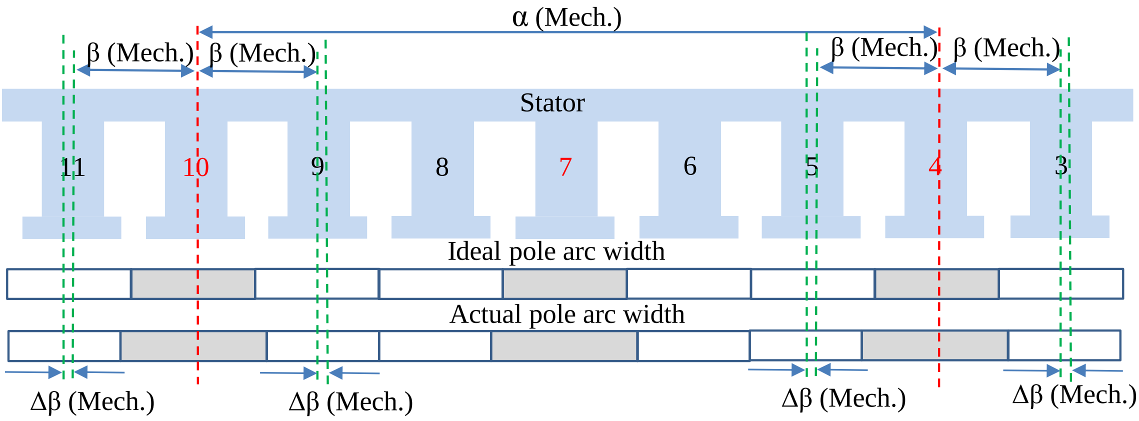

Fig. 7.10 Influence of the consequent exciting teeth on pole arc width and air-gap permeance axes.

By re-examination of the EMF vectors shown in Fig. 7.9, it can be further deduced that the third order of harmonic is introduced to the synthetic voltage, which can no longer be neutralized by the positive and negative coils. In contrast, the second and the fourth orders of voltage harmonics still will not exist due to the unchanged relative angles between positive and negative components. As a verification, the FE method is employed, with the voltages of different coils (coil groups) shown in Fig. 7.11. It can be seen that a series of harmonics exist in the output voltage of a single coil, whilst even orders of harmonics can be eliminated in the synthetic voltage of coil groups (3# and 9#, 5# and 11#). In addition to the fifth order of harmonic, the third order component with the magnitude of 18.2mV is introduced in the synthetic output voltage of sine phase, resulting in the aforementioned position detection errors.

From the foregoing analyses, the origins of the third order voltage harmonic for the 24-slot 2-X VR resolver have been verified, mainly due to two aspects. Firstly, a series of air-gap permeance harmonics (including the third order) are introduced by the sinusoidal rotor since the actual magnetic flux though the air-gap is not along straight lines. Secondly, the phase angle between exciting teeth and adjacent output teeth is slightly varied by consequent distributions of exciting teeth, and the third order of voltage harmonic in positive coils fails to compensate that in negative coils.

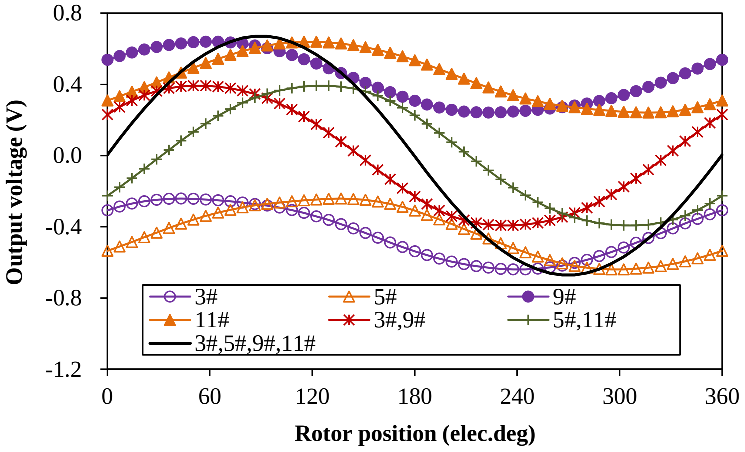

(a) Voltage waveforms

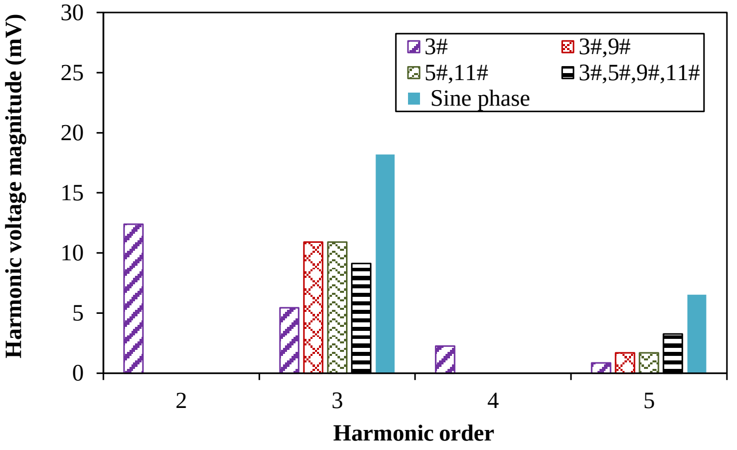

(b) voltage harmonics (constant and fundamental components not shown)

Fig. 7.11 Output waveforms and harmonic distributions in different coils of sine phase (K=1.9).

7.4.2 Improvement by AAPH Rotor

The origins of voltage harmonics in the objective VR resolver have been investigated, and in this section a novel design of rotor contour by auxiliary air-gap permeance harmonics is introduced in order to eliminate the voltage harmonics and improve the position detection accuracy.

According to the foregoing analyses, the third order of voltage harmonic proves to be the primary cause of electric angle error. Due to the consequent distribution of exciting teeth, the third order of voltage harmonic can be induced by the same order of air-gap permeance. Therefore, a potential solution by injecting auxiliary air-gap permeance is proposed, with the air-gap length function described by:

$$\delta = \frac{K\delta_{min}}{1 + (K - 1)\cos(p\theta) - k\cos(3p\theta)} \tag{7. 6}$$

where k is defined as the third-harmonic factor. According to (7.5), a comparison of the rotor contours by different values of the factor k is carried out, with the corresponding rotor radii shown in Fig. 7.12. As can be seen, the minimum rotor radius significantly increases from 26.32 mm to 33.16 mm when k slightly increases from 0 to 0.10, although the maximum rotor radius almost remains stable.

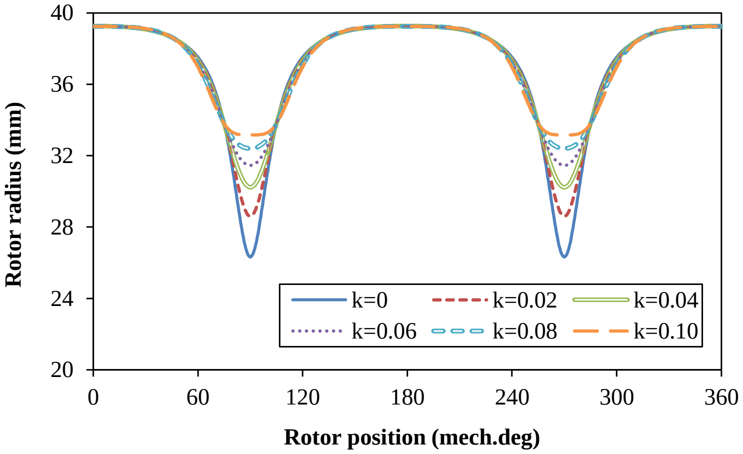

Fig. 7.12 Rotor radii by different third-harmonic factors (K=1.9)

Based on the identical stator and windings shown in Fig. 7.1, FE models are established with different rotor contours of the proposed design employed. Similarly, a comparison of the output voltages and corresponding electric angle errors is carried out, as shown in Fig. 7.13. It can be seen that the fundamental output voltage almost remains stable at 1.37 V when the third-harmonic factor k increases from 0 to 0.11. However, remarkable variations are introduced in the third order of voltage harmonic. At first, it decreases from 18.2mV to 0.3 mV as the factor k increases from 0 to 0.09. Afterwards the harmonic begins to rise again. Therefore, a minimum harmonic of the third order can be achieved when k in the air-gap length function equals to 0.09, which also guarantees the lowest electric angle error, as shown in Figs. 7.13 (b) and (c). As a result, the proposed design by auxiliary permeance is effective to improve the voltage harmonics as well as the detection accuracy of the objective VR resolver.

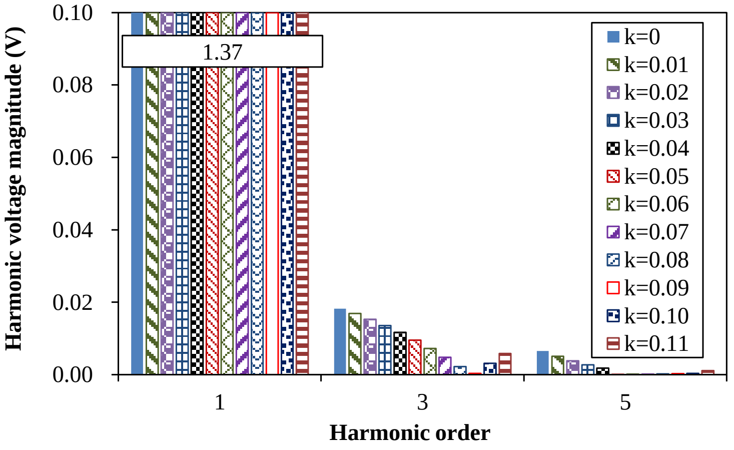

(a) Voltage harmonics

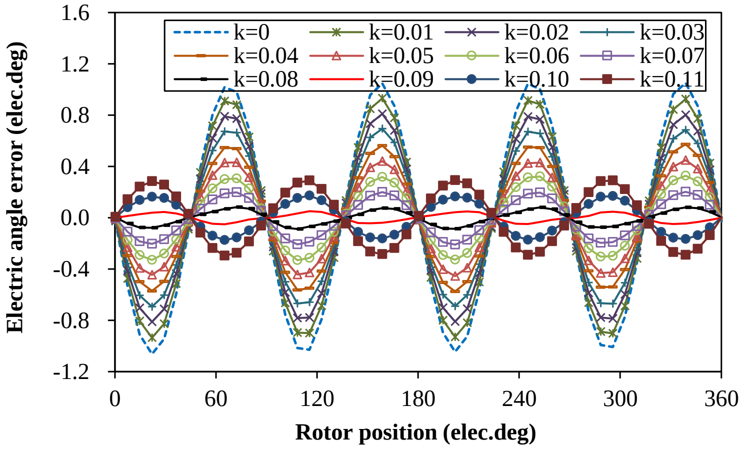

(b) Electric error waveforms

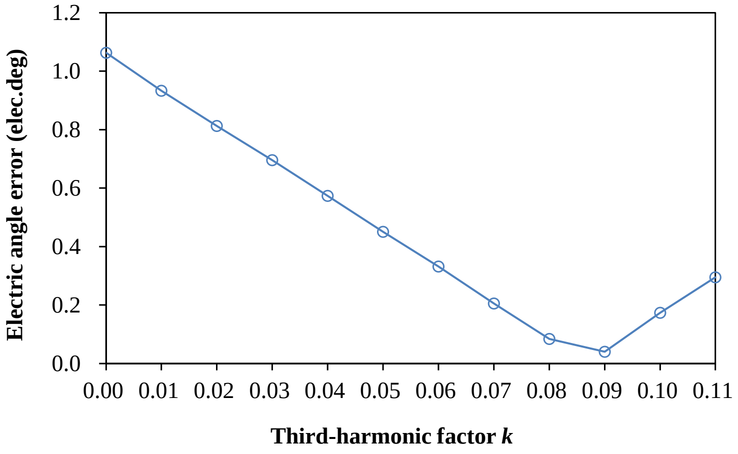

(c) Electric error magnitudes

Fig. 7.13 Influence of auxiliary third-harmonic permeance.

As shown in Fig. 7.14, the two rotor designs with and without auxiliary air-gap permeance are illustrated, together with an overall evaluation of key parameters listed in Table 7.1. It can be seen that the two designs have almost the same input/output inductances, which is mainly due to the identical constant component of air-gap permeance. In addition, the transformation ratios also guarantee that similar magnitude of voltages can be obtained by the two designs. However, the electric angle error is significantly improved, decreasing from ±1.05 °to ±0.04° with the auxiliary air-gap permeance employed. Moreover, despite the very similar minimum air-gap lengths, the maximum air-gap length decreases from 13.68 mm to 7.20 mm, which allows more flexible design of the rotor shaft.

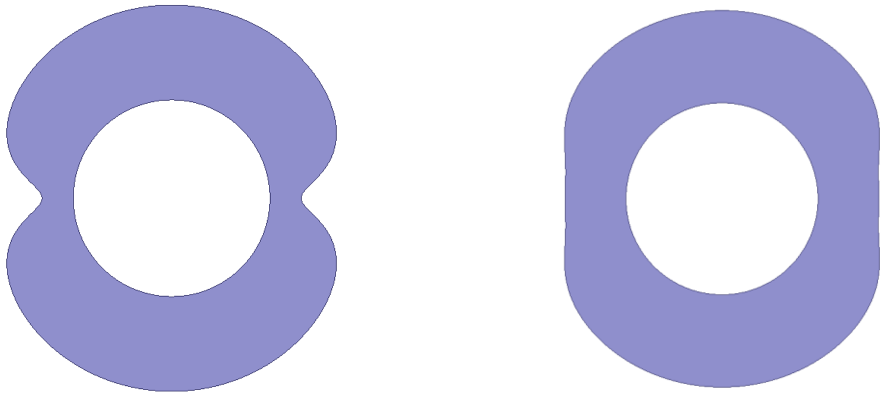
(a) K=1.9, k=0 (b) K=1.9, k=0.09

Fig. 7.14 Comparison of rotor contours with and without injecting the 3rd air-gap permeance.

TABLE 7.1

MAIN PARAMETERS IN DESIGNS WITH AND WITHOUT AUXILIARY AIR-GAP PERMEANCE (K=1.9)

Items	k=0	k=0.09
Minimum air-gap length (mm)	0.72	0.76
Maximum air-gap length (mm)	13.68	7.20
Input inductance (uH)	1.55	1.55
Output inductance (uH)	5.07	5.08
Transformation ratio	0.289	0.296
Electric angle error (elec. Deg.)	±1.05 °	±0.04 °

In summary, not only is the magnitude of output voltages effectively enhanced but also the detection accuracy of the VR resolver is significantly improved. Consequently, the aforementioned conflict in the VR resolver topology can be well solved by the proposed design method.

7.4.3 Further Application in a Conventional VR Resolver Topology

Not restricted to the foregoing VR resolver topology, the proposed design with auxiliary permeance can be further employed in conventional VR resolvers. As described in chapter 2, another topology of VR resolvers has been proposed [GE15b], of which the number of stator slots are four times of the rotor saliencies. Several advantages can be achieved by this kind of resolvers. For example, the sine and cosine output coils with identical number of turns are located on alternate stator teeth, and the amplitude error (or quadrature error) caused by round-off of coil turns for sinusoidally distributed windings can be avoided. However, the detection accuracy is still influenced by voltage tooth harmonics because of the special stator slots and rotor saliencies combination, especially the third order of harmonics. Based on the same main parameters shown in Table 1, a 20-slot 5-X resolver model of this resolver topology is established, as shown in Fig. 7.15.

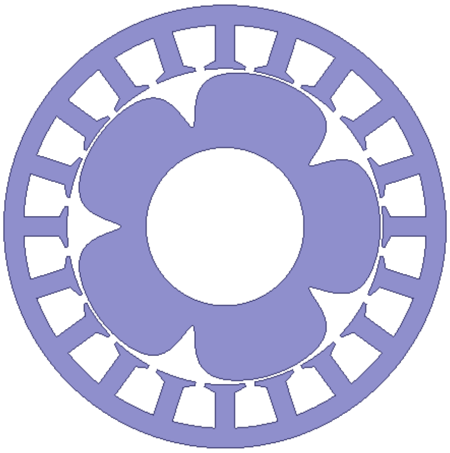

(a) Stator and rotor

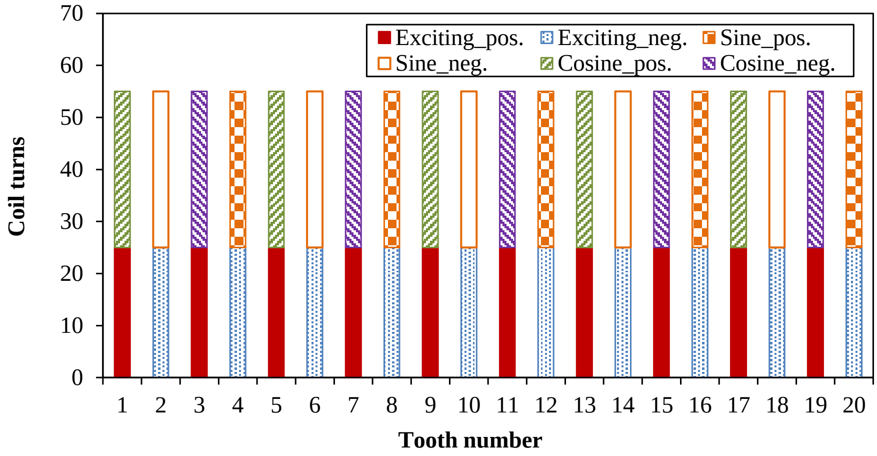

(b) Winding distributions

Fig. 7.15 A 5-X VR resolver with 20 stator slots.

Similarly, a comparison of the output voltage harmonics is carried out between the 5-X resolver designs with and without auxiliary third order of air-gap permeance by FE method, as well as the corresponding electric angle errors, as shown in Fig. 7.16. It can be seen that the third order of voltage harmonic is reduced from 17.3 mV to very low extent with an optimal auxiliary air-gap permeance employed (*k*=-0.032), although the fundamental voltage almost remains stable at 1.22 V. Also, the improvement can be reflected on the position detection accuracy, with the electric angle error decreasing from ±0.8 °to less than ±0.02 °. Therefore, the problem of voltage tooth harmonics with this resolver topology (*Z*=4*p*) can be also solved though the proposed design.

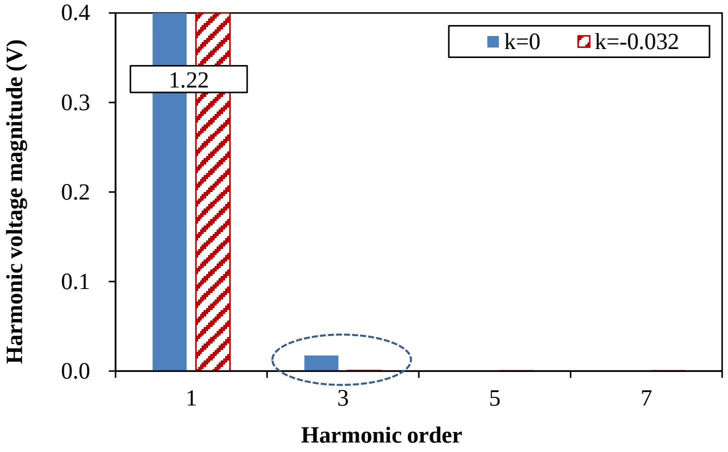

(a) Voltage harmonics

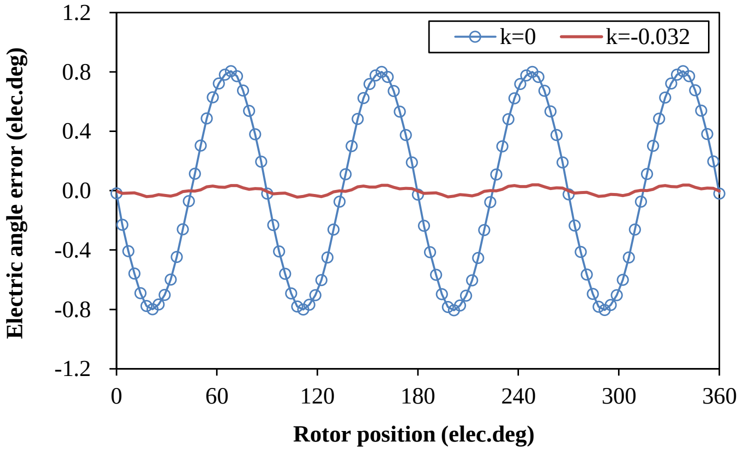

(b) Electric angle errors

Fig. 7.16 Influence of auxiliary third-harmonic permeance on the 5-X resolver (*K*=1.9).

7.5 Prototype and Test

Based on the parameters shown in Table 7.1 and Fig. 7.1 (b), prototypes are fabricated to verify the foregoing analyses, including one stator and two different rotors (with and without auxiliary permeance), as shown in Fig. 7.17. Firstly, the main parameters of the prototypes are measured, i.e. the input/output inductances and the transformation ratio, as shown in Table 7.2. It can be seen that very similar inductances can be obtained by the two resolver prototypes, due to the identical component of constant air-gap permeance. Moreover, the transformation ratio also remains stable when different rotors are employed, which is mainly due to the unchanged fundamental component of air-gap permeance, which also verifies the foregoing analyses. In addition, the parameters obtained by 3-dimensional (3D) FE method are also illustrated for comparison. As can be seen, the measured values agree well with the results by 3D FE method. However, the inductances almost increase by 35% when compared with the results shown in Table 7.1, due to the end leakage of this pancake design. Therefore, the 3D FE method is usually necessary for accurate prediction of the inductances. In addition, the measured transformation ratios indicate that similar output voltages can be obtained by the two rotor designs.

(a) Stator

(b) Conventional rotor K=1.9

(c) Proposed rotor K=1.9, k=0.09

Fig. 7.17 VR resolver prototypes.

In order to evaluate the position detection accuracy, a platform based on dSPACE 1005 is established, as shown in Fig. 7.18. The resolver prototype is integrated to a PM motor, in which a 5000-revolution encoder is co-axially installed. When the motor is driven to rotate, position signals (A, B and Z) from the encoder and the resolver (together with the decoding unit) are both input to the dSPACE I/O board for comparison. Due to the high detection accuracy of encoder, the difference can represent the electric angle error of the prototype.

TABLE 7.2

COMPARISON OF MAIN PARAMETERS BETWEEN PROTOTYPES WITH AND WITHOUT AUXILIARY AIR-GAP PERMEANCE HARMONICS

Items	K=1.9, k=0		K=1.9, k=0.09	
	Measured	3D FE	Measured	3D FE
Input inductance (uH)	2.13	2.15	2.14	2.15
Output inductance (uH)	6.34	6.83	6.42	6.86
Transformation ratio	0.17	0.21	0.17	0.21

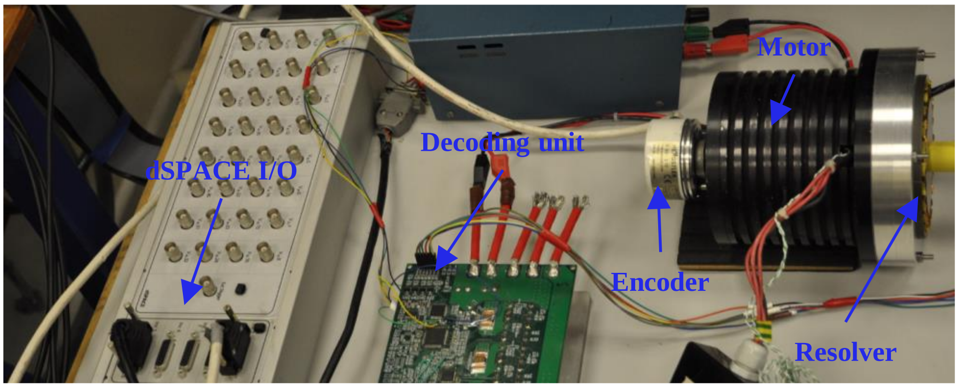

Fig. 7.18 Test platform.

When the motor is driven to rotate at a constant speed, the analogue output voltages of the prototype with the proposed rotor are firstly captured with a 10 kHz 5V exciting signal applied to the exciting winding, as shown in Fig. 7.19. It can be seen that two phases of orthogonal voltages can be obtained in the sine and cosine windings respectively without obvious DC components, which preliminarily indicates the normal operating characteristics of the proposed design and the proper fabrication of windings.

Then, the detection accuracy of the two prototypes are tested by the platform, with the electric errors shown in Fig. 7.20. As can be seen, due to the reduction of third-order voltage harmonics, the electric error decreases from ±2.0 ° to ±0.97 ° by the proposed design, which is sufficient for the requirements of many industrial applications. However, it should be also noted that asymmetric coil locations and installing eccentricity potentially exist during the prototype fabrication and test, whilst certain amount of DC components in the output voltages are inevitable and result in the residual first-order of electric angle errors, which can be further eliminated by improving winding fabrication and installing concentricity.

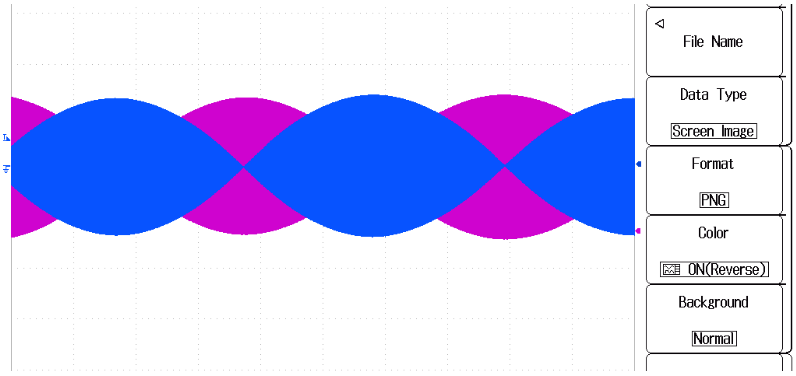

File Name

Data Type: Screen Image

Format: PNG

Color: ON(Reverse)

Background: Normal

Fig. 7.19 Output voltages of the prototype with proposed rotor.

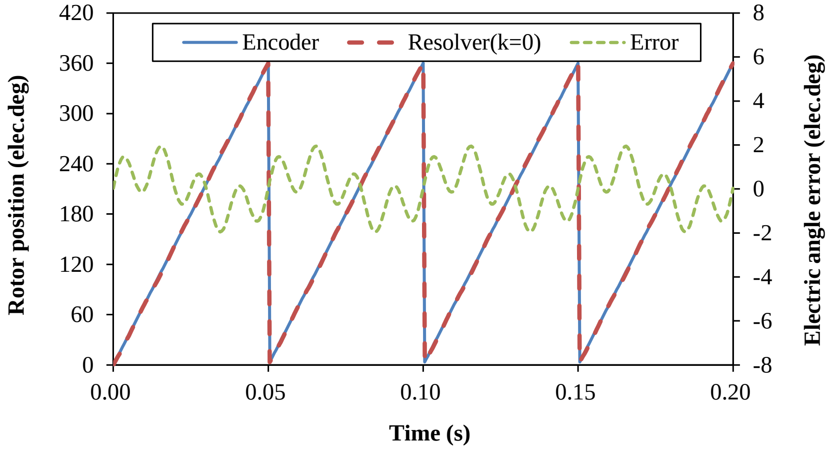

(a) Prototype with conventional rotor

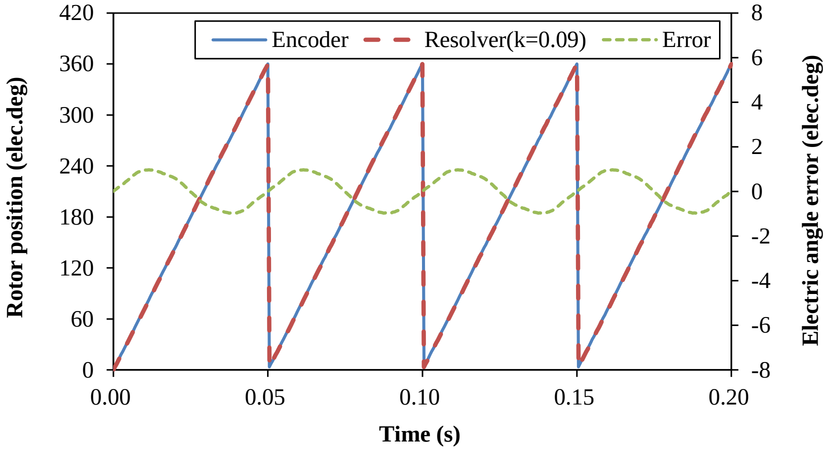

(b) Prototype with the proposed rotor

Fig. 7.20 Position detection accuracy of the prototypes (600 rpm).

7.6 Conclusion

Two fundamental designs of rotor contours have been analysed and compared in this chapter, i.e. the sinusoidal and eccentric designs. It is found that the output voltage harmonics significantly increase when larger maximum air-gap lengths are employed to enhance the output voltages, which deteriorate the position detection accuracy. Based on the foregoing NTWVRR model, the origins of voltage harmonics are investigated, which are mainly due to two aspects. Firstly, a series of air-gap permeance harmonics (including the third order) are introduced by the sinusoidal rotor since the actual magnetic flux through the air-gap is not along straight lines to the rotor center. Secondly, the phase angle between exciting teeth and adjacent output teeth is slightly varied due to the consequent distributions of exciting teeth, and the third order of voltage harmonic in positive coils fails to compensate that in negative coils.

In order to solve the problem, a novel design of rotor contour by injecting auxiliary air-gap permeance harmonics (AAPH rotor) is proposed for the NTWVRR model, through which the conflict between high output voltages and high detection accuracy can be well solved. In addition, the proposed AAPH rotor can also be employed in a conventional VR resolver topology (Z=4p), which is verified by a 5-X resolver.

Prototypes have been fabricated and tested, as a verification of the foregoing analyses.

CHAPTER 8 INVESTIGATION ON DETECTION ACCURACY OF VARIABLE RELUCTANCE RESOLVERS ACCOUNTING FOR MANUFACTURING TOLERANCES

8.1 Introduction

In the foregoing chapters, a novel VR resolver topology with non-overlapping tooth-coil windings (NTWVR) has been proposed to simplify the manufacturing process of conventional VR resolvers, with a novel design of rotor contour by injecting auxiliary air-gap permeance harmonics (AAPH) further proposed to reduce the voltage harmonics and improve the detection accuracy. Moreover, the proposed design of rotor contour can also be employed in a conventional VR resolver topology with alternate output windings (Z=4p) to reduce the tooth harmonics in output voltages.

However, the manufacturing and assembling tolerances in resolvers are usually inevitable, e.g. the asymmetric coil locations, the assembling eccentricities, etc. Therefore, it is necessary to investigate the corresponding influence on the detection accuracy. Moreover, in order to identify the sensitivities of different resolver designs, comparison of the influence should be carried out between the conventional and the proposed VR resolver topologies. Considering the similar stator slot number and the increasing demand of 5-X resolver products, the aforementioned 5-X resolver by 20 stator slots is investigated and compared with the 24-slot NTWVR resolver, with the sinusoidal and the AAPH rotors employed respectively.

8.2 Asymmetric Coil Locations

For VR resolvers, three sets of coils are wound on the stator teeth, i.e. the exciting coils, the SINE and the COSINE coils, whilst potential asymmetric coil locations may be introduced during the winding fabrication, as shown in Fig. 8.1. Four typical non-ideal coil locations in the slot are investigated, i.e. outer & bottom, outer & top, inner & bottom and inner & top, which are radially or horizontally different from the expected coil location.

In order to illustrate the corresponding influence, it is assumed that a non-ideal output coil of the SINE (or COSINE) phase is at one of the four asymmetric locations whilst all the other coils are at the expected locations in the slots. For comparison, the aforementioned conventional VR resolver and the NTWVR resolver topologies will be investigated with the sinusoidal and the AAPH rotors employed, respectively. Compared with the expected coil location (marked as the coordinate origin), the top and the bottom locations are staggered by -1mm and 1mm in radial direction respectively, while the outer coil location is horizontally staggered by -2mm (the staggered distances are exemplified according to the actual slot dimensions).

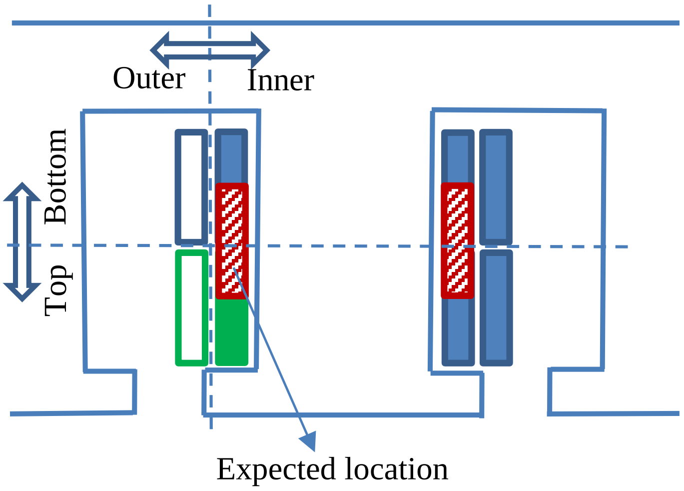

Fig. 8.1 Four typical coil locations in stator slot.

8.2.1 Conventional VR Resolvers with Sinusoidal and AAPH Rotors

Based on the aforementioned conventional VR resolver topology with alternate output windings, as shown in Fig. 8.2, the influence of asymmetric coil locations on the position detection accuracy is investigated in this section.

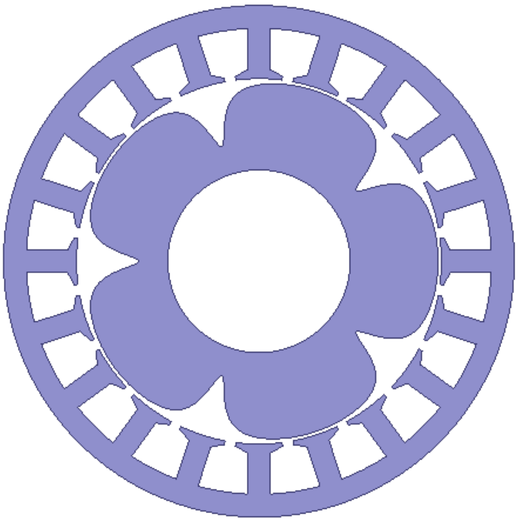

(a) Stator and rotor

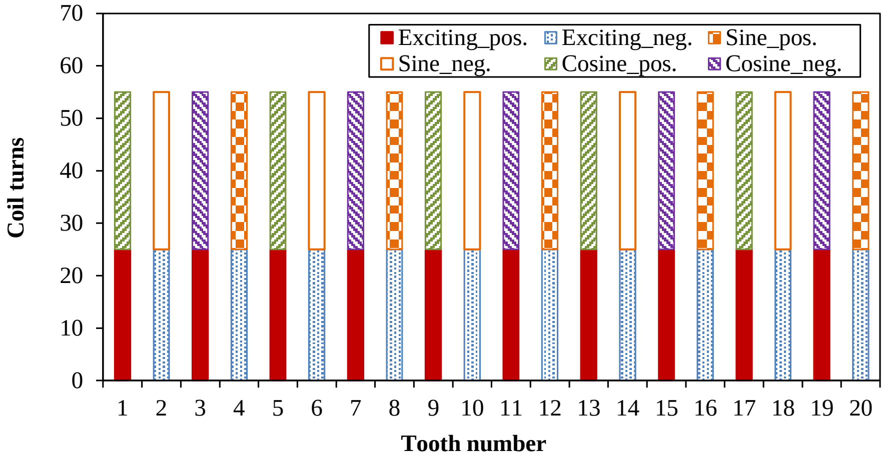

(b) Winding distributions

Fig. 8.2 A conventional 5-X VR resolver with 20 stator slots.

Firstly, the resolver model with a sinusoidal rotor (K=1.9, k=0) is analysed, with the voltage harmonics and corresponding electric angle errors shown in Fig. 8.3. As can be seen from Fig. 8.3 (a), different voltages (mainly the DC components) are induced in the test coil with the four different coil locations considered. Moreover, the DC voltage components corresponding to the outer coil locations and the top locations are lower, compared with the inner and the bottom locations respectively, which means that the minimum and maximum DC voltages are induced when the coil is at the outer & top and inner & bottom locations respectively. Therefore, the DC voltages in positive and negative coil groups cannot compensate each other, resulting in the residual DC components in the synthetic output voltages, as shown in Fig. 8.3 (b). It can be seen that when the coil is at outer & top location, the maximum residual DC component exists in the synthetic output voltage whilst the minimum residual DC voltage is corresponding to the outer & bottom coil location. The influence can also be reflected on the detection accuracies, with the corresponding electric angle errors shown in Fig. 8.3 (c). As can be seen, the electric error is potentially increased from ±0.8° to ±1.2° by the asymmetric coil locations. However, the electric error still presents the fourth order of variation, due to the significant third order of intrinsic voltage harmonics.

Moreover, the influence of asymmetric coil locations is also investigated on the VR resolver with an optimal AAPH rotor (K=1.9, k=-0.0032). Similarly to the above analyses, the voltage induced in the test coil is illustrated with the four asymmetric coil locations considered, as well as the voltage harmonics in the synthetic output voltage and the corresponding electric angle error, as shown in Fig. 8.4. By comparison between Fig. 8.3 (b) and Fig. 8.4 (b), it can be found that very similar fundamental and DC voltage components are induced in the output windings (including the test coil), with the maximum and the minimum output voltages corresponding to the outer & top and outer & bottom coil locations respectively. However, the third order of voltage components are significantly reduced with the AAPH rotor employed, which obviously reduces the corresponding electric angle errors, as shown in Fig. 8.4 (d). Different from that in the resolver with the sinusoidal rotor, it can be seen that the maximum electric error only increases to ±0.4° with the same asymmetric coil locations considered. Moreover, the fourth order of electric errors for the sinusoidal rotor are almost removed and replaced by the first order of variations, which are caused by the third order and the residual DC output voltage components respectively.

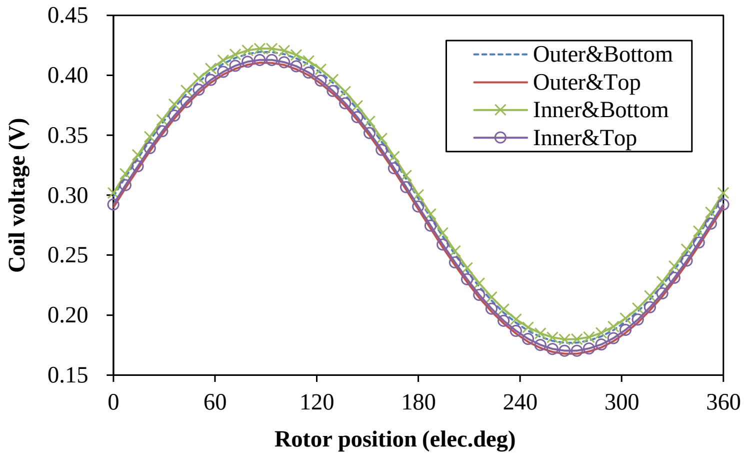

(a) Voltages in coils at the four different locations

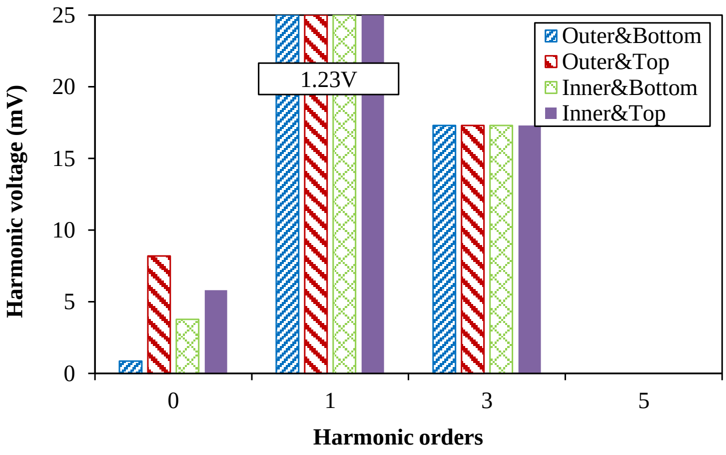

(b) Harmonics in the synthetic output voltage of phase with asymmetric coil

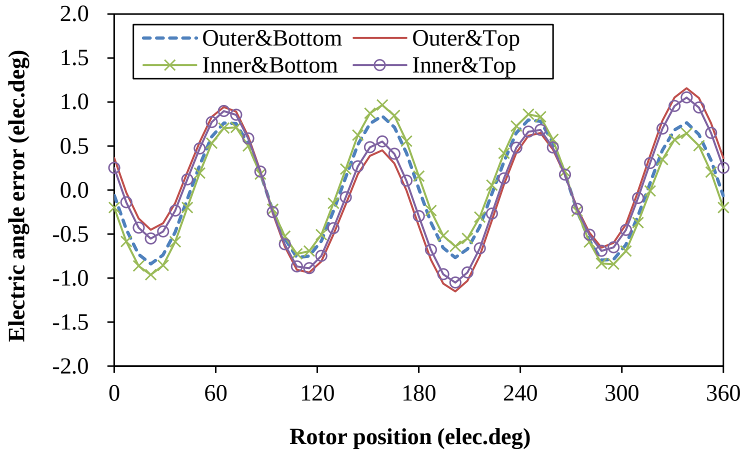

(c) Electric angle errors with the asymmetric coil considered

Fig. 8.3 Influence of asymmetric coil locations on output voltage and electric error (conventional VR resolver with sinusoidal rotor).

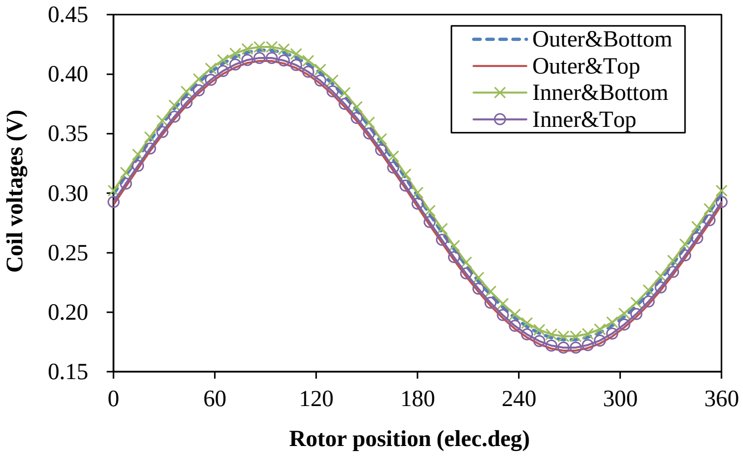

(a) Voltages in coils at the four different locations

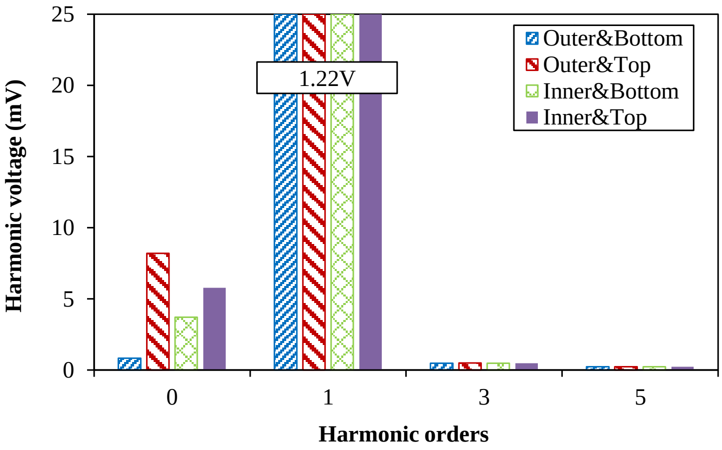

(b) Harmonics in the synthetic output voltage of phase with the asymmetric coil

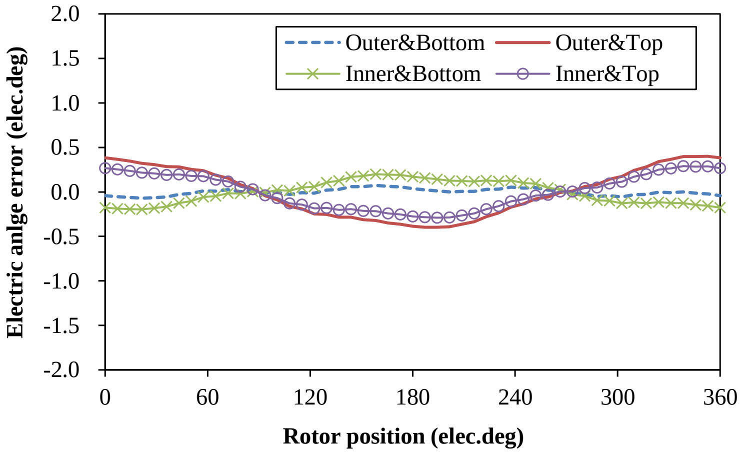

(c) Electric angle errors with the asymmetric coil considered

Fig. 8.4 Influence of asymmetric coil locations on output voltage and electric error (conventional VR resolver with AAPH rotor).

8.2.2 NTWVR Resolvers with Sinusoidal and AAPH Rotors

Similar to the foregoing analyses of convention VR resolvers, the influence of asymmetric coil locations is also investigated on the NTWVR resolvers, as shown in Fig. 8.5.

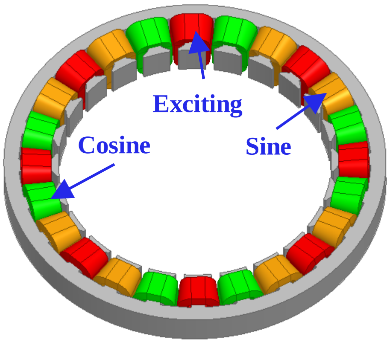

(a) Stator and windings

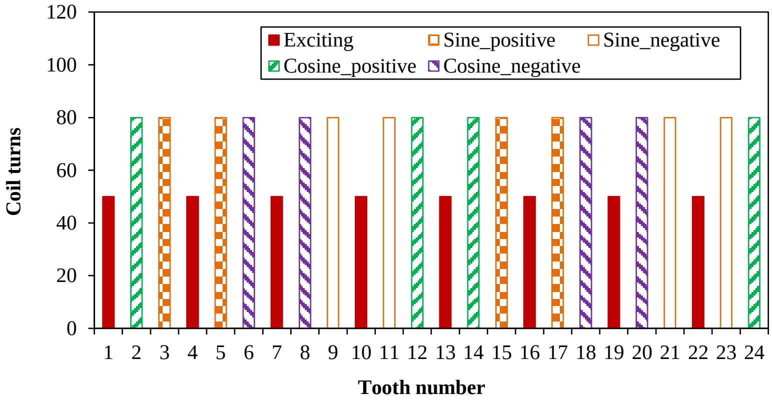

(b) Winding distributions

Fig. 8.5 Stator and windings of the 2-X NTWVR resolver [GE15a].

With asymmetric coil locations considered, the voltages in the test coil, the synthetic voltage harmonics and the corresponding electric angle errors of the NTWVR resolvers with sinusoidal and AAPH rotors are illustrated in Fig. 8.6 and Fig. 8.7 respectively. It can be seen that the maximum DC component is induced when the test coil is at the outer & bottom location while the minimum value exists at the inner & top location, which is different from that of conventional VR resolvers and will be analysed in the next part. For the resolver with sinusoidal rotor, the electric error is increased from ±0.8 °to ±1.5 °(when the test coil is at the outer & bottom location). Due to the significant third order of voltage component, the electric error remains the fourth variation. With the AAPH rotor employed, the third order of voltage harmonic is removed and the electric error is mainly caused by the residual DC component due to the asymmetric coil locations. Therefore, the fourth order of electric angle error is replaced by the first order, as shown in Fig. 8.7 (c). It can be seen that the electric error increases to less than ±0.6 °, with the asymmetric coil locations considered.

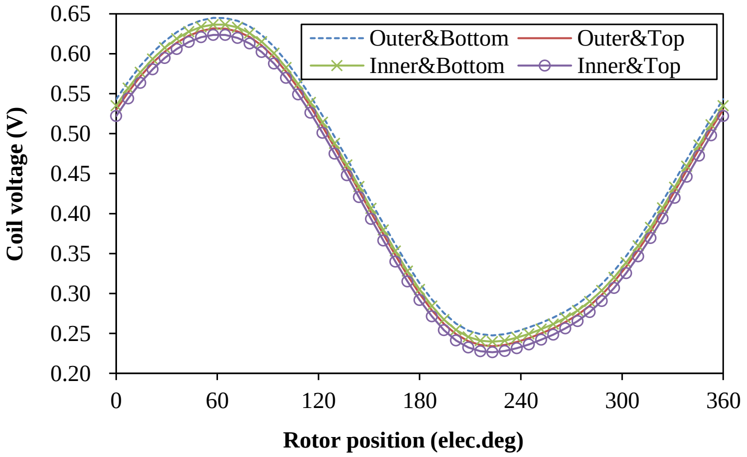

(a) Voltages in coils at the four different locations.

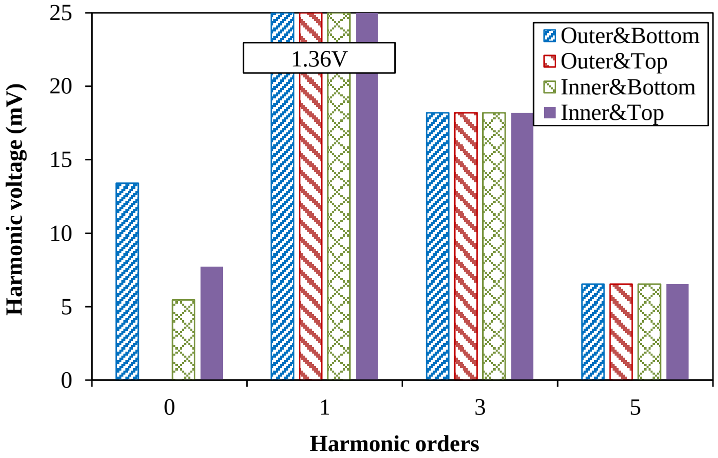

(b) Harmonics in the synthetic output voltage of phase with the asymmetric coil.

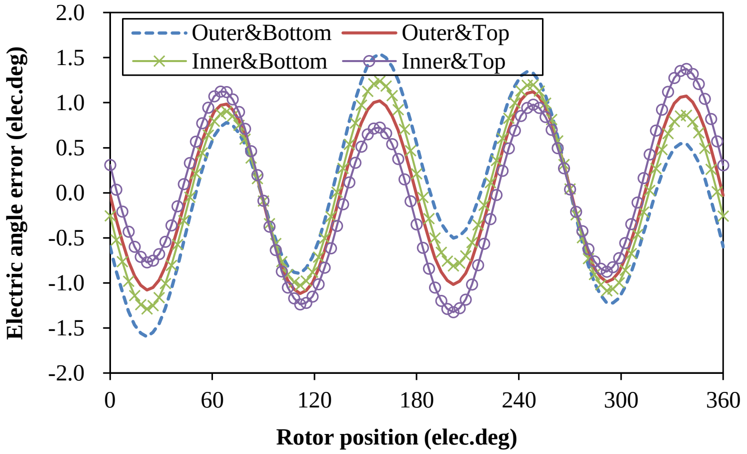

(c) Electric angle errors with the asymmetric coil considered.

Fig. 8.6 Influence of asymmetric coil locations on output voltage and electric error (NTWVR resolver with sinusoidal rotor).

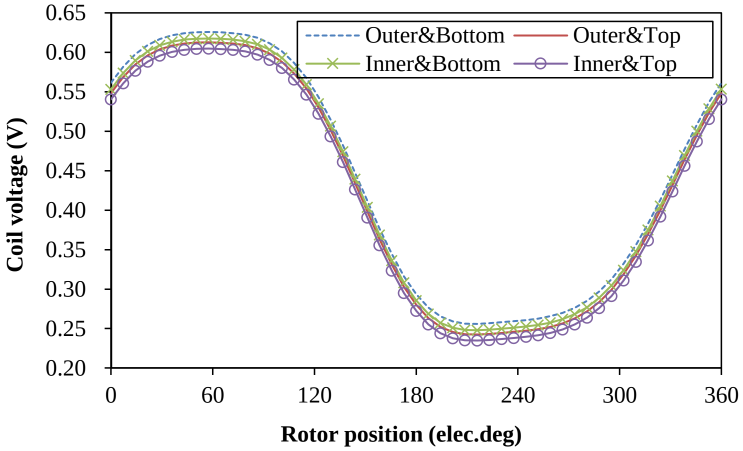

(a) Voltages in coils at the four different locations.

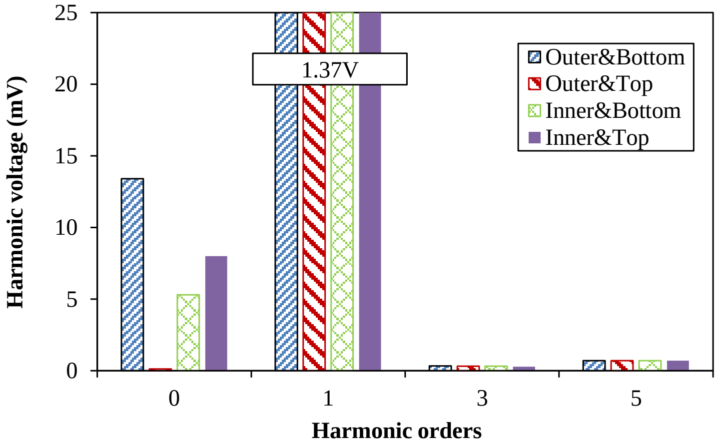

(b) Harmonics in the synthetic output voltage of phase with the asymmetric coil.

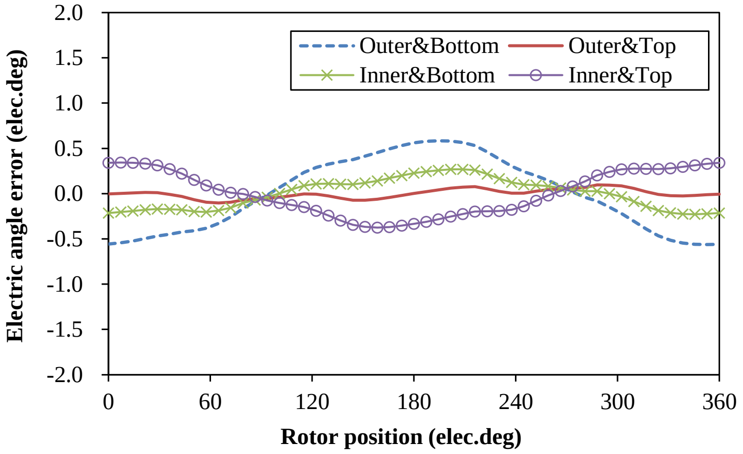

(c) Electric angle errors with the asymmetric coil considered.

Fig. 8.7 Influence of asymmetric coil locations on output voltage and electric error (NTWVR resolver with AAPH rotor).

8.2.3 Comparison of Coil Location Influences between Different Resolver Designs

The influence of asymmetric coil locations have been investigated for conventional and the NTWVR resolvers respectively. It is proven that residual DC voltage components are introduced in output voltages, which result in the first order of electric angle errors. However, different influences are introduced between the conventional and the NTWVR resolvers – higher DC voltages are induced in the coil at inner & bottom locations of conventional resolvers whilst the outer & bottom locations of NTWVR resolvers correspond to higher DC voltages.

In order to investigate the difference, the flux distributions of the two resolver topologies are illustrated in Figs. 8.8 (a) and (b) respectively. As can be seen, significant leakage flux exists in the slots, which presents different features between the two resolver topologies. For conventional VR resolvers, exciting coils with opposite polarities are wound on adjacent stator teeth and reverse leakage flux exists in the slot. It can be deduced that the coil at the inner & bottom location receives less amount of the reverse flux, which results in higher value of DC voltage component. In contrast, the exciting coils of NTWVR resolvers are in consequent distributions, and the leakage flux in the slot follows in identical direction of the main flux. Therefore, the coil at the outer & bottom location links more leakage flux and a higher DC voltage is obtained (DC voltage ratio refers to the ratio between DC and fundamental components produced in the coil), which can be seen from Fig. 8.8 (c). In addition, the detection accuracies with asymmetric coil locations considered are also compared, as shown in Fig. 8.8 (d). It can be seen that the electric errors can also be reduced to within ±0.6 ° with the AAPH rotor employed.

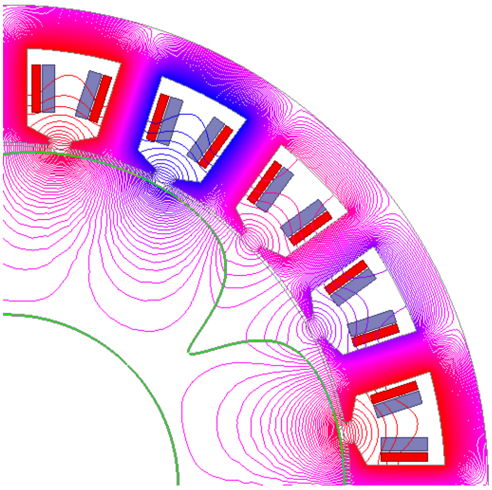

(a) Leakage flux in conventional resolvers

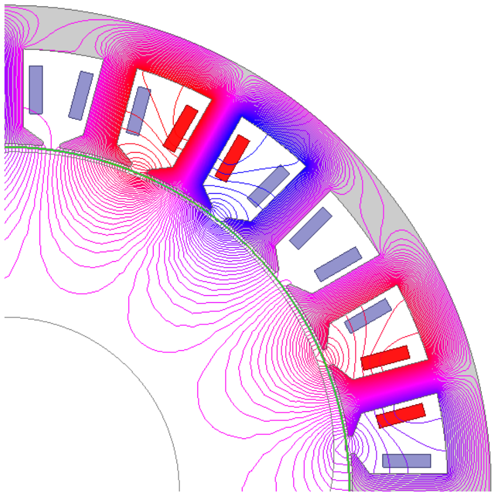

(b) Leakage flux in NTWVR resolvers

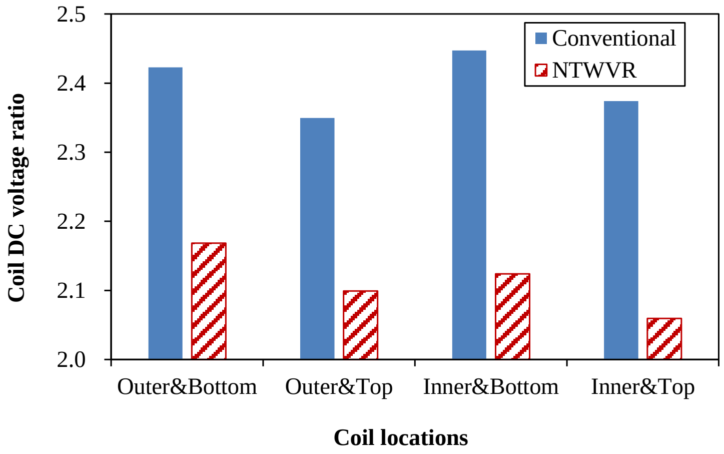

(c) DC voltage ratios at different coil locations

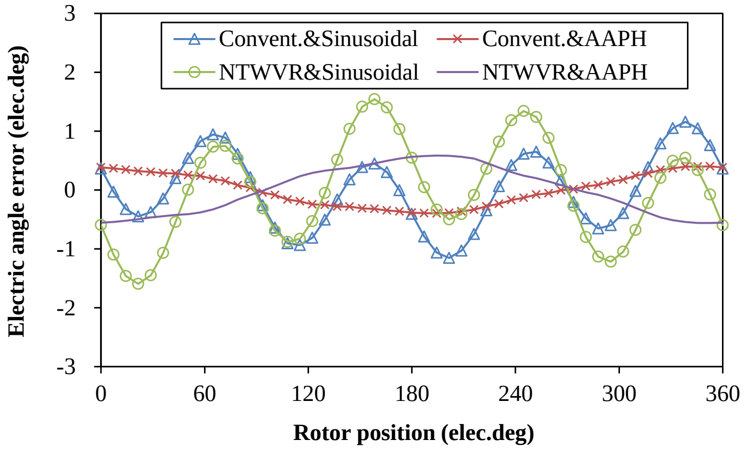

(d) Max. electric errors for different resolvers

Fig. 8.8 Origins of different DC voltages for different coil locations and electric errors in conventional and NTWVR resolvers.

Based on the analyses, the detection accuracy may deteriorate with asymmetric coil locations considered, due to the residual DC components in output voltages. Considering the consequent distribution of exciting teeth, the outer coil location in the slot results in higher DC voltage component for the NTWVR resolver, which is different from that of conventional VR resolvers. In addition, the detection accuracy can also be significantly improved by AAPH rotors even with the asymmetric coil locations considered.

8.3 Assembling Eccentricity

As it is well known, the assembling eccentricity is always inevitable for VR resolvers, including the static and the dynamic styles. Therefore, it is necessary to investigate the corresponding influences. Also, comparisons are carried out between the conventional and the NTWVR resolvers with sinusoidal and AAPH rotors, in order to identify the sensitivity.

8.3.1 Conventional VR Resolvers With Sinusoidal and AAPH Rotors

Similarly, the influence of assembling eccentricities on conventional VR resolvers is firstly investigated with sinusoidal and AAPH rotors employed. Fig. 8.9 illustrates the voltage harmonics and electric angle errors of conventional resolver using a sinusoidal rotor with different values of eccentricities considered. It can be seen that the electric errors almost remain stable at ±0.8 ° when the eccentricities increase to 0.10mm, for both the static and the dynamic styles, which is mainly due to the constant component of the third-order output voltages.

For comparison, the conventional VR resolver using an AAPH rotor is also investigated, with the voltage harmonics and the electric angle errors shown in Fig. 8.10. It can be found that the third-order voltage harmonics increase from 0.5mV to 1.5mV when the eccentricities increase to 0.10mm, which increases the electric angle errors from ±0.04 ° to ±0.10 ° with the fourth order of variation. However, it can be seen that the detection accuracy is also significantly improved by employing the AAPH rotor, even with the static and dynamic eccentricities considered.

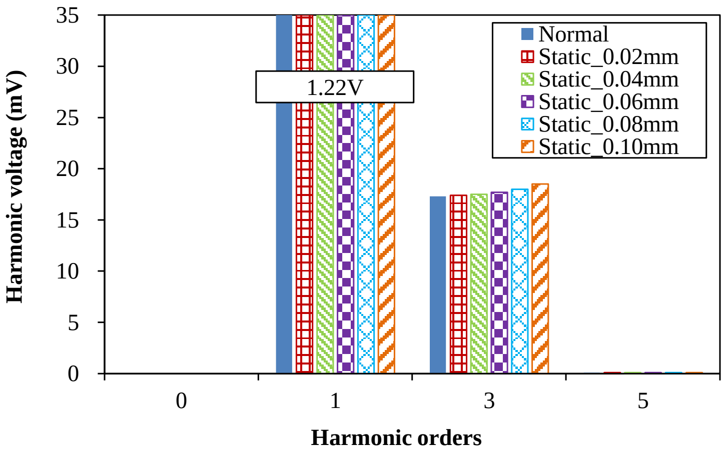

(a) Voltage harmonics by static eccentricity

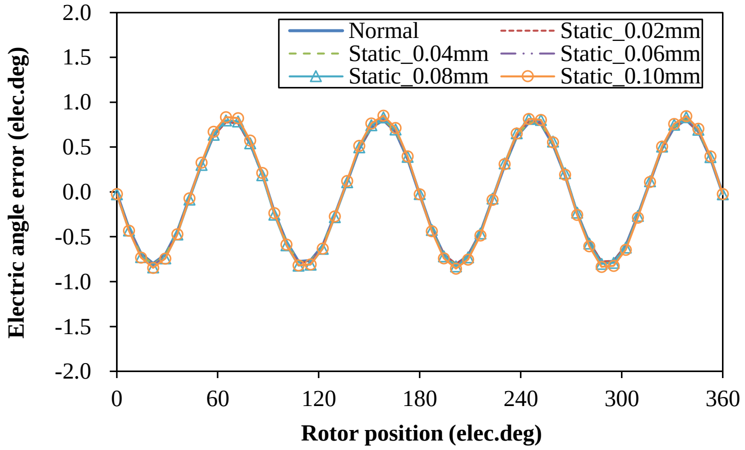

(b) Electric errors by static eccentricity

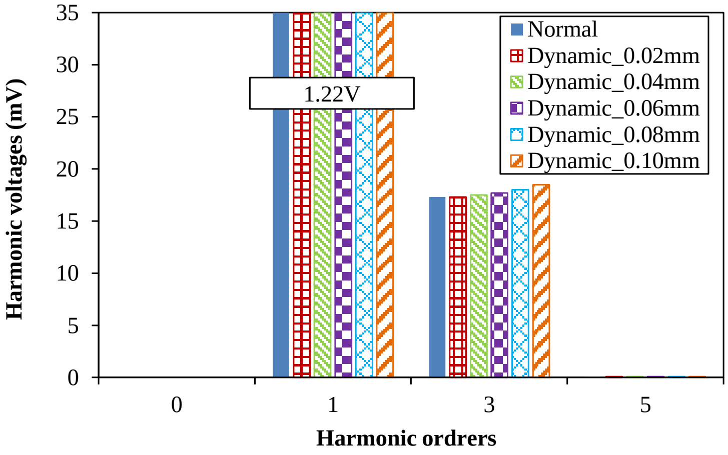

(c) Voltage harmonics by dynamic eccentricity

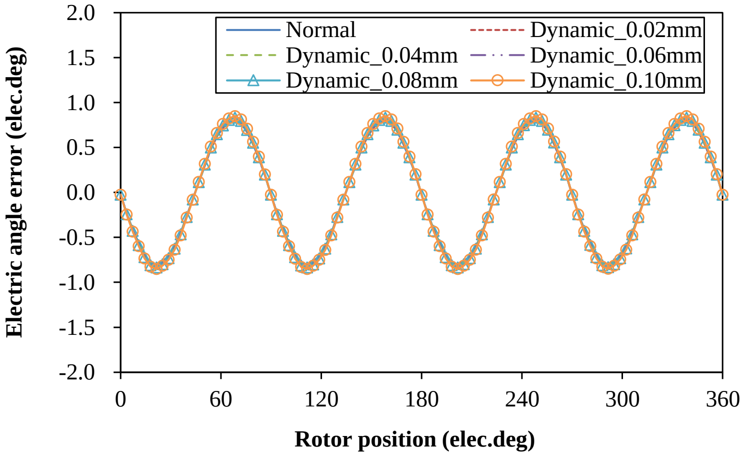

(d) Electric errors by dynamic eccentricity

Fig. 8.9 Voltage harmonics and electric angle errors caused by eccentricities (conventional resolver with sinusoidal rotor).

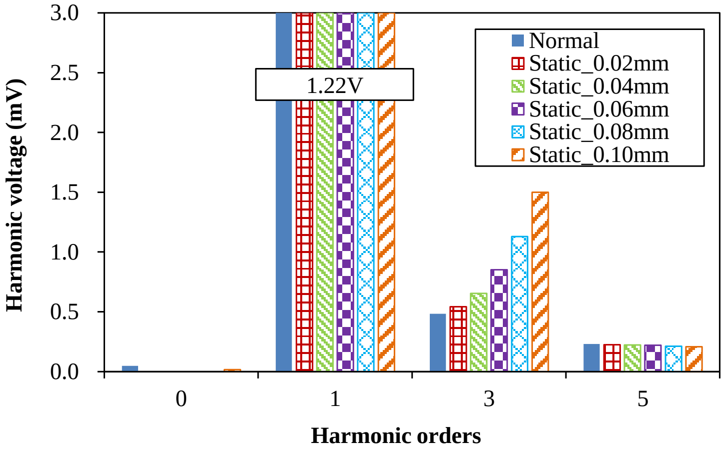

(a) Voltage harmonics by static eccentricity

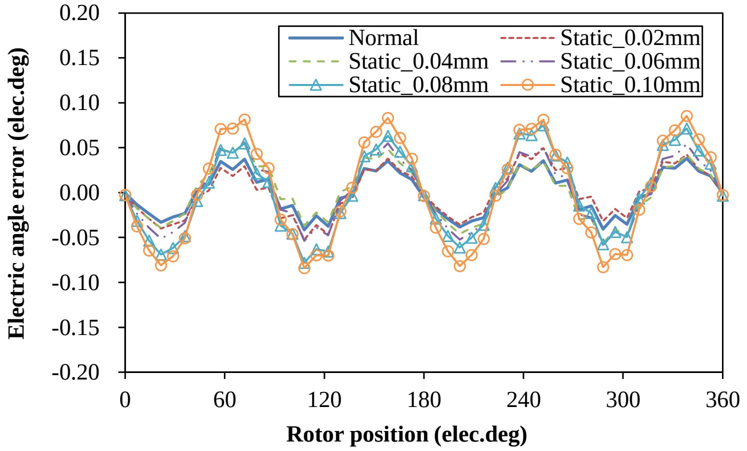

(b) Electric errors by static eccentricity

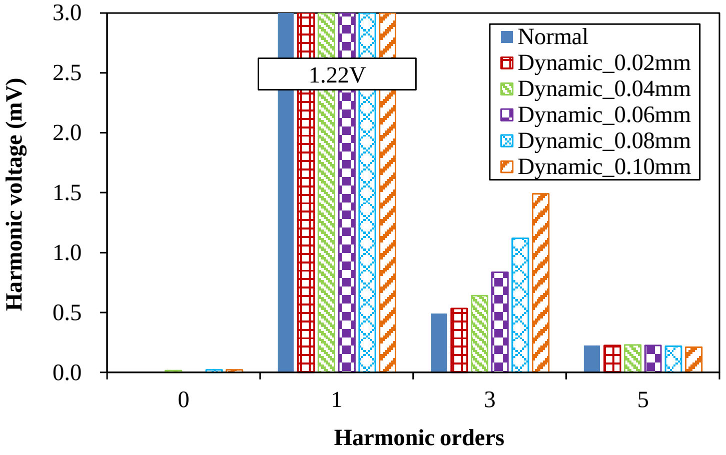

(c) Voltage harmonics by dynamic eccentricity

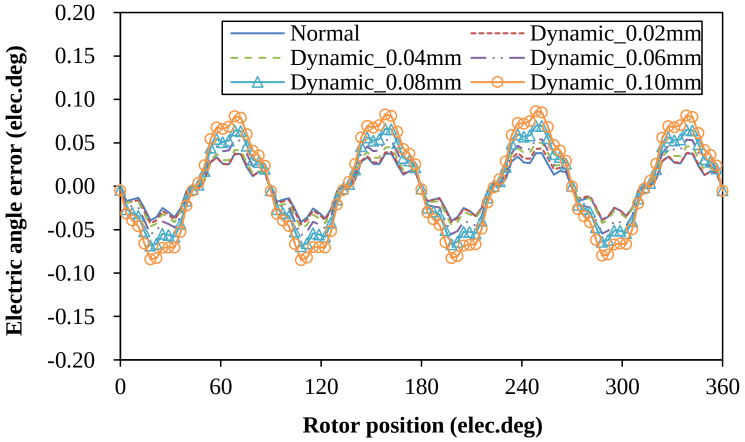

(d) Electric errors by dynamic eccentricity

Fig. 8.10 Voltage harmonics and electric angle errors caused by eccentricities (conventional resolver with AAPH rotor).

8.3.2 NTWVR Resolvers with Sinusoidal and AAPH Rotors

For the NTWVR resolver, the influences of assembling eccentricities are also analysed with sinusoidal and AAPH rotors employed, as shown in Fig. 8.11 (sinusoidal rotor) and Fig. 8.12 (AAPH rotor) respectively.

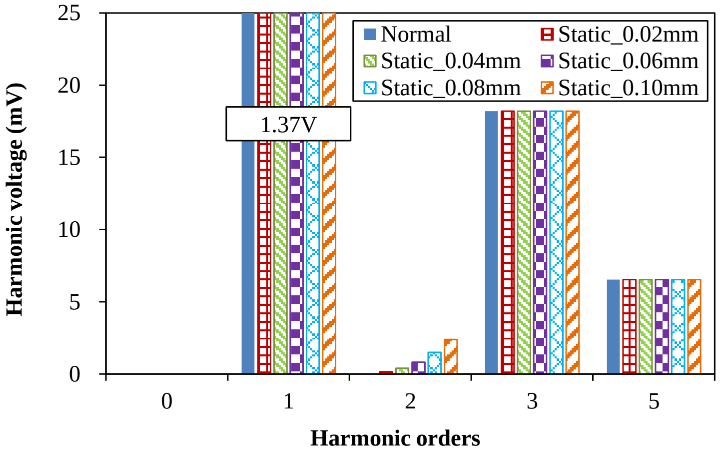

(a) Voltage harmonics by static eccentricity

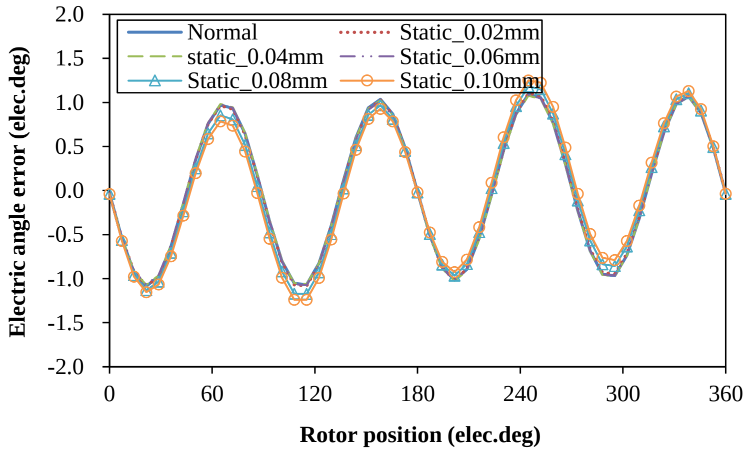

(b) Electric errors by static eccentricity

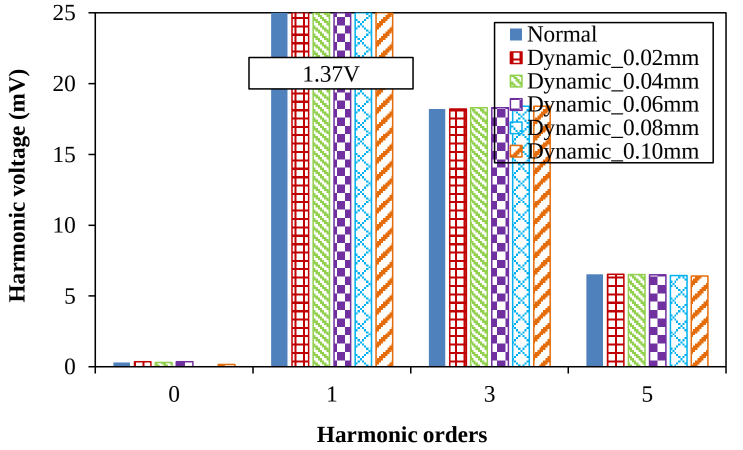

(c) Voltage harmonics by dynamic eccentricity

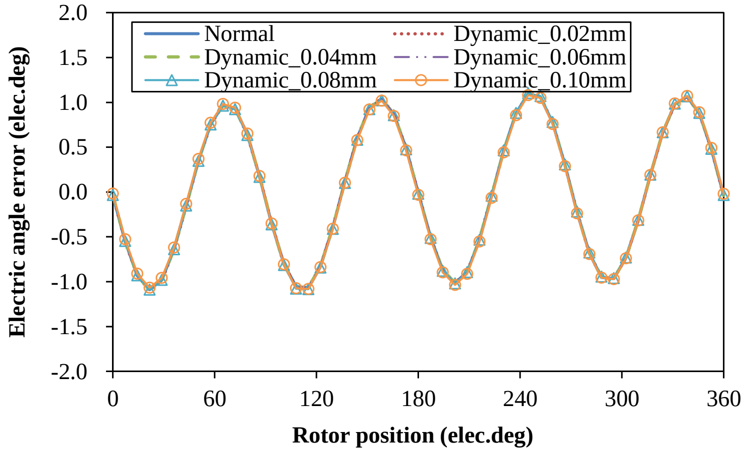

(d) Electric errors by dynamic eccentricity

Fig. 8.11 Voltage harmonics and electric angle errors caused by eccentricities (NTWVR resolver with sinusoidal rotor).

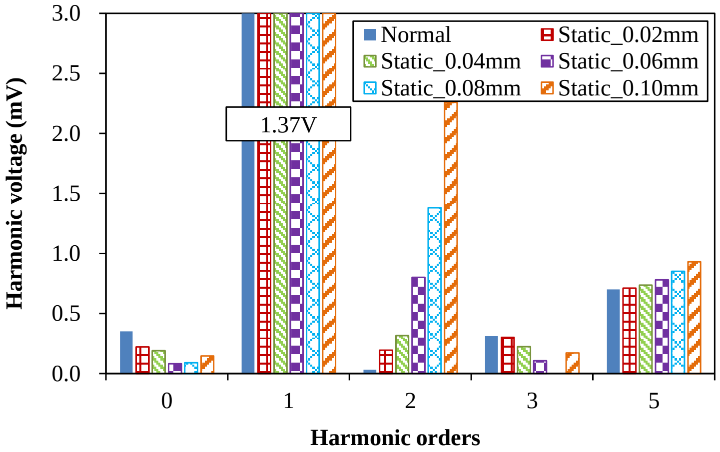

(a) Voltage harmonics by static eccentricity

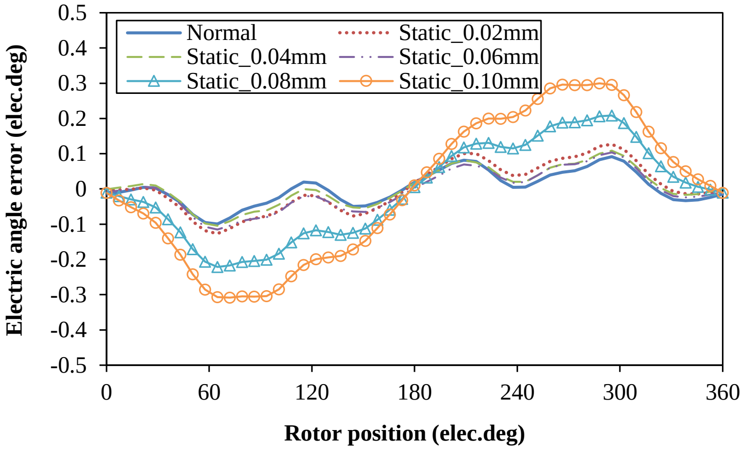

(b) Electric errors by static eccentricity

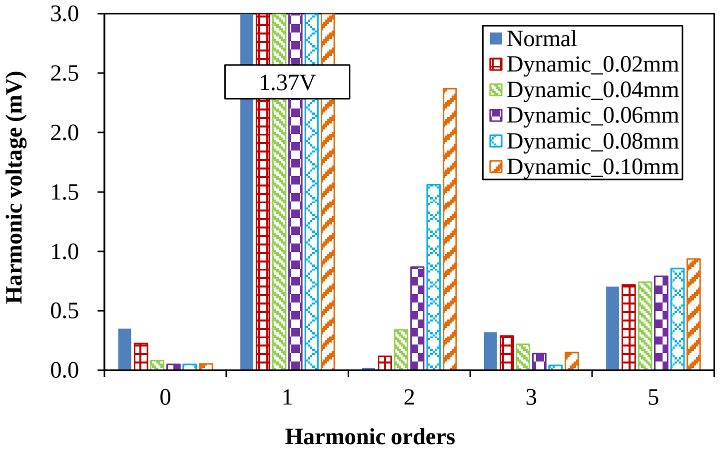

(c) Voltage harmonics by dynamic eccentricity

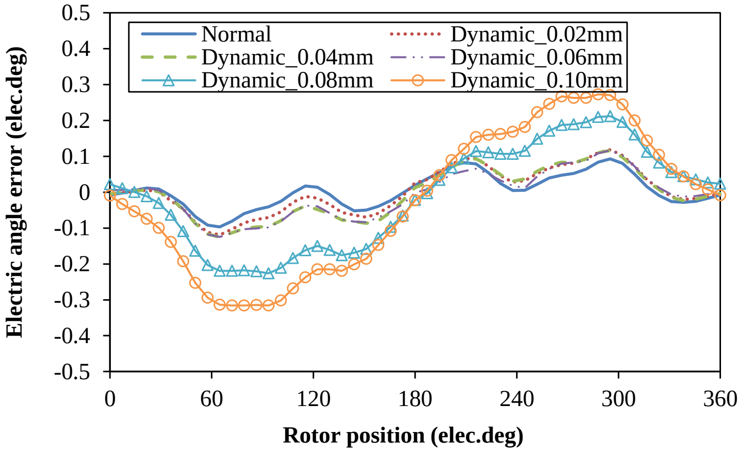

(d) Electric errors by dynamic eccentricity

Fig. 8.12 Voltage harmonics and electric errors caused by eccentricities (NTWVR resolver with AAPH rotor).

Similar to the conventional resolver, the electric errors of NTWVR resolver remain stable at ±1.0 ° with the sinusoidal rotor employed, which is mainly due to the almost constant component of the third-order voltage harmonics. With the AAPH rotor employed, the third-order voltage components are significantly reduced. However, the second-order voltage harmonic can no longer be eliminated with eccentricities considered, which increases to 2.3mV for a 0.10mm static eccentricity. As a consequence, the electric error rises to ±0.3 ° with the first-order of variations.

8.3.3 Comparison of Eccentricity Influence between Different Resolvers

Based on the analyses, the influence of assembling eccentricities on the detection accuracy is compared between the conventional and NTWVR resolvers, exemplified by a typical value of 0.06mm static eccentricity, as shown in Fig. 8.13. It can be seen the electric errors almost remain stable at similar levels with sinusoidal rotor employed - ±0.8 ° and ±1.0 ° respectively. Due to the significant improvement on the third-order voltage harmonics, the detection accuracies of conventional and NTWVR resolvers can also be improved by employing the AAPH rotor, even with eccentricities considered, both within the range of ±0.10 °.

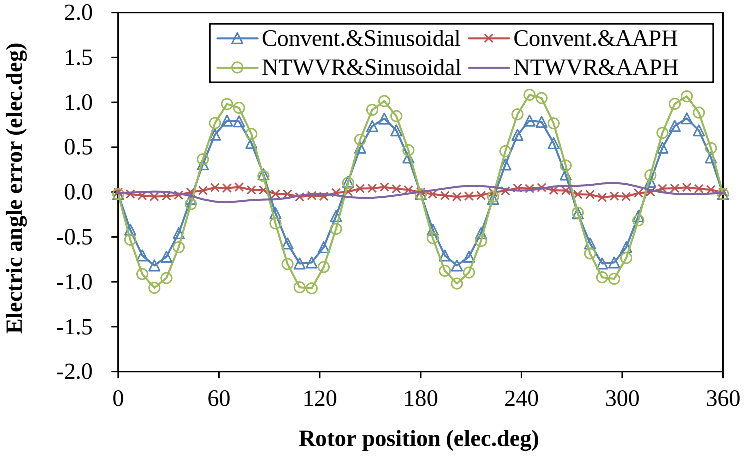

Fig. 8.13 Comparison of electric angle errors between different resolvers with a typical static eccentricity (0.06mm) considered.

8.4 Conclusion

The influence of manufacturing and assembling tolerances on the detection accuracy has been investigated and compared between conventional and NTWVR resolvers in this chapter, including the asymmetric coil locations and assembling eccentricities.

With asymmetric coil locations considered, residual DC components will be introduced in the synthetic output voltages, which result in the first-order of electric angle errors. However, different influences are introduced by this tolerance in the conventional and NTWVR resolvers, which are mainly due to the different distributions of exciting coils.

With assembling eccentricities considered, the third-order voltage harmonic increases slightly and results in the fourth-order of electric errors for the conventional VR resolver with the AAPH rotor employed. For NTWVR resolver, the second-order voltage harmonic can no longer be compensated, which results in the first-order of electric angle errors.

In addition, resolvers with sinusoidal rotors are not sensitive to the tolerances, due to the high magnitudes of intrinsic third-order voltage harmonics. For resolvers with AAPH rotors, the detection accuracy is a little sensitive to these tolerances due to the increase of additional voltage harmonics. However, the detection accuracy of the two resolver topologies is still much higher than that of resolvers with sinusoidal rotors.

CHAPTER 9 GENERAL CONCLUSIONS AND DISCUSSIONS

9.1 General Conclusions

In order to boost the competitiveness of machine products, an effective way is to develop designs with simplified manufacturing process and decreased sensitivity to manufacturing tolerances. This thesis has investigated and identified the influence of manufacturing tolerances on cogging torque and other electromagnetic performance in different IPM machines, as a reference for selecting proper machine configurations. Moreover, novel winding configurations have been proposed to simplify the manufacturing process of VR resolvers with novel rotor contours further proposed to improve the detection accuracy and the sensitivity to typical tolerances.

9.1.1 Cogging Torque of IPM Machines

During the manufacturing process of IPM machines, different cogging torque harmonics may be potentially introduced, including the residual component of fundamental order and the additional components of lower orders, neither of which can be effectively reduced by the conventional step-skewing method. Based on a 12-slot/8-pole IPM machine, the two cases have been firstly investigated.

A. Residual Cogging Torque Components of the Fundamental Order

When the conventional step-skewing method is employed to reduce the cogging torque (the 24^{th} order), a residual component of the target order always exists even when the machine is ideally fabricated, which proves to be due to the 3D end effect and the axial flux interaction between adjacent rotor steps. In order to eliminate the component, two optimal step-skewing methods have been proposed and compared, i.e. step-skewing rotor by optimal skewing angles and by optimal step lengths. Moreover, design considerations have been further proposed accounting for the manufacturing process, i.e. the materials of silicon-steel laminations and PMs, and the tolerance of axial assembling gaps between rotor steps, which require consequent corrections on the proposed skewing methods.

In addition, the residual cogging torque components of the fundamental order may also be introduced by the step-skewing angle tolerances during the rotor fabrication, the magnitude of which is closely related to the original cogging torque values.

B. Additional Cogging Torque Components of Lower Orders

It has been proven that lower orders of additional cogging torque components are introduced in IPM machines with the manufacturing tolerances considered, i.e. the PM diversity, the assembling eccentricities and the non-ideal stator out-of-roundness by tooth-bulges. With the PM diversity (e.g. uneven PM remanence and PM dimensional tolerances) considered, the 12th order of additional cogging torque is produced, and the most sensitive case has been identified amongst multiple random distributions – the consequent distribution of four non-ideal PMs. With the tooth-bulges considered, the 8th order of additional cogging torque is introduced. Through the similar method, the most sensitive case of non-ideal stator out-of-roundness has been obtained – four tooth-bulges belonging to the same phase. In addition, vector diagrams representing cogging torque vectors by different non-ideal PMs or tooth-bulges are employed, based on which the magnitudes of additional cogging torques activated by different distributions of non-ideal PMs and tooth-bulges can be specified.

As a reference for selecting proper designs, the influence of manufacturing tolerances has been compared amongst different IPM machine configurations, i.e. different rotor contours and different slot/pole combinations, which are designed for similar average output torque. On the one hand, it has been proven that the sinusoidal design is less sensitive to the PM diversity, based on the comparison between 12-slot/8-pole IPM machines by the sinusoidal and eccentric rotor contours. Moreover, both of the two rotor designs prove to be sensitive to the tooth-bulges during the assembling of modular stator segments, especially when four tooth-bulges belonging to the same phase exist. On the other hand, comparison has also been carried out between 12-slot/8-pole and 12-slot/10-pole IPM machines, which illustrates that the 10-pole design is much less sensitive to tooth-bulges (the most sensitive case also proves to be four tooth-bulges belonging to the same phase) but more sensitive to PM diversity (the most sensitive case: two adjacent non-ideal PMs and their opposite).

For verification, the field spatial harmonics under ideal and non-ideal conditions have been investigated and compared respectively, followed by the tests on different prototypes.

In addition, the influence of manufacturing tolerances on other electromagnetic performance has also been investigated and compared. Compared with that on cogging torque, the influence of manufacturing tolerances on the back EMF and the on-load torque is found to be less sensitive, although the torque ripple deteriorates due to additional back EMF harmonics and cogging torque components.

To conclude, the analyses of cogging torque in IPM machines are summarized:

(a) Due to the end effect and axial flux interaction between rotor steps, the residual cogging torque component of the fundamental order is introduced, which can be eliminated by the proposed step-skewing methods.

(b) Additional cogging torque components of lower orders are introduced with the manufacturing tolerances considered, i.e. PM diversity, assembling eccentricity, non-ideal stator out-of-roundness by tooth-bulges, and skewing angle errors. To evaluate the influence by different distributions of tolerances, cogging torque vector diagrams have been established.

(c) With the PM diversity considered, the most sensitive cases for 12-slot/8-pole and 12-slot/10-pole designs prove to be the consequent distribution of four non-ideal PMs and the distribution of two adjacent non-ideal PMs and their opposite, respectively. It has been also proven that the 10-pole design is more sensitive than the 8-pole design, and the eccentric design is more sensitive than the sinusoidal design.

(d) With stator tooth-bulges considered, the most sensitive case for the two slot/pole combinations has been generalized as the distribution of four tooth-bulges belonging to the same phase. Based on comparison, it has shown that no obvious improvement can be achieved with the sinusoidal rotor contour employed, whilst the 12-slot/10-pole design proves to be much less sensitive than the 12-slot/8-pole design.

9.1.2 VR Resolvers

The relationship between the numbers of stator teeth, winding polarities and rotor saliencies has been analytically derived, which enables identical stator and winding to be commonly used by variant poles of resolvers. Based on the established relationship, harmonic levels amongst different stator slot and rotor pole combinations can be effectively evaluated through an index defined in this thesis. As a deduction, the ‘close-slot-pole’ concept is proposed for the design of multi-polar VR resolvers. Twelve stator teeth with alternate output windings are proposed for a 5-X resolver, which can partially simplify the manufacturing process and solve problems with existing products, due to the non-overlapping output windings with uniform coils employed. The feasibility is verified by FE analyses and tests on a resolver prototype. Similar designs can also be extended to a wide range of stator slot and rotor pole combinations, amongst which the number of stator slots is 12 and its multiples.

Further improvement on windings has been investigated and a novel VR resolver topology with non-overlapping tooth-coil windings has been proposed. It is proven that basic functions as a position sensor can be fully performed by the winding arrangement. The most significant advantage for this design is the separation of exciting coils, SINE and COSINE output coils, which are located on different stator teeth. A further improvement is that both of the two output windings are composed of uniform coils, rather than the sinusoidally distributed coils as in a conventional VR resolver. Consequently, the manufacturing process is significantly simplified. Moreover, the proposed resolver topology enables identical stator and windings to be commonly utilized by 3 different poles of resolvers, and feasible stator slot/rotor pole combinations for this novel topology are summarized. A 2-X resolver of the proposed design has been established for HEV/EV applications, which significantly reduces the winding-fabrication duration. With actual application conditions (i.e. operating speed and assembling eccentricity) considered, the proposed design has been proven to be suitable for HEV/EV systems. In addition, when the identical 24-slot stator and windings are employed in 10-X and 14-X resolvers (with the same air-gap lengths), the theoretical output voltages decrease to 75% and 53% respectively, due to variation of the fundamental air-gap permeance. Prototypes based on similar dimensions of the resolver used in Prius machine have been fabricated to verify the foregoing analyses.

Moreover, due to the magnetic flux flowing through the air-gap is not along straight lines towards the rotor centre, especially in regions with large air-gap lengths, which inevitably introduces a series of air-gap permeance harmonics. In order to improve the detection accuracy of the proposed VR resolver, a novel design of rotor contour by injecting auxiliary air-gap permeance harmonics has been further proposed. For the VR resolver topology with non-overlapping tooth-coil windings, the origins of the voltage harmonics and the corresponding electric angle errors have been investigated. Due to the consequent distributions of exciting teeth, a phase angle shift is introduced between exciting teeth and adjacent output teeth, which results in the third order of residual output voltage harmonic. With an optimal auxiliary air-gap permeance harmonic employed in the rotor contour, the voltage harmonic is effectively eliminated and the electric angle error is also significantly improved. In addition, the proposed design can also be employed to eliminate the voltage tooth harmonics in a conventional VR resolver topology of which the stator teeth number is four times of rotor saliencies, e.g. the 20-slot/5-X resolver. Prototypes have been fabricated to verify the effectiveness of the proposed design.

Finally, the influence of manufacturing and assembling tolerances on the detection accuracy has also been investigated for the conventional and the proposed VR resolvers, including asymmetric coil locations and assembling eccentricities. It is proven that additional voltage harmonics are introduced with the tolerances considered, which increase the electric errors to some extent. Compared with the sinusoidal rotor used in conventional products, the novel rotor design with auxiliary permeance harmonics can significantly improve the detection accuracy, even with these tolerances considered.

To conclude, the analyses of VR resolvers in this thesis are summarized:

(a) The relationship between the numbers of stator teeth, the winding polarities and the rotor saliencies has been analytically derived, based on which an index is defined to select proper stator slot and rotor pole combinations.

(b) Alternate output windings with uniform coils have been proposed to partially simplify the output winding fabrication.

(c) A novel VR resolver topology with non-overlapping tooth-coil windings has been proposed, and the identical stator (and windings) can be employed in different poles of resolvers. With the actual application conditions considered, the proposed resolver proves to be a strong candidate for HEV/EV applications.

(d) A novel design of rotor contour by injecting auxiliary air-gap permeance harmonics has been proposed to eliminate the output voltage harmonics and improve the detection accuracy, which can be also employed to eliminate the tooth harmonics in a conventional VR resolver topology (Z=4p).

(e) The influence of asymmetric coil locations and assembling eccentricities has been investigated and compared between different designs of VR resolvers, which indicates that the design by the proposed rotor contour can be employed to improve the detection accuracy even with manufacturing tolerances considered.

9.2 Future Work

As for future work, follow-up investigations can be further carried out accounting for the manufacturing process of IPM machines and VR resolvers.

For IPM machines, it is necessary to develop improved manufacturing process to avoid the aforementioned sensitive cases of tolerances. Moreover, the manufacturing process of spoke-type IPM machines should also be investigated, including:

(a) Simplified punching process (Appendix-C).
(b) Post-assembly magnetization techniques.
(c) Modular rotor techniques.
(d) Hybrid excitation techniques.
(e) Mechanical flux weakening techniques.

In addition to the cogging torque index, special attention should also be paid to other performance of IPM machines, e.g. on-load torque quality, noise and vibration, etc.

For VR resolvers, the influence of external magnetic field on the detection accuracy requires further investigation, as a reference for the integration and assembling of this kind of sensors. Moreover, due to the high price of commercial decoding chips, an urgent issue is to develop reliable software-based decoding methods for low cost applications. Furthermore, the phase delay at high operating speeds due to the bandwidth limitation of low-pass filter should also be considered. In addition, the integration of VR resolvers and bearings attracts increasing interest and the corresponding manufacturing process requires special attention. Besides the VR resolvers, other position sensors should also be investigated to satisfy the requirements of different industrial applications.

REFERENCES

[ACK92] B. Ackermann, J. H. H. Janssen, R. sotteck, and R. I. Van Steen, “New technique for reducing cogging torque in a class of brushless DC motors,” *Proc. IEE-Electr. Power Appl.*, vol. 139, no. 4, pp. 315-320, Jul. 1992.

[ADM08] Solid rotor resolver (Rotasyn), Admotec Precision AG, Switzerland, 2008.

[AKI03] H. Akita, Y. Nakahara, N. Miyake, and T. Oikawa, “New core structure and manufacturing method for high efficiency of permanent magnet motors,” in *Conf. Rec. IEEE IAS Annu. Meeting*, Salt Lake City, UT, Oct. 2003, vol. 2, pp. 367-372.

[ANA08] Variable resolution resolver-to-digital converter (AD2S80), Analog Devices, Inc., U.S.A., 2008.

[AUS10] Magnetic encoder IC’s, Austriamicrosystems, Austria, 2010.

[AUN13] N. L. H. Aung, C. Bi, A. A. Mamun, C. S. Soh, and Y. Q. Yu, “A demodulation technique for spindle rotor position detection with resolver,” *IEEE Trans. Magn.*, vol. 49, no. 6, pp. 2614-2619, Jun. 2013.

[AZA12] Z. Azar, Z. Q. Zhu, and G. Ombach, “Investigation of torque-speed characteristics and cogging torque of fractional-slot IPM brushless AC machines having alternate slot openings,” *IEEE Trans. Ind. Appl.,* vol. 48, no. 3, pp. 903-912, Mar. 2012.

[BAR08] M. Barcaro, L. Alberti, A. Faggion, L. Sgarbossa, M. D. Pre, and N. Bianchi, “Experimental tests on a 12-slot 8-pole integrated starter-alternator,” in *18th Elect. Mach. Conf. (ICEM),* Vilamoura, Portugal, Sep. 2008, pp. 1-6.

[BEN09] L. Ben-Brahim, M. Benammar, and M.A. Alhamadi, “A resolver angle estimator based on its excitation signal,” *IEEE Trans. Ind. Elect.*, vol. 56, pp. 574-580, Feb. 2009.

[BEN13] M. Benammar and A.S.P. Gonzales, “A novel resolver converter based on a modified tracking method,” in *10th IEEE Int. Conf. Networking, Sensing and Control*, Evry, France, Apr. 2013, pp. 586-590.

[BIA02] N. Bianchi and S. Bolognani, “Design techniques for reducing the cogging torque in surface-mounted PM motors,” *IEEE Trans. Ind. Appl.*, vol. 38, no. 5, pp. 1259-1265, Sep./Oct. 2002.

[BIA07] N. Bianchi and S. Bolognami, “Influence of rotor geometry of an IPM motor on sensorless control feasibility,” *IEEE Trans. Ind. Appl.*, vol. 43, no. 1, pp.87-96, 2007.

[BOL11] S. Bolognani, S. Calligaro, R. Petrella, and M. Sterpellone, “Sensorless control of IPMSM using PWM excitation: Analytical developments and implementation issues," in *Symp. Sensorless Control for Electric. Drives,* 2011, pp. 64-73.

[BRI04] F. Briz, M. W. Degner, P. Garcia, and R. D. Lorenz, "Comparison of saliency-based sensorless control techniques for AC machines," *IEEE Trans. Ind. Appl.*, vol. 40, no. 4, pp. 1107-1115, 2004.

[CAR98] F. Caricchi, F. Crescimbini, and O. Honorati, "Low-cost compact permanent magnet machine for adjustable-speed pump application," *IEEE Trans. Ind. Appl.*, vol. 34, no. 1, pp. 109-116, Jan./Feb. 1998.

[CHA08] K. T. Chau, C. C. Chan, and C. H. Liu, "Overview of permanent-magnet brushless drives for electric and hybrid electric vehicles," *IEEE Trans. Ind. Electron.*, vol. 55, no. 6, pp. 2246-2257, Jun. 2008.

[CHA09] F. Chai, Y. L. Pei, X. M. Li, B. Guo, and S. K. Cheng, "The performance research of starter-generator based on reluctance torque used in HEV," *IEEE Trans. Magn.*, vol. 45, no. 1, pp. 635-638, Jan. 2009.

[CHE00] S. K. Chen, "Parameter calculation," in *Electrical Machine Design*, Beijing, China: CMP, 2000, ch. 4, pp. 50-62.

[CHE10a] N. Chen, S. L. Ho, and W. N. Fu, "Optimization of permanent magnet surface shapes of electric motors for minimization of cogging torque using FEM," *IEEE Trans. Magn*., vol. 46, no. 6, pp. 2478-2481, Jun. 2010.

[CHE10b] H. S. Chen, D. G. Dorrell, and M. C. Tsai, "Design and operation of interior permanent magnet motors with two axial segments and high rotor saliency," *IEEE Trans. Magn*., vol. 46, no. 9, pp. 3664-3675, Sep. 2010.

[CHE14] Z. F. Chen, C. L. Xia, Q. Geng, and Y. Yan, "Modeling and analysing of surface-mounted permanent-magnet synchronous machines with optimized magnetic pole shape," *IEEE Trans. Magn.*, vol. 50, no. 11, pp. 8102804, Nov. 2014.

[CHI09] C. Song, Z. Zheng, and X. Longya, "Sliding-mode sensorless control of direct-drive PM synchronous motors for washing machine applications," *IEEE Trans. Ind. Appl.*, vol. 45, no. 2, pp.582-590, 2009.

[CHU13] W. Q. Chu and Z. Q. Zhu, "Investigation of torque ripples in permanent magnet synchronous machines with skewing," *IEEE trans. Magn*., vol. 49, no. 3, pp. 1211-1220, Mar. 2013.

[COE12] I. Coenen, M. van der Giet, and K. Hameyer, "Manufacturing tolerances: estimation and prediction of cogging torque influenced by magnetization faults," *IEEE Trans. Magn*., vol. 48, no. 5, pp. 1932-1936, May 2012.

[CUI12] S. Cui and H. Ge, "Stator structure design and analysis of variable reluctance resolver for hybrid-vehicle motor drive," in *Proc.7th Int. Power Electronics and Motion Control Conf.*, Harbin, China, Jun. 2012, pp. 2587-2592.

[DAN14] C. T. Dang, W. Zhou, L. C. Ying and N. Z. Tong, “Analysis and reducing method of cogging torque on permanent magnet AC servo motor,” in *17th Elect. Mach. & Syst. (ICEMS)*, Hangzhou, China, Oct. 2014, pp. 2136-2140.

[DEG98] M. W. Degner, and R. D. Lorenz, “Using multiple saliencies for the estimation of flux, position, and velocity in AC machines,” *IEEE Trans. Ind. Appl.*, vol. 34, no. 5, pp. 1097-1104, 1998.

[DUB02] M. R. Dubois, H. Polinder, and J. A. Ferreira, “Magnet shaping for minimal magnet volumein mahcines,” *IEEE Trans. Magn.*, vol. 38, no. 5, pp. 2985-2987, Sep. 2002.

[DUT08] R. Dutta and M. F. Rahman, “Design and analysis of an interior permanent magnet (IPM) machine with very wide constant power operation range,” *IEEE Trans. Energy Conver.*, vol. 23, no. 1, pp. 25-33, Mar. 2008.

[DUT12] R. Dutta, L. Chong, and M. F. Rahman, “Design and experimental verification of an 18-slot/14-pole fractional-slot concentrated winding interior permanent magnet machine,” *IEEE Trans. Energy Convers.*, vol. 28, no. 3, pp. 181-190, Dec. 2012.

[EAS97] J. F. Eastham, D. M. Ionel, M. J. balchin, and T. Betzer, “Finite element analysis of an interior-magnet brushless D.C. machine, with a step-skewed rotor,” *IEEE Trans. Magn.*, vol. 33, no. 2, pp. 2117-2119, Mar. 1997.

[ESA06] J. Esaki, S. Isogawa, and T. Sako, “Method for manufacturing ring-shaped magnet material and manufacturing apparatus used therefor,” U.S. Patent US20060042342 A1, Mar. 2, 2006.

[EPC06] Optical encoders and accessories. Encoder products company (EPC), U.S.A., 2006.

[EVA10] S. A. Evans, “Salient pole shoe shapes of interior permanent magnet synchronous machines,” in *Int. Conf. Electr. Mach (ICEM).*, Roma, Italy, Sep. 2010, pp. 1-6.

[FEI10] W. Fei and P. C. K. Luk, “A new technique of cogging torque suppression in direct-drive permanent-magnet brushless machines,” *IEEE Trans. Ind. Appl.*, vol. 46, no. 4, pp. 1332-1340, Aug. 2010.

[FEI11] W. Fei, P. C. K. Luk, J. X. Shen, B. Xia, and Y. Wang, “Permanent-magnet flux-switching integrated starter generator with different rotor configurations for cogging torque and torque ripple mitigations,” *IEEE Trans. Ind. Appl.*, vol. 47, no. 3, pp. 1247-1256, May/Jun. 2011.

[FEI12] W. Fei, P. C. K. Luk, and J. X. Shen, “Torque analysis of permanent-magnet flux switching machines with rotor step skewing,” *IEEE Trans. Magn.*, vol. 48, no. 10, pp. 2664-2673, Oct. 2012.

[FEI13] W. Fei and Z. Q. Zhu, “Comparison of cogging torque reduction in permanent magnet brushless machines by conventional and herringbone skewing techniques," *IEEE Trans. Energy Convers.*, vol. 28, no. 3, pp. 664-674, Sep. 2013.

[FIG11] J. Figueiredo, "Resolver models for manufacturing," *IEEE Trans. Ind. Electron.*, vol. 58, no. 8, pp. 3693-3700, Aug. 2011.

[GAL14] R. Gale, "Variable reluctance resolver having integral electromagnetic interference shield and rotary electric machine having same," US Patent, 20140070672, May 13, 2014.

[GAO07] Q. Gao, G. M. Asher, M. Sumner, and P. Makys, "Position estimation of AC machines over a wide frequency range based on space vector PWM excitation," *IEEE Trans. Ind. Appl.*, vol.43, no. 4, pp. 1001-1011, 2007.

[GAS09] L. Gasparin, A. Cernigoj, S. Markic, and R. Fiser, "Additional cogging torque components in permanent-magnet motors due to manufacturing imperfections," *IEEE Trans. Magn.*, vol. 45, no. 3, pp. 1210-1213, Mar. 2009.

[GE12] X. Ge, "Market investigation on EPS machine topologies," Welling Motor Manufacturing Co., Ltd., Shanghai, China, Rep. 01-Mar-2012, Mar. 2012.

[GE15a] X. Ge, Z. Q. Zhu, R. Ren, and J. T. Chen, "A novel variable reluctance resolver with nonoverlapping tooth-coil windings," *IEEE Trans. Energy Convers.*, vol. 30, no. 2, pp. 784-794, May 2015.

[GE15b] X. Ge, Z. Q. Zhu, R. Ren, and J. T. Chen, "Analysis of windings in variable reluctance resolver," *IEEE Trans. Magn.*, vol. 51, no. 5, # 8104810, May 2015.

[GEO00] K. Georg, "Permanenterregte Synchronmaschine," German Patent Application DE 198 51 883 A1, May 18, 2000.

[GOS13] J. Goss, D. Staton, R. Wrobel, and P. Mellor, "Brushless AC interior-permanent magnet motor design: comparison of slot/pole combinations and distributed vs concentrated windings," in *Energy Convers. Congr. And Expo.*, Denver, Sep. 2013, pp. 1213-1219.

[GUO12] X. H. Guo, X. M. Zhuang, F. Zhao, R. M. Fang, and X. F. Lu, "Decoding principles and applying analysis of decoder chip-AD2S1200 for resolver," *Micro Motors*, vol. 45, no. 6, pp. 52-56, Jun. 2012.

[GUE11] J. A. Guemes, A. A. Iraolagoitia, J. J. Del Hoyo, and P. Fernandez, "Torque analysis in permanent-magnet synchronous motors: a comparative study," *IEEE Trans. Energy Convers.*, vol. 26, no. 1, pp. 55-63, Mar. 2011.

[HAN89] D. C. Hanselman, R. E. Thibodeau, and D. J. Smith, "Variable reluctance resolver design guidelines," in *15th Annual Conf. of the IEEE Ind. Elect. Society*, Philadelphia, U.S.A., Nov. 1989, vol. 1, pp. 203-208.

[HAN91] D. C. Hanselman, "Techniques for improving resolver-to-digital conversion accuracy", *IEEE Trans. Ind. Elect.*, vol. 38, no. 6, pp. 501-504, Dec. 1991.

[HAN97] D. C. Hanselman, "Effect of skew, pole count and slot count on brushless motor radial force, cogging torque and back EMF," *Proc. IEE-Electr. Power Appl.*, vol. 144, no. 5, pp. 325-330, Sep. 1997.

[HOL98] J. Holtz, "Sensorless position control of induction motors – an emerging technology," *IEEE Trans. Ind. Electron.*, vol. 45, no. 6, pp. 840-852, 1998.

[HOL05] J. Holtz and J. Juliet, "Sensorless acquisition of the rotor position angle of induction motors with arbitrary stator windings," *IEEE Trans. Ind. Appl.*, vol. 41, no. 6, pp. 1675-1682, 2005.

[HOS07] R. Hoseinnezhad, A. Bab-Hadiashar, and P. Harding, "Calibration of resolver sensors in electromechanical braking systems: a modified recursive weighted least-squares approach," *IEEE Trans. Ind. Electron.*, vol. 54, no. 2, pp. 1052-1060, Apr. 2007.

[HUA11] Y. Hua, M. Sumner, G. Asher, Q. Gao, and K. Saleh, "Improved sensorless control of a permanent magnet machine using fundamental pulse width modulation excitation," *IET Electron. Power Applicat.*, vol. 5, no. 4, pp. 359-370, 2011.

[HWA98] C. C. Hwang, S. B. John, and S. S. Wu, "Reduction of cogging torque in spindle motor for CD-ROM drive," *IEEE Trans. Magn.*, vol. 34, no. 2, pp. 468-470, Mar. 1998.

[HWA01a] S. M. Hwang, K. T. Kim, W. B. Jeong, Y. H. Jung, and B. S. Kang, "Comparison of wibration sources between symmetric and asymmetric HDD spindle motors with rotor eccentricity," *IEEE Trans. Ind. Appl.*, vol. 37, no. 6, pp. 1727-1731, Nov./Dec. 2001.

[HWA01b] S. M. Hwang, J. B. Eom, Y. H. Jung, D. W. Lee, and B. S. Kang, "Various design techniques to reduce cogging torque by controlling energy variation in permanent magnet motors," *IEEE Trans. Magn.*, vol. 37, no. 4, pp. 2806-2809, Jul. 2001.

[ISL04] M. S. Islam, S. Mir, and T. Sebastian, "Issues in reducing the cogging torque of mass-produced permanent-magnet brushless DC motor," *IEEE Trans. Ind. Appl.*, vol. 40, no. 3, pp. 813-820, May/Jun. 2004.

[ISL09] R. Islam, I. Husain, A. Fardoun, and K. McLaughlin, "Permanent-magnet synchronous motor magnet designs with skewing for torque ripple and cogging torque reduction," *IEEE Trans. Ind. Appl.*, vol. 45, no. 1, pp. 152-160, Feb. 2009.

[ISL10] R. Islam and I. Husain, "Analytical model for predicting noise and vibration in permanent-magnet synchronous motors," *IEEE Trans. Ind. Appl.*, vol. 46, no. 6, pp. 2346-2354, Aug. 2010.

[JAN95] P.L. Jansen and R. D. Lorenz, “Transducerless position and velocity estimation in induction and salient AC machines,” *IEEE Trans. Ind. Appl.*, vol. 31, no. 2, pp. 240-247, 1995.

[JAN97] G. H. Jang, J. W. Yoon, K. C. Ro, N. Y. Park, and S. M. Jang, “Performance of a brushless DC motor due to the axial geometry of the permanent magnet,” *IEEE Trans. Magn.*, vol. 33, no. 5, pp. 4101-4103, Sep. 1997.

[JAN01] S. M. Jang, S. S. Jeong, D. W. Ryu, and S. S. Choi, “Design and analysis of high speed slotless PM machine with halbach array,” *IEEE Trans. Magn.,* vol. 37, no. 4, pp. 2827-2830, Jul. 2001.

[JAN03] J. H. Jang, S. K. Sul, J. I. Ha, K. Ide, and M. Sawamura, “Sensorless drive of surface-mounted permanent-magnet motor by high-frequency signal injection based on magnetic saliency,” *IEEE Trans. Ind. Appl.*, vol. 39, no. 4, pp. 1031-1039, 2003.

[JIN10] H. M. Jing, “Analysis and design of EPS system,” Delta Power Electronics Co., Shanghai, China, Rep. MR-OCT-2010, Oct. 2010.

[JIA09] X. Jiang, J. Xing, Y. Li, and Y. Lu, “Theoretical and simulation analysis of influences of stator tooth width on cogging torque of BLDC motors,” *IEEE Trans. Magn.*, vol. 45, no. 10, pp. 4601-4604, Oct. 2009.

[KAK13] W. Kakihara, M. Takemoto, and S. Ogasawara, “Rotor structure in 50 kW spoke-type interior permanent magnet synchronous motor with ferrite permanent magnets for automotive applications,” in *Energy Conver. Congr. And Expo.* (ECCE), Denver, U.S.A., Sep. 2013, pp. 606-613.

[KAM12] K. Kamiev, J. Montonen, M. P. Ragavendra, J. Pyrhonen, J. A. Tapia, and M. Niemela, “Design principles of permanent magnet synchronous machines for parallel hybrid or traction application,” *IEEE Trans. Ind. Electron.*, vol. 60, no. 11, pp. 4881-4890, Oct. 2012.

[KHA12] D.A. Khaburi, “Software-based resolver-to-digital converter for DSP-based drives using an improved angle-tracking observer,” *IEEE Trans. Instrum. Meas.*, vol. 61, no. 4, pp. 922-929, Jan. 2012.

[KIM04] Y. K. Kim, J. J. Lee, J. P. Hong, and Y. Hur, “Analysis of cogging torque considering tolerance of axial displacement on BLDC motor by using a stochastic simulation coupled with 3-D EMCN,” *IEEE Trans. Magn.*, vol. 40, no. 2, pp. 1244-1247, Mar. 2004

[KIM09] K. C. Kim, C. S. Jin, and J. Lee, “Magnetic shield design between interior permanent magnet synchronous motor and sensor for hybrid electric vehicle,” *IEEE Trans. Magn.*, vol. 45, no. 6, pp. 2835-2838, Jun. 2009.

[KIM10] K. C. Kim, S. J. Hwang, K. Y. Sung, and Y. S. Kim, “A study on the fault diagnosis analysis of variable reluctance resolver for electric vehicle,” in *IEEE Sensors*, Hawaii, U.S.A., Nov. 2010, pp. 290-295.

[KIM13a] H. S. Kim, Y. M. You, and B. I. Kwon, "Rotor shape optimization of interior permanent magnet BLDC motor according to magnetization direction," *IEEE Trans. Magn.*, vol. 49, no. 5, pp. 2193-2196, May 2013.

[KIM13b] K. C. Kim, "Analysis on the characteristics of variable reluctance resolver considering uneven magnetic fields," *IEEE Trans. Magn.*, vol. 49, no. 7, pp. 3858-3861, Jul. 2013.

[KIM14] K. C. Kim, "A novel method for minimization of cogging torque and torque ripple for interiror permanent magnet synchronous motor," *IEEE Trans. Magn.*, vol. 50, no. 2, #7019604, Feb. 2014.

[KRO57] G. Kronacher, "Design, performance and application of the 261odelli resolver," *Bell System Technical Journal*, vol. 36, no. 6, pp. 1487-1500, Nov. 1957.

[LAT06] R. Lateb, N. Takorabet, and F. M. Tabar, "Effect of magnet segmentation on the cogging torque in surface-mounted permanent-magnet motors," *IEEE Trans. Magn.*, vol. 42, no. 3, pp. 442-445, Mar. 2006.

[LEI11] R. Leidhold, "Position sensorless control of PM synchronous motors based on zero-sequence carrier injection," *IEEE Trans. Ind. Electron.*, vol. 58, no. 12, pp. 5371-5379, 2011.

[LI88] T. Li and G. Slemon, "Reduction of cogging torque in permanet magnet motors," *IEEE Trans. Magn.*, vol. 24, no. 6, pp. 2901-2903, Nov. 1988.

[LI07] Y. Li, Z. Q. Zhu, D. Howe, and C. M. Bingham, "Improved rotor position estimation in extended back-emf based sensorless PM brushless AC drives with magnetic saliency accounting for cross-coupling magnetic saturation," in *IEEE Int. Elect. Mach. and Drives Conf., IEMDC 2007*, pp. 214-219, Antalya, Turkey, 2007.

[LI08] W. T. Li and S. R. Huang, "Rotor shape design and analysis of variable-reluctance resolver for hybrid-vehicle motor drive applications," *Elect. Mach. & Control Applicat.*, vol. 35, no. 5, pp. 6-10, May 2008.

[LI09] Y. Li, Z. Q. Zhu, D. Howe, and C. M. Bingham, "Improved rotor position estimation by signal injection in brushless AC motors, Accounting for Cross-Coupling Magnetic Saturation" *IEEE Trans. Ind. Appl.*, vol. 45, no. 5, pp. 1843-1850, 2009.

[MAK09] H. Makiuchi, Y. Kikuchi, H. Mimura, A. Kojima, H. Wakiwaka, and K. Tashiro, "Reduction method of external magnetic field effect on VR resolver," in *IEEE Research and Development*, UPM Serdang, Malaysia, Nov. 2009, pp. 208-211.

[MAS96] K. Masaki, Y. Fukuzawa, K. Kitazawa, T. Azuma, N. Naganuma, and T. Hosoda, "Sinusoidally distributed winding method suitable for a detector winding," U.S. Patent, 5486731, Jan. 23, 1996.

[MIR13] H. Mirahki and M. Moallem, “Design improvement of interior permanent magnet synchronous machine for integrated starter alternator application,” in *Elect. Mach. & Drive Conf* (ICEM)., Chicago, IL, May 2013, pp.382-385.

[MOM09] M. F. Momen and S. Datta, “Analysis of flux leakage in a segmented core brushless permanent magnet motor,” IEEE Trans. Energy Convers., vol. 24, no. 1, pp. 77-81, Feb. 2009.

[MUR02] A. Murray, B. Hare, and A. Hirao, “Resolver position sensing system with integrated fault detection for automotive applications,” in *Proc. IEEE Sensors,* Florida, U.S.A., Jun. 2002, vol. 2, pp. 864-869.

[NAK15] M. Nakano, Y. Morita, and T. Matsunaga, “reduction of cogging torque due to production tolerances of rotor by using dummy slots placed partially in axial direction,” *IEEE Trans. Ind. Appl.*, vol. 51, no. 6, pp. 4372-4382, Nov./Dec. 2015.

[PHC00] OEM770 servo drive user guide, Parker Hannifin Corporation, UK, 2000.

[PAR14] S. I. Park and K. C. Kim, “Study on the optimal design of a novel slotless resolver by FEM,” *IEEE Trans. Magn.*, vol. 50, no. 11, Nov. 2014.

[PEL12] G. Pellegrino, A. Vagati, B. Boazzo, and P. Guglielmi, “Comparison of induction and PM synchronous motor drives for EV application including design examples,” *IEEE Trans. Ind. Applicat.*, vol. 48, no. 6, pp. 2322-2332, Nov. 2012.

[PER09] E. Peralta-Sanchez and A. C. Smith, “Line-started permanent-magnet machines using a canned rotor,” *IEEE Trans. Ind. Appl.*, vol. 45, no. 3, pp. 903-910, May/Jun. 2009.

[QAM14] N. Abou Qamar, C. J. Hatziadoniu, and H. Wang, “Speed error mitigation for a DSP-based resolver-to-digital converter using autotuning filters,” *IEEE Trans. Ind. Electron.*, vol. 62, no. 2, pp. 1134-1139, Jul. 2014.

[QIA14] H. Qian, H. Guo, Z. Y. Wu, and X. F. Ding, “Analytical solution for cogging torque in surface-mounted permanent-magnet motors with magnet imperfections and rotor eccentricity,” *IEEE Trans. Magn.*, vol. 50, no. 8, #8201615, Aug. 2014.

[RED12] P. B. Reddy, A. M. EL-Refaie, K. K. Huh, J. K. Tangudu, and T. M. Jahns, “Comparison of interior and surface PM machines equipped with fractional-slot concentrated windings for hybrid traction applications,” *IEEE Trans. Energy Convers.*, vol. 27, no. 3, pp. 593-602, Sep. 2012.

[REF10] A. M. EL-Refaie, “Fractional-slot concentrated-windings synchronous permanent magnet machines: opportunities and challenges,” *IEEE Trans. Ind. Electron.*, vol. 57, no. 1, pp. 107-121, Jan. 2010.

[REN13] R. Ren, X. Ge, J. T. Chen, and Z. Q. Zhu, “Method of stator winding and related products,” Chinese Patent, 103280936 A, May 15, 2013.

[SAR08] S. Sarma, V. K. Agrawal, and S. Udupa, “Software-based resolver-to-digital conversion using a DSP,” *IEEE Trans. Ind. Electron.*, vol. 55, pp. 371-379, Jan. 2008.

[SCH94] M. Schroedl, and P. Weinmeier “Sensorless control of reluctance machines at arbitrary operating conditions including standstill,” *IEEE Trans. Power Electron.*, vol. 9, no. 2, pp. 225-231, 1994.

[SET96] R. Setbacken, “System performance and application tradeoffs determine the choice between encoders and resolvers in brushless servos,” *Power Convers. Intell. Motion*, vol. 22, no. 5, pp. 69–76, May 1996.

[SHA08] L. Shao, Z. J. Tang, K. Maki, H. Funato, J. Moore, and G. Saikalis, “Integrated simulation and analysis of resolver sub-system for HEV electric drive,” in *Vehicle Power and Propulsion Conf.* (VPPC), Harbin, China, Sep. 2008, pp. 1-5.

[SHA12] J. Shang, H. Wang, and W.Q. Wang, “The analysis of multi-pole axial flux reluctance resolver with sinusoidal rotor,” in *Proc.7th Int. Power Electron. Motion Control Conf.*, Harbin, China, Jun. 2012, pp. 1206-1209.

[SIM12] J. H. Sim, J. W. Jung, Y. H. Kim, B. H. Lee, and J. P. Hong, “Optimum design of SPMSM with concentrated windings and unequal tooth widths for EPS,” in *2012 IEEE Vehicle Power and Propulsion Conf. (VPPC)*, Seoul, South Korea, Oct. 2012, pp. 191-195.

[SON11] X. L. Song and Y. X. Wang, “Analysis on impedance matching of signal windings of variable-reluctance resolver,” *Micro Motors*, vol. 44, no. 2, pp. 9-12, Feb. 2011.

[STA06] C. S. Staines, C. Caruana, G. M. Asher, and M. Sumner, “Sensorless control of induction machines at zero and low frequency using zero sequence currents,” *IEEE Trans. Ind. Electron.*, vol. 53, no. 1, pp. 195-206, 2006.

[SUN04] L. Z. Sun, J. B. Zou, and Y. P. Lu, “New variable-reluctance resolver for rotor-position sensing,” in *Int. Technical Conf. IEEE Region 10*, ChiangMai, Thailand, Nov. 2004, vol. 4, pp. 5-8.

[SUN08] L. Z. Sun, “Analysis and improvement on the structure of variable reluctance resolvers,” *IEEE Trans. Magn.*, vol. 44, no. 8, pp. 2002-2008, Aug. 2008.

[TAN13] K. Tanaka and I. Sasada, “A method of producing Z-pulse output from thin axial resolver,” *IEEE Trans. Magn.*, vol. 49, no. 7, pp. 3937-3940, Jul. 2013.

[TAM02] Smartcoder (AU6802N1) specifications, Tamagawa Seiki Co. Ltd., Japan, 2002.

[TAM04] Brushless resolvers (Smartsyn FA-solver), Tamagawa Seiki Co. Ltd., Japan, 2004.

[TEN14] A. Tenconi, S. Vaschetto, and A. Vigliani, “Electrical machines for high-speed applications: design considerations and tradeoffs,” *IEEE Trans. Ind. Electron.*, vol. 61, no. 6, pp. 3022-3029, Jun. 2014.

[TIN15] F. Tinazzi and M. Zigliotto, “Torque estimation in high-efficiency IPM synchronous motor drives,” *IEEE Trans. Energy Convers.*, vol. 30, no. 3, pp. 983-990, Mar.2015.

[TSU06] T. Tsuruta, H. Kanebako, N. Otsuki and D. Zhang, “Permanent Magnet Embedded Motor,” U.S. Patent 7 042 127 B2, May 9, 2006

[TUD12] T. Tudorache and I. Trifu, “Permanent-magnet synchronous machine cogging torque reduction using a hybrid model,” *IEEE Trans. Magn.*, vol. 48, no. 10, pp. 2627-2632, Oct. 2012.

[WAN01] J. Q. Wan, X. Li, and G. Hong, “The analysis and design of high-speed brushless resolver plus R/D converter shaft-angle measurement system,” in *Elect. Mach. Syst.*, Shenyang, China, Aug. 2001, pp. 289–292.

[WAN05] S. Wang, D. Youn, H. Moon, and J. Kang, “Topology optimization of electromagnetic systems considering magnetization direction,” *IEEE Tran. Magn.*, vol. 41, no. 5, pp. 1808-1811, May 2005.

[WAN10] D. Wang, X. Wang, Y. Yang, and R. Zhang, “Optimization of magnetic pole shifting to reduce cogging torque in solid-rotor permanent-magnet synchronous motors,” *IEEE Trans. Magn.*, vol. 46, no. 5, pp. 1228-1234, May 2010.

[WAN12] D. Wang, X. Wang, M. K. Kim, and S. Y. Jung, “Integrated optimization of two design techniques for cogging torque reduction combined with analytical method by a simple gradient descent method,” *IEEE Trans. Magn.*, vol. 48, no. 8, pp. 2265-2276, Aug. 2012.

[XIA15] C. L. Xia, Z. Zhang, and Q. Geng, “Analytical modelling and analysis of surface mounted permanent magnet machines with skewed slots,” *IEEE Trans. Magn.*, vol. 51, no. 5, #8104508, May 2015

[XIN09] J. W. Xing, Y. Li, and Y. P. Lu, “Simulation and experimental study on influence of coil positions on accuracy of variable reluctance resolver,” *Small & Special Machines*. No. 1, pp. 1-3, Jan. 2009.

[XIO13] F. Xiong and X. F. Wang, “Design of a low-harmonic-content wound rotor for the brushless doubly fed generator,” *IEEE Trans. Energy Convers.*, vol. 29, no. 1, pp. 158-168, Nov. 2013.

[YOO09] A. Yoo and S. K. Sul, “Design of flux observer robust to interior permanent-magnet synchronous motor flux variation,” *IEEE Trans. Ind. Appl.*, vol. 45, no. 5, pp. 1670-1677, 2009.

[ZHU95] Z. Q. Zhu and D. Howe, “Magnetic field analysis and inductances of brushless DC machines with surface-mounted magnets and non-overlapping stator windings,” *IEEE Trans. Magn.*, vol. 31, no. 3, pp. 2115-2118, May 1995.

[ZHU00] Z. Q. Zhu and D. Howe, “Influence of design parameters on cogging torque in permanent magnet machines,” *IEEE Trans. Energy Convers*., vol. 15, no. 4, pp. 407-412, Dec. 2000.

[ZHU01] Z. Q. Zhu and D. Howe, “Halbach permanent magnet machines and applications: a review,” *IEE Proc. Elect. Power Appli.*, vol. 148, no. 4, pp. 299-308, Jul. 2001.

[ZHU05] Z. Q. Zhu, S. Ruangsinchaiwanich, D. Ishak, and D. Howe, “Analysis of cogging torque in brushless machines having nonuniformly distributed stator slots and stepped rotor magnets,” *IEEE Trans. Magn*., vol. 41, no. 10, pp. 3910-3912, Oct. 2005.

[ZHU07] Z. Q. Zhu and D. Howe, “Electrical machines and drives for electric, hybrid, and fuel cell vehicles,” *Proc. IEEE*, vol. 95, no. 4, pp. 746-765, Apr. 2007.

[ZHU09] Z. Q. Zhu, “A simple method for measuring cogging torque in permanent magnet machines,” in *Proc. IEEE Power Energy Soc. Gen. Meet*., Jul. 2009, pp. 1-4.

[ZHU11] Z. Q. Zhu, “Sensorless operation of permanent magnet brushless DC and AC drives-basic and novel machine design and control aspects,” in *8th Int. Conf. Power Electron.-ECCE Asia*, Shilla Jeju, Jeju, Korea, May 30, 2011.

[ZHU12] Z. Q. Zhu, Z. Azar, and G. Ombach, “Influence of additional air gaps between stator segments on cogging torque of permanent-magnet machines having modular stators,” *IEEE Trans. Magn*., vo. 48, no. 6, pp. 2049-2055, Jun. 2012.

[ZHU14] Z. Q. Zhu, L. J. Wu, and M. L. Mohd Jamil, “Influence of pole and slot number combinations on cogging torque in permanent-magnet machines with static and rotating eccentricities,” *IEEE Trans. Ind. Appl*., vo. 50, no. 5, pp. 3265-3277, Feb. 2014.

Appendix-A Stator and Rotor Laminations of IPM Machines

(These figures are removed for confidentiality reasons)

1. Stator

Fig. A.1 Drawing of stator lamination.

2. Rotor

(a) 8-pole eccentric rotor contour

(b) 8-pole sinusoidal rotor contour

(c) 10-pole eccentric rotor contour

Fig. A.2 Drawings of different rotor laminations.

Appendix-B Stator and Rotor Laminations of VR Resolvers

(These figures are removed for confidentiality reasons)

1. 5-X VR Resolver

(a) Stator

(b) Rotor

Fig. B.1 5-X VR resolver with 12 stator slots.

2. 2-X VR Resolver

(a) Stator

(b) Sinusoidal rotor contour 1

(c) Sinusoidal rotor contour 2

(d) AAPH rotor contour

Fig. B.2 2-X NTWVRR resolvers with 24 stator slots.

Appendix-C A Spoke-Type IPM Machine with Novel Alternate Airspace Barriers and Reduction of Unipolar Leakage Flux by Step-Staggered Rotor

C.1 Introduction

Nowadays interior permanent magnet (IPM) machines are increasingly used in industrial and domestic applications, due to the superiority in several aspects compared with surface-mounted permanent magnet (SPM) machines [AZA12], [WAN08], [MIR13], [RED14], [RAH08]. Firstly, higher mechanical reliability can be achieved with the permanent magnets (PMs) embedded in the rotor core and additional bindings are not necessary, which also simplifies the manufacturing process. Secondly, the risk of demagnetization under over-load conditions can be reduced, as the PMs do not directly face the air-gap. Thirdly, the rectangular shape of PMs employed in IPM machines guarantees more efficient use of PM materials and lower overall cost can be achieved. Moreover, a higher potential reluctance torque can be produced due to the saliency effect, especially in integral-slot motors.

According to the placement modes of PMs, IPM machines can be mainly divided into two categories: the radial type [JAH86], [DUT08], [WU09], [WAN12] and the spoke type [HWA09], [KAK13a], [IBR14], [KIM13a]. The most significant advantage of the spoke-type IPM machines is the flux-focusing effect of two adjacent PMs, which enhances the air-gap flux density and the output capability. Therefore, a more efficient use of the PM materials can be realized in the spoke-type IPM machines which become strong candidates for many applications, especially when costs are emphasized.

Despite these advantages described above, some issues still exist for the spoke-type IPM motors. The first one is the leakage flux reduction, especially around the rotor inner circumference. Several methods have been investigated to solve this problem. As a common approach [TAN97], [DEM13], nonmagnetic materials are employed, e.g. nonmagnetic stainless-steel shaft, through which the leakage flux can be effectively reduced. However, it significantly complicates the manufacturing process and increases the cost. Another approach [LEE04], [KIM13b], [DEM14] is to employ inner airspace barriers between adjacent PMs. However, the width of the iron ribs between the barriers should be strictly restricted, and then a conflict exists with the requirements of punching process for silicon-steel laminations [QI09]. In some cases, effective leakage reduction and convenient punching process cannot be achieved simultaneously. In addition, spoke-type IPM motors with auxiliary radial PMs (in consequent-pole styles) are proposed recently in order to improve the magnetic field distributions [GE12], [RAH14], [BOU14]. Such approaches introduce the second issue, described as magnetization of the end shaft, which reduces the life expectation of the bearings, even poses a threat to the reliability of the machine system. The two issues hinder further applications of spoke-type IPM machines and few solutions to the issues can be found in literature.

With the manufacturing process considered, this paper proposes a spoke-type IPM machine by a novel step-staggered rotor with alternate airspace barriers in order to reduce the leakage flux around the rotor inner circumference, as well as magnetization of the end shaft. Firstly, comparisons between spoke-type IPM motors with conventional and alternate airspace barriers are carried out by 2-dimensional (2D) finite element (FE) method, including torque capability and mechanical strength. Secondly, the 3-dimensional (3D) FE method is employed to investigate the influence of end leakage flux, and unipolar leakage flux is introduced - resulting in magnetization of the end shaft, which can be eliminated through the step-staggered rotor. As an extension, the unipolar leakage flux proves to be a common problem with conventional consequent-pole PM machines, and the effectiveness of step-staggered method is investigated. Finally, prototypes with three different rotors are fabricated and tested in order to verify the analyses, including the magnetic field on the surface of end shaft and the output capability.

C.2 A Spoke-Type IPM Machine with Alternate Airspace Barriers

Recently, spoke-type IPM machines become worldwide hotspots. With the PMs tangentially magnetized, the air-gap flux density can be significantly enhanced due to the flux-focusing effect of adjacent PMs. However, the leakage flux around the inner circumference of the rotor should be effectively reduced for actual products. Fig. C.1 illustrates conventional approaches with non-magnetic materials employed [TAN97], [DEM13]. It is obvious that the manufacturing process is very complicated, although the leakage flux can be largely reduced. Another approach is to employ airspace barriers, as shown in Fig. C.2 (a). Without additional non-magnetic materials, the manufacturing process is simplified. However, the width of iron ribs between adjacent airspace barriers in certain products is subject to the punching process, for example at least 3 times of the lamination depth [QI09]. Therefore, the effect of leakage reduction will be limited. In this section, a spoke-type IPM rotor with alternate airspace barriers is proposed, as shown in Fig. C.2 (b). As can be seen, the number of airspace barriers is reduced to half of the pole number, and iron ribs only locate under PMs with an identical polarity.

Based on main parameters of a typical electric power steering (EPS) motor shown in Table I, two spoke-type IPM models with conventional and alternate airspace barriers are established.

With identical stator employed, comparisons are carried out between the two models, including the leakage flux distribution and the torque capability.

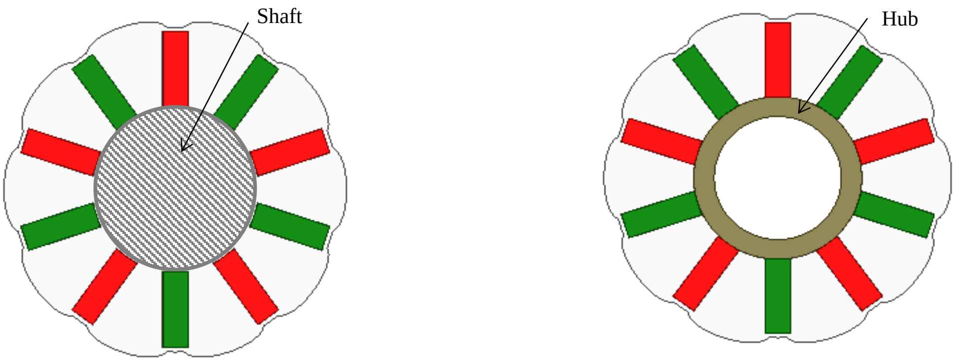

(a) Stainless-steel shaft [TAN97]

(b) Copper hub [DEM13]

Fig. C.1 Reduction of leakage flux in spoke-type IPM rotors with nonmagnetic materials.

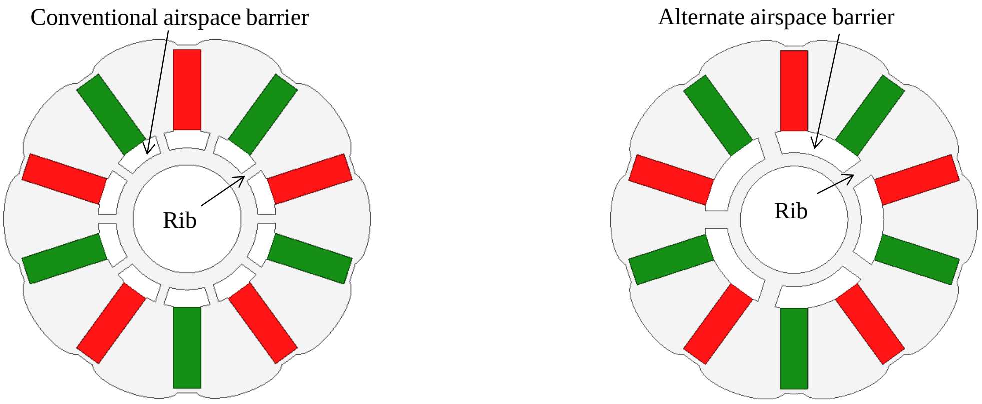

(a) Conventional barriers

(b) Alternate barriers

Fig. C.2 Spoke-type IPM rotors with conventional and alternate airspace barriers.

TABLE C.1

MAIN PARAMETERS OF SPOKE-TYPE IPM MODELS

Parameters	Values
Stator slots / rotor poles	12/10
Stator outer diameter (mm)	80
Stator inner diameter (mm)	42
Lamination axial length (mm)	44.45
End shaft length (mm)	30
Airspace barriers depth (mm)	2.5
Minimum air-gap length (mm)	0.5
PM size (mm/mm/mm)	44.45/9/3
PM residual remanence (T, 20 ℃)	1.18
Winding turs in series per phase	24

First, no-load flux distributions of the two spoke-type IPM models are investigated by 2D FE analysis module of the Maxwell software, as shown in Fig. C.3. It can be seen that the model with alternate airspace barriers can better reduce the leakage flux around the rotor inner circumference, even with higher width of iron ribs, which is mainly due to the much lower permeance of airspace barriers involved in the leakage path.

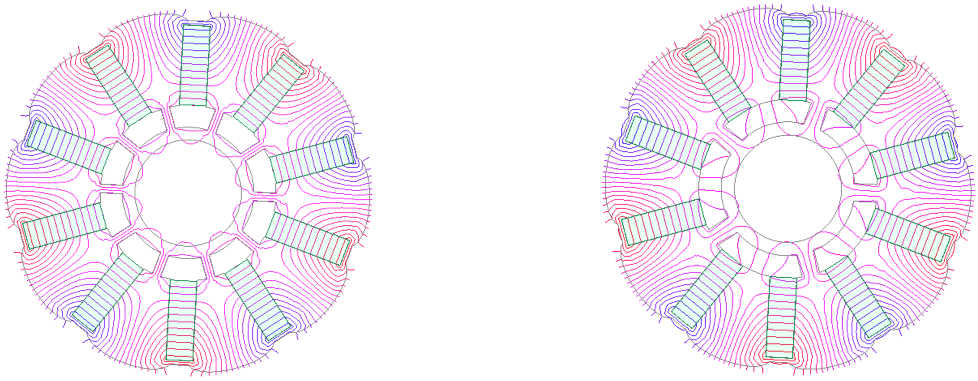

(a) Rotor with conventional barriers (b) Rotor with alternate barriers

Fig. C.3 Comparison of flux distribution on no load (stator part not shown).

As it is well known, the width of iron ribs significantly influences the effect of leakage flux reduction in IPM motors. Therefore, the torque capabilities under different widths of iron ribs are investigated and compared between the two models, as shown in Fig. C.4. It can be seen that the torque of the design with conventional airspace barriers decreases from 4.48 Nm to 3.70 Nm when the rib width increases from 1.0mm to 3.0mm, which indicates that the torque capability of the conventional design is very sensitive to the rib width. Therefore, an inevitable reduction of the torque capability is always introduced when wider iron ribs are employed for simplified manufacturing process, which is a typical problem for the application of spoke-type IPM machines in industrial and domestic systems, especially for medium and small size machines, e.g. the EPS motors, the washing machine motors, etc. In contrast, the torque produced by the design with alternate airspace barriers proves to be not so sensitive, only slightly decreasing from 4.70 Nm to 4.57 Nm. Therefore, the torque capability will not deteriorate even with wider iron ribs, which simplifies the punching process of the spoke-type IPM machines. In the following investigation, the width of iron ribs for the spoke-type IPM machines with alternate airspace barriers is selected as 2.0mm, through which a 4.60 Nm average torque can be obtained.

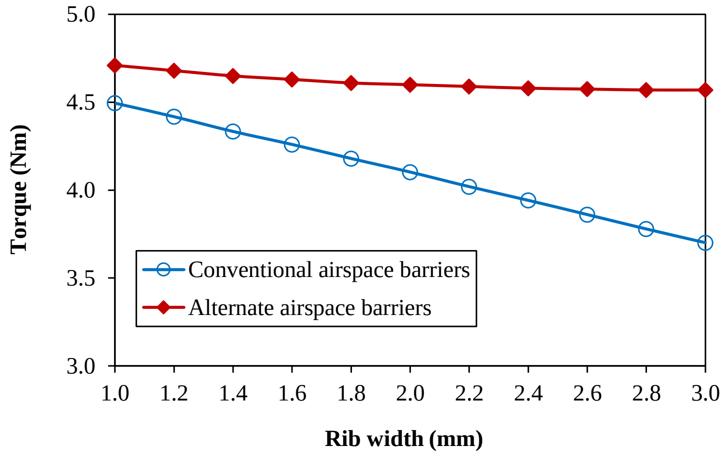

Fig. C.4 Influence of iron rib width on torque capability.

As an important index, the mechanical strength of the spoke-type IPM rotor is investigated and compared with the rotor with conventional airspace barriers (1mm iron ribs). With the axial symmetry considered, the 2D FE static structural module of the Ansys software can be employed (mesh by Triangles of 0.5mm ~2.0mm sizes), including the analyses of mechanical stress and deformation, as shown in Fig. C.5. It can be seen that the rotor deformation is negligible, and the maximum mechanical stress is 34.4MPa at the speed of 5000rpm. Therefore, a sufficient safety margin can be achieved, when compared with the ultimate strength of conventional silicon-steel lamination materials. Moreover, the mechanical strength of the proposed IPM rotor will be further investigated and improved in the following section.

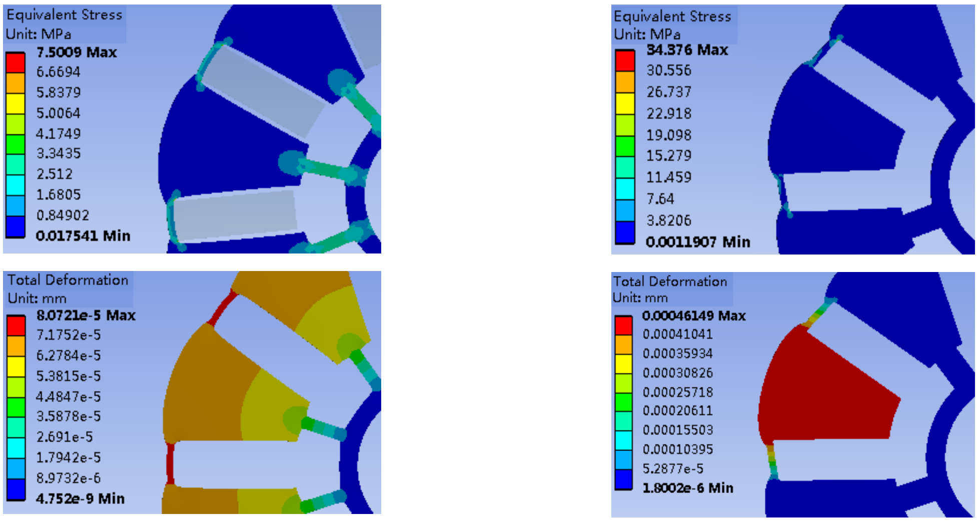

(a) Rotor with conventional barriers. (b) Rotor with alternate airspace barriers

Fig. C.5 Comparison of mechanical strength (5000rpm).

C.3 Unipolar Leakage Flux and Reduction by Step-Staggered Rotor

Usually, the end leakage flux in spoke-type IPM machines should not be neglected, which makes the output capability different from the 2D FE results. In this section, the 3D FE analysis module of the Maxwell software is employed to investigate the influence of end leakage flux in the aforementioned spoke-type IPM machine with alternate airspace barriers, including the torque capability and the leakage flux distribution in the end shaft. With an 80A rated current applied, the torque performance can be obtained and a comparison between the 2D and 3D FE results is carried out, as shown in Fig. C.6. It can be seen that the average torque of the machine with alternate airspace barriers decreases from 4.6 Nm to 4.4 Nm, with the 3D end leakage flux considered. Usually, it is necessary to consider the influence of end leakage flux during the design of spoke-type IPM machines, especially for designs with flat shapes.

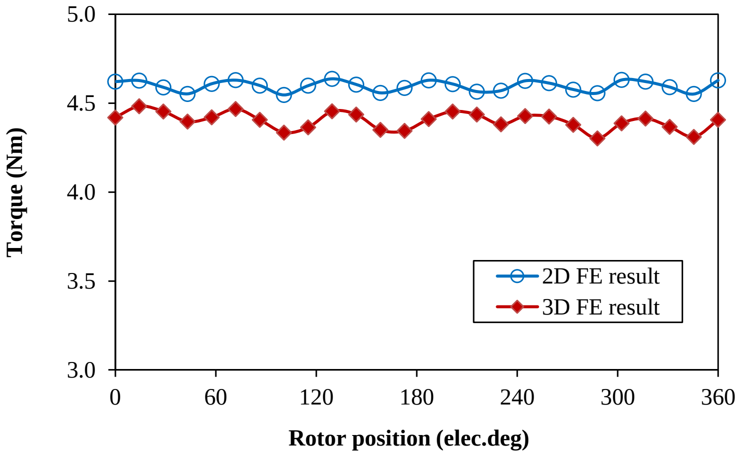

Fig. C.6 Torque comparison between 2D FE and 3D FE results (alternate airspace barriers, 2mm iron rib).

In addition to the reduction of torque capability, it is still necessary to further investigate the leakage flux distribution and corresponding influence. Firstly, the flux density on the surface of end shaft is obtained, as shown in Fig. C.7 (a), in which a limited length (12mm) of end shaft is shown in order to clearly illustrate the flux distribution. It can be seen that the flux density is around 0.07T in average, including certain fluctuation up to 0.1T. Further, Fig. C.7 (b) illustrates the flux density vector on the surface of end shaft. It is found that the vector follows a uniform direction (inward for this model), which indicates that the unipolar leakage flux is introduced. Actually, this phenomenon is mainly due to the alternate distributions of magnetic iron ribs. Based on the flux distributions, the path of end leakage flux through the end shaft can be obtained, as shown in Fig. C.7 (c). Similar distributions of the leakage flux can be also deduced for the other four pole pairs of the model. As can be seen, the end shaft (together with the air) and the magnetic iron ribs provide the inward and outward paths for the end leakage respectively, which results in unipolar leakage flux in the end shaft.

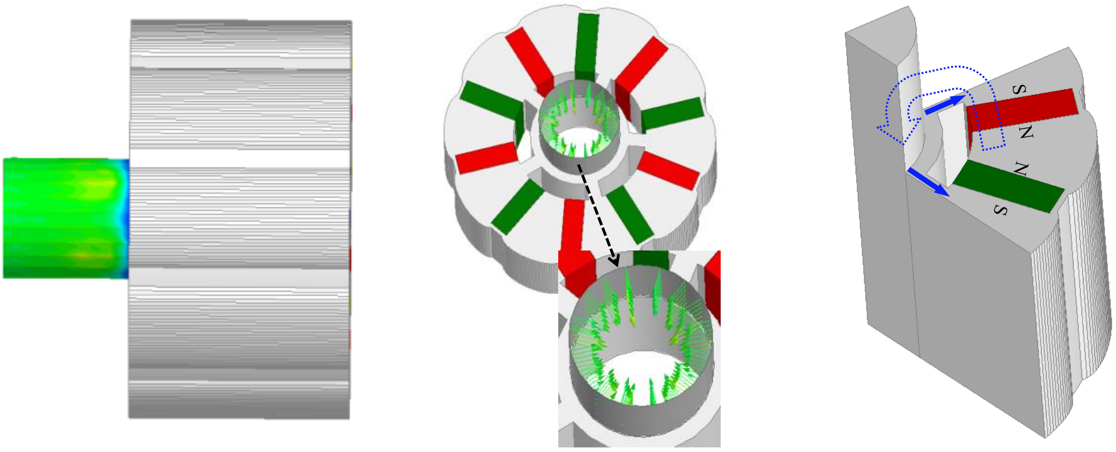

(a) Flux density (b) Flux density vector (c) Path of end leakage flux

Fig. C.7 Magnetic field at the end shaft and the path of end leakage flux.

According to features of the end leakage flux described above, the proposed spoke-type IPM machine has the issue - magnetization of the end shaft. Due to the unipolar leakage flux, ferromagnetic materials can be attracted by the end shaft. Undesirable consequences may be caused with magnetization of the end shaft considered. Not only is the life expectation of the bearings influenced, but it also poses a potential threat to the reliability of the machine system.

In order to solve the problem of unipolar leakage flux and magnetization of the end shaft, a step-staggered rotor is proposed in this section, as shown in Fig. C.8. It can be seen that the proposed rotor has two (even number) steps of equal length, and the iron ribs of which are tangentially staggered by one pole pitch.

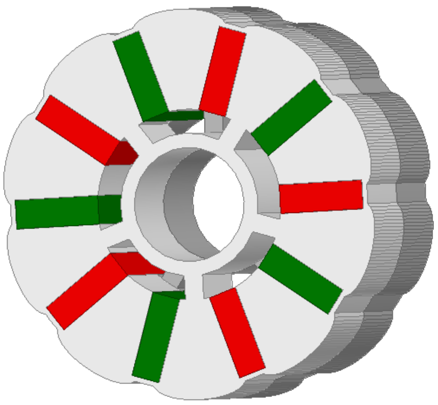

Fig. C.8 Step-staggered rotor with alternate airspace barriers.

Similarly, the flux density and the flux density vector on the surface of the end shaft are re-examined by 3D FE analyses, as shown in Fig. C.9 (a) and Fig. C.9 (b) respectively. With the step-staggered rotor employed, the end leakage flux can be significantly improved. On the one hand, the flux density at the surface of end shaft decreases from 0.07T to very low extent, which indicates that much less end leakage flows through the end shaft. On the other hand, the unipolar leakage flux no longer exists, which effectively eliminates magnetization of the end shaft in principle. Actually, the fundamental path of leakage flux flowing through the inner iron ribs can be deduced, as shown in Fig. C.9 (c). With the step-staggered rotor employed, the iron ribs of the two rotor steps serve as the inward and outward paths for the leakage flux, respectively, whilst the end shaft is no longer involved in the fundamental paths.

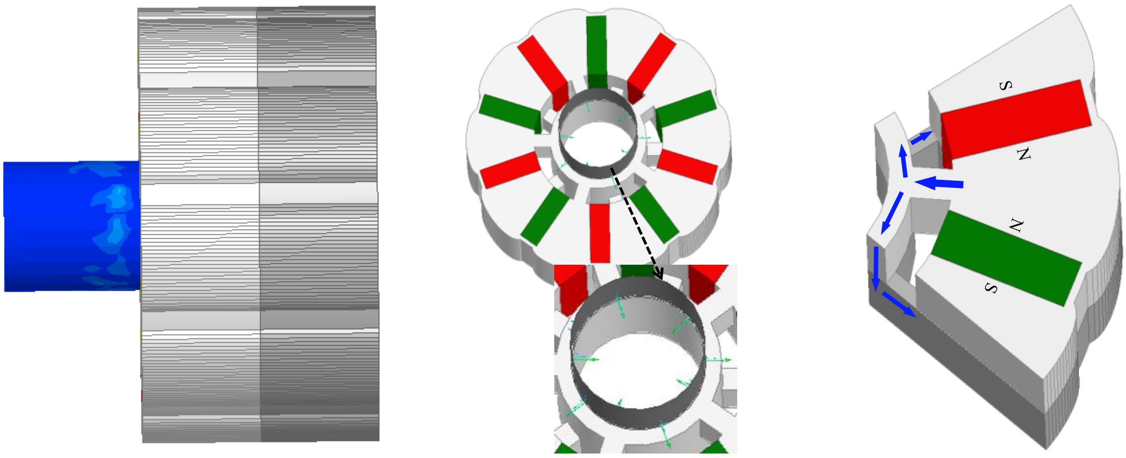

(a) Flux density (b) Flux density vector (c) Path of leakage flux

Fig. C.9 Magnetic field at the end shaft and the path of end leakage flux in the step-staggered rotor.

In order to further investigate the improvement of leakage flux, a comparison of the flux density at different positions of the end shaft surface is carried out between the proposed spoke-type IPM machines having rotors with and without staggered steps, respectively, as shown in Fig. C.10. In order to fully consider the end leakage flux, the axial length of end shaft is selected as 30mm, which is similar to the radial distance between stator and shaft outer circumferences. For the rotor without staggered steps, unipolar leakage flux exists and the flux density is up to 0.01T for positions within the axial length of 4mm. As the axial distance increases, the flux density decreases and almost remains stable at 0.04T, as shown in Fig. C.10 (a). With the step-staggered rotor employed, the leakage flux density around the end shaft surface is significantly reduced to very low extent, although certain fluctuation (±0.02T) remains at positions adjacent to the rotor end surface, as shown in Fig. C.10 (b). More importantly, unipolar leakage flux is eliminated, replaced by bipolar leakage flux, and it can be further deduced that the magnetization of end shaft is effectively minimized.

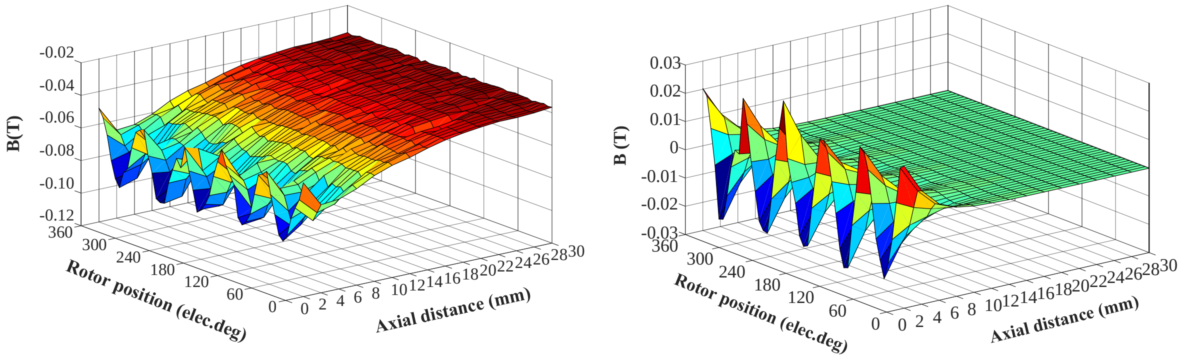

(a) Rotor without staggered steps.

(b) Rotor with staggered steps.

Fig. C.10 Comparison of flux density at different positions of the end shaft surface.

Due to the different paths of leakage flux, the torque capability is re-assessed for the proposed spoke-type IPM machine with step-staggered rotor. With the 3D FE method employed, the torque performance of the proposed design is obtained and a comparison is carried out between the machines having rotors with and without staggered steps, respectively, as shown in Fig. C.11 (a). It can be seen that the average torque slightly decreases from 4.40 Nm to 4.32 Nm, which is mainly caused by a little more leakage flux flowing through the iron ribs of the step-staggered rotor. In addition, a comparison of the torque-current characteristics between the two designs is carried out with the current increasing from 0 to 80A, which also indicates the approximate torque capability, as shown in Fig. C.11 (b).

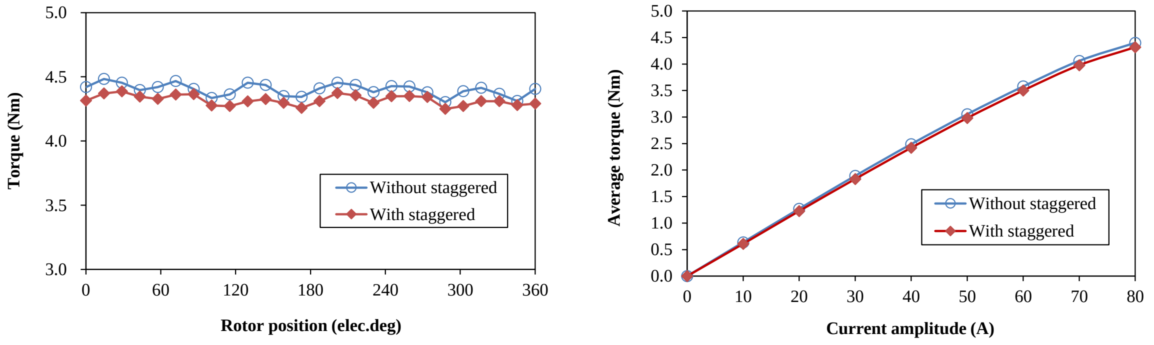

(a) Torque at rated current

(b) Torque-current characteristics

Fig. C.11 Comparison of torque capability between rotors with and without staggered steps.

In addition to the foregoing electromagnetic performance, mechanical strength of the spoke-type IPM machine having step-staggered rotor with alternate airspace barriers is also investigated. Due to the axial asymmetry, the 3D FE static structural module of the Ansys software is employed (mesh by Tetrahedrons of 0.5mm~2.0mm sizes), with mechanical stress and deformation shown in Fig. C.12. Compared with the mechanical stress shown in Fig. C.5, the maximum value at the speed of 5000rpm is decreased from 34.4 MPa to 21 MPa with the step-staggered rotor employed. Therefore, the manufacturing process of spoke-type IPM machines can be effectively simplified, without obvious deterioration of the mechanical strength.

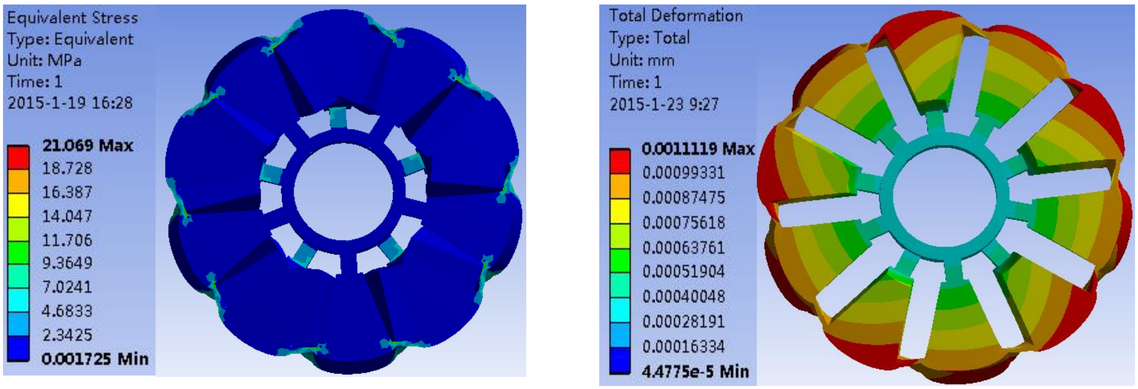

(a) Mechanical stress (b) Deformation

Fig. C.12 Mechanical strength of the proposed spoke-type IPM rotor (5000rpm).

It should be noted that the foregoing analyses of mechanical strength are based on the fundamental model of the proposed design at a typical maximum speed of EPS motor. However, for high-speed applications, e.g. the washing machine systems, magnetic and structural trade-off designs should be usually involved to satisfy the mechanical strength requirements. Since the torque capability is not sensitive to the iron rib width, wider iron ribs employed in the proposed design exhibits good manufacturability and mechanical reliability.

C.4 Experimental Validation

In order to verify the foregoing analyses, prototypes based on the main parameters shown in Table I are fabricated, including one common stator and three different spoke-type IPM rotors with conventional airspace barriers (1mm iron ribs), alternate airspace barriers (2mm iron ribs) and step-staggered alternate airspace barriers (2mm iron ribs) respectively, as shown in Fig. C.13.

(a) Stator part (b) Rotor with conventional airspace barriers

(c) Rotor with alternate airspace barriers. (d) Step-staggered rotor with alternate airspace barriers

Fig. C.13 Spoke-type IPM machine prototypes.

For the first step, the magnetic field on the surface of the end shaft is measured with a gauss-meter, and Fig. C.14 illustrates the field results of the three different rotors respectively. As can be seen, the magnetic field at the end shaft increases from 0.001T to 0.042T, with alternate airspace barriers employed. Even for different rotor positions, the magnetic field remains an identical direction, which agrees well with the 3D FE analyses and verifies magnetization of the end shaft. For the step-staggered rotor, the leakage field at the end shaft is effectively improved, decreasing to 0.005T, which indicates that magnetization of the end shaft is no longer a problem for the step-staggered rotor with alternate airspace barriers. However, it should be also noted that the field of 0.005T is still higher than the 3D FE result, which is mainly due to the two asymmetric rotor steps during the prototype fabrication. Actually, the magnetic field at the end shaft can be further reduced to lower extent by employing more staggered rotor steps (e.g. four steps), through which the influence of manufacturing tolerances can be reduced.

(a) Rotor with conventional airspace barriers

(b) Rotor with alternate airspace barriers

(c) Step-staggered rotor with alternate airspace barriers.

Fig. C.14 Flux density at the end shaft.

In addition to the magnetic field at the end shaft, electromagnetic performance of the proposed design are also tested and compared with the 3D FE results, including the back electromagnetic force (EMF) and the static torque. Fig. C.15 (a) illustrates the line back EMF of the prototype with the proposed design. It can be seen that the test result agrees well with the 3D FE analyses, both of which have the magnitude of about 2.8V at the speed of 370rpm. Furthermore, the static torque can be obtained with a DC current applied to the three phases of windings (Ia = 20A, Ib = -10A, Ic = -10A), and the peak value is proven to be 1.15 Nm, which agrees well with the results by 3D FE method.

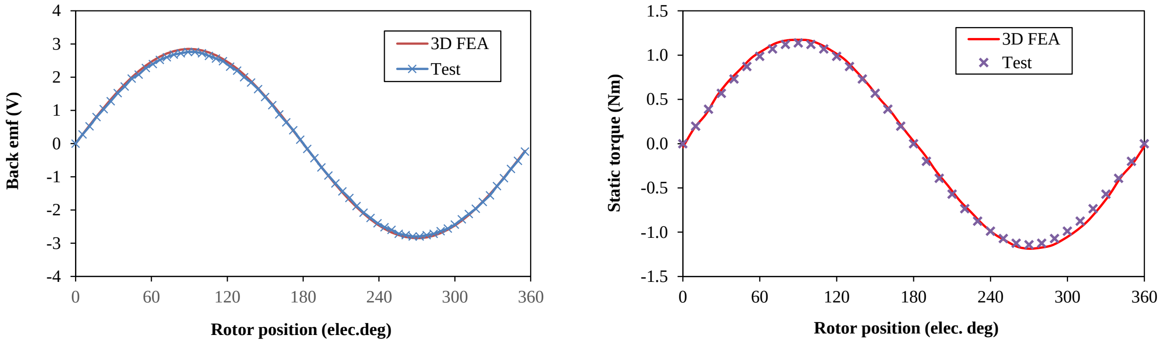

(a) Line back EMF at 370rpm

(b) Static torque by 20A DC current

Fig. C.15 Comparison of 3D FE and test results.

C5. Unipolar Leakage Flux in Consequent-Pole Pm Machines

Investigations have been made on the unipolar leakage flux in the spoke-type IPM machine with alternate airspace barriers, resulting in magnetization of the end shaft, which can be eliminated by the step-staggered rotor. In this section, the end leakage flux distribution in consequent-pole PM machines is further investigated, as an extension of the foregoing analyses.

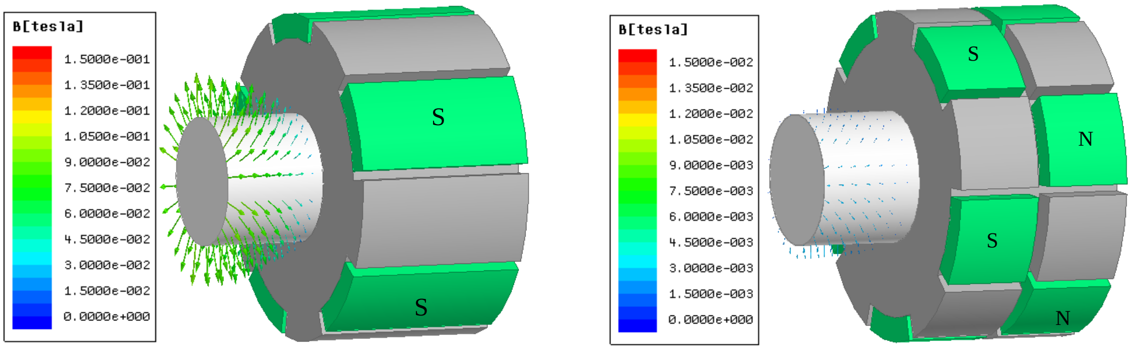

(a) basic consequent-pole rotor (b) step-staggered consequent-pole rotor

Fig. C.16 Flux density vector at the end shaft of consequent-pole PM machine.

Based on similar parameters shown in Table I, a typical consequent-pole PM machine model is established. With the 3D FE method employed, the end leakage flux distribution on the end shaft surface is obtained, as shown in Fig. C.16 (a). It can be seen that unipolar leakage flux is also introduced, which results in magnetization of the end shaft. Similar to the step-staggered rotor proposed in the previous section, a rotor with step-staggered PMs - which was used in hybrid consequent-pole PM machines [TAP03] - is employed to improve the end leakage flux distribution, as shown in Fig. C.16 (b). As can be seen, the flux density on the end shaft surface is significantly reduced from 0.07T to a very low extent, which verifies the effectiveness of the step-staggered method. Not restricted to the surface-mounted consequent-pole PM machines, similar phenomenon proves to exist in radial-type IPM machines with consequent-pole styles, in which the step-staggered method can be also employed to solve the common problems.

Recently, spoke-type IPM machines with auxiliary radial PMs in consequent-pole styles are proposed in order to improve the flux distributions [GE12], [RAH14], and [BOU14], as shown in Fig. C.17. According to the topology, 3D FE models are established and analyzed, based on similar parameters listed in Table C-I. It can be seen from Fig. C.18 (a) that the unipolar leakage flux is also introduced, as well as magnetization of the end shaft. Similarly, the problem can be also effectively solved through the proposed step-staggered method, as shown in Fig. C.18 (b).

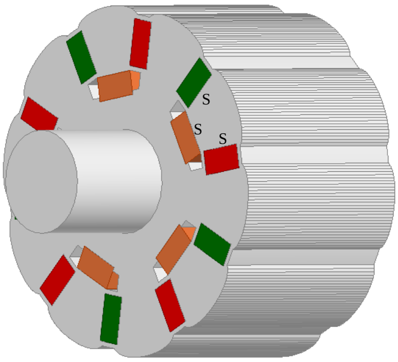

Fig. C.17 Spoke-type IPM machine with auxiliary radial PMs arranged in consequent-poles.

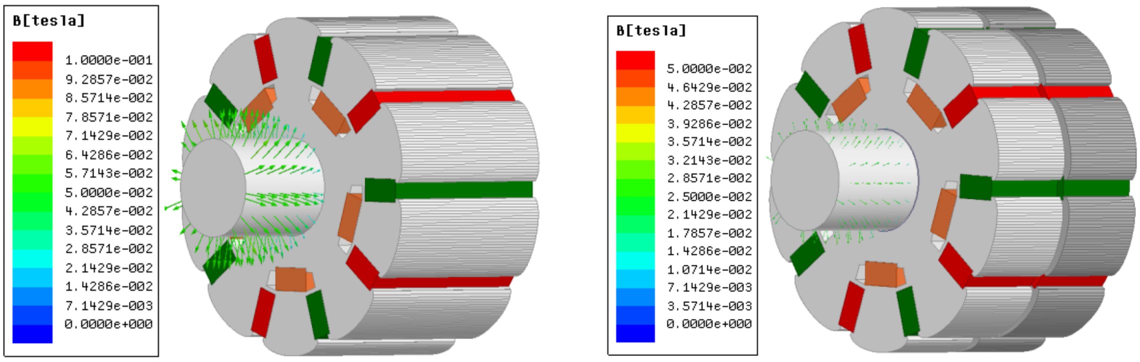

(a) Without step-staggered PMs

(b) With step-staggered PMs

Fig. C.18 Flux density vector at end shaft of spoke-type IPM machine with auxiliary PMs.

However, it should be also noted that additional axial air-gaps between the steps are usually necessary when the step-staggered method is employed in consequent-pole PM machines, which can effectively reduce the leakage flux and make an efficient use of the PM materials. In addition, the 3D FE method should be employed in order to make a more accurate prediction of related performance, with the 3D end leakage flux in such topologies considered.

C.6 Conclusion

A spoke-type IPM machine using a novel step-staggered rotor with alternate airspace barriers has been proposed in this paper, which significantly simplifies the manufacturing process of conventional spoke-type IPM rotors without obvious deterioration of the mechanical strength at a high operating speed. Furthermore, unipolar leakage flux has been proved to be a common problem with consequent-pole PM machines, resulting in magnetization of the end shaft, which can be effectively reduced by the step-staggered method. Prototypes with different rotors have been fabricated and tested to verify the analyses, including the magnetic field and the torque capability.

REFERENCES

[AZA12] Z. Azar, Z.Q. Zhu, and G. Ombach, “Investigation of torque-speed characteristics and cogging torque of fractional-slot IPM brushless AC machines having alternate slot openings,” *IEEE Ind. Appl.*, vol. 48, no. 3, pp. 903-912, Mar. 2012.

[BOU14] K. Boughrara, R. Ibtiouen, and N. Takorabet, “Analytic calculation of magnetic field and electromagnetic performances of spoke type IPM topologies with auxiliary magnets,” in *Int. Conf. Elect. Mach.* (ICEM), Berlin, Germany, Sep. 2014, pp. 51-57.

[DEM13] Y. Demir, O. Ocak, and M. Aydin, “Design, optimization and manufacturing of a spoke type interior permanent magnet synchronous motor for low voltage-high current servo applications,” in *Int. Elect. Mach. & Drive Conf.* (IEMDC), Chicago, IL, May 2013, pp. 9-14.

[DEM14] Y. Demir and M. Aydin, “Design of a spoke type IPM synchronous motor with segmented rotor for low DC voltage applications,” in *Energy Conver. Congr. and Expo.* (ECCE), Pittsburgh, USA, Sep. 2014, pp. 3556-3561.

[DUT08] R. Dutta and M.F. Rahman, “Design and analysis of an interior permanent magnet (IPM) machine with very wide constant power operation range,” *IEEE Trans. Energy Conver.*, vol. 23, no. 1, pp. 25-33, Mar. 2008.

[GE12] X. Ge, J.T. Chen, and Z.Q. Zhu, “Rotary motor with consequent –pole PM rotor,” Chinese Patent, 102570662A, Jul. 11, 2012.

[HWA09] K.Y. Hwang, J.H. Jo, and B.I. Kwon, “A study on optimal pole design of spoke-type IPMSM with concentrated winding for reducing the torque ripple by experiment design method,” *IEEE Trans. Magn.*, vol. 45, no. 10, pp. 4712-4715, Sep. 2009.

[IBR14] M. Ibrahim and P. Pillay, “Design of high torque density variable flux permanent magnet machine using Alnico magnets,” in *Energy Conver. Congr. and Expo*. (ECCE), Pittsburgh, USA, Sep. 2014, pp. 3535-3540.

[JAH86] T.M. Jahns, G.B. Kliman, and T.W. Neumann, “Interior permanent-magnet synchronous motors for adjustable-speed drives,” *IEEE Trans. Ind. Appl.*, vol. 22, no. 4, pp. 738-747, Jul. 1986.

[KAK13] W. Kakihara, M. Takemoto, and S. Ogasawara, “Rotor structure in 50 kW spoke-type interior permanent magnet synchronous motor with ferrite permanent magnets for automotive applications,” in *Energy Conver. Congr. and Expo*. (ECCE), Denver, U.S.A., Sep. 2013, pp. 606-613.

[KIM13a] S. Kim, J. Cho, S. Park, T. Park, and S. Lim, “Characteristics comparison of a conventional and modified spoke-type ferrite magnet motor for traction drives of low-speed electric vehicles,” *IEEE Trans. Ind. Appl.*, vol. 49, no. 6, pp. 2516-2523, May 2013.

[KIM13b] D.Y. Kim, J.K. Nam, and G.H. Jang, “Reduction of magnetically induced vibration of a spoke-type IPM motor using magnetomechanical coupled analysis and optimization,” *IEEE Trans. Magn.*, vol. 49, no. 9, pp. 5097-5105, Apr. 2013.

[LEE04] B.K. Lee, G.H. Kang, J. Hur, and D.W. You, “Design of spoke type BLDC motors with high power density for traction applications,” in 39th *IAS Annu. Meeting Conf. Rec. of IEEE* 2004, Oct. 2004, pp. 1068-1074.

[MIR13] H. Mirahki and M. Moallem, “Design improvement of interior permanent magnet synchronous machine for integrated starter alternator application,” in *Elect. Mach. & Drive Conf.* (IEMDC), Chicago, IL, May 2013, pp.382-385.

[QI09] W.D. Qi, “Punching,” in Concise design handbook of punching tools, Beijing, China: BITP, 2009, ch.2, pp. 24-74.

[RAH08] M.A. Rahman, “Advances of interior permanent magnet (IPM) wind generators,” in *Int. Conf. Elect. Mach. Syst.* (ICEMS), Wuhan, China, Oct. 2008, pp. 2228-2233.

[RAH14] M.M. Rahman, K.T. Kim, and J. Hur, “Design and optimization of neodymium-free spoke-type motor with segmented winding-shaped PM,” *IEEE Trans. Magn.*, vol. 50, no. 2, pp. 865-868, Feb. 2014.

[RED14] P.B. Reddy, K.K. Huh, and A.M. EL-Refaie, “Generalized approach of stator shifting in interior permanent-magnet machines equipped with fractional-slot concentrated windings,” *IEEE Trans. Ind. Electron*., vol.61, no. 9, pp. 5035-5046, Jan. 2014.

[TAN97] R.Y. Tang, “Permanent magnet synchronous generators,” in *Modern permanent magnet machines*, Beijing, China: CPM, 1997, ch. 8, pp. 273-292.

[TAP03] J.A. Tapia, F. Leonardi, and T.A. Lipo, “Consequent-pole permanent-magnet machine with extended field-weakening capability,” *IEEE Trans. Ind. Appl.*, vol. 39, no. 6, pp. 1704-1709, 2003.

[WAN08] A.M. Wang, H.M. Li, and C.T. Liu, “On the material and temperature impacts of interior permanent magnet machine for electric vehicle applications,” *IEEE Trans. Magn.*, vol. 44, no. 11, pp. 4329-4332, Nov. 2008.

[WAN12] K. Wang, Z.Q. Zhu, G. Ombach, and W. Chlebosz, “Optimal rotor shape with third harmonic for maximizing torque and minimizing torque ripple in IPM motors,” in *Int. Conf. Elect. Mach.* (ICEM), Marseille, France, Sep. 2012, pp. 397-403.

[WU09] L.J. Wu, Z.Q. Zhu, J.T. Chen, Z.P. Xia, and G.W. Jewell, “Optimal split ratio in fractional-slot interior permanent-magnet machines with non-overlapping windings,” *IEEE Trans. Magn.*, vol. 46, no. 5, pp. 1235-1242, Dec. 2009.

PUBLICATIONS

Journal papers published or in press:

(1) **X. Ge**, Z.Q. Zhu, R. Ren, and J.T. Chen, "Analysis of windings in variable reluctance resolver," *IEEE Trans. on Magnetics,* vol.51, no.5, pp.8104810, May 2015.

(2) **X. Ge**, Z.Q. Zhu, R. Ren, and J.T. Chen, "A novel variable reluctance resolver with non-overlapping tooth-coil windings," *IEEE Trans. on Energy Conversion*, vol.30, no.2, pp.784-794, June 2015.

(3) **X. Ge**, Z.Q. Zhu, "A novel design of rotor contour for variable reluctance resolver by injecting auxiliary air-gap permeance harmonics," *IEEE Trans. on Energy Conversion*. vol.31, no.1, pp. 345-353, Sep. 2015.

(4) **X. Ge**, Z.Q. Zhu, J.B. Li, and J.T. Chen, "A spoke-type IPM machine with novel alternate airspace barriers and reduction of unipolar leakage flux by step-staggered rotor," *IEEE Trans. on Industry Application*. In press.

(5) **X. Ge**, Z.Q. Zhu, R. Ren, and J.T. Chen, "A novel variable reluctance resolver for HEV/EV applications," *IEEE Trans. on Industry Application*. In press.

(6) Z.Q. Zhu, D. Wu, and **X. Ge**, "Investigation of voltage distortion in fractional slot interior permanent magnet machines having different slot and pole number combinations," submitted to *IEEE Trans. on Energy Conversion*. Revised.

(7) D. Wu, Z. Q. Zhu, and **X. Ge**, "Terminal voltage distortion in interior permanent magnet machines with fractional slot concentrated windings by different slot and pole number combinations," submitted to *IEEE Trans. on Energy Conversion*. Revised.

(8) D. Wu, Z. Q. Zhu, and **X. Ge**, "Effectiveness of terminal voltage distortion minimization methods in fractional slot surface-mounted permanent magnet machines considering local magnetic saturation," submitted to *IEEE Trans. on Energy Conversion*. Revised.

(9) Y. Oner, Z. Q. Zhu, L. J. Wu, **X. Ge**, H. L. Zhan, and J. T. Chen, "Analytical on-Load sub-domain field model of permanent magnet vernier machine," *IEEE Trans. on Industrial Electronics*. In press.

(10) D.J. Evans, Z. Q. Zhu, H.L. Zhan, Z.Z. Wu, and **X. Ge**, "Flux-weakening control performance of partitioned stator switched flux PM machines," *IEEE Trans. on Industry Application*. In press.

(11) C.C. Awah, Z.Q. Zhu, Z.Z. Wu, H.L. Zhan, J.T. Shi, D. Wu, and **X. Ge**, “Comparison of partitioned stator switched flux permanent magnet machines having single- or double-layer windings,” *IEEE Trans. on Magnetics*, vol. 52, no. 1, pp. 9500310, 2016.

(12) Y. Oner, Z. Q. Zhu, L.J. Wu, **X. Ge**, “Analytical sub-domain model for predicting open-circuit field of permanent magnet Vernier machine accounting for tooth tips,” *COMPEL: The International Journal for Computation and Mathematics in Electrical and Electronic Engineering*, vol.35, no.2, 2016.

(13) Y. Oner, Z. Q. Zhu, L.J. Wu, **X. Ge**, “Sub-domain analytical model for armature reaction field of permanent magnet Vernier machine,” *COMPEL: The International Journal for Computation and Mathematics in Electrical and Electronic Engineering*, vol.35, no.2, 2016.

(14) C. C. Awah, Z. Q. Zhu, Z. Z. Wu, D. Wu, and **X. Ge**, “High torque density magnetically geared switched flux permanent magnet machines,” *COMPEL: The International Journal for Computation and Mathematics in Electrical and Electronic Engineering*, vol.35, no.2, 2016.

Submitted:

(15) **X. Ge**, Z.Q. Zhu, G. Kemp, D. Moule, and C. Williams, “Optimal step-skewing methods for cogging torque reduction accounting for 3-dimensional effect of interior permanent magnet machines,” submitted to *IEEE Trans. Energy Conversion*.

(16) **X. Ge** and Z. Q. Zhu, “Additional cogging torque components in interior permanent magnet machines accounting for manufacturing tolerances,” submitted to *IEEE Trans. Magnetics*.

(17) **X. Ge** and Z. Q. Zhu, “Influence of manufacturing tolerances on cogging torque in interior permanent magnet machines with eccentric and sinusoidal rotor contours,” submitted to *ECCE 2016*, submitted to *IEEE Trans. on Industry Application.*

(18) **X. Ge** and Z. Q. Zhu, “Sensitivity of manufacturing tolerances on cogging torque in interior permanent magnet machines with different slot/pole number combinations,” submitted to *ECCE 2016*, submitted to *IEEE Trans. on Industry Application.*

(19) Z. Q. Zhu and **X. Ge**, “Optimal step-skewing methods for permanent magnet machines with different PM materials accounting for cogging torque, axial unbalanced force and unipolar leakage flux,” submitted to *IEEE Trans. Energy Conversion*.

Conference papers:

(1) **X. Ge**, Z.Q. Zhu, R. Ren, and J.T. Chen, "A novel variable reluctance resolver for HEV/EV applications," in *International Electric Machines. & Drive Conference* (IEMDC) 2015.

(2) **X. Ge**, Z.Q. Zhu, J.B. Li, and J.T. Chen, "A spoke-type IPM machine with novel alternate airspace barriers and reduction of unipolar leakage flux by step-staggered rotor," in *International Electric Machines. & Drive Conference* (IEMDC) 2015.

(3) Y.J. Zhou, Z.Q. Zhu, and **X. Ge**, "Comparison of torque densities in alternate wound-field switched flux machines," in *International Conference on Electrical Machines and Systems* (ICEMS) 2014.

(4) W.Q. Chu, Z.Q. Zhu, J. Zhang, **X. Ge**, X. Liu, D. Stone, and M. Foster, "Comparison of electrically excited and interior permanent magnet machines for hybrid electric vehicle applications," in *International Conference on Electrical Machines and Systems* (ICEMS) 2014.

(5) D.J. Evans, Z.Q. Zhu, Z.Z. Wu, H.L. Zhan, and **X. Ge**, "Comparative analysis of parasitic losses in partitioned stator switched flux pm machines with double- and single-layer windings," in *International Electric Machines. & Drive Conference* (IEMDC) 2015.

(6) D.J. Evans, Z.Q. Zhu, H.L. Zhan, Z.Z. Wu, and **X. Ge**, "Mechanical flux-weakening of partitioned stator switched flux PM machine," in *International Electric Machines. & Drive Conference* (IEMDC) 2015.

(7) H. Hua, Z.Q. Zhu, M. Zheng, Z.Z. Wu, and **X. Ge**, "Performance comparison of partitioned stator machines with NdFeB and ferrite magnets," in *International Electric Machines. & Drive Conference* (IEMDC) 2015.